

Abdullah Al-Hamdi

**SYNTHESIS AND COMPARISON OF
THE PHOTOCATALYTIC ACTIVITIES OF ANTIMONY,
IODIDE, AND RARE EARTH METALS ON SnO₂ FOR THE
PHOTODEGRADATION OF PHENOL AND
ITS INTERMEDIATES UNDER UV,
SOLAR AND VISIBLE LIGHT IRRADIATIONS**

Thesis for the degree of Doctor of Science (Technology) to be presented with due permission for public examination and criticism in the Auditorium of MUC, Mikkeli University Consortium, Mikkeli, Finland on the 18th of August, 2017, at noon.

Acta Universitatis
Lappeenrantaensis 760

- Supervisor Professor Mika Sillanpää
Department of Chemical Technology
Laboratory of Green Chemistry
Lappeenranta University of Technology
Mikkeli, Finland
- Reviewers Professor. Leslie Petrik
Department of Chemistry
University of the Western Cape
Bellville 7535 South Africa
- Professor. Jana Drbohlavová
Faculty of Electrical Engineering and Communication at BUT
University of Brno
Czech Republic
- Opponent Professor. Ulla Lassi
Head of the Unit, D.Sc. (Tech.)
University of Oulu, Faculty of Technology
Research Unit of Sustainable Chemistry
Oulu, Finland

ISBN 978-952-335-116-5
ISBN 978-952-335-117-2 (PDF)
ISSN-L 1456-4491
ISSN 1456-4491

Lappeenrannan teknillinen yliopisto
Yliopistopaino 2017

ABSTRACT

Abdullah M. Al-Hamdi

Synthesis and comparison of the photocatalytic activities of antimony, iodide, and rare earth metals on SnO₂ for the photodegradation of phenol and its intermediates under UV, solar and visible light irradiations

Lappeenranta 2017

232 pages

Acta Universitatis Lappeenrantaensis 760

Diss. Lappeenranta University of Technology

ISBN 978-952-335-116-5, ISBN 978-952-335-117-2 (PDF), ISSN-L 1456-4491,

ISSN 1456-4491

The tremendous amounts of pollutants being dumped into the water have become a major problem all over the world which let researchers to focus on. These chemicals are stubborn toxins not easily eliminate, difficult to keep up can go transformations under certain conditions, after conversion might become more toxic than their parent molecule. There are many ways to withdraw these organic compounds from the water sources, the cheapest way is to use photocatalytic material oxides like SnO₂ through harnessing the sunlight and using it for photocatalytic degradation processes. Photocatalysis by advanced oxidation processes is a most popular and promising method of taking away these contaminants such as phenol and its intermediates form water.

Tin dioxide (SnO₂) has already been used in detecting some of toxic gases and involved in many other technological applications. SnO₂ is a strong oxidizing agent and a powerful reducing catalyst, a variety of techniques utilized to improve the photocatalytic activities of SnO₂ including doping and others. Photodegradation of phenol in the presence of SnO₂ Nps under UV light irradiation is known to be an effective photocatalytic process. However, phenol photodegradation under solar and visible light irradiation is less effective due to the large band gap (BG) of SnO₂. In this study, pure SnO₂ catalysts been synthesized by a sol-gel method using tin tetrachloride, ethanol and water. For the synthesis of SnO₂ doped with species containing different ions such as [gadolinium (Gd), cerium (Ce), Lanthanum (La), neodymium (Nd), iodine (I) and antimony (Sb)], different

concentrations of these dopants such as (0.01%, 0.1%, 0.2%, 0.3%, 0.4%, 0.6%, 0.8%, 1.0%, and 1.1%) were mixed and dissolved separately in ethanol and water later added to the precursor solution. At the final stages ammonia was added to cause gelation of the sol. The sol-gel formed was washed and prepared at low temperature to obtain the SnO₂ nanoparticles (Nps).

SnO₂ powders been characterized by X-ray diffraction (XRD), scanning electron microscope (SEM), transition electron microscope (TEM) and the specific surface area was estimated by Brunauer–Emmett–Teller (BET) analyser. Several analytical techniques were used in the analysis of phenol and its byproducts such as high performance liquid chromatography (HPLC), UV-Vis spectrophotometry, gas chromatography (GC), capillary electrophoresis (CE), total organic carbon (TOC) measurements, Fourier transformer infrared (FTIR) and by determining chemical oxygen demand (COD) from the pollutant. The results show that a decrease in the particle size from 8 to 1.8 nm and increase in the surface area up to 58 m²/g upon increasing of different doping contents from 0% to 1.1% as they incorporate into SnO₂.

In this study, The optimum parameters were found to be catalyst loading (65 mg/50.00 mL), light intensity (8 W mercury lamp, 300 W xenon lamp or sunlight during full sunny days), reaction time (2-3 h), phenol concentration (10 ppm), 4 L/min of an optimum air flow, sampling time (12-13), sample volume (250.00 mL), and pH of the reaction medium was (5.7). The GC study shows that the irradiation of the catalyst by UV light was found to enhance phenol photodegradation in the first 30 min of the experiment. The UV-Vis investigation of the treated phenol samples indicates that phenol molecules initially transform to byproducts, which also optically absorb in the similar region as phenol. In this study, for photocatalysis experiments on phenol photodegradation the optimum condition applied under UV light irradiation allowed more than 95% of phenol degradation with SnO₂/La 0.6 wt. % after 2 h. Also, 95% of phenol was found to degrade with the photoactivity of SnO₂/Sb 0.6 wt. % under solar light irradiations, the same amount of phenol photodegradation was found with SnO₂/Gd 0.6 wt. % under visible light irradiation and with exactly the same optimum conditions only changing the light

source. HPLC results show that the intermediates are in the order catechol (Cat) > resorcinol (Res) > hydroquinone (HQ) > benzoquinone (BQ), but the last stages of phenol photodegradation show isopropanol (2-P) and acetic acid (AA). The reaction of phenol photodegradation results indicate that it takes place when light radiation photoexcites a catalyst in the presence of oxygen, hydroxyl radical ($\cdot\text{OH}$) is generated to attack phenol and reacts with OH^- to produce Cat or HQ, which on continuous oxidation breaking them down leading to the formation of aliphatic acids and finally yielding carbon dioxide (CO_2) and water (H_2O). In fact, the mineralization process starts early during the photocatalytic degradation process as Fourier transform infrared FTIR results showed that the phenol molecules are converted to CO_2 in the early stages and continued until all phenol are removed. The change in the concentration of phenol affects the pH of the solution due to the intermediates formation during the photodegradation of phenol. Clear correlations between the results obtained from these multiple measurements were found, and a kinetic pathway for the degradation process was proposed. A maximum of 0.02228 min^{-1} of propanol and a minimum of AA $0.013412 \text{ min}^{-1}$ were recorded.

Keywords: Tin dioxide, nanoparticles, semiconductor, phenol and phenolic compounds, water purification, rare earth doping, transition metal doping, photocatalysis, visible light photocatalysis

Acknowledgements

The research work for this PhD thesis was conducted at the laboratory of Green Chemistry in Mikkeli from April 2012–Aug 2017.

I am extremely grateful to my supervisor Professor Mika Sillanpää for providing me the opportunity to carry out this study and for his support throughout the whole course of this work.

I would like to thank Professor Joydeep Dutta for his valuable guidance on experimental work and preparation of the manuscripts.

I am very grateful to the staff of the Laboratory of Green Chemistry for all their support and assistance. Most of all I would like to thank Dr. Eveliina Repo and Mikko Rantalankila for their priceless help during my work. Finally, my gratitude also goes to colleagues and friends from the research group Chair in Nanotechnology, Water Research Centre at Sultan Qaboos University, Muscat Oman.

List of publications

- I. **A. M. Al-Hamdi**, M. Sillanpää, J. Dutta (2014). Photocatalytic degradation of phenol in aqueous solution by rare-earth-doped SnO₂ nanoparticles. *Journal of Material Science*, 49, pp. 5151-5159.
- II. **A. M. Al-Hamdi**, M. Sillanpää, J. Dutta (2015). Photocatalytic degradation of phenol by iodine doped tin oxide nanoparticles under UV and sunlight irradiation. *Journal of Alloys and Compounds*, 618, pp. 366-371.
- III. **A. M. Al-Hamdi**, M. Sillanpää, Tanujjal Bora, J. Dutta (2016) Efficient photocatalytic degradation of phenol in aqueous solution by SnO₂/Sb nanoparticles. *Applied Surface Science*, 370 pp 229-236.
- IV. **A. M. Al-Hamdi**, M. Sillanpää, J. Dutta (2015). Gadolinium doped tin dioxide nanoparticles: an efficient visible light active photocatalyst. *Journal of Rare Earths*. 33 12 pp 1275–1283.
- V. **A. M. Al-Hamdi**, M. Sillanpää, J. Dutta (2015). Intermediate formation during photodegradation of phenol using La doped tin dioxide nanoparticles, *Journal of Research on Chemical Intermediates*. 42 pp 3055-3069.
- VI. **A. M. Al-Hamdi**, Uwe Rinner, Mika Sillanpää (2017) Tin dioxide as a photocatalyst for water treatment: A review, *Process Safety and Environmental Protection*. 107 pp190-205.

AUTHORS CONTRIBUTION IN THE PUBLICATIONS

- I.** The author carried out all experiments, analysed the data, and prepared the first draft of the manuscript.
- II.** The author carried out all experiments, analysed the data, and prepared the first draft of the manuscript.
- III.** The author carried out all experiments, analysed the data, and prepared the first draft of the manuscript.
- IV.** The author carried out all experiments, analysed the data, and prepared the first draft of the manuscript.
- V.** The author carried out all experiments, analysed the data, and prepared the first draft of the manuscript.
- VI.** The author carried out all experiments, analysed the data, and prepared the first draft of the manuscript.

OTHER PUBLICATIONS BY THE SAME AUTHOR

A. M. Al-Hamdi, J. R. Williams, S. M. Z. Al-Kindy, A. E. Pillay (2006). Optimization of a high-performance liquid chromatography method to quantify bilirubin and separate it from its photoproducts, *Applied Biochemistry and Biotechnology*. 3 (135) 209-218,

CONFERENCES

A. M. Al-Hamdi, M. Sillanpää, J. Dutta, Photocatalytic degradation of phenol in aqueous solution by rare-earth-doped SnO₂ nanoparticles, Global Issues in Multidisciplinary **Academic Research**, **Gimar**, **2015**. Dubai U.A.E.

Contents

Abstract

Acknowledgements

Contents

List of publications	8
LIST OF TABLES	17
LIST OF FIGURES	18
Nomenclature	23
CHAPTER 1	29
1 Introduction	29
1.1 Background	29
1.2 Phenol	29
1.3 Semiconductor photocatalysis	32
1.4 Semiconductor photocatalysts	35
1.5 Research objectives	38
1.6 Hypothesis	39
1.7 Research questions addressed	40
1.8 Research approach.....	40
1.9 Scope of study	42
1.10 Delimitations of study	43
1.11 Methodology	44
1.12 Structure of the report.....	44
2 CHAPTER 2	47
2.1 Tin dioxide (SnO ₂) catalysts.....	47
2.2 Photocatalytic activity of SnO ₂ in aqueous solution	51
2.2.1 Electron hole pairs generation.....	52
2.2.2 Traps for holes	52
2.2.3 Traps for electrons	52
2.3 Application of undoped SnO ₂ in the photocatalytic degradation of organic pollutants	55
2.3.1 Improving SnO ₂ photodegradation efficiency	57
2.3.2 Improving photodegradation efficiency by selective doping of SnO ₂	57
2.3.2.1 SnO ₂ coupled with other semiconductors	57

2.3.3	SnO ₂ doped with metal and metalloids	64
2.3.3.1	SnO ₂ doped with RE metals	65
2.3.3.2	SnO ₂ doped with TMs	67
2.3.3.3	SnO ₂ doped with metalloids	70
2.3.3.4	Other metals doped SnO ₂	71
2.3.4	SnO ₂ doped with non-metal ions	75
2.3.4.1	Iodine doped tin oxide	75
2.4	SnO ₂ synthesis methods	78
2.4.1	Sol-gel	78
2.4.1.1	Dip-coating	79
2.4.1.2	Spin coating	79
2.4.1.3	Laminar flow coating	79
2.4.1	Coprecipitation	79
2.4.2	Hydrothermal and solvothermal methods	81
2.4.3	Pyrolysis	82
2.4.4	Soft chemistry	82
2.4.5	Polyolmediated fabrication	83
2.4.6	Chemical vapour deposition	83
2.4.7	Solid state reaction	83
2.4.8	Mechanochemical reaction	84
2.4.9	Milling technique	84
2.4.10	Thermal decomposition and electrodeposition	84
2.4.11	Insertion methods	84

3	Experimental	87
3.1	Chemical and materials	87
3.2	Photocatalyst preparation	88
3.2.1	Synthesis of pure (control) SnO ₂ Nps	88
3.2.2	Synthesis of doped SnO ₂ Nps	89
3.2.2.1	Synthesis of SnO ₂ /I Nps	89
3.2.2.2	Synthesis of SnO ₂ /Nd Nps	91
3.2.2.3	Synthesis of SnO ₂ /La Nps	91
3.2.2.4	Synthesis of SnO ₂ /Ce Nps	92
3.2.2.5	Synthesis of SnO ₂ /Sb Nps	93
3.2.2.6	Synthesis of SnO ₂ /Gd Nps	94
3.3	Sol-gel preparation	96
3.3.1	Sol-gel method	96
3.4	Powder preparation	97
3.5	Reactors	98
3.5.1	UV photocatalytic reactor	98
3.5.2	Visible light photocatalytic reactor	99
3.5.3	Solar light photocatalytic reactor	100
3.6	Experimental procedures	101
3.6.1	Optimization of experimental parameters	101
3.6.1.1	Catalyst loading	101

List of publications

3.6.2	Pollutant concentration	101
3.6.3	Effect of the pH of the solution.....	102
3.6.4	Sampling from the reactor.....	103
3.7	Characterization techniques	104
3.7.1	X-ray diffraction method (XRD)	104
3.7.1.1	Operating procedure for Rigaku Miniflex.....	104
3.7.2	Scanning electron microscopy (SEM)	105
3.7.3	Transmission electron microscopy (TEM)	105
3.7.4	The Brunauer-Emmett-Teller (BET) method	105
3.7.5	Fourier Transform Infrared Spectroscopy (FTIR)	105
3.8	Analytical methods.....	106
3.8.1	UV-Vis spectrophotometer	106
3.8.1.1	Sample preparation.....	106
3.8.1.2	UV-Vis analysis	106
3.8.2	Total organic carbon analyser (TOC)	107
3.8.3	Chemical oxygen demand (COD).....	107
3.8.3.1	Colorimetric method for the measurement of COD	107
3.9	High performance liquid chromatography (HPLC)	108
3.9.1	HPLC analysis.....	109
3.9.1.1	HPLC mobile phase preparation	109
3.10	Gas chromatography (GC)	110
3.10.1	Sample preparation	110
3.10.2	Chemical analysis	111
3.11	Capillary electrophoresis (CE)	112
3.11.1	Photolytic degradation	114
4	Results and discussion	115
4.1	Motivation for studying phenol and its byproducts.....	115
4.2	Characterization of the synthesis materials	116
4.2.1	X-ray diffraction analysis (XRD)	116
4.2.2	Crystallinity.....	121
4.2.1	BET surface area.....	122
4.2.2	Electron microscopic analysis (SEM).....	127
4.2.3	Transmission microscopic analysis (TEM).....	129
4.3	Optical activity	133
4.4	Parameters affecting phenol photodegradation in an aqueous solution dispersion of SnO ₂	136
4.4.1	Effect of pH.....	136
4.4.2	Effect of initial phenol concentration.....	139
4.4.3	Effect of catalyst loading	142
4.4.4	Effect of air	143
4.4.5	Light intensity	144
4.4.5.1	Light λ	144
4.5	Photocatalytic degradation	145
4.5.1.1	Method development.....	152

4.5.2	Phenol photodegradation.....	153
4.5.2.1	Under UV light irradiation	154
4.5.2.2	Under solar light irradiation	156
4.5.2.3	Under visible light irradiation	157
4.6	TOC removal during phenol degradation (TOC)	158
4.7	Intermediate products of phenol photodegradation.....	165
4.7.1	HPLC separation technique	165
4.7.1.1	Method development.....	169
4.7.2	COD photodegradation measurement	173
4.7.3	GC Analysis technique.....	175
4.7.4	CE to monitor phenol and its byproducts.....	176
4.7.5	FTIR spectrum of phenol samples	178
4.8	Degradation mechanism of phenol involving the O-H bond (Formation mechanism)	179
4.8.1	Hydroquinone (HQ)	182
4.8.2	Benzoquinone (BQ)	182
4.8.3	Catechol (Cat)	183
4.8.4	Resorcinol (Res).....	183
4.8.5	Acetic acid (AA)	183
4.8.6	Isopropanol (2-P)	183
4.9	Photocatalytic degradation of different aromatic compounds.....	184
4.10	Kinetics of phenol degradation.....	186
5	Conclusions and future research	191
5.1	Recommendations	193
6	References	195
	Publications	233

LIST OF TABLES

Table 1: Oxidation potential [57-59]	32
Table 2: Band-gap energy of some photocatalysts [94-96, 104].....	35
Table 3: Properties of SnO ₂ [117, 167, 168, 170]	50
Table 4 Some photocatalytic activities of SnO ₂	56
Table 5. Improved SnO ₂ photocatalytic efficiency by TiO ₂ and ZnO semiconductors .	58
Table 6: Improved photocatalytic efficiency by coupled semiconductor.....	63
Table 7 Improved photocatalytic efficiency by RE metals	67
Table 8: Improved photocatalytic efficiency by RE metals	69
Table 9 Improved SnO ₂ photocatalytic efficiencies by Sb doped	71
Table 10 Enhanced photocatalytic activity of SnO ₂	74
Table 11: Comparison of some non-metal ion doped SnO ₂	77
Table 12: Chemicals and materials used in this study.....	87
Table 13: Comparison % of dopants and volume of SnO ₂ values.....	95
Table 14: Standard concentrations with the absorbance's of phenol	113
Table 15: Calculated crystallite of different 0.6 % doped and undoped SnO ₂ Nps from (110) peak using the Debye-Scherrer analysis	123
Table 16: Calculated crystallite size of different SnO ₂ /Sb Nps from (110) peak using the Debye-Scherrer analysis	124
Table 17: Comparison of phenol degradation after 2.5 h of irradiation with various dopants.....	155
Table 18: Comparison of phenol photodegradation after 2.5 h of solar irradiation	156
Table 19: Comparison of photocatalytic performance of different doped SnO ₂ Nps on phenol degradation	164
Table 20: Kinetic parameters of phenol and its byproducts degradation in photocatalysis by SnO ₂ /La nanoparticle.....	187
Table 21: Kinetic parameters of phenol degradation by SnO ₂ /I Nps	188

LIST OF FIGURES

Figure 1 Chemical structure of phenol and its byproducts [34-39].....	30
Figure 2: Comparison of the search term “Photocatalysis” in Scopus articles	36
Figure 3: SnO ₂ cell structure [88, 125, 152, 164, 165][166].....	49
Figure 4: Schematic representation of the oxidation process taking place on the crystal surface [115, 191]......	53
Figure 5: Different chemical photoproducts expected from phenol photodegradation [196-198]	54
Figure 6: Diagram arrangement of the photoreactor system	99
Figure 7: Diagram arrangement of the visible reactor system.....	100
Figure 8: Diagram arrangement of the solar reactor system	100
Figure 9: Calibration curve of peak area vs. concentrations (ppm) of phenol at t=0 min).	111
Figure 10: Calibration curve of absorbance vs. concentrations of phenol at t=0	114
Figure 11: X-ray diffraction (XRD) patterns of undoped SnO ₂ , SnO ₂ /I 0.2 wt. % and SnO ₂ /I 1.0 wt. % Nps synthesized by sol-gel process.....	117
Figure 12: X-ray diffraction XRD patterns of undoped SnO ₂ , SnO ₂ /Gd 0.6 wt. % and SnO ₂ /Sb 0.6 wt. % Nps synthesized by sol-gel method.	118
Figure 13: X-ray patterns of undoped SnO ₂ , SnO ₂ /Gd 0.6 wt. %, SnO ₂ /La 0.6 wt. % SnO ₂ /Nd 0.6 wt. % and SnO ₂ /Ce 0.6 wt. % Nps synthesized by sol-gel process.	119
Figure 14: XRD patterns of undoped SnO ₂ , SnO ₂ /Sb 0.2 wt. %, SnO ₂ /Sb 0.4 wt. %, and SnO ₂ /Sb 0.6 wt. % Nps synthesized by sol-gel method.	120
Figure 15: Crystallite size of undoped SnO ₂ , SnO ₂ /Ce 0.6 wt.%, SnO ₂ /Nd 0.6 wt.%, SnO ₂ /La 0.6 wt.%, SnO ₂ /Gd 0.6 wt.%, SnO ₂ /I 1.0 wt.% and SnO ₂ /Sb 0.6 wt.%, all these Nps were synthesized in the same way by sol-gel method and the parameters were same for the doping and undoping.....	122
Figure 16: Surface area calculated of undoped SnO ₂ , SnO ₂ /Ce 0.6 wt. %, SnO ₂ /Nd 0.6 wt. %, SnO ₂ /La 0.6 wt. %, SnO ₂ /Gd 0.6 wt. %, SnO ₂ /I 1.0 wt. % and SnO ₂ /Sb 0.6 wt.%	126
Figure 17: SEM images of a-undoped SnO ₂ , b-SnO ₂ /Nd 0.6 wt. %, c-SnO ₂ /Ce 0.6 wt. %, d-SnO ₂ /La 0.6 wt. % Nps synthesized by sol-gel method.....	127
Figure 18: Typical SEM images of a-SnO ₂ /I 1.0 wt. % and b-SnO ₂ /Gd 0.6 wt. % Nps	128

LIST OF FIGURES

Figure 19: Typical SEM image of SnO ₂ /Sb 0.6 wt. % Nps synthesized by sol-gel process	129
Figure 20: HR-TEM of a-undoped SnO ₂ , b-SnO ₂ /Nd 0.6 wt. %, c-SnO ₂ /Ce 0.6 wt. %, d-SnO ₂ /La 0.6 wt. % Nps.....	130
Figure 21: Typical HR-TEM of SnO ₂ /Gd 0.6 wt. % Nps synthesized by sol-gel process	131
Figure 22: HR-TEM of (a) control SnO ₂ (b) SnO ₂ /I, 1.0 wt. % Nps synthesized by sol gel process.	132
Figure 23: Typical HR-TEM of SnO ₂ /Sb 0.6 wt. % Nps synthesize by sol-gel.....	132
Figure 24: HR-TEM of SnO ₂ /Sb 0.6 wt. % Nps light field and dark field on images .	133
Figure 25: Optical absorption of SnO ₂ , SnO ₂ /Sb 0.4 wt. %, and SnO ₂ /Sb 0.6 wt. % Nps	134
Figure 26: Typical optical absorption of undoped SnO ₂ , 0.6 wt. %, Ce doped SnO ₂ , 0.6 wt. %, Nd doped SnO ₂ and 0.6 wt. %, La doped SnO ₂ Nps dried samples collected from a suspension in aqueous media.	135
Figure 27: Optical absorption of undoped SnO ₂ , and 1.0 wt. %, I doped SnO ₂ Nps....	136
Figure 28: Effect of pH adjusted value on phenol photodegradation rate, (65 mg/50.00 mL) of (SnO ₂ /Ce 0.6 wt. %), under UV light irradiation, reaction time (2-3 h), sampling time (12-13), sample volume (250.00 mL) and inlet air flow 4 L/min.	137
Figure 29: Effect of pH changes as a function of time for (65 mg/50.00 mL) SnO ₂ /I 1.0 wt. % Nps under UV light irradiation, reaction time (3 h), sampling time (12-13), sample volume (250.00 mL) and inlet air flow 4 L/min.....	138
Figure 30: Effect of initial phenol concentration on the photodegradation process for phenol concentrations (5, 10, 25, 50 ppm), catalyst loading (65 mg/50.00 mL) SnO ₂ /Gd 0.6 wt.%), under UV light irradiation, reaction time (2-3 h), sampling time, (12-13), sample volume (250.00 mL), pH of the reaction medium (5.7) and inlet air flow 4 L/min.	140
Figure 31: Effect of different catalysts loading 65 mg /50 mL, 75 mg/50 mL and 100 mg/50 mL on the photodegradation process by (0.6 wt. % SnO ₂ /Nd), each loading has 10 ppm phenol concentration, under UV light irradiation, reaction time (2-3 h), sampling time, (12-13), sample volume (250.00 mL), and pH of the reaction medium (5.7) and inlet air flow 4 L/min.....	142
Figure 32: A comparative Figure for 0.6 wt. % of SnO ₂ /La for effect of dissolved oxygen and without dissolved oxygen at optimum conditions	144
Figure 33: Comparison of photoactivity of 0.6 wt. % SnO ₂ /La Nps under UV and visible light irradiation at optimum conditions	146
Figure 34: Decrease of phenol concentrations without catalyst UV only, with (65 mg/50.00 mL) of SnO ₂ undoped (control), SnO ₂ /Nd 0.2 wt.% and SnO ₂ /Nd 0.6 wt.%	

LIST OF FIGURES

- under UV light irradiation, reaction time (2-3 h), sampling time, (12-13), sample volume (250.00 mL), pH of the reaction medium (5.7) and inlet air flow 4 L/min..... 147
- Figure 35: Decrease of phenol concentrations (each 10 ppm) upon (65 mg/50.00 mL) of SnO₂/Ce 0.1 wt.%, SnO₂/Ce 0.2 wt. %, SnO₂/Ce 0.4 wt. % and SnO₂/Ce 0.6 wt. % under UV light irradiation, reaction time (2-3 h), sampling time (12-13), sample volume (250.00 mL), pH of the reaction medium (5.7) and inlet air flow 4 L/min. 148
- Figure 36: Decrease of phenol concentration (each 10 ppm), upon (65 mg/50.00 mL) of SnO₂/La 0.1 wt. %, SnO₂/La 0.2 wt.%, SnO₂/La 0.4 wt. % and SnO₂/La 0.6 wt. % under UV light irradiation, reaction time (2-3 h), sampling time (12-13), sample volume (250.00 mL), pH of the reaction medium (5.7) and inlet air flow 4 L/min 149
- Figure 37: Decrease of phenol concentration each (10 ppm) with 65 mg/50 mL of SnO₂/I, (0.01, 0.1, 0.2, 0.3, 0.4, 0.1 and 1.1 wt.% under UV light irradiation reaction time (2-3 h), sampling time (12-13), sample volume (250.00 mL), pH of the reaction medium (5.7) and inlet air flow 4 L/min..... 150
- Figure 38: Decrease of phenol concentrations with undoped SnO₂ and SnO₂/Sb (0.2, 0.4, 0.6, 0.8 wt. %) under UV light irradiation with catalyst (65 mg/50.00 mL) reaction time (2-3 h), sampling time, (12-13), sample volume (250.00 mL), pH of the reaction medium (5.7) and inlet air flow 4 L/min 151
- Figure 39: Comparison of the decrease of phenol concentrations degradation with 65 mg/50 mL of undoped SnO₂ and different SnO₂/I (0.01, 0.2, 0.3, 0.4, 1.0 wt.%) Nps, under solar light irradiation, reaction time (2-3 h), sampling time, (12-13), sample volume (250.00 mL), pH of the reaction medium (5.7) and inlet air flow 4 L/min 152
- Figure 40: Spectra of phenol photodegradation and reduction in the intensity of 10 ppm phenol peak observed by UV-Vis spectrophotometry in the presence of 65 mg/50 mL of SnO₂/La 0.6 wt. % Nps, under UV light irradiation, reaction time (2-3 h), sampling time, (12-13), sample volume (250.00 mL), pH of the reaction medium (5.7) and inlet air flow 4 L/min. 153
- Figure 41: Comparison of the decrease of phenol concentrations degradation with 65 mg/50 mL of SnO₂/Gd 0.4 wt. % and SnO₂/Gd 0.6 wt. % Nps, under visible light irradiation, reaction time (2-3 h), sampling time, (12-13), sample volume (250.00 mL), pH of the reaction medium (5.7) and inlet air flow 4 L/min 157
- Figure 42: TOC removal from phenol solutions during 2.5 h of photocatalytic degradation by photolysis, undoped SnO₂, and SnO₂/Nd (0.2 and 0.6 wt. %), under UV light irradiation, reaction time (2-3 h), sampling time, (12-13), sample volume (250.00 mL), pH of the reaction medium (5.7) and inlet air flow 4 L/min 158
- Figure 43: TOC removal from phenol solutions during 2.5 h of photocatalytic degradation by SnO₂/La (0.1 0.2 0.4 and 0.6 wt. %) under UV light irradiation, reaction time (2-3 h), sampling time, (12-13), sample volume (250.00 mL), pH of the reaction medium (5.7) and inlet air flow 4 L/min 159

LIST OF FIGURES

- Figure 44: TOC removal from phenol solutions of 10 ppm concentrations during 2.5 h of photocatalytic degradation by SnO₂/Ce (0.1, 0.2, 0.4 and 0.6 wt. %) under UV light irradiation, reaction time (2-3 h), sampling time, (12-13), sample volume (250.00 mL), pH of the reaction medium (5.7) and inlet air flow 4 L/min 160
- Figure 45: TOC removal from phenol solutions during 2.5 h of photocatalytic degradation by photolysis, SnO₂ [undoped (control)] SnO₂/Sb, (0.2, 0.4 and 0.6 wt. %) under UV light irradiation, reaction time (2-3 h), sampling time, (12-13), sample volume (250.00 mL), pH of the reaction medium (5.7) and inlet air flow 4 L/min 161
- Figure 46: Comparison of the decrease of phenol degradation with undoped and SnO₂/I (0.01, 0.2, 0.3, 0.4, 1.0 and 1.1 wt.%) under UV light irradiation, reaction time (2-3 h), sampling time, (12-13), sample volume (250.00 mL), pH of the reaction medium (5.7) and inlet air flow 4 L/min 162
- Figure 47: TOC removal from 10 ppm phenol solutions during 2.5 h of photodegradation upon 65 mg/50 mL of SnO₂/Gd (0.6, 0.4 and 0.2 wt.%), under solar light irradiation reaction time (2-3 h), sampling time, (12-13), sample volume (250.00 mL), pH of the reaction medium (5.7) and inlet air flow 4 L/min 163
- Figure 48: Spectra of 10 ppm phenol photodegradation before and after 60 min UV light irradiation upon 65 mg/50 mL of SnO₂/Ce 0.6 wt. %, reaction time (2-3 h), sampling time, (12-13), sample volume (250.00 mL), pH of the reaction medium (5.7) and inlet air flow 4 L/min 165
- Figure 49: Comparison of the decrease of phenol concentrations with 0.6 wt. % SnO₂/Sb photocatalysis under solar light irradiation as measured by monitoring the phenol peak in HPLC 166
- Figure 50: 10 ppm of phenol photodegradation analysed by HPLC upon effect of 65 mg/50 mL of SnO₂/I 1.0 wt. % Nps by solar irradiation light at (0, 30, 90 and 120 min), reaction time (2-3 h), sampling time (12-13), sample volume (250.00 mL), pH of the reaction medium (5.7) and inlet air flow 4 L/min 167
- Figure 51: Evolution of different intermediates on 10 ppm phenol concentration detected by HPLC upon 65 mg/50 mL of SnO₂/Sb 0.6 wt. % under solar light irradiation, reaction time (2-3 h), sampling time (12-13), taken at (0, 15, 30, 45, 60, 75, 90, 105, 120, 135, 150, 165, and 180 minutes), sample volume (250.00 mL), pH of the reaction medium (5.7) and inlet air flow 4 L/min 168
- Figure 52: Separation of (10 ppm AA, 10 ppm HQ, 10 ppm Res, 10 ppm BQ, 10 ppm Cat, 10 ppm phenol, form 10 ppm benzoic acid and 10 ppm parabens (methyl paraben) mixtures observed by (HPLC) mobile phase (45% CH₃OH + 55% H₂O). Abbreviations; acetic acid; AA:hydroquinone; HQ: Resorcinol; Res: catechol; Cat. 170
- Figure 53: 10 ppm Phenol photodegradation before and after 150 min of 65 mg/50 mL of SnO₂/Gd 0.6 wt. % Nps, under visible light irradiations and optimized HPLC conditions and appearance of its different byproducts with the other parameters kept constants . 171

LIST OF FIGURES

Figure 54: Evolution of phenol byproducts during phenol photo degradation in the presence of 65 mg/50 mL of SnO ₂ /La 0.6 wt. % Nps under solar light irradiation with the other parameters kept constant	172
Figure 55: Examples of different phenol isomers Abbreviations:Catechol;Cat;Hydroquinone:HQ;Resorcinol:Res	173
Figure 56: Comparison between the COD and the HPLC analysis during 2.5 h of phenol photodegradation by the same catalyst 65 mg/50 mL of SnO ₂ /Gd 0.6 wt. % for both analysis both under solar light irradiation with the other parameters kept constants...	174
Figure 57: Reduction in the intensity of phenol peak observed by GC upon UV light irradiation degradation of phenol in the presence of 65 mg/50 mL of SnO ₂ /La 0.6 wt. % with the other parameters kept constants.....	175
Figure 58: Reduction in the intensity of phenol peak observed by GC upon solar light degradation of phenol in the presence of 65 mg/50 mL of 1.0 wt. % SnO ₂ /INps with the other parameters kept constant	176
Figure 59: Different chemical byproducts produced from 10 ppm phenol photodegradation before its mineralization to CO ₂ and H ₂ O as it analysed by CE under visible light irradiation upon 65 mg/50 mL of SnO ₂ /Gd 0.6 wt.% at pH 5.7 and with the other parameters kept constant	177
Figure 60: 10 ppm of phenol photodegradation upon 65 mg/50 mL of SnO ₂ /Sb 0.6 wt. % Nps at pH 5.7 which mineralized to CO ₂ as indication observed by FTIR under UV light irradiation after 2 h with the other parameters kept constant	178
Figure 61: Possible formation of phenoxide ion in water from phenol.....	179
Figure 62: Possible degradation mechanism of phenol and resonance stability of phenoxide, and the formation of benzoquinone intermediate	180
Figure 63: Different chemical photoproducts produced from phenol photodegradation before its mineralization by CO ₂ and H ₂ O build up from results given by UV-Vis, HPLC, CE, GC and FTIR with the reports from the literature [190, 196]	181
Figure 64: Degradation of 10 ppm phenol and its byproducts (2-P, phenol, BQ, HQ, Cat, Res, and AA) after 2.5 h treatment with SnO ₂ /La 0.6 wt. % under solar light irradiation, with the other parameters kept constant	185
Figure 65: Kinetic study of photodegradation of phenol and its intermediates in the presence of 65 mg/50 mL of SnO ₂ /La 0.6 wt. % Nps under solar light irradiation with the other parameters kept constant	186
Figure 66: Schematic presentation of the SnO ₂ photocatalytic mechanism [207, 441]	188

Nomenclature

Nomenclature

In the present work, variables and constants are denoted using *slanted style*, vectors are denoted using **bold regular style**, and abbreviations are denoted using regular style.

Latin alphabet

A	area	m^2
a	constant	–
C_D	drag coefficient	–
c_p	specific heat capacity at constant pressure	$\text{J}/(\text{kgK})$
c_v	specific heat capacity at constant volume	$\text{J}/(\text{kgK})$
d	diameter	m
\mathbf{F}	force vector	N
f	frequency	Hz
g	acceleration due to gravity	m/s^2
h	heat transfer coefficient	$\text{W}/(\text{m}^2\text{K})$
h	enthalpy	J/kg
\mathbf{j}	flux vector	m/s
L	characteristic length	m
l	length	m
M	torque	Nm
m	mass	kg
N	number of particles	–
\mathbf{n}	unit normal vector	–
p	pressure	Pa
q	heat flux	W/m^2
r	radius	m
T	temperature	K
t	time	s
q_m	mass flow	kg/s
V	volume	m^3
v	velocity magnitude	m/s
\mathbf{v}	velocity vector	m/s
x	x-coordinate (width)	m
y	y-coordinate (depth)	m
z	z-coordinate (height)	m

Greek alphabet

α	thermal expansion coefficient	1/K
α	(alfa)	
β	(beta)	
Γ	(capital gamma)	
γ	(gamma)	
Δ	(capital delta) usually used for change without slanting: Δ	
δ	(delta) notice the difference to ∂ (partial differential) symbol in equations	
ε	(epsilon)	
ϵ	(epsilon variant, Unicode 03F5, compare with equation symbol ϵ)	
ζ	(zeta)	
η	(eta)	
Θ	(capital theta)	
θ	(theta)	
ϑ	(theta variant, Unicode 03D1, compare with equation symbol ϑ)	
ι	(iota)	
κ	(kappa)	
Λ	(capital lambda)	
λ	(lambda)	
μ	(mu)	
ν	(nu) this is similar as Latin ν (vee), avoid using	
Ξ	(capital xi)	
ξ	(xi)	
\omicron	(omikron) this is similar as Latin o (oh), avoid using	
Π	(capital pi)	
π	(pi) usually reserved for mathematical value $\pi = 3.14159\dots$	
ρ	(rho)	
ϱ	(rho variant, Unicode 03F1, compare with equation symbol ϱ)	
Σ	(capital sigma) often used for sum without slanting: Σ	
σ	(sigma)	
ς	(final sigma)	
τ	(tau)	
υ	(upsilon)	
Φ	(capital phi)	
ϕ	(phi variant, Unicode 03D5, compare with equation symbol ϕ)	
\emptyset	(oh with stroke, Unicode 00D8, comp. with "empty set" in eq. symbols: \emptyset)	
φ	(phi)	
χ	(chi)	
Ψ	(capital psi)	
ψ	(psi)	
Ω	(capital omega)	
ω	(omega)	

Nomenclature

Dimensionless numbers

Ar	Archimedes number
Bi	Biot number
Fo	Fourier number
Gr	Grashof number
Nu	Nusselt number
Pr	Prandtl number
Re	Reynolds number
Sh	Sherwood number
St	Stanton number
Ste	Stefan number
Stk	Stokes number

Superscripts

p	partial layer
*	dimensionless

Subscripts

p	particle
eff	effective
g	gas
s	solid
l	liquid
max	maximum
min	minimum
tot	total

LIST OF ABBREVIATIONS

2D	two dimensional
3D	three dimensional
CFD	computational fluid dynamics
LES	large eddy simulation
PDF	probability density function
AA	acetic acid
AOP	advanced oxidative processes
Al	aluminium
BG	band gap
BQ	benzoquinone
BPA	bisphenol A
CE	capillary electrophoresis
Ce	cerium
COD	chemical oxygen demand
CB	conduction band
DMSs	diluted magnetic semiconductor
e^-	electron
$e^- - h^+$	electron hole
h^+	hole
EDS	endocrine disrupting compounds
Eu	europtium
FTIR	Fourier transform infra-red
GC	gas chromatography
Au	gold
HPLC	high performance liquid chromatography
HQ	hydroquinone
OH	hydroxyl group
$\cdot\text{OH}$	hydroxyl radical
I	iodine
2-P	isopropanol
La	lanthanum
Nps	nanoparticles
Nd	neodymium
ODMS	oxide-dilute magnetic semiconductor
O	oxygen
ppm	parts per million
Pd	palladium
Pt	platinum
RE	rare earth
Res	resorcinol
SEM	scanning electron microscopy
SNHs	semiconductor nano-hetero-structures
Ag	silver

Nomenclature

NaOH	sodium hydroxide
SPE	solid phase extraction
Sn	tin
Sn-O	tin-oxygen
TEM	transmission electron microscopy
TOC	total organic carbon
TM	transition metal
UV	ultraviolet
UV-Vis	ultraviolet-visible
VB	valence band
XRD	x-ray diffraction

CHAPTER 1

1 Introduction

1.1 Background

Contamination of water and air with different hazardous chemicals can cause severe health effects [1-3]. Many phenols, phthalates, endocrine disrupting compounds, benzoic acids, parabens and other toxins are released into the environment [4-6]. Growth of these pollutants in our environment will influence human life and the surroundings [7-11]. In fact, these compounds contact the air and water as a result of transferring from industrial places, discharging from refinery factories of oil and coal-tar, distilling from wood or energy, continuous leaking chemicals from livestock dips, and discharging of domestic sewage into the ground or spreading rotting vegetation around. [12-25]. Many of these contaminants have carcinogenic properties and pose both an immediate and a long-term threat to society and the environment in general [26]

1.2 Phenol

Phenol is a hazardous, recalcitrant compound, abundant in industrial waste water [27, 28]. Phenol is also found in ground water, toxic even at low concentrations [29]. Phenol is difficult to completely degrade by common treatment methods. Phenol is lethal to microorganisms, was found in the surroundings of its existence even at low toxicity. Phenol is produced worldwide at a rate of about 6 million ton annually, with a significantly increasing trend [30]. Phenols as polyphenols are natural components of many substances distribute in our food such as tea, wine, smoked food and fruits can act as antioxidants [31]. Phenol is available in explosives, dyes and textile products, likewise is obtainable from the combustion of tobaccos and fossil fuels [12, 32]. European Union and other countries have included some phenolic compounds in their list of priority pollutants [33].

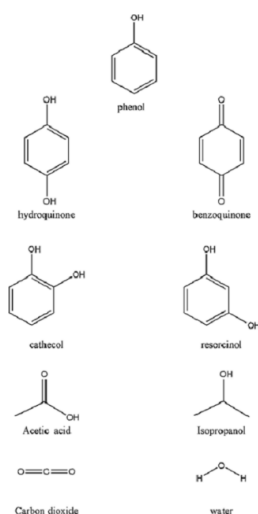


Figure 1 Chemical structure of phenol and its byproducts [34-39]

Figure 1 shows the chemical structure of phenol and some of its byproducts. Phenol has a hydroxyl group (OH) attached to 6 carbon atoms benzene (aromatic) ring. The electron rich aromatic ring makes phenol important in electrophilic aromatic substitution with the oxidation reactions.

Phenol compounds are toxic chemicals and slowly degrade forming different byproducts. Most of these intermediates are of environmental concern and can be roughly divided into quinones and carboxylic acids. Some phenol byproducts could be more toxic than phenol itself, which cause symptoms such as muscle weakness, convulsions and coma upon contact with human skin. In fact, many intermediate compounds may arise from phenol photodegradation including BQ, Res, Cat, HQ, AA, and 2-P.

BQ is one of the main and the first intermediates formed before ring opening to shape aliphatic or carboxylic acids. Due to the electron deficiency of a benzene ring, the very reactive $\cdot\text{OH}$ reacts with the substituted ring and not with the substituent [40]. OH attachment to the benzene ring is polar, and isomeric distribution is difficult to determine because of its chemical and physical properties slightly differ. Its life time is very short, in addition, to the rapid unimolecular or bimolecular reactions [41]. BQ has a slower

degradation rate than phenol but it is much more toxic [42]. Consequently, it is very important to diminish the amount of BQ formed in the system and to accelerate the ring opening technique.

Res is used in the production of dyes, plastics and synthetic fibres [43]. Cat is an aromatic alcohol soluble in water, used to produce food additives, hair dyes, and antioxidants [44]. HQ is used in the pharmaceutical, food, and chemical industries [45]. Studies of the photocatalytic oxidation of phenol on illuminated titanium oxide (TiO_2) also confirmed that intermediates such as Cat, Res and HQ were present in their analysed reaction mixtures [46]. In another study, HQ and BQ been synthesized through electrochemical oxidation of phenol, to treat waste water [47]. Other scientists reported that phenol could be oxidized but complete TOC removal was not achieved [48, 49].

Most conventional water treatment processes have been reported for the removal of organic compounds, include physicochemical methods. These procedures are grouped to purify wastewater into three techniques: chemical pretreatments by coagulation-flocculation or precipitation, adsorption, and ion exchange or membrane processes [50-54]. Even though great improvement of water treatment processes has been accomplished. In most cases the effectiveness of these methods are often impracticable and many of these techniques are costly, when using for larger scale applications [55]. Furthermore, these procedures are nondestructive, insufficient, may transfer pollutants to another new non polluted site (water surface) or have other limitations. These limitations have motivated the search for more efficient and cleaner technologies to overcome the ever increasing threat to future water security. In turn, this has led to the advancement and adoption of new and improved water purification methods.

The effective methods for removing organic pollutants from water include advanced oxidative processes (AOPs), the most potential techniques for eliminating organic toxins even on a larger scale [56-58]. The magic basis lays on the activity of AOPs is to generate $\cdot\text{OH}$ on the catalyst surface. AOPs are characterized by their catalytic, photochemical properties, which then oxidatively degrade the organic and inorganic

pollutants present in water to harmless end products such as carbon dioxide (CO_2) and water (H_2O) [59-63]. AOPs techniques can draw on a combination of chemical and physical agents such as a catalyst and ultraviolet (UV) light [64]. $\cdot\text{OH}$ are unstable and reactive electrophiles since they react in a rapid and non-selective way with almost all electron rich organic compounds [65, 66]. The properties of the catalysts very well established and show varied oxidative performances when exposed to irradiation [67]. Such photocatalytic protocols are extremely effective. This is because the intermediary formed $\cdot\text{OH}$ possess an oxidation potential of 2.8 V, demonstrating slower rates than fluorine (F), but faster than hydrogen peroxide (H_2O_2), potassium permanganate (KMnO_4) and other oxidants as is shown in Table 1 below [57, 59, 68].

Table 1: Oxidation potential [57-59]

Oxidant	Oxidation potential (Volts)
Flourine (F_2)	3.03
Hydroxyl radical ($\cdot\text{OH}$)	2.80
Ozone (O_3)	2.07
Hydrogen peroxide (H_2O_2)	1.78
Potassium permanganatge (KMnO_4)	1.68
Chlorine (Cl_2)	1.36

The oxidation potentials are placed in order of decreasing potentials as they are shown in Table 1 above. The Table indicates that the fluorine has the highest potential and $\cdot\text{OH}$ comes next which is higher than ozone.

1.3 Semiconductor photocatalysis

Photocatalysis has received much attention in recent decades as a promising environmental remediation technique because of its ability to completely remove organic and inorganic toxins from water pollutants [69-72]. Many researchers have used photocatalysis to undertake environmental problems and to get rid of hazardous chemicals from different sources. Fujishima and Honda in 1972, was succeeded for the first time in this inventive area of research [73]. They reported the photoelectrochemical

decomposition of water on n-type titanium dioxide (TiO₂) anode and platinum (Pt) cathode upon exposure to UV illumination. This work attracted the attention of many scientists in a comprehensive field [73].

Photocatalysis is a combination reaction between photochemistry and a solid material [74]. Many researchers have practised photocatalysis to face environmental problems and to eliminate hazardous chemicals from different sources. Semiconductor photocatalysis for the unabated release of toxic organic and inorganic pollutants into the air and water has been a research priority, since it is an effective green technology for water treatment and the complete elimination of toxic chemicals in the environment, with clear advantages over other treatment methods [75].

It has been exhibited the practise of different light sources for carrying out dissimilar photodegradation studies and many investigations emphasis on the use UV light. The source of UV irradiation is mainly mercury vapour lamp. Mercury lamps been used for suitability and when the photodegradation of the compounds is low. Mercury lamps own adequate energy to produce electron hole ($e^- - h^+$) pairs within the catalyst, which activate the formation of radicals and result in the oxidative degradation of the contaminants. The UV photoreactor λ region is higher than the X-ray λ region which is ≤ 100 nm, but is shorter than the visible λ region which is > 400 nm of the electromagnetic radiation [76]. Mercury lamps with an intensity maximum close to peak λ of 253.7 nm, which is UV-C electromagnetic radiation [77]. Mercury lamps need relatively high energy to run, have mercury need cooling, and have a short life time. Mercury lamps quite expensive to operate contain hazardous material and might expose their contents to the environment when being broken. Because of these disadvantages and heavily application uses, it is a necessity to replace mercury lamps by the light emitting diodes (LED) or xenon lamps [78-81]. The LED is not much enough for producing UV-C electromagnetic radiation, but it can further improved [81]. Xenon lamps release radiation at λ of 240 nm and non-toxic compared to mercury but it gives ozone which also dangerous to the environment [81]. Another alternative is to use solar light, which is the most abundant, free clean source of energy available for providing

environmentally friendly, green chemical processes. Sunlight is unlimited, least expensive composed of 4-5% of the radiation in the UV region of the electromagnetic spectrum which gives off enough energy to yield reactive radicals [82]. Researchers showed that more solar energy falls from sunlight on our planet in one h than all the energy used by humans for the year [83]. Since the source of sunlight is infinite, applications of photocatalytic processes with this source have attracted considerable interest [84].

In a semiconductor the BG is a significant factor for explaining the potential of a material to act as a semiconductor or insulator. The lower energy BG [also called as conduction band (CB)] is filled by electrons while the upper energy BG [known as valence band (VB)] is empty of electrons. The energy difference between the VB and CB is called the energy BG (BGE) (E_{bg}) is responsible for the electronic properties of the material [85, 86]. Fermi level is a measure of equilibrium (hypothetical energy level of electrons) between a solid material underneath the CB and above the VB for n and p-type materials [87].

The interfacial electronic properties of semiconductors are generally measured by the presence of small amounts of impurities doping in the crystal structure of the metal oxide. Impurities regularly control the physical and chemical properties of semiconducting materials. It is possible to reconstruct the SnO₂ surface, giving rise to a host of different surface situations. This is making the metal oxide capable of creating a crystal structure with incomplete oxygen sites. [88].

These doping either generate an excess of free holes as it is in p-type semiconductor, or free electrons as in n-type semiconductor. In n-type semiconductor SnO₂ O deficiency O may be caused either by O vacancies or Sn interstitial atoms with reduction of some Sn⁺⁴ to Sn⁺² [89-91]. The doping process by adding donor or acceptor impurities alters the Fermi level and replaces the CB in the n-type or replaces the VB in the p-type semiconductor which consequently narrows the distance between the E_{bg} and the two bands [92, 93].

As a rule if the E_{bg} between the CB and VB narrows, less energy is needed to excite the electrons. Thus the improvement of the photocatalytic activity can be noticed upon the irradiation of the catalyst in the visible region [94].

1.4 Semiconductor photocatalysts

Scientists have made rapid and significant advances in the field of semiconductor materials, which has attracted significant interest due to its numerous practical applications [95-99]. Essential characteristics of a photocatalyst include stability and the absence of resulting secondary pollution.

It is well known that morphological and structural characteristics affect the photocatalytic activity of a semiconductor [100].

Many researchers have been reported that titanium dioxide (TiO_2), zinc oxide (ZnO), and tin dioxide (SnO_2) are the most prominent photocatalysts. Semiconductors as (TiO_2) with a BG of (3.2 eV), (ZnO 3.3 eV) and (SnO_2) which has a large BG energy (3.6 eV), are the most ideal photocatalysts for the degradation of dyes, phenols and pesticides [29, 98, 101]. By doping the metal oxide with impurities reduces the E_{bg} and electromagnetic radiation with lower energy (to be fit in the visible light region) and can be utilized to activate the catalyst, possibly increasing photocatalytic activity. Below, In the Table 2 shows the BGs of a variety of metal oxides [82, 102, 103].

Table 2: Band-gap energy of some photocatalysts [94-96, 104].

Photocatalyst	Band-gap energy (eV)	Photocatalyst	Band-gap energy (eV)
Si	1.1	ZnO	3.3
TiO_2 (rutile)	3.0	TiO_2 (anatase)	3.2
SnO_2	3.6	SnO	~ 2.5 - 3.0
WO_3	2.7	CdS	2.4
ZnS	3.7	ZnO	3.2

These semiconductors have been recognized as preferable materials for photocatalytic processes due to their high photosensitivity, nontoxic nature, low cost and chemical stability [105-107]. Exposure to UV or solar irradiation during photolysis may initiate

organic degradation. Green plants use solar lights to produce O_2 and H_2O through photosynthesis. Dead bodies also undergo chemical transformation to produce oil [108]. Energy supplied by absorbing a photon of light enables excitation of reactant molecules to promote degradation reactions [59]. TiO_2 photocatalysts have received the most attention from a number of researchers [109].

Scientists put additional interest in the progress of photocatalysis research which is indicated by the huge number of research publications exhibited over the previous years.

Photocatalysis research literature survey with other metal oxides key words is summarized in Figure 2 (source, Scopus, May 2017). According to this investigation, photocatalysis research has generated approximately $> 42,713$ articles about the application of TiO_2 , ZnO and SnO_2 . As photocatalysts which have been published to date, the most publications were dealt with TiO_2 . Solar irradiation or visible light irradiation is also widely investigated. As a survey nearly 14,334 articles listed in Scopus, TiO_2 and ZnO are the most popular and widely studied photocatalyst materials, with more than half of the literature reporting the use of TiO_2 , while only over 3,593 paper on ZnO have been published to date. Unlike other photocatalysts, SnO_2 has not been thoroughly studied about 531 articles in Scopus. In spite of the countless benefits of SnO_2 and the complete absence of secondary pollution due to photoerosion [110]. In addition, the rutile structure of SnO_2 is very similar to that of TiO_2 , but as photocatalyst material is not widely reported as it shown in Figure 2 [111, 112].

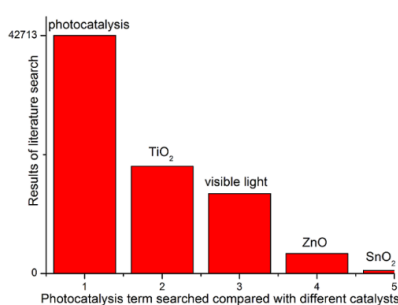


Figure 2: Comparison of the search term “Photocatalysis” in Scopus articles

In a typical photocatalysis process, the breakdown of an organic compound (phenol) in an aerated solution can be summarized as in equation 1.



The reaction takes place when UV radiation photoexcites a semiconductor catalyst in the presence of oxygen, $\cdot\text{OH}$ is generated to attack oxidizable contaminants, breaking down molecules yielding CO_2 , and H_2O . The reaction is applied for the oxidization of almost any organic substance due to its positive oxidation potential [113]. Unfortunately, the swift recombination rate of the photogenerated $e^- - h^+$ pairs hinders the industrial application of these semiconductors as it will be discussed in the following subjects [114, 115].

Observing the environment is essential to protect the neighborhood and the surroundings from the previously mentioned toxins. Nanotechnology can identify these pollutants, and give clues about removing them from the water. By controlling different contaminations in the environment, would require less labor and not much energy in the future [116]. Nanotechnology has the capability of creating functional materials, devices and systems with new properties through manipulating of matter in the range of about 0.1-100 nm [117].

The quality of these Nps completely depends on their phase, size, shape and dimension [118, 119]. Improving scalable and simple routes to construct nanomaterials with a convenient size and microstructure is very important in nanotechnology and synthetic chemistry [120].

Nanotechnology covers many knowledge areas such as chemistry, physics, engineering, material science and biology. Nanomaterials have unique electrical, physical, chemical, and magnetic properties, which can be manipulated [121, 122]. These Nps have been studied from both experimental and theoretical points of view due to their potential application in solar energy conversion and photocatalysis [123, 124]. Nanotechnologists have the ability to produce controlled Nps, which are mainly applied in catalysis to

improve chemical reactions, cut down the amount of catalytic materials, getting good results, saving money and reducing pollutants, such as materials that supply clean water from polluted ones.

Water is important for human life and if it is not clean would create many environment disaster applications. Researchers could synthesize Nps and decide how to apply their chemical and physical properties for various kinds of toxic site remediation. Monitoring the environment at the beginning of the pollution created is necessary to prevent pollution, discover solutions or when to degrade environmentally dangerous toxins. The use of Nps to detect water contamination and remediate through degradation of poisonous materials to safe minerals is getting appeal from researchers everywhere.

Nanotechnology can be used to reduce the cost through different aspects. Priority comes by breaking down of big molecules (chemically or physically) into smaller materials of desired shapes and sizes, also by building up nanostructures, by bringing in individual atoms and molecules together.

1.5 Research objectives

The main objective of this research project is to focus on the development of new nanostructured and nanosized semiconductor based photocatalysts for the treatment of phenol and its byproducts present in water samples under UV, visible or sun light irradiation. This study aims to attain fundamental experiment research, focusing on the preparation, characterization and application of nanoparticle photocatalysis for the treatment of water.

- (i) Synthesis and preparation of SnO₂ nanosize and nanostructured photocatalyst (SnO₂) by sol-gel method with particle size smaller than 50 nm.
- (ii) Synthesis and preparation of doped Nps with varies dopants (0.01-1.1 wt. %) doped SnO₂ for higher photonic efficiency.
- (iii) Characterization of prepared nanostructured photocatalyst for structural, chemical properties using XRD, SEM, HR-TEM and BET.

- (iv) Identification of common pollutants like phenol, HQ, BQ, Res, Cat, AA and 2-P.
- (v) Fabrication of batch mode photocatalytic reactors for laboratory scale model.
- (vi) Photocatalytic degradation of phenol, HQ, BQ, Res, Cat, AA and 2-P using prepared nanoparticle photocatalysts in batch reactors.
- (vii) Determination of the rate and extent of photodegradation employing UV-Vis spectrophotometer, HPLC, GC-MS, CE, FTIR, COD and TOC analyzer.
- (viii) Evaluation of the performance of different doped and supported photocatalysts on the photocatalytic degradation of the pollutants.
- (ix) Kinetic studies to evaluate the constants and rate of pollutant degradation.
- (x) Identification of the nature of the intermediates by GC-MS, HPLC and CE.
- (xi) Identification of intermediates in the photodegradation and thereby mechanistic pathway for photodegradation.
- (xii) Determination of the mineralization process using FTIR.
- (xiii) Design of batch reactors for UV, visible and solar applications.
- (xiv) Application of photodegradation of phenol using prepared Nps photocatalysts for large scale

1.6 Hypothesis

Organic pollutants from water, such as phenol and its intermediates can be completely photodegraded and mineralized into carbon dioxide (CO₂) and water (H₂O) using different tin dioxide (SnO₂) dopants at ambient conditions. The influence of Lanthanum (La) doped SnO₂ can be determined as an efficient candidate for practical application in the field of photocatalysis. Gadolinium (Gd) doped SnO₂ can be used as visible light induced nanoparticle photocatalyst, as well as antimony (Sb) doped SnO₂ designed as an efficient photocatalyst under solar light irradiation.

1.7 Research questions addressed

- i) Can a small amount of doping such as (0.01 wt. % of ions) on SnO₂ effects on phenol photodegradation?
- ii) What are the effects of chemical and physical parameters on phenol photodegradation?
- iii) Can the high surface area of SnO₂ be improved with doping of different ions?
- iv) Can Nps be synthesized by simple methods?
- v) Can the bath for an easy and simple solar reactor be designed?
- vi) Can large scale and industrial waste water containing toxic organic compounds be analyzed by this simple process?
- vii) How do the intermediates in the phenol photodegradation process can be detected and quantified in the solution, and do the concentrations of the intermediates grow with time during the analysis?
- viii) What are the pathways for producing intermediates for the phenol photodegradation process?
- ix) How do the optimization of some analytical instrumentation methods can be performed and involved in the phenol photodegradation analysis?
- x) Is it possible to detect CO₂ during the mineralization process, and when does it appear during the analysis?
- xi) Can SnO₂ Nps by the sol-gel method at room temperature be synthesized and become suitable for large scale production.
- xii) To what extent can phenol molecules be photodegraded and what parameters influence photodegradation efficiency the most?

1.8 Research approach

In this study, SnO₂ Nps are synthesized by doping with different ions following sol-gel procedure. The main requirement was to create Nps in large scale, low cost, large surface area and small particle sizes.

The detailed approaches of this study include:

SnO₂ has a BG of 3.6 eV, to check if normally absorbs in the ultraviolet region of the electromagnetic spectrum.

SnO₂ can be easily doped n-type with antimony or p-type with others and make SnO₂ ideal for enhanced photocatalytic activities. The CB edges in n-type oxide like SnO₂ are deep below the vacuum level and are thus relatively easy to dope which is controlled by the compensation by the native defects. Doping occurs by moving the Fermi energy to the band edge leading to the spontaneous formation. To prepare SnO₂ for visible light photocatalysis, the SnO₂ Nps photocatalyst should be competent of absorbing visible radiation > 400 nm and also should be able to reduce the recombination of the photogenerated electrons.

Control SnO₂ and different doped SnO₂ Nps were prepared and characterized.

The performance of a SnO₂ catalyst contributes to its activity and study of the photocatalysis. It is then to examine the capability of photocatalysis in removing pollutants phenol and its byproducts.

The influence of phenol concentration on the photodegradation efficiency was examined.

The rate of phenol photodegradation was evaluated by changing dopant percentages (wt. %) while the other parameters were kept constant.

The rate of different pollutants at fixed concentrations was calculated.

Optimization of chemical and physical parameters, such as light intensity, catalyst loading, reaction time, sampling time, sample volume, pH of the reaction medium, and pollutant concentration all these parameters were examined and their influence on phenol photodegradation efficiency was assessed.

Design of batch photoreactors for UV, visible and solar applications

Analysis of contaminant samples

Water samples were prepared to contain different pollutants, initial and final solutions were qualitatively and quantitatively investigated using several analytical techniques such as UV-Vis spectrophotometer, chemical oxygen demand spectrophotometer (COD), high performance liquid chromatography (HPLC), gas chromatography (GC-MS), capillary electrophoresis (CE), and total organic carbon (TOC) analyzer.

Detection, identification and characterization of mineralization products species such as CO₂ were detected by Fourier transformer infrared spectroscopy (FTIR) analysis.

Identification of the nature of the intermediates was evaluated by UV-Vis, GC-MS, HPLC and CE analytical instrumentation.

The different intermediate products of phenol were detected UV-Vis spectrophotometer, High performance liquid chromatography (HPLC), gas chromatography GC-MS, CE, and TOC analyzer.

1.9 Scope of study

The current study examines the synthesis of pure and doped SnO₂ Nps with different doped ions by the sol-gel process. The work also examines the possibility of photocatalysis as a treatment technique to remove phenol and its byproducts from water samples. The examination of the photocatalytic processes was based on the laboratory scale batch system. In this system SnO₂ was used as a better catalyst in its undoped and doped form with other ions. Preparation of SnO₂ catalyst and determine its optical properties. Development of the reaction runs in the reactor for photodegradation of phenol and its byproducts, which examine the effect of different SnO₂ at the optimum conditions in the reactor. The study shows quantification and identification of byproducts in phenol photodegradation and the determination are done by using different analytical techniques. Major aromatic and aliphatic intermediates with a comparison of how much of each can be formed and disappeared during the phenol

photodegradation process. According to the current experimental conditions and to the observations made from the analytical instrumental analysis, a degradation pathway was also designed in the study. On the other hand, the detection and quantification of free radical species were not covered in this work; in addition, the quantification of CO₂ was also not covered.

1.10 Delimitations of study

The main effects of the work involve the following aspects: According to the industrial applications objected in this thesis involve low cost synthesis processes, so the sol-gel procedure for synthesizing SnO₂ Nps was used, developed and improved. The Sol-gel technique can be used to prepare materials with large surface area; it also can be used with controlled amounts of doping. As the sol-gel process is a low temperature process, its crystal growth rate is also slow. SnO₂ Nps either undoped or doped with ions were synthesized by simple sol-gel method and characterized using different characterization techniques. These characterized catalysts either (undoped or doped SnO₂ Nps) were involved in phenol photodegradation with its byproducts. The three group of compounds investigated in this thesis are Phenol, aromatic and aliphatic acids. The performance and the comparison of different undoped and doped SnO₂ Nps for the analysis of phenol and its byproducts were also estimated and calculated. Relevant methods and tools for the investigation were identified based on a literature review. Laboratory photodegradation experiments using phenol in water as a contaminant was included, as well as the development of new analytical methods or optimization, modification of existing methods in order to analyze lower concentrations or additional compounds. The evaluation of different methods used in this study with the tools applied were based on the performed field and the laboratory investigations and existing literature. The goal was to address their specificity as a qualitative indicator of phenol photodegradation and also to recognize their limitations.

1.11 Methodology

- a- Capability of the photocatalytic process in treating phenol and its byproducts was analysed.
- b- A literature survey to understand some of advanced oxidation processes (AOPs) for treating phenol in water, comparing it to other techniques.
- c- A literature survey about SnO₂ preparation techniques
- d- A literature survey of the photocatalytic process
- e- Various methods applied for the characterization and identification of the Nps.
- f- Experiments to identify the intermediates appeared during the photodegradation process for phenol.
- g- Understand the mechanism pathway of phenol photodegradation.
- h- Simple kinetic analysis of some doped SnO₂ Nps.

1.12 Structure of the report

This report has been presented in five chapters.

Chapter 1

The first chapter is an introduction of the work, consisting of background, motivations main aims and objectives, hypothesis, answering the research questions, research approach, scope of the study, delimitations of the study, methodology; it also shows the structure of the report.

Chapter 2

In chapter two of the report, the study begins with a literature review of SnO₂. Literature review on different examples of doping SnO₂ with different other oxides, literature review examples on doping with metals and the example is antimony. Also the literature review on doping with nonmetals such as Iodine. Literature review upon doping with RE metals and the examples taken are La, Gd, Nd and Ce. Literature review for different synthesis methods used to synthesize SnO₂.

Chapter 3

In chapter 3, chemical materials, procedures, preparation of different techniques are shown. Procedures to synthesize different doped and undoped Nps are in chapter 3. Explanations of different experimental reactors and reaction conditions as well as different parameters that must be examined in this study will be found in this chapter. Physical equipment's, characterization instruments and analytical techniques which are all used in this study are in this chapter, with the experimental methods data collection.

Chapter 4

Results and discussion, includes characterization of different Nps by different instrumentations such as XRD, SEM, TEM, and BET. The effect of some parameters of the degradation efficiency was also looked at. The degradation was studied by monitoring the change in contaminant concentration on employing HPLC analysis. The mineralization of phenol was also determined by TOC and COD analysis. Study of the effect of irradiation time on phenol photocatalytic degradation by GC explained. Intermediates or byproducts of the phenol photodegradation were also differentiated. The kinetics degradation of phenol and its byproducts was examined. A photocatalytic mechanism was proposed based on the results accumulated.

Chapter 5

The last chapter gives a summary of the conclusion of the research with the future work and some recommendations for the future studies.

2 CHAPTER 2

2.1 Tin dioxide (SnO₂) catalysts

SnO₂ is one of the most important rutile structures, known as cassiterite, stannic oxide or tin(IV) oxide also is an amphoteric colorless solid [125]. SnO₂ is an inorganic compound that mix low electrical resistance, high electrical conductivity, high optical transparency in the visible region (90%) of the electromagnetic range [88]. SnO₂ also known by its high reflectivity in the infrared region, and is characterized by good chemical and thermal stability [89, 126]. The electrical properties of the metal oxide can additionally be attributed to the presence of the native defects in SnO₂ structure [127]. These kinds of defects donate to make an important reduction of the energy BG, therefore, developing the semiconductor properties of the metal oxide. In this regard, extra O anions activate the oxidation of Sn⁺² to Sn⁺⁴ consequently to regulate the total electrical neutrality of the material [128]. This property also promotes a reversible conversion of the surface composition from stoichiometric surface with Sn⁴⁺ can be reduced to Sn²⁺, which changes the surface electronic structure of the material [88]. Mixed cation reduction leads to the formation of Sn 5s that lies deep within the BG [88]. In addition, SnO₂ powerful oxidizing properties fix the semiconductor to be a perfect apparatus for the degradation of toxins from different wastewater foundations. Due to these advantageous, SnO₂ has been involved in several processes. In conjunction with, the metal oxide was known as a catalyst, it has the capability to tailor its microstructural properties making it useful in photocatalysis. O vacancies in SnO₂ prepare it to be involved in a wide range of applications, such as heterogeneous catalysis, field-effect devices and sanitary disinfection [129-132]. SnO₂ characterized as a sensor, such as photovoltaic devices, pH, and biosensors, gas sensors identify the outflow of reducing gases such as H₂, S, CO, detect toxic and combustible gases in the air, other techniques applied in food industry, environmental monitoring and medical technology [133-143]. In fact, the high sensitivity of SnO₂ in sensors towards CO and H₂, can be promoted by doping. The affinity of SnO₂ to CO and H₂ increases as grain size of the semiconductor

reduces, and such increase in the catalytic activity [144]. SnO₂ used as a raw material for transparent films, infra-red mirror. SnO₂ used as multifunctional oxide materials, because of their potential applications in optoelectronic devices [145-147] and devices with lattice parameters [148].

As it was explained in the previous chapter, that the rutile structure of TiO₂ matches the crystal phase of SnO₂ [111, 149]. The (dimensions of the unit cell are: a=b=0.47374 nm and c=0.31864 nm, and with space group no.= P4₂/mnm (136) [150, 151]. The SnO₂ is a polar crystal with tin(IV) has a tendency to acquire octahedral. Possessing SnO₂ an octahedral system is a vital for high photocatalytic activity, since it upsurges the flexibility of $e^- - h^+$ pairs and accordingly affects the possibility of their arriving the reaction sites on the surface of the photocatalyst [152-154].

A scientist worked on the rutile structure and the thermal stability of SnO₂, reported that the annealing temperature increased the crystallite sizes with a spherical shape. It was found that the crystallites contained hydroxyls in their lattice and generated Sn vacancy sites into the structure. When samples were annealed, the Sn vacancy sites decreased as a result of the dehydroxylation process. It was noticed, that the presence of the hydroxyls modified the tin-oxygen (Sn-O) bonds, enlarged the lattice parameters and resulted in asymmetry in the rutile Sn-O octahedron. [155]. Zhao et al. reported porous SnO₂ nanostructures consisting of nanoplates through thermal decomposition of a mixed solution of dibutyltin dilaurate and AA. The results showed that AA had an important effect on the formation of SnO₂ and exceptional catalytic activity toward methanol decomposition. [156]. A study compared two types of SnO₂ powders prepared from different precursors was subjected to the influence of specific treatments. These treatments were (calcination procedures, different Sn precursors, and surfactants on the textural and catalytic properties). The samples showed higher catalytic activity in ethyl acetate oxidation and enhanced selectivity toward CO₂ by SnO₂ Nps were prepared from tin(IV) tertabutoxide precursor [157]. Gu and colleagues investigated the luminescence properties of SnO₂ Nps, found the size of the single tetragonal crystalline phase with 2.6 nm diameter. The group reported that the luminescence was related to the recombination

of electrons (e^-) in singly occupied O vacancies with photoexcited holes (h^+) in the VB [158]. SnO₂ is an attractive oxide for electrically activated emission, as it possesses stability, and all acid alkali resistant properties comparable to TiO₂ [111, 159]. The first photoresponse nanodevice based on monolayer SnO₂ photodetectors, presented ultrahigh photocurrent and sensitivity, exceptional stability, and produced linearity [160].

In fact, SnO₂ has a dual valency surface property, with Sn possibly gaining an oxidation state 4⁺ or (2⁺ for stannous oxide or as it called SnO) [88]. SnO [Tin(II) oxide] is another main form of SnO₂ called stannous oxide not to be confused with stannic oxide or cassiterite which is less characterized than SnO₂, with tin in the oxidation state of 2⁺ [88]. SnO displays a smaller energy BG, which lies between 2.5–3 eV. SnO anodes in lithium ion batteries (LIB) are recognized by their high energy density, high power, smooth discharge, light weight, and the fact that they are environmentally friendly [161, 162]. In these batteries, electrodes composed of nanocrystalline particles display high levels of capability and better cycle ability [163].

Figure 3 shows SnO₂ unit cell, in the Figure each tin(IV) (Sn⁴⁺) atom is bordered by six O ions and each O ion is fenced by three tin(IV) ions, so it has the structure of (6, 3) coordination. [88, 125, 152, 164].

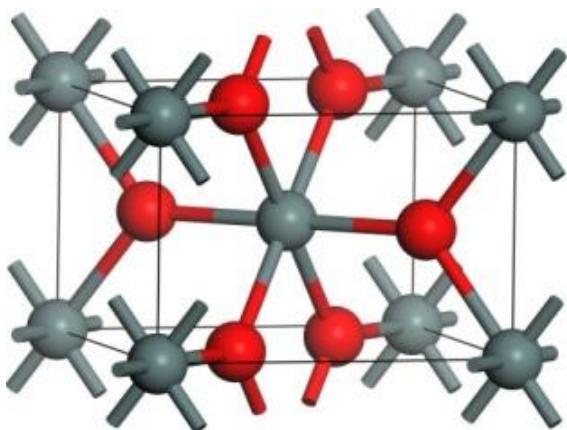


Figure 3: SnO₂ cell structure [88, 125, 152, 164, 165][166]

Metal oxide semiconductors such as TiO_2 , ZnO and SnO_2 are more desirable photocatalytic materials due to their high photosensitivity, nontoxicity nature, low costly, chemical, and thermostability [167, 168]. Metal oxides also have high surface activity, large number of active sites, good ability to absorb light radiation, biologically and chemically inert, photostable, inexpensive, not liable to photocorrosion [169]. They are known as stable rutile phase good ability to absorb oxygen and decrease the recombination rate of electron-hole pairs $e^- - h^+$ [170-175]. Oxides also possess many key material properties such as superconductivity, ferroelectricity, and magnetism [88, 176].

SnO_2 Nps with rutile structure was widely examined between the other nanometal semiconductor oxides because of the high surface area, low toxicity, high temperature resistance also due to their sensitivity to decrease and oxidize gases [177]. All These electronic and chemical properties of SnO_2 nanostructures make them exciting materials, with significant potential to assist both fundamental research and practical applications.

Some of the different physicochemical characteristics of SnO_2 are mentioned in Table 3

Table 3: Properties of SnO_2 [117, 167, 168, 170]

Crystal structure	Rutile structure
Lattice constant	$a = 0.47374 \text{ nm}$ and $c = 0.31864 \text{ nm}$
Molecular weight	150.69 g/mol
Density	6.90 g/mol
Melting point	1500-1630 °C
Boiling point	1800-1900 °C

As it mentioned SnO_2 combines many positive properties and found in many useful applications which can be exploited for nanostructured materials. In addition, to the previous advantages of the metal oxide, its application as a catalyst for the degradation of organic pollutants is also appreciated [178-181]. The most commonly used gas

sensing materials are ZnO and SnO₂ because TiO₂ has the disadvantage that its conductivity is enhanced by the formation of bulk oxygen vacancies. Also in comparison to other semiconductors SnO₂ synthesized Nps have many advantages over others. Commercial SnO₂ and TiO₂ Nps were chosen for comparison with the synthesized SnO₂ to evaluate the absorb capacity of the dye with all the practical parameters for the three types were kept the same and stable. The synthesized SnO₂ Nps were shown better removal ability than the commercial materials (SnO₂ and TiO₂). This was characterised to the very minute diameter and high surface area of the synthesized SnO₂. Also due to their higher recombination resistances, faster charge transport, and more efficient charge separation. All the previous factors with the particle size, surface to volume ratio and crystallinity of the nanorods, increased the physical properties of the metal oxide [182, 183]. In addition, thin SnO₂ nanowires, can also be applied in a universal and low cost method to build field emitters with long term stability [184, 185].

2.2 Photocatalytic activity of SnO₂ in aqueous solution

The surface of SnO₂ is characterized by O vacancies acts as a sink. O deficiency in SnO₂ is important because it is an electron donor which enhance its properties as an n-type semiconductor [186]. A study had shown that energetically favourable reconstructions of the SnO₂ (110) and (101) surfaces result in surface oxygen deficiency [88, 187]. These oxygen vacancies bind with electrons forming an excitation energy level below the CB of SnO₂. SnO₂ has a BG of 3.6 eV, resembles to activation energy to irradiation with UV light. This BG corresponds to photons of a photoreactor of 350 nm which sits in the UV-A range. The SnO₂ material is well suited as a photocatalyst for removing of hazardous compounds from wastewater [169].

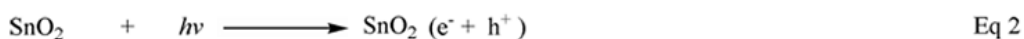
In an aqueous environment, pollution adsorbed to the catalyst surface. When the catalyst with the pollution exposed to irradiation of sufficient energy, the photogenerated $e^- - h^+$ pairs are generated to activate the oxidative degradation of organic molecules. The adsorbed solution broken down under the light and the final products desorbed. Due to the chemical stability, low toxicity, high photosensitivity, cheap, and preferable material for AOPs the insoluble SnO₂, metal oxide can be applied in the photodegradation of

environmentally toxic elements and harmful chemicals in wastewater. The processes of heterogenous photocatalysis on different semiconductors were explored during the last decades. Recently, scientists have improved maintainable procedures for the photodegradation of phenols and many other toxins by using different irradiation sources [71, 188].

The overall process is explained in the following reactions which involve different steps as shown below

2.2.1 Electron hole pairs generation

The path originates with the activation of the photocatalyst and the formation of $e^- - h^+$ pairs (Eq. 2).



2.2.2 Traps for holes

The $e^- - h^+$ pairs which generated above in (eq1) travel to the surface of the semiconductor. With the effect of the light, water molecules generate highly reactive radical holes h^+ . The h^+ migrate to the pollutant adsorbed to the surface (water molecules $\text{H}_2\text{O}_{\text{ads}}$) and react with the catalyst. Thus, the hole in the VB h^+ is capable of producing $\cdot\text{OH}$ by 2 ways, either through absorbed water (Eq.3) or through the reaction of hydroxyl anions (Eq.4).

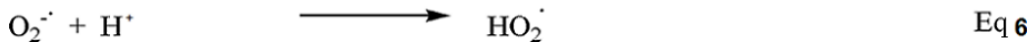


2.2.3 Traps for electrons

The generated electrons e^- , which migrated to the surface and the molecular dissolved oxygen, acts as acceptor species in the oxidation-reduction reaction. The e^- activate the production peroxy radical anions (superoxide anions) (and hydroperoxyl anions (Eq. 5) upon reaction with dissolved oxygen [189].



In addition, the resulted free radicals have strong oxidation ability are then protonated and formed highly reactive hydroperoxyl radicals in the presence of H^+ (Eq. 6)



or in the presence of H_2O (Eq. 7) [190]. The free radicals can oxygenate or degrade the organic compounds. $\cdot\text{OH}$ has no selectivity to reactant, makes critical effect in photocatalyzing, but high active electron $\text{O}_2^{\cdot -}$ super oxide anions has strong oxidation ability also can mineralize phenol.



Eventually, all the starting compounds and intermediates are converted into CO_2 and H_2O upon reaction with the above mentioned reactive species, as it stated in the previous equations.

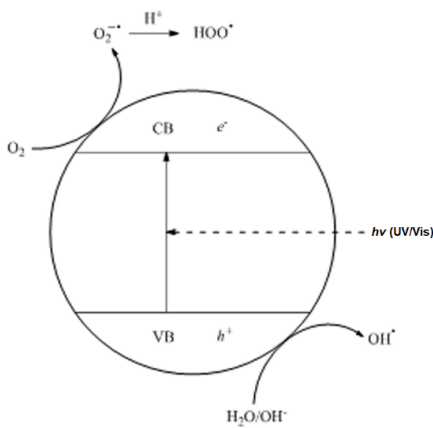


Figure 4: Schematic representation of the oxidation process taking place on the crystal surface [115, 191].

Following the observations made from the previous reactions above and from many literature reviews and reports. The overall process is schematically outlined in Figure 4 above [91, 318].

In Figure 4 above, shows that the pollutant adsorbed to the surface and the light broken the adsorbed pollutant into $e^- - h^+$. The formation $\cdot\text{OH}$ of the reactive species are formed by the reactions of holes (h^+) with absorbed H_2O or OH^- , and via H_2O_2 from the superoxide ion O_2^- [192]. Reduction of oxygen in aerated solution to form O_2^- and H_2O_2 enables in maintaining of the charge neutrality and driving the photocatalytic activity [135]. Later, H_2O_2 would photodecompose to $\cdot\text{OH}$ and react with the substrate [193]. As it was explained, the O vacancies in SnO_2 , can donate O and play an important role in photocatalysis [194, 195].

Many researchers showed that the main products formed from phenol photodegradation led to the formation of a mixture of byproducts such as Cat, BQ, Res and HQ as shown in Figure 5. These photoproducts further react with $\cdot\text{OH}$ and could be mineralize to CO_2 and H_2O as it shown in the Figure below [196-198].

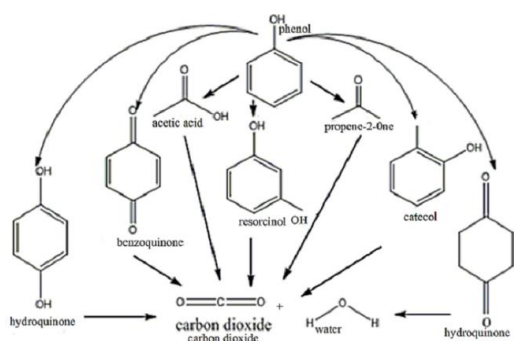


Figure 5: Different chemical photoproducts expected from phenol photodegradation [196-198]

2.3 Application of undoped SnO₂ in the photocatalytic degradation of organic pollutants

2.3 Application of undoped SnO₂ in the photocatalytic degradation of organic pollutants

Many researchers have been demonstrated to show the capability of the pure, undoped SnO₂ material in the photocatalytic applications, since it has the ability to mineralize the target pollutants. The pure SnO₂ has relatively high BG energy (3.6eV) which limits its using to UV light since it has enough energy to trigger the metal oxide.

In the case of pure SnO₂ the visible light does not has sufficient energy to activate the formation of $e^- - h^+$ pairs.

Recent examples are summarized below in the coming Table 4. SnO₂ photocatalytic activity has attracted many researchers due to its potential application of dyes, Tamima and his group prepared SnO₂ nanocrystals from amino acid chelated Sn salts and were used in degradation experiments of Rhodamine B. The study results showed that the synthesis materials were succeeded to degrade the sample in a close to 100% decomposition of the dye concentration after irradiation within 150 min [199]. Comparable outcomes were also gained when SnO₂ Nps synthesized from Sn oxalate using an eggshell membrane. The SnO₂ nanocrystalline were also used for the Rhodamine B degradation. An excellent of 95% degradation in the concentration of the dye was appeared after exposing the solution to UV irradiation for about 1 h [200]. Another green method was used to synthesize undoped SnO₂ Nps, and this was employed in the oxidative degradation of different dyes such as Methylene blue, Eosin Y and Congo red. The authors reported 100% degradation of the dye after 40 min of irradiation measured by UV-Vis, but TOC results showed about 83.3% after 80 min of irradiation [121]. SnO₂ Nps were synthesized by using aqueous extract, were involved in the degradation of Congo red. The results showed higher % of degradation of the dye [201].

Table 4: Some photocatalytic activities of SnO₂

Pollutant	Source of light	Experimental conditions	Degradation efficiency	Comments	Ref.
RhB	250W Hg lamp $\lambda > 365$ nm	C: 50mg/50mL P: 1.0×10^{-5} M	Excellent photocatalytic degradation of RhB	High degradation of the dye due to its small size	[199]
RhB	UV	Different Conc. of SnO ₂ P: 1.0×10^{-6} M	94% degradation after 60 min	photons striking the catalyst	[200]
MB, Eosin Y Congo red	UV	C: 2.5×10^{-6} M SnO ₂ P: 2.7×10^{-6} M	Showed excellent photocatalytic results for the dyes degradation	50% degradation after 20-30 min	[121]
Congo red	$\lambda > 365$ nm	C: 0.25g SnO ₂ P: 1.0×10^{-6} M	Higher degradation of the dye	pseudo-1 st order rate $k=0.9212$	[201]
Violet 4 BSN dye	125 W UV 254 nm	C: 10 mg SnO ₂ P: 25 mg/L dye	100% of the dye in 40 min	Steady after 120 min of UV	[177]
Congo R	Hg lamp UV source	C: 2 mg SnO ₂ Nps P: 3 mL of 10 mg/L	The extract fruit has the capacity to reduce SnCl ₄ to SnO ₂ Nps	SnO ₂ not is good in photocatalytic activity as well as antioxidant capacity	[202]

Abbreviations: Rhodamine B: RhB; concentration of catalyst: C; concentration of pollutant: P; minute: min; ultraviolet: UV; nanoparticless: Nps;

Another researcher synthesized SnO₂ Nps by amino acid tyrosine under UV light irradiation in photodegrading Violet 4 BSN dye. The removal of degradation rate reached up to > than 95% in the presence of these Nps. [177]. All the results of recently synthesized SnO₂ Nps indicated that the semiconductor not only have good photocatalytic activity, but also a high antioxidant capacity against free radicals. Consequently, SnO₂ Nps is an important material can be significantly employ in many industries including the previous applications beside its use in photocatalytic and cosmetic appliances [202].

2.3 Application of undoped SnO₂ in the photocatalytic degradation of organic pollutants

2.3.1 Improving SnO₂ photodegradation efficiency

Despite the great potential of SnO₂ semiconductors for photocatalytic applications, and the antioxidant capacity of the Nps against free radicals [202] its experimental applicability as a pure material is incomplete because of the high activation energy of the metal oxide. This activation energy is in equivalent to irradiation with UV light, and the direct (swift) recombination rate of the photogenerated conduction electron (e^-_{CB}) in the Sn 4d(5S) band and with a hole in the O 2P valence band (h^+_{VB}) [115]. To improve the industrial application of SnO₂, and to enhance the photocatalytic activity, the recombination rate of $e^- - h^+$ pairs requires to be inhibited [203]. One of the options is to dope other semiconductors of different electron energy BG to the metal oxide. Possibly the photocatalytic activity of the new combination material is then improved because it would decrease the recombination rate of $e^- - h^+$ pairs and lower the activation energy [204, 205].

Cristante and its group doped TiO₂ thin films organofunctionalized with 2-aminothiazole ligand and adsorbed Pd(II) ions. The doping method improved the transfer of metal legend load to the metal oxide, prevented $e^- - h^+$ pairs recombination and influenced the photocatalytic activity of the material [206]. In addition, other factors also significantly affect the overall efficiency of the photocatalytic process. Parameters such as the temperature of the reaction mixture [207], the pH of the aqueous solution [208], and the light intensity or the λ of the photon source are significant parameters which require to be carefully optimized and checked [209].

2.3.2 Improving photodegradation efficiency by selective doping of SnO₂

2.3.2.1 SnO₂ coupled with other semiconductors

Free electrons cannot absorb visible light directly in SnO₂; this requires an additional scattering mechanism, such as the coupling of e^- . Coupling SnO₂ with either narrow or wide BG semiconductors is significantly enhanced the charge separation and increased

the photocatalytic activity [210, 211]. SnO₂ has repeatedly been used in combination with TiO₂ semiconductors [212].

Table 5. Improved SnO₂ photocatalytic efficiency by TiO₂ and ZnO semiconductors

Coupled	Light source/ Pollutant	Experimental conditions	Photodegradation efficiency	Ref.
SnO ₂ /TiO ₂	250-W xenon Lamp P: Acid orange 7	C: 0.54mg/cm ² ; P: 1.2 × 10 ⁻⁴ mol/L	The coupled oxide enhanced rate of photocatalytic degradation of the dye more than the oxide alone.	[213]
SnO ₂ /TiO ₂	2×30 W UV Lamps P: MB	C: 0.05g/100mL; P: 5 × 10 ⁻⁵ mol/L	TiO ₂ doped with 5 wt.% SnO ₂ showed better photocatalytic activity	[214]
TiO ₂ / SnO ₂	300 W Hg lamp P: MB	C: 0.05g/100mL; P: 2 × 10 ⁻⁵ mol/L	TiO ₂ doped with 5.6% Sn showed best photocatalytic activity	[215]
SnO ₂ / TiO ₂	UV lamp P: RhB	C: 0.1g /100; P: 1×10 ⁻⁵ mol/L	70% more degradation than with pure oxide about 92% decolorization RhB	[216]
ZnO/ SnO ₂	UV Hg lamp P: MO	C: 0.25g/100mL; P: 20 mg/L	The calcination temperature affected particle sizes.	[96]
ZnO/ SnO ₂	500-W Xe lamp P: RhB	C: 0.01g/10mL; P: 1x10 ⁻⁵ mol L ⁻¹	The coupled semiconductor exhibited higher photocatalytic activity than ZnO or SnO ₂	[217]
ZnO/ SnO ₂	50 W Hg lamp P: RhB	P: 100mL/10.0 ppm	Increased photocatalytic activity of ZnO/SnO ₂ nanofibers	[218]
ZnO/ TiO ₂ / SnO ₂	500W high-pre. Hg lamp Methyl orange	Irradiation time 120 min	Much lower Better photocatalytic activity	[219]

Abbreviations: Rhodamine B: RhB; Methyl orange: MO; Methylene blue: MB; concentration of catalyst: C; concentration of pollutant: P.

TiO₂ and SnO₂ are n-type semiconductors and with BG energies greater than 3.0 eV which also display an absorption in the UV region. It is obvious that both of the semiconductors don't meet the criterion, thus doping is so far the only option.

2.3 Application of undoped SnO₂ in the photocatalytic degradation of organic pollutants

Researchers addressed the fortunate photodegradation of an azo dye (Acid orange 7) in the presence of doped SnO₂. It was reported that a ratio of SnO₂/TiO₂ of 2:1 to be the most effective for the degradation process [213]. Furthermore, SnO₂/TiO₂ coupled synthesized by other groups resulted in higher photocatalytic reactivity of doped material compared with undoped TiO₂ [212, 220].

Peng and colleagues prepared SnO₂/TiO₂ nanotubes with different SnO₂ concentrations by the simple solvothermal process. The results showed that the composite photocatalyst material allowed for increased absorption of Methylene blue on the catalyst surface, resulted in high concentration levels due to their high absorptive properties. Composite photocatalyst also decreased the recombination rate of $e^- - h^+$ pairs and resulted in higher photocatalytic activity. The authors reported that the combination composites photocatalyst with 5% SnO₂ doping had the enhanced photocatalytic efficiency [214]. The best photocatalytic activity was also achieved with 5.6 at. % of Sn/TiO₂. The suspension evaluated the degradation of Methylene blue under UV irradiation. Although the wide energy BGs of Sn and TiO₂ semiconductors, the absorption edge of Sn/TiO₂ shifted towards longer λ with increasing amount of Sn. Mixing the two metal oxides directed the gathering of e^- in the CB of SnO₂ and the photogenerated h^+ in the VB of TiO₂, thus the doping energy level of Sn⁴⁺ ions was formed. Doping Sn/TiO₂ shifted to smaller energy BG and favoured more $e^- - h^+$ pairs when illuminated with UV light, thus enhanced the photocatalytic activity [215].

SnO₂/TiO₂ composite materials synthesized by sol-gel method showed good results in the decolourization of about 92% of Rhodamine B. The availability of 10% of SnO₂ after 3 h irradiation gave only 70% with pure TiO₂. The results showed that SnO₂ reduced the particle size, increased the oxidizing power thus, and increased the photocatalytic activity of the samples [215, 216].

All the results discussed above are summarized in Table 5.

Zhang and his group doped ZnO/SnO₂ nanocomposite binary mixed oxide the coupled photocatalytic activity was examined for the photodegradation of Methyl orange under

UV light. The results exhibited that the calcination temperature strongly affected the particle size of the coupled particles. It was discovered by the authors that the coupled oxides ZnO/SnO₂ showed better photocatalytic activity for the degradation of Methyl orange than ZnO or SnO₂ alone [96].

Wen and co-workers carried out a study on doped mesoporous SnO₂ with a low concentration of ZnO (m-SnO₂/ZnO). They investigated the photocatalytic activities of m-SnO₂/ZnO and m-ZnO by the photocatalytic oxidation of Rhodamine B under UV irradiation. The authors reported that the photocatalytic activity of m-SnO₂/ZnO was higher than that of m-ZnO. The enhancement of the photocatalytic activity for m-SnO₂/ZnO might be due to the bigger surface area and enhanced charge separation that derive from the combined mesoporous [217].

Yet, doping with a small concentration of ZnO was resulted a huge positive effect on the photocatalytic properties of the metal oxide. The coupled ZnO/SnO₂ system also showed higher photocatalytic activity than the pure ZnO and pure SnO₂ for the degradation of the Rhodamine B. This improved photocatalytic activity in the degradation of the dye under UV light irradiation could be explained by the formation of a ZnO/SnO₂ hetero-junction in the ZnO/SnO₂ nanofibers and the high surface area which activated the separation of generated $e^- - h^+$ pairs [218].

Wang et al. [219] prepared a ternary mixture of ZnO, TiO₂ and SnO₂ in the molar ratio of 4:1:1 followed by heating the powder at 200-1300 °C and tested the material for its photocatalytic properties in the degradation of Methyl orange. The prepared mixture showed enhanced photocatalytic activity for the degradation of Methyl orange compared to the pure metal oxides at 500 °C. The photocatalytic activity of the mixture decreased when the calcination temperature exceeded 700 °C, due to the formation of photoinactive ZnTiO₄, Zn₂SO₄ and Zn₂Ti_{0.5} Sn_{0.5} O₄. When the mixture heated to 1300 °C for a prolonged time, the mixture completely lost its photocatalytic properties and became totally inert.

All results discussed above are also summarized in Table 5.

2.3 Application of undoped SnO₂ in the photocatalytic degradation of organic pollutants

Visible light Cr₂O₃/SnO₂, synthesized by the coprecipitation method and the molar ratio of chromium to tin was 1:2 respectively, calcined at 400 °C for 2 h. The material was successively exhibited the highest photocatalytic activity of Rhodamine B reached to 98% in just 60 min and this rate of the nanocomposites was higher than the rate of P25 by about 3.5 times because it had smaller particle size of 10 nm and higher surface area of 38 m²/g [221].

Xia et al. [97] prepared Fe₂O₃/SnO₂ by coprecipitation method, parameters such as the phase composition, crystallite size, BET surface area and optical absorption of the samples changed considerably with different heat temperatures. The photocatalyst exhibited extraordinary photocatalytic activity with Acid Blue 62 and they reported that it could be degraded in 60 min under irradiation of the visible light ($\lambda > 400$ nm). The authors also showed that sample with a molar ratio of iron to tin of 2:1 has better crystallization, when it calcined at 400 C for 3 h. The group also exhibited that the photocatalytic activity of the nanocomposite enhanced obviously as particle size decreased until reached to a diameter of about 15 nm with highest surface area.

Niu and his group synthesized SnO₂/ α Fe₂O₃ by hydrothermal method. The formation semiconductor nanoheterostructures (SNHs) exhibited enhanced photocatalytic activity under visible or UV irradiation when compared to pure α Fe₂O₃ mainly due to effective $e^- - h^+$ pairs separation at the interfaces of the SNHs [222].

SnO₂/V₂O₅ nanowires were synthesized by hydrothermal and wet chemical method. The photocatalytic behaviour of coreshell was examined for the photodegradation of Toluidine blue “O” dye (TBO). The results showed that the nanowires had enhanced photocatalytic activity for the degradation of the dye under UV light than with pure V₂O₅ and bulk due to its large surface area and efficient charge separation of SnO₂/V₂O₅ couple structure [223].

Doping SnO₂ to the Cu₂O using hydrazine as a reducing agent in aqueous solution significantly had a positive effect on the photocatalytic activity of CuO₂ for waste water treatment. The results showed that when the amount of CuO on the surface of

SnO₂/Cu₂O decreased, the photocatalytic activity of Cu₂O for the degradation of trifluralin increased [167].

SnO₂ Nps were synthesized by a sol-gel process and used as a support via deposition-precipitation method. The catalytic activity of the particles affected by the optimum loading of the CuO which was about 8 wt. %. The CuO/TiO₂/SnO₂ catalysts showed higher catalytic activity than CuO/TiO₂, and CuO/SnO₂ catalysts. The results indicated that due to the availability of large amount of CuO which formed the active site for CO oxidation in the CuO/TiO₂/SnO₂ catalyst [224].

Copper oxide (CuO) doped SnO₂ been synthesized as nanocomposites prepared by simple precipitation method. The photocatalytic activity of CuO/SnO₂ examined for the photodegradation of colour Acid Blue 62 as a probe reaction under xenon light irradiation. The uppermost photocatalytic activity was gained with a combination of CuO and SnO₂ in a molar ratio of 1:1 and the calcination temperature was 500 °C for 3 h. The nanocomposite gained from this technique was known to have a high surface area and good crystallization. [225].

A novel visible-light-driven of tin disulfide (SnS₂) doped SnO₂ nanocomposite photocatalyst was described by Zhang and co-workers. The photocatalytic properties of the nanocomposite was examined by the degradation of Methyl orange in water under visible light and $\lambda > 420$ nm. The results showed that the mixed SnS₂/SnO₂ Nps compared to SnO₂ had better photocatalytic activity. The rigid attachment of SnO₂ to SnS₂ Nps facilitated the e^- transfer and decreased the site agglomeration, which helped to achieve high photocatalytic activity. The enhanced photocatalytic activity is also due to the matched band potentials of both semiconductors in addition, somewhat shorter BG of SnS₂ which activated the transfer of e^- from CB of SnS₂ to SnO₂ after photoactivation [226].

Cerium dioxide (CeO₂) doped SnO₂ nanocomposites been prepared and their catalytic activity was examined in the degradation of leather Direct Black 38 in aqueous solutions under irradiation with solar light. The preparation contained different concentrations of CeO₂ doped SnO₂. The results indicated that when the metal oxide was doped with 7

2.3 Application of undoped SnO₂ in the photocatalytic degradation of organic pollutants

wt. % of CeO₂, it showed the best effective photocatalyst for the degradation of the dye (DB38) in aqueous solution under sunlight [227].

Table 6: Improved photocatalytic efficiency by coupled semiconductor

Coupled	Light source/ Pollutant	Experimental conditions	Photodegradation efficiency	Ref.
Cr ₂ O ₃ /SnO ₂	Sun light; P: RhB	C: 0.5g/L; P: 0.5 g/L	98.0% degradation under visible light irradiation	[221]
SnO ₂ /Fe ₂ O ₃	1000 Xe lamp; P: Acid blue 62	P: 50mg/L	98.0% of Acid blue 62 in 60 min under visible light at $\lambda > 400$ nm	[97]
SnO ₂ / α Fe ₂ O ₃	4 WUV lamps; P: MB	C: 50mg /150ml; P: 1x10 ⁻⁵ mol/L	High activity of the catalyst under visible or UV irradiation	[222]
SnO ₂ /V ₂ O ₅	SnO ₂ /V ₂ O ₅ ; P: Toluidine blue "O"	C: 15mg /50mL; P: 0.5mmol	High activity of nanowires	[223]
SnO ₂ /Cu ₂ O	400W Hg lamp; P: Trifluralin	C: 50mg/80mL; P: 50mg/L	SnO ₂ doping increased catalytic activity of the nano-crystals	[167]
SnS ₂ /SnO ₂	1000W Xe lamp; P: Acid Blue 62	C: 300 mg/L; P: 40 mg/L	Enhanced photocatalytic activity for the couple	[226]
CdS/SnO ₂	300 W Xe lamp; P: benzyl alcohol	C: 50mg/20mL; P: CH ₃ CN	Oxidation of benzyl alcohol to benzaldehyde	[228]
BiOCl/ SnO ₂	500W Xe lamp; P: RhB; MO; MB	C: 25 mg/L; P: 0.01 mol/L	High photocatalytic activity for RhB degradation under visible light	[229]

Abbreviations: Rhodamine B: RhB; Methyl orange: MO; Methylene blue: MB concentration of catalyst: C; concentration of pollutant: P.

In another study coreshell nanorods fabricated by synthesizing SnO₂ Nps with a solvent-assisted interfacial reaction and under visible light irradiation showed increased photocatalytic activity for benzyl alcohol to benzaldehyde. Cadmium sulphide (CdS) which has small BG energy (of 2.4 eV) doped with SnO₂ (3.6 eV), the later firmly could be attached on the surface of CdS. The results showed enhanced photocatalytic activity for the oxidation of benzyl alcohol to benzaldehyde under visible light irradiation was higher than for the pure semiconductors. The results showed that in acetonitrile solution, O₂⁻ and the h⁺ pairs are the principle reactive species responsible for the above oxidation process [228].

Bismuth oxychloride (BiOCl) coupled with SnO₂ Nps, showed visible light performance photocatalytic activities. The photocatalytic activity of BiOCl/SnO₂ was evaluated by measuring the degradation of Rhodamine B under visible light irradiation. The composite exhibited higher photocatalytic activity compared to the control one. The n-type of SnO₂ increased the separation rate and inhibited the direct recombination rate of the photo-induced $e^- - h^+$ [229].

Some of the most promising results discussed above are summarized in Table 6.

As it was mentioned earlier that SnO₂ sensor can be promoted by the addition of small amounts of metals such as Pt and palladium Pd. Here in this section it shown that addition of Pd to SnO₂ improved the antimicrobial activity used in biological studies. The photocatalytic antimicrobial activity over SnO₂, TiO₂ and their Pd doped thin film samples were examined against *Escherichia coli* (*E. coli*), *Staphylococcus aureus* (*S. aureus*), *Saccharomyces cerevisiae* (*S. cerevisiae*) and *Aspergillus aiger* (*A. aiger*) spores. The authors reported that higher antimicrobial activity was achieved with TiO₂/PdO more than with SnO₂. In fact, the addition of 1wt. % Pd enhanced the activity of either PdO/TiO₂ or PdO/SnO₂ coatings. The results also showed that presence of the strong cell wall produced high protection to photocatalytic inactivation which organized itself in terms of the slow initiation The photocatalytic antimicrobial efficiency for different microorganisms and spores decreased in the order *E. coli*>*S. aureus*>*S.cerevisiae*>*A. aiger* [230]

2.3.3 SnO₂ doped with metal and metalloids

Doping semiconductors with metal ions has proved to be one of the best ways of improving visible light photocatalytic activity for the oxidation and reduction degradation of organic compounds [231]. In fact, nanoparticle materials have attracted many scientists to build up visible light photocatalysts not only to solve environmental problems but also for the application in renewable energy sources. Usually, photocatalysts need narrow energy BG, efficient optical absorption ability, and high surface area, chemically stable and low cost materials.

2.3 Application of undoped SnO₂ in the photocatalytic degradation of organic pollutants 65

2.3.3.1 SnO₂ doped with RE metals

Earlier, researchers modified SnO₂ catalysts by doping metals with SnO₂ for the oxidation of CO and propane and noticed no improvement in the catalytic activity of SnO₂ toward CO [232].

On the other hand, doping different RE ions onto TiO₂ such as La, cerium (Ce), erbium, praseodymium, Gd, Nd, and samarium (Sm) doped Nps enhanced their photocatalytic activities [233]. Moreover, the introduced RE metals in the form of metal oxides (RE₂O₃) at TiO₂ surface, exhibited higher photocatalytic activity even in the visible range of the electromagnetic spectrum. When TiO₂ doped RE elements demonstrated potential in red shifting absorption edge and enhanced the photocatalytic activity of TiO₂ more than undoped TiO₂ under visible light irradiation. Literature data referred to the red shift of this kind due to the charge transfer transition between $f e^-$ of RE ion and the TiO₂ CB or VB [234]. The doped oxide cations affected the material electronic distribution, caused the absorption of oxygen species and created high surface area with smaller sizes [235-237]. In ytterbium (Yb) doped TiO₂, caused highest photocatalytic activity under visible light in the range from 420 – 475. The mechanism for this visible light sensitization was possibly due to decreased crystallite size, increased BET surface area, Additionally, prevention $e^- - h^+$ pairs recombination, availability of higher absorption sites created oxygen vacancies and surface defects thus, enhanced the efficiency of the system [238]. Doping TiO₂ with RE ions also effected on the optical properties, decreased the BG energy and enhanced the photocatalytic activity of the metal oxide in the visible region [203, 239]. RE metals are inefficient by doping onto SnO₂ increases their sensitization efficiently because of their potential applications in optoelectronic technology and their direct excitation of the infra f shell [240-242].

The intense luminescent properties and f-f electronic transitions RE metals have been applied in the production of lasers, fluorescent displays and lamp [243]. Reports on RE metals doped SnO₂ Nps such as micro lasers, multi-coloured displays, and luminescent labels also exist [244, 245]. SnO₂/Gd influenced the appearance of magnetic properties [246]. Europium oxide (Eu₂O₃) has been examined extensively for a variety of optical

and electronic properties [247-249]. The effect of Eu on electrocatalytic characteristic of Sb/SnO₂ electrodes was also investigated. The results indicated that the performance of the prepared electrodes was strongly influenced by the treatment temperature and the RE metal doping content. SnO₂/Eu produced smaller sizes, larger surface areas and active sites on the electrode surface which improved electrocatalytic oxidation [250]. RE/SnO₂ produced nanopowders 15-20 nm in size and showed luminescence activities [110]. There is an acid/base relation between the RE oxides and the metal oxide [110, 251, 252]. SnO₂ is an acidic isoelectronic point (iep) 4 -7 on the other hand, RE oxides are basic. For instance, La₂O₃ iep 10-12 but Y₂O₃ iep ~ 11 [253]. La/SnO₂ explained the acid/base properties clearly when was used as sensor for ethanol gas. The sensitivity of the metal promoted with the addition of La₂O₃. The enhancement of the gas is due to the oxidation reaction of the gas. The catalytic activity of the gas enhanced since it has been related to the electronegativity of the cations present in the system and thus acid/base characteristics [254]. The same effect was gained in the oxidation of methanol, which led to selectivity changes for methanol decomposition [255].

The effect of CO₂ on SnO₂ also indicated significant differences in the oxides acid/base behaviour sites [122, 256].

Interestingly, Ce ions doped to the metal oxide got a lot of consideration due to the redox couple (Ce³⁺/Ce⁴⁺) allows a shift from RO_x to R₂O_{x+1} like (CeO₂ to Ce₂O₃) The presence of oxygen vacancies with the mobility of bulk oxygen species enhances the catalytic property [257, 258]. Doping TiO₂ metals with RE ions is already known and experienced because of their special incompletely occupied 4*f* and empty 5*d* orbitals electronic configuration, improved their activity. In fact, the specific 4*f* of Ce plays a crucial role in generating and directing the *e*⁻ - *h*⁺ pairs to advance the visible light absorption [259]. Another advantage of Ce metal is plentiful on earth as Ce oxide Ce₂O₃ having BGs in the visible region and oxygen vacancies assisting in visible light absorbing photocatalysis [260].

SnO₂/Sm Nps resulted in increased surface area and a reduction on the BG energy confirmed the enhanced photocatalytic degradation of different dyes over the undoped samples [261].

2.3 Application of undoped SnO₂ in the photocatalytic degradation of organic pollutants

Cui and his group compared doping three kinds of REs on Ti/Sb-SnO₂ electrodes and examined for the degradation of BQ, HQ and Cat with other aliphatic acids. The results indicated that the aliphatic acid with higher oxygen content or more double bonds is more readily to be oxidized. The results showed that the contaminant acid with more oxygen content or more double bonds structure was more readily degraded. Gd and europium were also used to dope SnO₂ and an increased activity of the photocatalyst was observed. Interestingly, in this study, Ce only marginally increased the activity of the catalyst [262]

Table 7 Improved photocatalytic efficiency by RE metals

Catalyst	Light source/ Pollutant	Experimental conditions	Photodegradation efficiency	Ref.
/SnO ₂	260 nm UV light; P: EV and BG	C: 0.233gm/10ml EV: 2.5×10^{-4} M BG: 2.5×10^{-4} M	The photocatalytic degradation enhanced in the presence Sm ³⁺ ions	[261]
/Sb/SnO ₂ Ti/Ce/Sb/SnO ₂ Ti/Gd/Sb/SnO ₂ Ti/Eu/Sb/SnO ₂	Potentiostat for organic degradation studies P: BQ	P: mg/L C: 100mg/L	Faster degradation of BQ because of electrophilic attack of OH	[262]

Abbreviations: samarium: Sm ethyl violet: EV; benzoquinone: BQ; brilliant green: BG; concentration of catalyst: C; concentration of pollutant: P.

Some of the most promising results discussed above are summarized in Table 7.

2.3.3.2 SnO₂ doped with TMs

TM compounds have been employed between the ionic and the metallic states of the metal, thus providing high catalytic activity of SnO₂.

Xu and colleagues doped SnO₂/Sn nanocrystals extremely active photocatalysts and used for the photodegradation of organic pollutants. This self-doped material was used for the degradation of Methyl orange under visible light irradiation in a short time. In this technique Sn²⁺ substituted with Sn⁴⁺ ions in the rutile structure, O vacancies are produced and sustained the overall neutral charge of the metal oxide, therefore decreased the band energies and enabled activation of the photocatalyst with visible light [263].

TMs like manganese, (Mn^{2+}) and Ce^{+3} with other RE ions helped to raise the O vacancies related luminescence which resulted from the formation of many more oxygen vacancies. Addition of manganese amounts resulted on the doping level influenced not only the structural, magnetic, electronic and the luminescence properties of the semiconductor but also enhanced the photocatalytic properties of the semiconductor [148, 264].

Even though, nano doped SnO_2 had larger surface area, smaller crystallite size and lower BGs, factors added towards enhanced photocatalytic activity. In fact, a total understanding of these correlations has to be very well known, and the mechanisms also remain a challenge to scientists.

Selenium (Se) SnO_2/Se synthesized by sol-gel process had high crystallinity and broadened width. The decreased crystallite size was in the range of 12-17 nm. The Nps advanced the electronic character of the nanomaterial and decreased in the energy BG from 3.6 to 2.9 eV [265].

Oldfield and his group deposited gold (Au) on SnO_2 , to show the capacity of the storage for the element since the electron density changes within the core can be observed through changes in the surface plasmon (SP) absorption band of the Au particle. The group observed the deposition of the metal oxide shell and the electron transfer processes spectrophotometrically, by using shifts in the surface plasmon (SP) band position of the Au core [266]. Au/ SnO_2 nanostructures synthesized by seed-mediated hydrothermal method, exhibited better catalytic performance in the photodegradation of Rhodamine B due to the separation of effective $e^- - h^+$ pairs at the SnO_2 -Au interfaces and strong localization of plasmonic near fields effect [267]. Others deposited Au/ SnO_2 Nps; the combined material was used for the photocatalytic degradation of RhodamineB (R6G). The results exhibited enhanced photocatalytic performance in the photodegradation of the dye due to the effected $e^- - h^+$ separation at the SnO_2/Au interfaces and the larger surface area [268].

Silver Ag/ SnO_2 nanocomposites exhibited higher photocatalytic activity under visible light for the degradation of Methyl orange, Methylene blue, 4-nitrophenol and 2-chlorophenol compared to pure undoped Nps. The authors showed that the Ag Nps

2.3 Application of undoped SnO₂ in the photocatalytic degradation of organic pollutants

induced visible light activity and facilitated efficient charge separation in the Ag-SnO₂ nanostructures [269].

There have been several studies of the magnetism of SnO₂ based DMS doped with transition metals. With nickel (Ni), it was found that the measured magnetic moment per Ni ion decreased when the amount of doping was increased [270].

Table 8: Improved photocatalytic efficiency by RE metals

Catalyst	Light source/ Pollutant	Experimental conditions	Photodegradation efficiency	Ref.
Sn/SnO ₂	300W Xe lamp; P: MO	C: 50mg/50mL; P: 10 mg/L	The nanocrystals enhanced degradation activity for the dye	[263]
Mn/SnO ₂	8 Hg lamp; P: MO	C: 45mg/100mL; P: 2.7x10 ⁻³ mol/L	Doping levels had strong influences on the photocatalytic activity	[148]
Au/SnO ₂	Hg W lamp; P: RhB	C: 100mg/40mL; P: 5mg/500mL	Enhanced the degradation activity of the dye with the treatment of the nanostructure	[271]
Au/SnO ₂	300 W 365 nm; P: R6G	C: 0.015gm/50mL; P: 1mmol/L 1mL	Highly activity of nanocrystals	[268]
Ag/SnO ₂	Visible light irradiation; P: MB 4-NP and 2CP	C: 2mg/20mL; C:10mg/20mL	nanocomposite enhanced the photocatalytic activity under visible light irradiation for the degradation of the dye	[269]

Abbreviations: Rhodamine B: RhB; Methyl orange: MO; Methylene blue: MB; 4-nitrophenol: 4-NP; 2-chlorophenols: 2-CP; concentration of catalyst: C; concentration of pollutant: P.

The magnetic properties of manganese SnO₂/Mn were also dependent on the Mn doping content [272]. Chromium SnO₂/Cr played an important role in tuning the ferromagnetism of SnO₂ nanostructures, in addition to the contribution of surface oxygen vacancies [273]. Room temperature ferromagnetism is also possible with TMs [274]. Yet many controversial results have been reported regarding magnetism in DMS [275]. These included TMs doped SnO₂ thin films and powders [239, 276-278], which led to the formation of energy states below the CB. These previous results effectively

increased visible light absorption in materials [279]. The previous experiments appear promising and will further be developed over the next coming years.

2.3.3.3 SnO₂ doped with metalloids

SnO₂ is an n-type metal oxide as well as Sb, also common for n-type dopant in SnO₂ [Sb doped tin oxide (ATO)]. In fact, the free electron in SnO₂ strongly enhanced when doped with Sb as in n-type thin films, optoelectronic devices, sensors, and other apparatuses used in pharmacology and medicine [280-282]. SnO₂/Sb with various Sb concentrations showed enhanced n-type electrical conductivity with a wide optical gap > 4eV and a high charge carrier density resulted in an excess of electrons so the addition of Sb modified the band structure of SnO₂ [137]. As SnO₂ is a n-type semiconductor, its tetravalent Sn⁴⁺ ~0.071 nm sites can substitute pentavalent Sb⁵⁺ ~0.065 nm ions. The larger pentavalent Sb⁵⁺ ions can replace tetravalent Sn⁴⁺ ions but the smaller trivalent (Sb³⁺~0.09 nm) cannot fit into the rutile SnO₂ structure. SnO₂/Sb led to the formation of donor levels and shifted the Fermi level towards the CB. [281] Substitution of Sn⁴⁺ by Sb⁵⁺ is found to be dominant at the lower Sb doping concentrations (typically less than 2 at. %) due to their similar ionic radii making an increase in the conductivity on SnO₂ [137, 140, 283-285]. On the contrary, doping with higher Sb concentrations resulted in reduction in the conductivity because of the precipitation of Sb oxides [286]. Reduction in Sb⁵⁺ states to Sb³⁺ states would result in the lowering on n-type conductivity due to the formation of the acceptor sites [287]. Electrodes are usually doped with Sb to improve its conductivity [288-290] as in SnO₂/Sb led to the formation of donor levels in the bulk, shifted the Fermi energy towards the CB edge. Behtash and co-workers examined the thermodynamic stability and the electronic properties of some pentavalent doped SnO₂ systems, which were found to energetically favour O-rich over O-poor conditions.[291] since Sb⁵⁺ replaced Sn⁴⁺ sites and left excess electrons. SnO₂/Sb enhances photocatalytic activity by decreasing the recombination rate of $e^- - h^+$ pairs. Sb dopant ions can act as $e^- - h^+$ pairs trap or can mediate in interfacial charge transfer, leading to increase charge separation in the photocatalyst. SnO₂/Sb was prepared on metal substrates resulted with a weak bonding

2.3 Application of undoped SnO₂ in the photocatalytic degradation of organic 71 pollutants

between the film and the substrate [292]. SnO₂/Sb deposited on glass substrate compared to the reflectance of on silicon, exhibited high energy gap and stayed transparent at a λ in the visible region. The results showed that the reflectance of SnO₂/Sb deposited on glass was reduced. It was clear that the roughness of the silicon advanced the reflectance and hence the optical parameters. [293]. SnO₂/Sb used for the oxidation of *p*-methoxy-phenol (PMP) in aqueous solution, the effects of applied potential with the initial concentration of the pollutant showed the formation of CO₂. CO₂ formation was low at potentials < 2.3 V while mineralization to CO₂ decreased as the concentration of PMP increased [294]. Ni/Sb/SnO₂ electrode effectiveness was examined for the electrochemical degradation of 4-CP. The results showed that the increased in electrode efficiencies for electrochemical oxidation of 4-CP was attributed to the production of highly reactive \cdot OH [295].

Table 9 Improved SnO₂ photocatalytic efficiencies by Sb doped

Catalyst	Light source/ Pollutant	Experimental conditions	Photodegradation efficiency	Ref.
SnO ₂ /Sb	Electrode potential; P: PMP	P: 0.1 mg/1000mL	Decreased degradation rate with increasing pollutant concentration	[294]
Ni/Sb/SnO ₂	UV light solar light 4-CP	P: 8mM (1028 mg/1000mL)	4-CP destruction was higher than the control	[295]

Abbreviations: 4-chlorophenol: 4-CP; *p*-methoxy phenol: PMP; concentration catalyst: C; concentration of pollutant: P.

Other scientists doped molybdenum on SnO₂ and showed extraordinary effects on the electrical and optical behaviour of SnO₂ films [296].

Results discussed above are summarized in Table 9

2.3.3.4 Other metals doped SnO₂

Doping SnO₂ with TMs or metalloids also affected the particle size, surface area and the BG energy of the Nps. Cobalt Co/SnO₂ exhibited decreased grain size, and caused an enhancement in the photocatalytic activity of 4-hydroxybenzoic acid (4-HBA). The UV-visible diffuse reflectance spectra of the samples exposed red shifts, and the optical BG energies decreased with the increased Co concentration. Complete photodegradation of

10 ppm of 4-HBA solution was gained, after irradiation with UV light for 1 h [152]. Co/SnO₂ Nps showed the substitution of Co²⁺ into Sn⁴⁺ resulted in the energy BG decreased with increased cobalt doping [297]. SnO₂/Co for pulsed laser deposited thin films led not only to high temperature ferromagnetism but also a giant magnetic moment [298]. A recent study by Zhao and colleagues confirmed that the temperature during the calcination process has a major effect on the photocatalytic properties of doped SnO₂ nanomaterials. With increasing calcination temperature, a decreased in the photocatalytic properties of the Nps was observed [299]. Zinc Zn/SnO₂ nanorods prepared by a hydrothermal method and examined by degrading Acid fuchsin. The Nps exhibited a greater photocatalytic activity rate than the pure SnO₂ powders, and showed an enhanced gas sensing ability towards methanol, ethanol and acetone by high sensitivity and fast response [300].

Iron Fe/SnO₂ Nps displayed higher performance by a sol-gel hydrothermal route, led to smaller size distribution, a greater surface area, better stability against agglomeration, improved thermal stability and a red shift in the UV absorbing band width with increasing amounts of the Fe³⁺ doping [301]. Fe/SnO₂ synthesized by sol-gel method showed efficient photocatalytic degradation of Rhodamine B under UV light. the results showed that the 5% Fe/SnO₂ Nps decomposed Rhodamine B by more than half after 2 h of an illumination time [302]. Fe/SnO₂ synthesized by pulsed laser pyrolysis. The particles size about 10 nm and well dispersed Nps triggered magnetic properties suggested the magnetization is not controlled by the amount of Fe [303].

Vanadium V/SnO₂ synthesized by sol-gel and used to examine the effect of doping concentration on structural, morphological and optical properties of prepared Nps. It was found the ferromagnetism behaviour dependent on the vanadium dopant content and a quenching in green luminescence was detected. Furthermore, the 5% sample of SnO₂/V exhibited higher photocatalytic activity than the control in decaying Methylene blue and Rhodamine B [275].

2.3 Application of undoped SnO₂ in the photocatalytic degradation of organic pollutants

SnO₂/V Nps synthesized by chemical coprecipitation reached an average of 5.4-7.7 nm in crystal size and the pores in the nanoparticle size of about 5-15 nm in diameter [304].

Selenium Se/SnO₂ gave an improved electronic character of the nanomaterial with a decreased energy BG and the minimum size of the Nps obtained was found within the range of 12- 17 nm [305].

SnO₂ is an oxidation catalyst which displayed good activity for carbon monoxide oxidation [306, 307].

SnO₂ is used in chemical applications as a support material for dispersed metal catalysts as in SnO₂/Pt and SnO₂/Pd synthesized as thin films, and could demonstrate high sensitivity to liquefied petroleum gases [308-310]. The high surface area of SnO₂ was used as a support for Pd catalysts, which are very active for the reduction of NO to N₂ at comparatively low temperatures [311].

Doping SnO₂ with metals such as Pt, Pd, ruthenium (Ru) and rhodium (Rh) improves its catalytic activities. The best results were achieved with SnO₂/Pt due to its high oxidation state [88, 312].

Dieguez and co-workers examined the influence of Pt and Pd impregnation in sol-gel fabricated SnO₂ Nps after calcination. This was shown to enhance gas sensor performance [313].

Another researcher examined low temperature oxidation of methane over a Pd catalyst supported on metal oxides. SnO₂/Pd was found to have excellent activity for the complete oxidation of methane [314].

Feng and colleagues doped Pd with SnO₂ Nps dispersed in mesoporous silica by a thermal decomposition method. Due to confinement of the pores of the mesoporous silica, SnO₂ nps grew rather slowly had a large surface area, formed nanochains and free

surfaces. The nanocomposite exhibited electrical conductivity and a high sensitivity to CO gas, even at a low operating temperature [315].

Table 10 Enhanced photocatalytic activity of SnO₂

Catalyst	Light source/Pollutant	Experimental conditions	Photodegradation efficiency	Ref.
SnO ₂ /Co	450 W Hg lamp; P: 4-HBA	C: 3 g/L; P: 4-HBA; C: 10 mg/L	Complete photodegradation of 4-HBA	[152]
SnO ₂ /Zn	500 W Hg lamp; P: AF	C: 100 mg/L; P: 4 mg/L	Degradation speeded up 8 times compared to pure	[300]
SnO ₂ /Zn	500 W Hg lamp; P: MO	C: 30 mg/L; P: 50 mL, 20mg/L	Photocatalytic MO degradation rate of Zn/SnO ₂ is higher than the undoped	[299]
SnO ₂ /Fe	250W UV light P: RhB	25 mg /0.050L; P: 25 mg/L	degraded the RhB solution by ~55 % after 2 h.	[302]
SnO ₂ /V	400 W UV lamp MB RhB	C: 50mg/0.050 L; P30 mg/L for both dyes	Highly activity of nanocrystals	[275]

Abbreviations. 4-hydroxy benzoic acid: 4-HBA; Rhodamine B RhB; Rhodamine 6G: R6G; concentration catalyst: C; concentration of pollutant: P. Acid Fuchsine: AF

In metal oxides, upon irradiation with an appropriate light energy, free electrons are excited to the empty CB leaving positively charged holes in the VB, resulting in the formation of $e^- - h^+$ pairs. In addition, a wide SnO₂ BG leads to a decrease in luminescence quenching effects and higher excitonic ionization energy [316]. Some work has been done on the luminescence properties of SnO₂, and the bands from SnO₂ were around 2.4-2.5 and 2.9-3.1 eV [241, 317-319].

A new method to obtain small sized SnO₂ powders for gas sensors was based on a microwave treatment with a frequency of 2.45 GHz that produced powder precursors in few min. The obtained Nps guaranteed a grain size even after 1000 °C and 8 h annealing [320]. Sensor occurrence and selectivity for liquefied petroleum gas has been improved using additives such as methane, silicon (Si) [321], and cesium (Cs) [322], or their oxides [168].

2.3 Application of undoped SnO₂ in the photocatalytic degradation of organic pollutants

Aluminium (Al)/SnO₂ Nps, tested for the influence of hydrothermal reaction time, the molar ratio of Sn/Al and the pH. The results showed that the particle core was rich in Sn, but the surface was rich in Al. Al/SnO₂ Nps exhibited best parameters at pH 5, Sn/Al ratio 4:1, and time 12 h at 160 °C [323]. Many scientists also examined CO₂ chemisorption on SnO₂ [252, 256, 324].

2.3.4 SnO₂ doped with non-metal ions

The wide BG of SnO₂ requires an excitation photoreactor, limiting its role because it reduces the absorption ability of the high energy UV portion of solar light, which accounts for its relatively low efficiency.

SnO₂ utilizes only about of~5% UV light, the rest~43% visible, and~52% infrared radiation to complete the photocatalytic process, and is not responsive to visible light where $\lambda > 400$ nm [325]. To find a solution for this limitation, extending the absorption of SnO₂ into the visible region enables it to utilize as much as 50% of the total sun light reaching the catalyst surface.

2.3.4.1 Iodine doped tin oxide

Wen used TiO₂ Nps codoped with iodine (I) and fluorine (F) to improve the degradation of Methylene blue under visible light irradiation. After prolonged sunlight illumination a complete removal of dye colour was noticed with the disappearance of some byproducts [326].

TiO₂/I were found to show improved photocatalytic properties for the oxidative degradation of phenol under UV and visible light irradiation more than the pure. When calcination temperature was 673 K, TiO₂/I Nps demonstrated stronger absorption in the 400-550 nm range through a red shift in the BG transition and were therefore able to efficiency oxidize pollutants at a longer λ [327].

The photocatalytic efficiency of TiO₂/I materials was also increased when it modified with SnO₂ Nps and used for photodegradation of 2-chlorophenol. The improved photocatalytic activity is obtained from the effect between the SnO₂ and TiO₂/I which

helped the efficiency of migration of the photogenerated $e^- - h^+$ pairs of the catalyst [196].

SnO_2/I isolated gap states located within the BG below the Fermi level above the valence band consisted of the oxygen 2P and tin 5S orbitals, which narrowed the optical BG to 3.5 eV. I 5p states appeared above the Fermi level and did not contribute to the gap states [291].

SnO_2/F coatings have been prepared using the mid-frequency pulsed DC closed field unbalanced magnetron sputtering technique in an Ar/O_2 atmosphere showed high chemical, structural stability, good electronic conductivity and a shift in the BG [328]. The shift in the BG due to the energy gap between the VB and the lowest energy state in the CB which found to increase in the carrier concentration [329]. The density of electronic states increased at the Fermi level with an increase in F concentration incorporated into the main SnO_2 matrix, due to the increase of the CB in F/SnO_2 [330]. SnO_2/F are characterized by O vacancies which further examined in the decomposition of the dye under UV illumination, to show the photocatalytic properties of the material. As a consequence, SnO_2/F showed a very high photocatalytic activity for the degradation of Rhodamine B compared to the pure SnO_2 [331].

In another study, when I was doped with TiO_2 the results showed that the concentration of the I is mainly located to the surface of the TiO_2 , and it rapidly decreased within the crystal structure because of un-favourable I-O interactions as I atoms preferred doping near the TiO_2 surface due to strong I-O repulsion [332]. In TiO_2/I Nps the recombination of the $e^- - h^+$ pairs is inhibited because of the doped I sites will not only catch electrons but also direct them to the surface of the adsorbed species (material) thereby enhancing the photocatalytic activity [204]. Continuous states at the site of TiO_2/I consists of 2p and or 5s orbitals of I⁵ and oxygen. The resulted 2p orbitals of the VB are favourable for the efficient trapping of $e^- - h^+$ pairs at the TiO_2/I particles. The Sn interstitials and O vacancies in SnO_2 were found to have low formation energies and a strong mutual attraction. The stability of the defects is due to the multi-valence of Sn, which donates O to the CB [333]. Elucidating the high conductivity and nonstoichiometric nature of

2.3 Application of undoped SnO₂ in the photocatalytic degradation of organic pollutants

SnO₂ as pointed in a previous section In the application of all these materials, charge carrier concentration and conductivity is further increased by extrinsic dopants, as has been demonstrated for SnO₂ [88]. It have been reported that Sb can act as a cation dopant but F can act as an anion dopant when doped and improved the conductivity of SnO₂ [334]. While SnO₂ powders have been utilized on a large scale in various fields of science and technology, there are not so many reports on preparation techniques. Thus, performance enhancement of SnO₂ remains a challenge, and it is extremely desirable to develop new, simplified methods for synthesizing SnO₂ Nps [279]. SnO₂ catalyst activity and selectivity could be significantly improved by incorporating of different hetero-elements [331, 333]. Additives are often mixed with the SnO₂ matrix to modify its microstructure and defect chemistry, which may enhance sensor response and selectivity to different target gases [88].

Seema and colleagues prepared a graphene (RGO)/SnO₂ composite [335] synthesized through a redox reaction and exhibited excellent electrical conductivity which improved the photocatalytic degradation of pollutants. When Methylene blue illuminated under solar light, the organic dye was rapidly and completely degraded compared to the control. The results showed that the composite might be also used in photodegradation of other dyes [335].

The results discussed above are summarized in Table below.

Table 11: Comparison of some non-metal ion doped SnO₂

Catalyst	Light source/ Pollutant	Experimental conditions	Photodegradation efficiency	Ref.
Graphine /SnO ₂	350W Xe lamp sunlight MB	C: 10mg/0.050L; P: 2.7× 10 ⁻⁵ M	The dye was degraded completely after 6 h	[335]
F/SnO ₂	125 W Hg lamp RhB	C: 0.1g/0.1L; P: 5 × 10 ⁻⁶ M	A very high photocatalytic efficiency	[331]

Abbreviations; Rhodamine B: RhB; Methylene blue: MB; concentration catalyst: C; concentration of pollutant: P.

2.4 SnO₂ synthesis methods

Researchers have developed the synthesis of SnO₂ Nps of different sizes, at different temperatures and above 350 °C [158, 336-338], transparent conducting electrodes [339-341]. It was found that the high temperature was applied to produce a crystalline material [342, 343], but other procedures for the preparation of crystalline SnO₂ nanostructures do not include high temperature treatment [344, 345].

Synthesis of SnO₂ nanowires, could be further converted to polycrystalline, a highly porous material used for gas sensors and ethanol sensors, practiced in the biomedical and chemical industries, food degradation, to supervise fermentation, and other processes [346-348]. All these sensors work at high temperatures, but sensors which operate at lower temperatures are advantageous for decreasing power consumption [349].

SnO₂ can be easily synthesized using various chemical methods.

2.4.1 Sol-gel

Sol-gel is a process for synthesizing materials from a liquid solution of organometallic precursors. The liquid solution hydrolysed and condensed to form a new phase (sol). The sol is made of solid particles of nm suspended in the liquid phase. The particles are later condensed in a new phase (gel) in which a solid molecule is immersed in the solvent. Drying the gel at low temperatures (25-80 °C), makes it possible to obtain porous solid Nps [350]. Sol-gel method is used to prepare TiO₂ thin films to degrade phenol, due to the improved transfer of metal legend load, which prevented $e^- - h^+$ pairs recombination [206]. Moreover, a comparative study using sol-gel synthesis, indicated that CuO/TiO₂/SnO₂, CuO/TiO₂ and CuO/SnO₂ synthesized by simple sol-gel dialytic processes which also used a support to prepare CuO supported catalysts through a deposition-precipitation method showed higher activity than the binary [224]. There are three methods for applying sol to the substrate.

2.4.1.1 Dip-coating

The first method is dip-coating, where the substrate is immersed in a solution and is taken up vertically, so that the solution solidifies later into a gel [351]. SnO₂ thin films were prepared by dip-coating deposition technique, and the suspension was synthesized by microwave induced thermohydrolysis of SnCl₄ aqueous solution in the presence of HCl, resulting in films of about 20 nm thickness [352, 353].

Adamyan et al. [354] explored the preparation of SnO₂ films with thermally stable Nps. They found that the SnO₂ synthesis could be achieved using two techniques: tin chloride hydrolysis, and hydrolysis of sodium stannate with phosphoric acid. The latter yielded more stability of grain size than the former.

2.4.1.2 Spin coating

Secondly, in the spin coating method, the solution is dropped onto a rotating glass substrate, rotated at 5000 rpm for 30 second using a Laurell spin coater [355].

2.4.1.3 Laminar flow coating

Thirdly, in the laminar flow coating method, the substrate is coated in an upside down position and pumped into a hole, so that a small amount of solution coats a large amount of substrate [356]. SnO₂ Nps prepared by the sol-gel method using SnCl₄·5H₂O and NH₄OH followed by heating at a high temperature showed luminescence around 400 nm, but its intensity decreased with the increased temperature [245]. Commonly, high temperature synthesis would decompose the particles directing to the aggregation, resulting in poor dispersability in different solvents and a decline in luminescence efficiency due to self-quenching.

2.4.1 Coprecipitation

In the coprecipitation method ammonia was added to the prepared solutions and the salts were precipitated. Later the precipitation was mixed and cooled to bring it down to room temperature [357, 358]. SnO₂/ZnO nanocomposite binary coupled was synthesized by

the homogenous coprecipitation method in the presence of ethyl acetate. The results showed that the controlled calcination temperature had an effect on the size of the doped oxide particles [359]. Another novel visible-light-activated $\text{SnO}_2/\text{Fe}_2\text{O}_3$ nanocomposite photocatalyst was synthesized by the coprecipitation method which gave best performance in sunlight photocatalysis [97]. $\text{SnO}_2/\text{CeO}_2$ nanocomposites were synthesized through coprecipitation method, contained different CeO_2 concentrations with 20 mL of 5 wt. % tetrapropyl ammonium bromide in ethanol. The photocatalyst exhibited good photocatalytic activity for the dye removal in just 60 min under visible light [227]. Hui-li et al prepared CuO-SnO_2 nanocomposite by the coprecipitation method, for the photodegradation of colour Acid Blue 42 as a probe reaction under xenon light irradiation. The highest photocatalytic activity, good crystallization, and a high surface area were achieved with a 1:1 molar ratio of Cu to Sn, calcined at 500 °C for 3 h. [225]. $\text{SnO}_2/\text{Cr}_2\text{O}_3$ visible light nanoparticle photocatalyst was synthesized by a coprecipitation method. The results showed at high loading concentrations, penetration of the light inside the reaction medium reduced because of light scattering and shielding effect by the catalyst particles [221]. Acrabas et al. [360] prepared nanosized SnO_2 powder via the homogenous precipitation method. SnO_2 Nps were precipitated from 0.01-1M SnCl_4 urea aqueous solutions by the decomposition of urea at ~90°C. The crystallite size of SnO_2 increased with increasing initial concentration and produced small few nanometers. Furthermore, calcination affected crystal growth and agglomeration, reduced the surface area of SnO_2 powders. SnO_2 was prepared from tin tetrachloride (SnCl_4) by precipitating SnCl_4 at room temperature in an aqueous solution (of 50% NH_4OH). The crystallites contained hydroxyls which resulted in asymmetry in the rutile tin-oxygen octahedron [155]. Sn ethoxide was synthesized from SnCl_4 and NH_3 in ethanol and the resulting Cl^- was eliminated by the precipitation of NH_4Cl . Sb and Al were synthesized in the same way which showed strong bonding between the film and the substrate [292].

2.4.2 Hydrothermal and solvothermal methods

The hydrothermal method was prepared by mixing the chemicals in distilled water. The pH was adjusted until a white gel appeared. The gel was stirred for some time and transferred to a closed vessel, such (Teflon line autoclave) with water. In the autoclave the pressure increased and the water remained liquid above its normal boiling temperature of 100 °C [199, 361].

SnO₂/Al Nps were hydrothermally synthesized resulted particle's rich in Sn and the surface rich in Al. The synthesis optimum condition was pH 5, Sn/Al ratio 4:1, and time 12 h at 160 °C [323]. SnO₂ Nps were synthesized from an amino-acid assisted hydrothermal method with controllable shape, doping and with size under 10 nm [199]. Mesoporous SnO₂ doped with a low concentration of ZnO (m-SnO₂/ZnO) was synthesized by the hydrothermal method using cetyltrimethylammonium bromide (CTAB) as a structure directing agent. Coupling of ZnO and SnO₂ exhibited high surface area with a stable structure against temperature [217]. One dimensional of SnO₂/V₂O₅ nanowires were synthesized by a combination of hydrothermal and wet chemical at room temperatures. The results showed that the SnO₂/V₂O₅ combination had large specific surface area and efficient charge separation which gave good photocatalytic behaviour [223]. Yang et al. [362] synthesized novel hexagon SnO₂ nanosheets in ethanol/water solution by hydrothermal process. Comparison experiments showed that when starting with materials such as SnCl₄·5H₂O, NaOH, hexadecyltrimethyl ammonium bromide and ethanol, the temperature increased from 140-180 °C, the edge length of the hexagon Nps increased from 300-450 nm to 700-900 nm. Different types of triangle and sphere were obtained when the ratio of water to ethanol decreased from 2 to 0.5, but when the concentration of NaOH increased from 0.15 M to 0.3 M, a hollow ring morphology could be obtained. Au/SnO₂ were synthesized by a low cost environmentally friendly solution using hydrothermal method to produce multicore shell of SnO₂/Au Nps. Due to the effective $e^- - h^+$ pairs separation at the combination interfaces and high localization of plasmonic near fields effects, the hybrid showed increase UV or visible photocatalytic abilities [267]. SnO₂/TiO₂ nanotubes composites were synthesized by simple solvothermal process. The TiO₂ nanotubes synthesized in

hydrothermal condition and then SnO₂ loaded on them by solvothermal process. The results showed that the composite photocatalyst with proper amount of SnO₂ doping gave best photocatalytic activity [214]. In another work Au nanoparticle doped to SnO₂ nanostructures been prepared by a solution based reaction with N,N-dimethylformamide in the presence of poly(vinyl pyrrolidone) as a solvent and poly(ethylene glycol) as a capping agent. The results showed that SnO₂ accumulated to as hollow hexapods [268]. Visible light driven of Ag/SnO₂ were synthesized using an electrochemically active biofilm (EAB) developed on plain carbon paper. The authors reported that silver Nps increased visible light activity and enabled pairs of $e^- - h^+$ pairs separation in the SnO₂/Ag nanocomposites so advanced its photoelectrochemical performance [269].

2.4.3 Pyrolysis

A pyrolysis method was used to investigate the effect of Eu on electrocatalytic characteristic of Ti/based SnO₂/Sb electrodes. The electrocatalytic activity of the electrodes were affected by the temperature and the doping content of Eu [250]. Sahm et al. [363] synthesized SnO₂ Nps for gas sensing by the flame spray pyrolysis method. The flame made SnO₂ Nps were highly crystalline, with a crystallite size about 17 nm, demonstrated high sensitivity and rapidly reduced propanol and oxidized NO₂ gases.

2.4.4 Soft chemistry

The soft chemistry method or (chimie douce) as it known in French, is similar to sol-gel method, it is possible to prepare materials from this method at low temperatures to synthesize reactive nanosized particles. In the procedure the chemicals mixed with a large amount of water, and stirred for several days until a cloudy solution appeared. Later the pH was adjusted and the gel removed from the beaker [364, 365]. This technique used to prepare nanosized particles of SnO₂ gel by using a one-step aqueous method with SnCl₂·2H₂O powder. The powder mixed with large amounts of water and stirred for 48 h. The resulted gel heated at 600 °C for 24 h and examined for the photocatalytic degradation of Congo red compared to the dried gel at room temperature for 48 h. The results showed 80% photocatalytic degradation of Congo red with the

average particle size compared to be between 2-3 nm. Even after heating the gel at 600 °C for 24 h, the synthesized particles remained in the nanosize range, about 25–30 nm. The wet gel that had not been dried contained fewer agglomerated particles and had higher photocatalytic activity for the degradation of Congo red solution [364].

The SnO₂ particles remained smaller than 6 nm using the second technique even after calcination at 750 °C.

2.4.5 Polyolmediated fabrication

Ng et al. [366] synthesized SnO₂ Nps with a diameter of less than 5 nm in air by the polyolmediated fabrication method, and refluxing of SnCl₄•2H₂O in ethylene glycol under vigorous stirring for 4 h at 195 °C in the air. The synthetic procedure was simple, cheap, straight forward, and could be approved for the large scale production of ultrafine SnO₂ nanosized particles. SnO₂/Sm was synthesized by the polyol procedure method, the results indicated the formation of a Sn-O bond and capping of the Nps by ethylene glycol, which gave a spherical shape for pure and doped SnO₂ Nps [261].

2.4.6 Chemical vapour deposition

Qu et al. [367] prepared an intriguing one dimensional nanostructure of SnO₂, included nanowires, dendritic nanorods, and falchion link nanosheets, by the chemical vapour deposition method. The effects of temperature and anodic Al oxide template, with or without (Au) catalyst particles on the morphology of the final product were investigated. Uniform nanowires 10-100 of micrometers in length and with a diameter of about 80 nm were obtained. Temperature and templates were the most important factors affecting the morphology of the product.

2.4.7 Solid state reaction

SnO₂ was prepared by mixing to ZnO and TiO₂, by solid state reaction and at calcination temperatures between 200–1300 °C. The results showed that solid state reaction did not take place among the SnO₂, ZnO and TiO₂ powders on the calcination up to 600 °C but

the formation of the inverse spinel of Zn_2TiO_4 and Zn_2SnO_4 was determined at 700-900 and 1100-1200 °C [219].

2.4.8 Mechanochemical reaction

SnO_2 Nps were obtained by mechanochemical reaction of $SnCl_2$ with sodium carbonate (Na_2CO_3) in the presence of sodium chloride ($NaCl$) as a diluent via heat treatment in the form of milled powder. This process increased the crystal size of SnO_2 Nps from 25 - 40 nm at temperatures ranging between 450-800 °C [368].

2.4.9 Milling technique

Legendre et al. [369] synthesized nanostructure tetragonal SnO_2 powder by milling Sn at room temperature under O in a vertical planetary ball-mill. The formation of SnO_2 was mechanically induced, and in a short milling time a powder of about 10 nm SnO_2 crystallites was produced.

2.4.10 Thermal decomposition and electrodeposition

Ti substrate deposited with other metal oxides such as $SnO_2/Sb_2O_3/Nb_2O_5/PbO_2$ by applying thermal decomposition and electrodeposition. The results showed that the electrode described as $Ti/SnO_2/Sb_2O_3/Nb_2O_5/PbO_2$ thin films. The surface of the thin films comprised pyramidal shape β - PbO_2 crystals. The electrode prepared had higher oxygen evolution and used successfully for phenol oxidation [370].

2.4.11 Insertion methods

Used in synthesis of inserting SnO_2 to Cu_2O using hydrazine as a reducing agent in aqueous solution significantly [167].

However, most of these synthesis procedures demand the uses of many dangerous and harmful chemicals, which are unsafe to all human beings and the environment. Consequently, it is essential to improve new low cost synthetic methods using nonhazardous materials for SnO_2 Nps synthesis [371].

The objective of this study then, is to follow the easy synthetic route through sol-gel method which can be formed at relatively low temperature to synthesize SnO₂ Nps. This makes it possible to generate ceramic materials at a temperature close to room temperature. Lowering the temperature also creates potential for industrial purposes as a low energy intensive synthesis process. Therefore, this procedure may enable the integration of glass soft dopants, fluorescent dye molecules, organic chromospheres in ceramic substrates, and applications in environmental cleaning. SnO₂ Nps were synthesized by dissolving the compound in a liquid, and through the process returning it as a solid. This technique can be used to prepare multicomponent compounds with a controlled stoichiometry. The precipitation process during synthesis facilitates combining at an atomic level, which results in small particles. A simple sol-gel process has been used to dope SnO₂ with different materials. Organometallic precursors are processed in liquid solution. Then the formation of an oxide network through hydrolysis and condensation reactions leads to the formation of a new (sol) phase. The sol is made of solid amorphous or crystalline particles with a few nm in size, suspended in a liquid phase. Condensation of the solid particles resulted in the formation of a gel in liquid solution, which is later, dried at a low temperature and Nps obtained.

The overall objective is to study the photocatalytic degradation of toxic organics present in water and wastewater.

The initial aim of this work was to focus on the development of undoped SnO₂ and different ions doped SnO₂ Nps followed by semiconductor based photocatalysis. This was modelled by treating a toxic organic compound (phenol) with the synthesized catalyst and degrading it under visible, sunlight or UV irradiation.

The fundamental experimental approach was originally based on the sol-gel method. The method was simplified to break down the cost and the time for making different Nps. The prepared SnO₂ Nps were characterized for structural and chemical properties using XRD, BET, SEM and HR-TEM methods. In addition, the rest analytical methods such as HPLC, GC, CE, FTIR, TOC, UV-Vis spectrophotometer measurements and the determination of COD for the toxin identification.

The application of photocatalysts of the Nps for the treatment of phenol and its byproducts (papers I-III). Parameters such as the effect of pH, effect of air, light intensity, the amount of catalyst, contaminant concentration, and reaction time, were varied and investigated to find the optimum conditions for phenol degradation.

Identification of the nature of phenol byproducts, description of the path of their appearance and disappearance during photocatalysis, and proposition of a mechanistic pathway for degradation route were all part of the objective.

In papers III-IV separation of phenol and its byproducts was studied using different HPLC columns. The retention time of the analysis was reduced from 15 to 5 min. Kinetic studies were evaluated to show the constants, and the rate of pollutant degradation was also been demonstrated and explained.

3 Experimental

3.1 Chemical and materials

Table 12: Chemicals and materials used in this study

Compound	Manufacturer/ supplier	Comments	Publ.
Tin (IV) chloride	Sigma-Aldrich	99%	I-V
La nitrate hexahydrate	Fluka	99.99%	I, IV-V
Cerium (III) chloride	Sigma-Aldrich	99%	I, IV
Ammonium cerium (IV) nitrate	Sigma-Aldrich	99%	I, IV
Neodymium (III) nitrate hexahydrate	Sigma-Aldrich	99%	I, IV
Ethanol	Merck	99%	I-V
Phenol	Sigma-Aldrich	Standard 99%	I-V
Sulphuric acid	Sigma-Aldrich	99%	I-V
Hydrochloric acid	Sigma-Aldrich	99%	I-V
Sodium hydroxide pellets	Sigma-Aldrich	99%	I-V
Methanol	Sigma-Aldrich	HPLC grade 99%	I-V
Sodium chloride	BDH	99%	I-III, IV
Iodine	Sigma-Aldrich	99%	II
Benzoquinone	BDH	AnalaR, 99%	II-V
Resorcinol	BDH	AnalaR, 99%	II-V
Acetic acid	Sigma-Aldrich	99%	II-V
Benzoic acid	BDH	AnalaR, 99%	II-III
Antimony (III) chloride	Fluka	99.99%	III
Catechol	Sigma-Aldrich	99%	III-V
Ethyl paraben	Sigma-Aldrich	99%	III
Sodium tetraborate	Merck	99.99%	IV
Sodium dihydrogen phosphate	Merck	99.99%	IV
Gadolinium (III) chloride	Sigma-Aldrich	99.99%	IV
Hydroquinone	Sigma-Aldrich	99.99%	IV-V
Propan-2-ol	Sigma-Aldrich	99%	V

Water	milipore	Milli-Q-purified analytical instruments	I-V
Ammonia	Merck	25% pH-adjustment	I-V
Silver nitrate	HoneyWell	99.9%	I-V

All the materials and chemicals that were used in this study are summarized in Table 12 above.

3.2 Photocatalyst preparation

3.2.1 Synthesis of pure (control) SnO₂ Nps

Nps containing pure SnO₂ were chemically synthesized by the sol-gel technique due to the following:

Firstly, 3.8827 mL of tin tetrachloride SnCl₄ (AR grade) was mixed with 50.00 mL of absolute alcohol (ethanol) and 50.00 mL of ultra-pure water (Milli-Q-purified) in a round bottom flask and used as a precursor for synthesizing undoped (control) SnO₂ Nps. To prepare 5.0000 g of SnO₂ from SnCl₄, molar mass of SnO₂=150.71 g/mol and SnCl₄ = 260.51 g/mol should be known. 5 g of SnO₂ $\times \frac{mol}{150.71SnO2g} \times \frac{260.51SnCl4g}{mol} = 8.6428 g$ of SnCl₄

The density of SnCl₄=2.226 g/mL.

Density=mass/volume, then the volume=mass/density

The volume of SnCl₄=8.6428 g/ 2.226g/mL=3.8827mL.

∴ 3.8827 mL of SnCl₄ will give 5.00 g of SnO₂.

3.8827 mL of SnCl₄ was dissolved in 50.00 mL ethanol in a 250 mL beaker as it explained with continuous and slowly stirring. On the top of the mixture added 50.00 mL of Milli-Q-purified. The mixture was subjected to vigorous stirring for 3 h at room temperature, until a colourless solution was obtained.

3.2.2 Synthesis of doped SnO₂ Nps

Different SnO₂ Nps containing different ions such as (I, Nd, La, Ce, Sb and Gd) have been synthesized with different percentages such as (0.01, 0.1, 0.2, 0.3, 0.4, 0.6, 0.8, 1.0 and 1.1 wt. %) using sol-gel process.

3.2.2.1 Synthesis of SnO₂/I Nps

I was used to dope with SnO₂ for synthesizing different SnO₂/I weight percentages and the percentage of I on SnO₂ was in concentration of (0.01, 0.1, 0.2, 0.3, 0.4, 1.0, and 1.1 wt. %).

For the synthesis of 1.1 wt. % of SnO₂/I Nps, 0.0550 g of I and 4.9450 g of SnO₂ were combined to give a total of 5.0000 g. To prepare 4.9450 g of SnO₂ from SnCl₄, the molar mass description was given before in section 3.2.1. Therefore, 3.8399 mL of SnCl₄ was dissolved in a 250 mL beaker contained 50.00 mL ethanol and 0.0550 g of I was added with continuous and slowly stirring with the addition of 50.00 mL of Milli-Q-purified. The mixture was subjected to vigorous stirring for 3 h at room temperature, until a colourless solution was obtained.

For the synthesis of 1.0 wt. % of SnO₂/I Nps, 0.0500 g of I and 4.9500 g of SnO₂ were combined to give a total of 5.0000 g. To prepare 4.9500 g of SnO₂ from SnCl₄, the molar mass description was given before in section 3.2.1. Therefore, 3.8438 mL of SnCl₄ was dissolved in a 250 mL beaker contained 50.00 mL ethanol and 0.0500 g of I was added with continuous and slowly stirring with the addition of 50.00 mL of Milli-Q-purified. The mixture was subjected to vigorous stirring for 3 h at room temperature, until a colourless solution was obtained.

For the synthesis of 0.4 wt. % SnO₂/I Nps, 0.0200 g of I and 4.9800 g of SnO₂ were combined to give a total of 5.0000 g. To prepare 4.9800 g of SnO₂ from SnCl₄, the molar mass description was given before in section 3.2.1. Therefore, 3.8671 mL of SnCl₄ was dissolved in a 250 mL beaker contained 50.00 mL ethanol and 0.0200 g of I was added with continuous and slowly stirring with the addition of 50.00 mL of Milli-Q-purified. The mixture was subjected to vigorous stirring for 3 h at room temperature, until a colourless solution was obtained.

For the synthesis of 0.3 wt. % of SnO₂/I Nps, 0.0150 g of I and 4.9850 g of SnO₂ were combined to give a total of 5.0000 g. To prepare 4.9850 g of SnO₂ from SnCl₄, the molar mass description was given before in section 3.2.1. Therefore, 3.8709 mL of SnCl₄ was dissolved in a 250 mL beaker contained 50.00 mL ethanol and 0.0150 g of I was added with continuous and slowly stirring with the addition of 50.00 mL of Milli-Q-purified. The mixture was subjected to vigorous stirring for 3 h at room temperature, until a colourless solution was obtained.

For the synthesis of 0.2 wt. % SnO₂/I Nps, 0.0100 g of I and 4.9900 g of SnO₂ were combined to give a total of 5.0000 g. To prepare 4.9900 g of SnO₂ from SnCl₄, the molar mass description was given before in section 3.2.1. Therefore, 3.8749 mL of SnCl₄ was dissolved in a 250 mL beaker contained 50.00 mL ethanol and 0.0100 g of I was added with continuous and slowly stirring with the addition of 50.00 mL of Milli-Q-purified. The mixture was subjected to vigorous stirring for 3 h at room temperature, until a colourless solution was obtained.

For the synthesis of 0.1 wt. % SnO₂/I Nps, 0.0050 g of I and 4.9950 g of SnO₂ were combined to give a total of 5.0000 g. To prepare 4.9950 g of SnO₂ from SnCl₄, the molar mass description was given before in section 3.2.1. Therefore, 3.8788 mL of SnCl₄ was dissolved in a 250 mL beaker contained 50.00 mL ethanol and 0.0050 g of I was added with continuous and slowly stirring with the addition of 50.00 mL of Milli-Q-purified. The mixture was subjected to vigorous stirring for 3 h at room temperature, until a colourless solution was obtained.

For the synthesis of 0.01 wt. % SnO₂/I Nps, 0.0005 g of I and 4.9995 g of SnO₂ were combined to give a total of 5.0000 g. To prepare 4.9995 g of SnO₂ from SnCl₄, the molar mass description was given before in section 3.2.1. Therefore, 3.8823 mL of SnCl₄ was dissolved in a 250 mL beaker contained 50.00 mL ethanol and 0.0005 g of I was added with continuous and slowly stirring with the addition of 50.00 mL of Milli-Q-purified. The mixture was subjected to vigorous stirring for 3 h at room temperature, until a colourless solution was obtained.

3.2.2.2 Synthesis of SnO₂/Nd Nps

Nd was used to dope with SnO₂ for synthesizing different SnO₂/Nd weight percentages and the percentage of Nd on SnO₂ was in concentration of (0.2, 0.6 wt. %).

For the synthesis of 0.2 wt. % SnO₂/Nd Nps, 0.0100 g of Nd and 4.9900 g of SnO₂ were combined to give a total of 5.0000 g. To prepare 4.9900 g of SnO₂ from SnCl₄, the molar mass description was given before in section 3.2.1. Therefore, 3.8749 mL of SnCl₄ was dissolved in a 250 mL beaker contained 50.00 mL ethanol and 0.0100 g of Nd was added with continuous and slowly stirring with the addition of 50.00 mL of Milli-Q-purified. The mixture was subjected to vigorous stirring for 3 h at room temperature, until a colourless solution was obtained.

For the synthesis of 0.6 wt. % SnO₂/Nd Nps, 0.0300 g of Nd and 4.9700 g of SnO₂ were combined to give a total of 5.0000 g. To prepare 4.9700 g of SnO₂ from SnCl₄, the molar mass description was given before in section 3.2.1. Therefore, 3.8594 mL of SnCl₄ was dissolved in a 250 mL beaker contained 50.00 mL ethanol and 0.0300 g of Nd was added with continuous and slowly stirring with the addition of 50.00 mL of Milli-Q-purified. The mixture was subjected to vigorous stirring for 3 h at room temperature, until a colourless solution was obtained.

3.2.2.3 Synthesis of SnO₂/La Nps

La was used to dope with SnO₂ for synthesizing different SnO₂/La weight percentages and the percentage of La on SnO₂ was in concentration of (0.1, 0.2, 0.4 and 0.6 wt. %).

For the synthesis of 0.1 wt. % SnO₂/La Nps, 0.0050 g of La and 4.9950 g of SnO₂ were combined to give a total of 5.0000 g. To prepare 4.9950 g of SnO₂ from SnCl₄, the molar mass description was given before in section 3.2.1. Therefore, 3.8788 mL of SnCl₄ was dissolved in a 250 mL beaker contained 50.00 mL ethanol and 0.0050 g of La was added by continuous and slowly stirring with the addition of 50.00 mL of Milli-Q-purified. The mixture was subjected to vigorous stirring for 3 h at room temperature, until a colourless solution was obtained.

For the synthesis of 0.2 wt. % SnO₂/La Nps, 0.0100 g of La and 4.9900 g of SnO₂ were combined to give a total of 5.0000 g. To prepare 4.9900 g of SnO₂ from SnCl₄, the molar

mass description was given before in section 3.2.1. Therefore, 3.8749 mL of SnCl_4 was dissolved in a 250 mL beaker contained 50.00 mL ethanol and 0.0100 g of La was added by continuous and slowly stirring with the addition of 50.00 mL of Milli-Q-purified. The mixture was subjected to vigorous stirring for 3 h at room temperature, until a colourless solution was obtained.

For the synthesis of 0.4 wt. % SnO_2/La Nps, 0.0200 g of La and 4.9800 g of SnO_2 were combined to give a total of 5.0000 g. To prepare 4.9800 g of SnO_2 from SnCl_4 , the molar mass description was given before in section 3.2.1. Therefore, 3.8671 mL of SnCl_4 was dissolved in a 250 mL beaker contained 50.00 mL ethanol and 0.0200 g of La was added with continuous and slowly stirring with the addition of 50.00 mL of Milli-Q-purified. The mixture was subjected to vigorous stirring for 3 h at room temperature, until a colourless solution was obtained.

For the synthesis of 0.6 wt. % SnO_2/La Nps, 0.0300 g of La and 4.9700 g of SnO_2 were combined to give a total of 5.0000 g. To prepare 4.9700 g of SnO_2 from SnCl_4 , the molar mass description was given before in section 3.2.1. Therefore, 3.8594 mL of SnCl_4 was dissolved in a 250 mL beaker contained 50.00 mL ethanol and 0.0300 g of La was added by continuous and slowly stirring with the addition of 50.00 mL of Milli-Q-purified. The mixture was subjected to vigorous stirring for 3 h at room temperature, until a colourless solution was obtained.

3.2.2.4 Synthesis of SnO_2/Ce Nps

Ce was used to dope with SnO_2 for synthesizing different SnO_2/Ce weight percentages and the percentage of Ce on SnO_2 was in concentration of (0.1, 0.2, 0.4 and 0.6 wt. %). For the synthesis of 0.1 wt. % SnO_2/Ce Nps, 0.0050 g of Ce and 4.9950 g of SnO_2 were combined to give a total of 5.0000 g. To prepare 4.9950 g of SnO_2 from SnCl_4 , the molar mass description was given before in section 3.2.1. Therefore, 3.8788 mL of SnCl_4 was dissolved in a 250 mL beaker contained 50.00 mL ethanol and 0.0050 g of Ce was added by continuous and slowly stirring with the addition of 50.00 mL of Milli-Q-purified. The mixture was subjected to vigorous stirring for 3 h at room temperature, until a colourless solution was obtained.

For the synthesis of 0.2 wt. % SnO₂/Ce Nps, 0.01 g of Ce and 4.9900 g of SnO₂ were combined to give a total of 5.0000 g. To prepare 4.9900 g of SnO₂ from SnCl₄, the molar mass description was given before in section 3.2.1. Therefore, 3.8749 mL of SnCl₄ was dissolved in a 250 mL beaker contained 50.00 mL ethanol and 0.0100 g of Ce was added by continuous and slowly stirring with the addition of 50.00 mL of Milli-Q-purified. The mixture was subjected to vigorous stirring for 3 h at room temperature, until a colourless solution was obtained.

For the synthesis of 0.4 wt. % SnO₂/Ce Nps, 0.0200 g of Ce and 4.9800 g of SnO₂ were combined to give a total of 5.0000 g. To prepare 4.9800 g of SnO₂ from SnCl₄, the molar mass description was given before in section 3.2.1. Therefore, 3.8671 mL of SnCl₄ was dissolved in a 250 mL beaker contained 50.00 mL ethanol and 0.0200 g of Ce was added with continuous and slowly stirring with the addition of 50.00 mL of Milli-Q-purified. The mixture was subjected to vigorous stirring for 3 h at room temperature, until a colourless solution was obtained.

For the synthesis of 0.6 wt. % SnO₂/Ce Nps, 0.0300 g of Ce and 4.9700 g of SnO₂ were combined to give a total of 5.0000 g. To prepare 4.9700 g of SnO₂ from SnCl₄, the molar mass description was given before in section 3.2.1. Therefore, 3.8594 mL of SnCl₄ was dissolved in a 250 mL beaker contained 50.00 mL ethanol and 0.0300 g of Ce was added by continuous and slowly stirring with the addition of 50 mL of Milli-Q-purified. The mixture was subjected to vigorous stirring for 3 h at room temperature, until a colourless solution was obtained.

3.2.2.5 Synthesis of SnO₂/Sb Nps

Sb was used to dope with SnO₂ for synthesizing different SnO₂/Sb weight percentages and the percentage of Sb on SnO₂ was in concentration of (0.2, 0.4, 0.6 and 0.8 wt. %). For the synthesis of 0.2 wt. % SnO₂/Sb Nps, 0.0100 g of Sb and 4.9900 g of SnO₂ were combined to give a total of 5.0000 g. To prepare 4.9900 g of SnO₂ from SnCl₄, the molar mass description was given before in section 3.2.1. Therefore, 3.8749 mL of SnCl₄ was dissolved in a 250 mL beaker contained 50.00 mL ethanol and 0.0100 g of Sb was added by continuous and slowly stirring with the addition of 50.00 mL of Milli-Q-purified.

The mixture was subjected to vigorous stirring for 3 h at room temperature, until a colourless solution was obtained.

For the synthesis of 0.4 wt. % SnO₂/Sb Nps, 0.0200 g of Sb and 4.9800 g of SnO₂ were combined to give a total of 5.0000 g. To prepare 4.9800 g of SnO₂ from SnCl₄, the molar mass description was given before in section 3.2.1. Therefore, 3.8671 mL of SnCl₄ was dissolved in a 250 mL beaker contained 50.00 mL ethanol 0.0200 g of Sb was added with continuous and slowly stirring with the addition of 50.00 mL of Milli-Q-purified. The mixture was subjected to vigorous stirring for 3 h at room temperature, until a colourless solution was obtained.

For the synthesis of 0.6 wt. % SnO₂/Sb Nps, 0.0300 g of Sb and 4.9700 g of SnO₂ were combined to give a total of 5.0000 g. To prepare 4.9700 g of SnO₂ from SnCl₄, the molar mass description was given before in section 3.2.1. Therefore, 3.8593 mL of SnCl₄ was dissolved in a 250 mL beaker contained 50.00 mL ethanol and 0.0300 g of Sb was added by continuous and slowly stirring with the addition of 50.00 mL of Milli-Q-purified. The mixture was subjected to vigorous stirring for 3 h at room temperature, until a colourless solution was obtained.

For the synthesis of 0.8 wt. % SnO₂/Sb Nps, 0.0400 g of Sb and 4.9600 g of SnO₂ were combined to give a total of 5.0000 g. To prepare 4.9600 g of SnO₂ from SnCl₄, the molar mass description was given before in section 3.2.1. Therefore, 3.8516 mL of SnCl₄ was dissolved in a 250 mL beaker contained 50.00 mL ethanol and 0.0400 g of Sb was added by continuous and slowly stirring with the addition of 50.00 mL of Milli-Q-purified. The mixture was subjected to vigorous stirring for 3 h at room temperature, until a colourless solution was obtained.

3.2.2.6 Synthesis of SnO₂/Gd Nps

Gd was used to dope with SnO₂ for synthesizing different SnO₂/Gd weight percentages and the percentage of Gd on SnO₂ was in concentration of (0.2, 0.4, and 0.6 wt. %).

Table 13: Comparison % of dopants and volume of SnO₂ values

Sl. No.	% of ions doped SnO ₂	Weight of SnO ₂	Amount of dopants (g)	Volume of SnCl ₄	Total volume
1	0.0%	5.0000 g	0.0000 g	3.8827 mL	5.0000 g
2	0.01%	4.9995 g	0.0005 g	3.8823 mL	5.0000 g
3	0.1%	4.9950 g	0.0050 g	3.8788 mL	5.0000 g
4	0.2%	4.9900 g	0.0100 g	3.8749 mL	5.0000 g
5	0.3%	4.9850 g	0.0150 g	3.8709 mL	5.0000 g
6	0.4%	4.9800 g	0.0200 g	3.8671 mL	5.0000 g
7	0.6%	4.9700 g	0.0300 g	3.8593 mL	5.0000 g
8	0.8%	4.9600 g	0.0400 g	3.8463 mL	5.0000 g
9	1.0%	4.9500 g	0.0500 g	3.8438 mL	5.0000 g
10	1.1%	4.9450 g	0.0550 g	3.8399 mL	5.0000 g

For the synthesis of 0.2 wt. % SnO₂/Gd Nps, 0.0100 g of Gd and 4.9900 g of SnO₂ were combined to give a total of 5.0000 g. To prepare 4.9900 g of SnO₂ from SnCl₄, the molar mass description was given before in section 3.2.1. Therefore, 3.8749 mL of SnCl₄ was dissolved in a 250 mL beaker contained 50.00 mL ethanol and 0.0100 g of Gd was added by continuous and slowly stirring with the addition of 50.00 mL of Milli-Q-purified. The mixture was subjected to vigorous stirring for 3 h at room temperature, until a colourless solution was obtained.

For the synthesis of 0.4 wt. % SnO₂/Gd Nps, 0.0200 g of Gd and 4.9800 g of SnO₂ were combined to give a total of 5.0000 g. To prepare 4.9800 g of SnO₂ from SnCl₄, the molar mass description was given before in section 3.2.1. Therefore, 3.8671 mL of SnCl₄ was dissolved in a 250 mL beaker contained 50.00 mL ethanol and 0.0200 g of Gd was added with continuous and slowly stirring with the addition of 50.00 mL of Milli-Q-purified. The mixture was subjected to vigorous stirring for 3 h at room temperature, until a colourless solution was obtained.

For the synthesis of 0.6 wt. % SnO₂/Gd Nps, 0.0300 g of Gd and 4.9700 g of SnO₂ were combined to give a total of 5.0000 g. To prepare 4.9700 g of SnO₂ from SnCl₄, the molar

mass description was given before in section 3.2.1. Therefore, 3.8593 mL of SnCl₄ was dissolved in a 250 mL beaker contained 50.00 mL ethanol and 0.0300 g of Gd was added by continuous and slowly stirring with the addition of 50.00 mL of Milli-Q-purified. The mixture was subjected to vigorous stirring for 3 h at room temperature, until a colourless solution was obtained.

Table 13 compares the different undoped and doped SnO₂ Nps, these catalysts have been used in different experiments.

3.3 Sol-gel preparation

3.3.1 Sol-gel method

SnO₂ synthesized and doped with different ions by sol-gel process at room temperature, Nps been prepared are suitable for large scale production. Applying low temperature procedure is always useful because of its less power consumption and better practical application. The synthesis process is simple and relatively inexpensive, which is based on the hydrolysis and condensation of metal ions to form metal oxide [372], providing a control on the size and the shape of Nps [373].

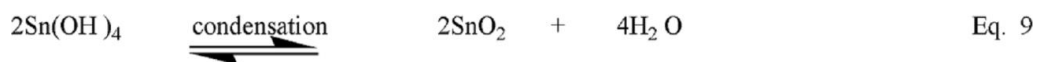
The sol-gel method offers several advantages such as high purity, better homogeneity, precise control over the stoichiometry, and capability to control the powder size and surface of metal oxides at lower temperatures [126, 160]. The basic benefit of the sol-gel method is the creation of materials at room temperature.

A liquid solution of organometallic precursors undergoes hydrolysis and condensation reactions, leading to the formation of a new phase

The alkoxy groups are substituted by hydroxide groups with the evolution of an inorganic network (sol).



The particles condensed in a new (gel) phase in which a solid macromolecule is immersed in a solvent. Drying the gel at a low temperature between 25 to 80 °C will serve to remove the liquid phase and make it possible to obtain porous solid matrices.



Two hydrolysed molecules liberate water (gel), upon linking together, which occurs through the destruction of the gel with the subsequent formation of nanoparticulate materials [259, 374-376]. While the reaction continues, the number of Sn-O-Sn bonds increases by the polymerization, which releases a macroscopic gel.

3.4 Powder preparation

When the colourless solution produced, the mixture was then condensed in a round bottom flask; the temperature was adjusted between 70-80 °C, and kept stable during the process. A white turbid colloidal solution of tin alkoxide appeared after heating the mixture under vacuum conditions [372]. The condensation process is done by refluxing the turbid solution at 70-80 °C for 1 h. After refluxing, the resultant solution was gelled for slowly stirring on a magnetic stirrer (Make PMC 502 series) at 200 RPM and while stirring into this mixture, (25%) of an aqueous ammonia solution was prepared into 0.1M solution was added in a drop wise manner (with a rate of 10 drops/min). On addition of roughly 50 drops of 0.1 M ammonia the sol-gel was formed within the 5 min. The solution was stirred continuously until a pH value of 8 was reached and the resulting gel poured and left to dry into a container for 48 h until it become totally gelled. Filtration and successive washing with Ultra-pure water was repeated several times to remove both ammonia and chloride ions until all chloride ions had been removed (by examining the filtrate solution using aqueous silver nitrate solution) The powder was then dried on a hot plate or in an oven at 80 °C and later transferred into an amber container and kept in the desiccator for future use. Prior to the analysis, the powder been grinded sonicated or diluted to obtain uniform particle size.

3.5 Reactors

The semiconductor catalyst is dispersed in powder form in the reaction solution containing the model compound. The apparatus consists of a mixing device, reactor vessel, and protected UV lamp, that can also be purged with air and oxygen. The reactor can be illuminated internally, where it is inserted into a quartz jacket or externally from the top, or it directly can be used by sunlight.

3.5.1 UV photocatalytic reactor

Figure 5 shows the UV photo reactor, which used in this study, where the inner insulator tube jacket is made of quartz, while the outer layer is made of glass tube. The arrangement in this photoreactor has two air flow distribution tubes, where it mixes the bubbles into the pollutant. The photoreactor was a cylindrical Pyrex-glass container with a 250 mL capacity, 50 mm internal diameter and 300 mm height. An 8 W medium pressure mercury lamp (Sankyo Denki, Osaka, Japan) with an intensity of about 80 W/m², as a 352 nm UV light source was used, situated axially at the center and the reaction temperature was kept at 25 °C to cool the photoreactor by means of water flowing. The air pump with a continuous speed was also combined to the air flow meter that was connected to the reactor outer tube to produce air (oxygen).

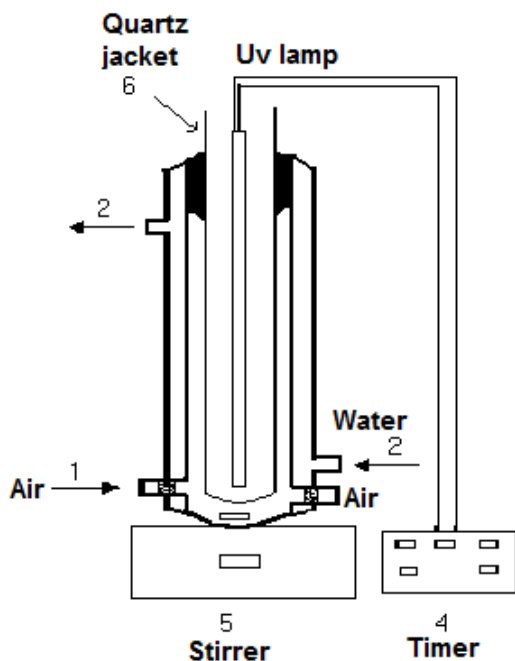


Figure 6: Diagram arrangement of the photoreactor system

3.5.2 Visible light photocatalytic reactor

A second photoreactor contains a Pyrex glass reactor with a cooling water jacket in 250 mL capacity 100 mm internal diameter and 200 mm height. A 300 W xenon lamp simulated visible light source (PLS-SXE300C, Beijing Perfect light Co., Ltd, China), and was placed 71 mm above the surface of the contaminant during the photodegradation studies. The light source in this system is parallel light and can be focused in one direction on the sample, so the photocatalytic effect can be narrowed. The system delivers maximum current of 20 A, and total optical power of 50 W.

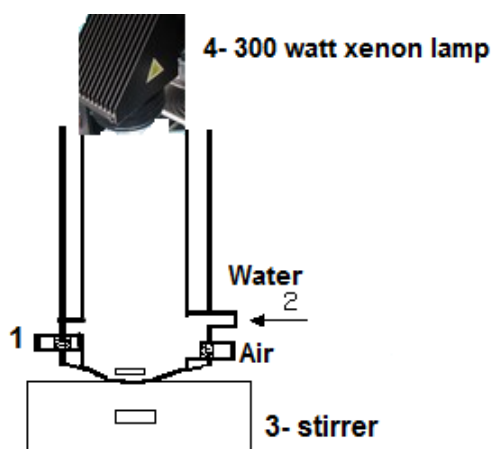


Figure 7: Diagram arrangement of the visible reactor system

3.5.3 Solar light photocatalytic reactor

A third photoreactor for the solar photocatalysis experiments was a borosilicate glass container with a 250 mL capacity, 100 mm internal diameter and 200 mm height. Sunlight was directed axially at the centre of the reactor. The photoreactor was kept in an open area in order to avoid reflected sunlight from the surroundings. All the natural sunlight experiments were conducted on full sunny days during 10:00-15:00 h when the incident power of the sunlight was measured to be between 80 and 90 kW/m².

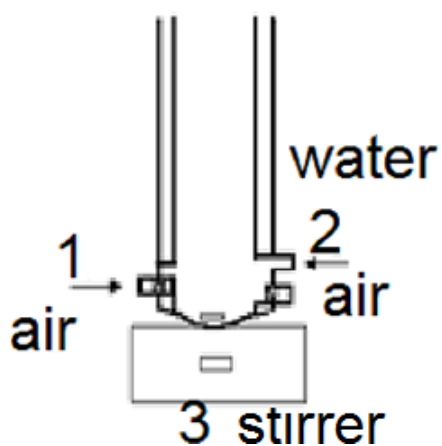


Figure 8: Diagram arrangement of the solar reactor system

3.6 Experimental procedures

3.6.1 Optimization of experimental parameters

To investigate the effects of SnO₂ and different concentrations of dopants on the photocatalytic activity of SnO₂ and its dopants, phenol and some of its intermediates were chosen as test contaminants. The study of the photodegradation of phenol and its byproducts in water was carried out at 25 °C using a water-cooled cylindrical glass batch photoreactor of 250 mL volume as described above. Based on different factors that need to be examined in this thesis, the following section briefly discusses external parameters such as follows: catalyst loading, light intensity, reaction time, phenol concentration, sampling time, sample volume, and pH of the reaction medium.

3.6.1.1 Catalyst loading

The amount of catalyst powder (photocatalyst) was kept at 65 mg as a mass in a 50.00 mL volume container (volumetric flask). It is important to find out the optimum loading of the catalyst to avoid excess catalyst using. Experiments on the catalyst loading have been carried out in the range of 65, 75 and 100 mg for 50.00 mL of solution to find out the best catalyst loading. The photocatalytic degradation of phenol exhibited best results from 65-75% at 150 min irradiation time, an increase in the loading amount above 75% did not give better removal rate and resulted in a decrease in the activity of the catalyst. A result why 65mg /50 0 mL catalyst dosage was used in all photocatalytic reactions. Other scientists reported that when TiO₂ overdosed, it decreased the light penetration to TiO₂ surface because the number of active sites on TiO₂ surface become almost constant [37]. In another work, also described that above the optimum of TiO₂ loading phenol degradation decreased [377].

3.6.2 Pollutant concentration

The initial concentration of the model pollutant of 100 ppm (phenol) was prepared as follows: exactly 0.1000 g of phenol was weighted and quantitatively transferred into a 1000.0 mL volumetric flask and brought to the calibration curve with milli-Q-pore H₂O.

Different solutions of 50, 25, 10 and 5 ppm were prepared by serial dilution of a 100 ppm initial concentration of phenol. These standards were prepared to measure the optimum concentration at which the model pollutant phenol solution might degrade rapidly, which means that the phenol concentration in the reactor would work competently. The photocatalytic degradation of phenol has been carried out at different initial concentrations starting from 5-50 ppm. Each standard was separately mixed in the reactor, while the other parameters were kept constant: such as catalyst loading (65 mg/50.00 mL), light intensity (8 W mercury lamp, 300 W xenon lamp and sunlight), reaction time (2-3 h), sampling time, (12-13), sample volume (250.00 mL), and pH of the reaction medium (5.7). The results showed an increase in the degradation of phenol at 10 ppm, but a slight decrease in the catalytic efficiency above 15 ppm. The best results gained were at 10 ppm, here with all the pollutant concentrations were taken at 10 ppm. 10 ppm phenol concentration was used for photocatalysis, an increase in the initial phenol concentration resulted in a decrease in the rates.

3.6.3 Effect of the pH of the solution

The pH of the solution was adjusted by either adding sodium hydroxide (NaOH) or sulphuric acid (H₂SO₄). The preparation of the acid and the base solutions was done as follows: about 0.6 mL of 18 M of H₂SO₄ was transferred into a 100.00 mL volumetric flask and made up to mark with Milli-Q-purified H₂O to prepare of 0.1 M. In the same way 0.1 M of NaOH was prepared by weighing about 0.4 g of NaOH into 100.00 mL volumetric flask and made up to mark with Milli-Q-purified H₂O. Exactly 250.00 mL of 10 ppm phenol solution was poured in 500 mL beaker in which a pH electrode was immersed. The pH of phenol was adjusted between values (3-8) and was fixed to the desired value by dropping amounts of H₂SO₂ or NaOH drop wise using a Pasteur pipette. During this procedure the solution was continuously stirred, but slowly using a small magnetic bar with the pH electrode inside the solution to adjust the pH value required to take care not to break the electrode. The prepared solution was kept in the freezer for further use. It is known that SnO₂ is an acidic oxide so phenol in that media will still remain weak acidic.

10 ppm phenol solution was used to carry out photocatalysis experiments. Before each test, the mixture was kept in the dark for 30 min under constant magnetic stirring to ensure that adsorption-desorption equilibrium was reached before illumination. The sample was then taken out at the end of the dark adsorption period, prior to turning the light on or before exposing to sunlight. When the lamp turned on, the irradiation time varied from 2-3 h; aliquots of the suspensions were collected and removed from the reactor every 15 or 30 min, inlet air flow 4 L/min.

3.6.4 Sampling from the reactor

At the beginning of the photocatalysis 10 ppm of phenol concentration was prepared in 250.00 mL volumetric flask and put into the reactor while 20 mL aliquots of the suspensions were collected and removed from the reactor every 15 min about 12-13 samples each batch were enough to analyse by all the analytical instruments. The experiment was performed at the following experimental parameters (65 mg/50.00 mL), light intensity (8 W mercury lamp, 300 W xenon lamp and sunlight), reaction time (2-3 h), phenol concentration (10 ppm) sampling time, (12-13), sample volume (250.00 mL), and pH of the reaction medium (5.7) at 25 °C. The photocatalyst particles were removed from the samples first by centrifugation (4,000 rpm, 5 min) using an Eppendorf centrifuge (system model 5810R) and then filtered through a 0.2 µm Millipore filter. Furthermore, the UV-Vis absorbance of phenol solutions sampled was recorded every 15 min. the unknown concentration of phenol solutions and its byproducts were calculated using the calibration curve.

To compare the photocatalytic activity of 10 ppm phenol with the other intermediates, organic chemicals such as 10 ppm HQ, 10 ppm BQ, 10 ppm Res, 10 ppm Cat, 10 ppm AA and 10 ppm 2-P were prepared in the same way exactly like phenol. First, preparing a stock in 1000.0 mL and then preparing the rest of the standards into 250.00 mL volumetric flask and used them in the same way as done for phenol photocatalytical experiments

3.7 Characterization techniques

3.7.1 X-ray diffraction method (XRD)

The crystalline phase of the synthesized SnO₂ and SnO₂-doped powders were analysed by X-ray powder diffraction (XRD) using a Miniflex 600 diffractometer (Rigaku, Japan) with Cu K_α radiation $\lambda=1.5418 \text{ \AA}$ operated at a voltage of 30 kV and a current of 15 mA. Diffractograms of the powders were recorded in 2θ scan configuration, in the 10-80 ° 2θ range, at steps of 0.02 °.

Prior to the analysis, the powder was grinded to obtain uniform particle size.

3.7.1.1 Operating procedure for Rigaku Miniflex

- 1- Turn ON the water chiller
- 2- Switch ON the computer
- 3- Turn on the machine from the back
- 4- Place the specimen powder evenly on the special glass provided for sampling to stay smoothly.
- 5- Put the sampling glass in the magnetic recognized holder carefully inside the machine.
- 6- Close the instrument door for the use.
- 7- Press the power ON switch
- 8- If the chiller reading is below 20, then the machine can be operated.
- 9- Launch the Miniflex guidance software.
- 10- Fill the parameters through the software administration- general measurement, fill folder, and file name, run to executive general measurement.
- 11- Start up the X-ray generator –control- XG control
- 12- At the end of the analysis, click control-XG control and click off the button the x-ray will be off.
- 13- Remove the sample and clean the area
- 14- Wait for 15 min to turn the power off
- 15- Turn off the water chiller.

3.7.2 Scanning electron microscopy (SEM)

To study the surface morphology of the prepared SnO₂ and different doped SnO₂ samples, SEM were carried out with JEOL (Japan) (JSM-5600LY) working at 30 kV. Powders of each doped and control SnO₂ were viewed by SEM for surface morphology as follows: 2 mm specimen was placed on the holder and positioned in the SEM instrument. To get the clear area of the powders, various scans at different magnifications led to multiple images. However, since the powders are less than 5 nm, some cases it was difficult to get a clear picture of the images even after large magnification.

3.7.3 Transmission electron microscopy (TEM)

In order to reach a better insight, the surface morphology of the powders by TEM with JEOL Schottky field emission microscope (JEM 2100F, Japan) working at 200 kV were further analysed. In order to minimize artefacts (improve in the features of the microstructure) during sample preparation, TEM samples were prepared by crushing the Nps and the powder were deposited on Cu supporting grid with holy carbon supporting films. For HR-TEM images of pure and differently doped SnO₂ np samples were diluted several times with high purity Milli-Q-purified and later sonicated with (JAC ultra sonic 210KODO) for some time to achieve a very special homogenized powder solution.

3.7.4 The Brunauer-Emmett-Teller (BET) method

200-300 mg of sample was degassed at 300 °C for 3 h under nitrogen (N₂) flow, followed by a six point N₂ adsorption carried out at a p/p₀ of 1 to 5 in Nova[®] 2200 analyser. The surface area was determined by gas adsorption technique using Nova[®] 2200 analyser software using the B E T method.

3.7.5 Fourier Transform Infrared Spectroscopy (FTIR)

A vertex 70 (FTIR) by Bruker optics (Germany) with attenuated total reflectance unit (ATR) was used to identify the existing bonds before and after phenol degradation with differently doped SnO₂ Nps powder. The FTIR range used was 4000-400 cm⁻¹ and the resolution was recorded at 4 cm⁻¹. The main object was to qualitatively monitor the

evolution of CO₂ during photodegradation of phenol which indicates the complete mineralization of phenol. The ATR sample holder was cleaned by dichloromethane and 0.5 mL of the contaminant was placed on it. After the background was selected, the baseline was corrected and the analysis was performed.

3.8 Analytical methods

3.8.1 UV-Vis spectrophotometer

The change in phenol concentration in each photodegraded solution was monitored by ultraviolet-visible (UV-Vis) spectrophotometer. The maximum absorbance of phenol was measured at respective λ_{max} of 269 nm in UV-Vis spectrometer (Perkin Elmer Lambda 45) through two Hellma precision cells made of quartz Suprasil. The percentage of degradation of phenol solution was calculated from the following equation [378]
Percentage degradation =

$$\left(\frac{C_0 - C_t}{C_0} \right) \times 100 \quad \text{Eq 10}$$

Where C₀ the initial concentration of phenol solution ppm is, C_t is the concentration of phenol solution after irradiation and after selected time interval ppm.

3.8.1.1 Sample preparation

The initial concentration of the model pollutant of 100 ppm (phenol) was prepared as follows: exactly 0.1000 g of phenol was weighted and quantitatively transferred into a 1000 mL volumetric flask and brought to the calibration curve with Milli-Q-purified H₂O. Different solutions of 50, 25, 10 and 5 ppm were prepared by serial dilution of a 100 ppm initial concentration of phenol. Each of these solutions was separately used to carry out photocatalysis experiments.

3.8.1.2 UV-Vis analysis

The both two cells washed and filled with deionized water and kept in the compartment in the UV instrument for a baseline set up using deionized water as a reference solution. After setting up the baseline, one of the cells was removed and the other cell stayed in

the machine as a reference. Washing and filling the removed cell with the sample of interest and putting it back into the UV compartment. The maximum absorbance of phenol was measured at respective λ_{\max} of 269 nm in UV-Vis spectrometer λ absorbance and other parameters could be obtained. To measure the concentration of these absorbance values, calibration curve of the standards solutions was prepared from (5-50 ppm) as it mentioned before.

3.8.2 Total organic carbon analyser (TOC)

TOC determines the carbon content present in water solution. To measure the carbon content, it is important to remove the inorganic carbon exists in the solution like carbonate (CO_3^{2-}), monohydrogencarbonate (HCO_3^-), bicarbonate and dihydrogencarbonate (H_2CO_3), some drops of concentrated phosphoric acid (84%) are added to the solution to yield CO_2 which degassed by running nitrogen from a cylinder. The sample of interest is injected in a TOC Analyser (TOC-VCPH Shimadzu) equipped with an auto sampler (ASI-V Shimadzu), in which the organic molecules are totally oxidized at 850 °C in the presence of a Pt catalyst. The amount of CO_2 liberated by the reaction is then determined by infrared spectrometry. Prior to injecting the samples into the instruments, the solutions were filtered through a syringe filter of 0.2 μm pore size to remove photocatalysts Nps.

3.8.3 Chemical oxygen demand (COD)

COD measures the quantity of oxygen equivalent used for the total oxidation of organic and mineral substances by excess of strong chemical oxidizing agent potassium dichromate in a mixture. The oxidation is carried out in an acid medium in the presence of the catalyst as silver sulphate; the oxidation could be performed for 2 h at 150 °C. It defines the total quantity of oxygen required for the degradation of organic compound to CO_2 and H_2O .

3.8.3.1 Colorimetric method for the measurement of COD

To determine the COD in phenol and its byproducts, samples were treated as follows: 2 mL of supernatant in a screw cap tube was amended with 0.05 g of mercury sulphate,

used to avoid the complexes and the interference of the chloride ion. 0.5 mL of 1.0 N potassium dichromate used in excess strong oxidizing agent and 2.5 mL of concentrated sulphuric acid (contained 5.5 mg silver sulphate per gram as a catalyst). The mixture in the tube refluxed for 2 h at 150 °C in a heater model DRB 200. After cooling, COD was determined by absorbance using Hach Lange model DR-2000 spectrophotometer with λ of 420 nm which shows directly the COD value. In order to use this method, samples should be diluted to bring them to the range of the standards in the tube.

3.9 High performance liquid chromatography (HPLC)

Phenol photodegradation products were analysed by HPLC using a P580 high-precision pump from Dionex (Germering, Germany), which fulfilled the requirement for a measured mobile phase delivery rate. Analysis of HPLC was carried out by:

Injector port: Is a manual injector a Rheodyne (Cotati) 8125 valve fitted with a 20 μ L loop. The selection of the loop is important according to the size of the column and the concentration of the pollutants analysed. In addition, it allows a constant injected volume which is very important for the quantitative analysis.

Detector: Dionex UVD 170/340S diode array detector jointed with a recorder to show the chromatogram. The detector measures the absorption of the light by the contaminant at the outlet of the column, when it enters the detector. The detector can be operated by a constant λ which is fixed by the operator through the software. Deuterium lamp is used at λ varying from 190-350 nm.

Pump: Thermo Scientific Dionex Ultimate 3000 Series. The pump includes the isocratic or the gradient system for the solvent (mobile phase) programming. The pump can perform in two ways:

Isocratic run, which means with an elution of constant solvent composition been prepared outside the system during all time of analysis.

Gradient run, the system will prepare and mix with a variation of the solvent mixture, prepared by the operator through the machine.

Columns: The column in HPLC also called stationary phase. The analysis of phenol and its byproducts was carried out and separated using different C18 columns. Supelco:

C18 column of (250 mm × 4.6 mm), composed of spherical micro-particles (4.6 μm) of silica transplanted with alkyl chains of C18. The second column was Restek C18 column of (150 mm × 3.0 μm), also composed of spherical micro-particles (3.0 μm) of silica transplanted with alkyl chains. Phenomenex: A C18 monolithic column of (50 mm × 4.6 mm) all these columns were maintained at room temperature. The attaining and the conducting of chromatograms are achieved by the software called chromeleon 6.2.

3.9.1 HPLC analysis

At the beginning of the analysis time, the mixture to be separated was injected in the injector port connected to the column. The mixture was diluted in the mobile phase and from the injector port the mixture was continued its way to the column.

3.9.1.1 HPLC mobile phase preparation

The mobile phase for the HPLC separation was prepared by mixing methanol with water at a ratio of 45:55. In a 100 mL measuring cylinder, 45 mL of methanol was mixed with 55 mL of Milli-Q H₂O later transferred into a 250 mL beaker with magnetic follower. The beaker was placed on a stirrer and stirred slowly with a pH electrode inside model (Mettler Toledo). The mobile phase was adjusted to pH 3.0 by adding drops of 0.1 M H₂SO₄ through 5 mL syringe. The preparation of the acid was explained earlier in section 3.5.4. The mobile phase (solvent) was filtered through 0.2 μm vacuum filter model (Millipore xx1009020) and sonicated by (JAC ultra sonic 2010 (P)[CE] KODO) model technical research Co., Ltd. for 10 min. If the mobile phase is well selected then the components of the mixture are unequally retained during the movement through the column which would give an indication of the consistence of the baseline. If the baseline is not consistent, checking for leakages or adjusting system pressure is necessary. From this point a phenomenon called retention, so the components of the unknown moved slower than the mobile phase. After elution from the column, the eluent passed through a diode array detector jointed with a recorder and showed the chromatogram. The detector was set at 254 nm to determine phenol and its byproducts. The mobile phase passed through the column created a signal as a baseline on the recorder or the integrator without the analyte and without stop. Phenol and its byproducts if separated would also

show the exit of each separated constituent and its peak time (retention time) is recorded on the detector. Photodegraded phenol and control samples were eluted at a flow rate of 1 mL/min or sometimes less depends on the column size. All the solvents were sonicated and filtered through vacuum system as it mentioned before.

3.10 Gas chromatography (GC)

3.10.1 Sample preparation

The solid phase extraction (SPE) columns (Chromabond C18 ec, octadecyl-modified silica, encapped, Macherey-Nagel) had a volume of 3 mL and 500 mg of C18 phase. The columns were first conditioned with three column volumes containing methanol (CH₃OH) and two column volumes containing 0.01 M hydrochloric acid (HCl). During the analysis, 200 mg of sodium chloride (NaCl) was added for every 1 mL of contaminant, and HCL (1M) concentration was used to adjust the pH to 2.0. A 2.5 mL sample of 10 ppm phenol was pipetted into the SPE column slowly at a flow rate of 0.5 mL/min and allowed to pass through the column. The sample was washed twice with 500 µL of 0.01 M HCl and dried under vacuum for 10 min, after which elution then carried out with 3×500 µL of methanol. Phenol standards (1-30 ppm) were prepared from the 100 ppm. Each standard (1, 5, 10, 20 and 30 ppm) were pipetted into the SPE column. After the extraction, the phenol standard was immediately injected into the GC injector for the analysis. The data obtained from the standard solutions gave the standard curve characteristic of each constituent, later plotted the peak area against its concentration and then measured the area to determine its concentration in the unknown mixture by OriginPro 8 as it shown in Figure 8.

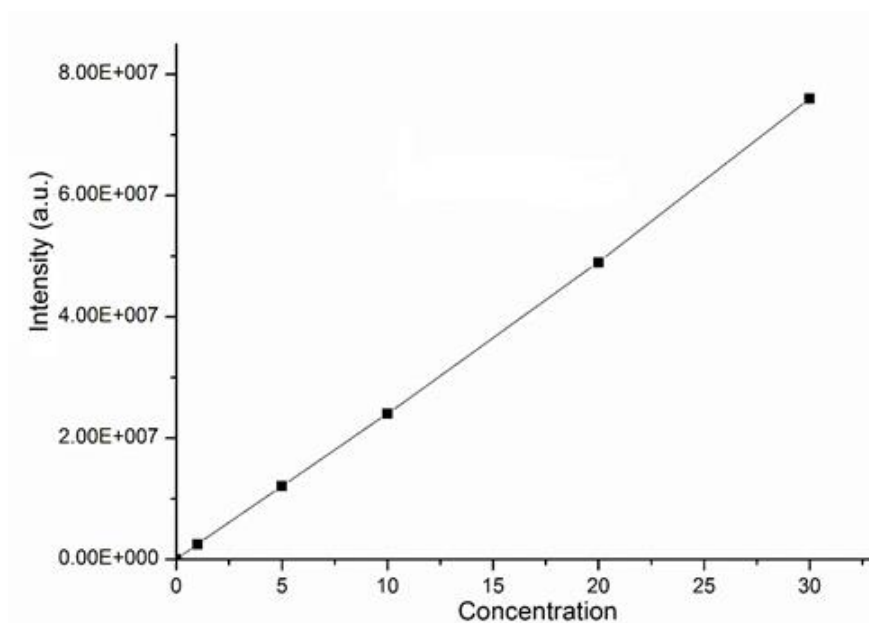


Figure 9: Calibration curve of peak area vs. concentrations (ppm) of phenol at $t=0$ min).

The analysed intensity of different standard solutions taken from the GC analysis were used to plot a calibration curve as seen in Figure 9, which shows a straight line. The recovery rate of SPE was evaluated with different concentrations of the contaminant and was found to be 95%. The extraction method was based on Macherey-Nagel Application No. 301860. The vacuum chamber for extraction was from J. T. Baker (BAKER spe-12G).

3.10.2 Chemical analysis

The collected fractions from the recovery rate of SPE were put in 2 mL GC vials, the fractions later injected into the GC/MS and the air bubbles were totally removed. The file name of each sample was recognized and stored. The following GC/MS instrumental conditions were applied:

GC-MS analysis was performed on Agilent 6890 GC system, coupled with mass spectrometry (GC-MS) was used for the determination of phenol concentration. The analysis was carried out using a HP-5 (Agilent, 5% phenyl methyl siloxane, capillary 30 m \times 320 μ m nominal) column. The injection mode was split less ratio of 10:1 and

the volume was 1 μL . Injector and detector temperatures were maintained at 300 $^{\circ}\text{C}$. Ultra-high purity helium (99.9999%) was used as a carrier gas with a constant flow of 1.2 mL/min. The injection, transfer line and ion source temperatures were 300, 230 and 200 $^{\circ}\text{C}$, respectively. The ionizing energy was 70 eV. Electron multiplier (EM) voltage was obtained and adjusted by autotuning. All data were obtained by collecting the full-scan mass spectra within the scan range 40-500 amu. The oven temperature program was varied as follows: started at 35 $^{\circ}\text{C}$ this temperature was held for 2 min and accelerated at a rate of 20 $^{\circ}\text{C}/\text{min}$ until it reached to 260 $^{\circ}\text{C}$ and thereafter held at 15 min up to 300 $^{\circ}\text{C}$ there it held for 1 min. The phenol and its byproducts spectra were identified by comparing the spectra obtained with mass spectrum libraries (NIST2011). The different phenol standard solutions been prepared in between (1-30 ppm) were also used for confirmation. By obtaining the y-axis value in Figure 9 which represents the peak value by

$$Y = 3E + 06x \quad \text{Eq 11}$$

Y goes for the intensity values, 3E+06 is the slope of the line and x is the unknown concentration that needs to be determined. Consequently, all the unknown concentrations of phenol and its different byproducts can be measured in the same way.

3.11 Capillary electrophoresis (CE)

CE was used to separate the components of a mixture for monitoring phenol and its byproducts with the P/ACE MDQ capillary electrophoresis system (Beckmann Coulter inc. Fullerton, Ca USA). CE uses a narrow capillary tube to separate large and small molecules in a high electric field. The separations were performed on a fused silica capillary 75 μm (i.d.) with a total length of 50 cm. The CE device was equipped with a photodiode array detector from (Beckmann Coulter inc.) with UV λ range started from 190 nm. The instrument was set up with the anode at the left side of the capillary and the cathode at the right. Data were collected, and processed with software called 32 Karat analyzer from Beckmann Coulter Inc. The buffer was prepared with 10 mmol sodium tetraborate and 10 mmol sodium dihydrogen phosphate in Milli-Q-purified water. The buffer prepared in the same way as the other chemical prepared in section

3.6.4. The pH of the buffer was adjusted to 8.0 for 3 min at 3.5 kPa. The samples were injected to the electrophoresis with a constant voltage of 20 kV (reversed polarity) for 7 min between runs; the capillary was rinsed with NaOH 1 mol/L and Milli-Q-purified water (138kPa), 1 min at a constant capillary temperature of 25 °C. The preparation of NaOH was done the same way as explained in part 3.6.4. For the determination and quantification of phenol, HQ, BQ, Cat, Res, 2-P and AA, the detection was done at 254 nm. Timing of the sampling was controlled by the instrument software. The samples were centrifuged at (10 000 rpm, 5 min) first by using Eppendorf centrifuge (system model 5810R) and then filtered through 0.1 µm and analysed after dilution.

To determine the concentrations of the absorbed values, solutions of standards (from 0.5-12 ppm) were prepared from the 100 ppm, each of these standards used with the samples were injected using 20 psi pressure.

Table 14: Standard concentrations with the absorbance's of phenol

Standard Conc. (ppm)	Absorbance
0.5	5.79E-4
2.0	2.33E-3
4.0	4.79E-3
6.0	6.98E-3
8.0	9.57E-3
10.0	0.0121
12.0	0.0143

The values of CE standards are tabulated in Table 14 showed that the absorbance of samples increased linearly with an increase of the standard concentration. Table 14 shows the obtained absorbance of the prepared phenol standard concentrations. The results of the absorbance of the prepared standards were used to plot a calibration curve as shown in the Figure 10. The absorbance for all other standards of phenol byproducts which used in this section are prepared and compared in the same way as it prepared for phenol.

In Figure 10 the relation between phenol concentrations and its absorbance shows a straight line. The calibration curve shows a straight line passing through the origin, so

it obeyed the equation: $y=mx$, where y gives absorbance values, m gives the slope of the line and x shows the unknown concentration. $y=0.0012x$, then $x=\frac{y}{0.0012}$, if the absorbance is measured on y -axis, the value on the x -axis could be calculated easily. In this way all the solutions of the standards, unknowns and the other byproducts can be extrapolated.

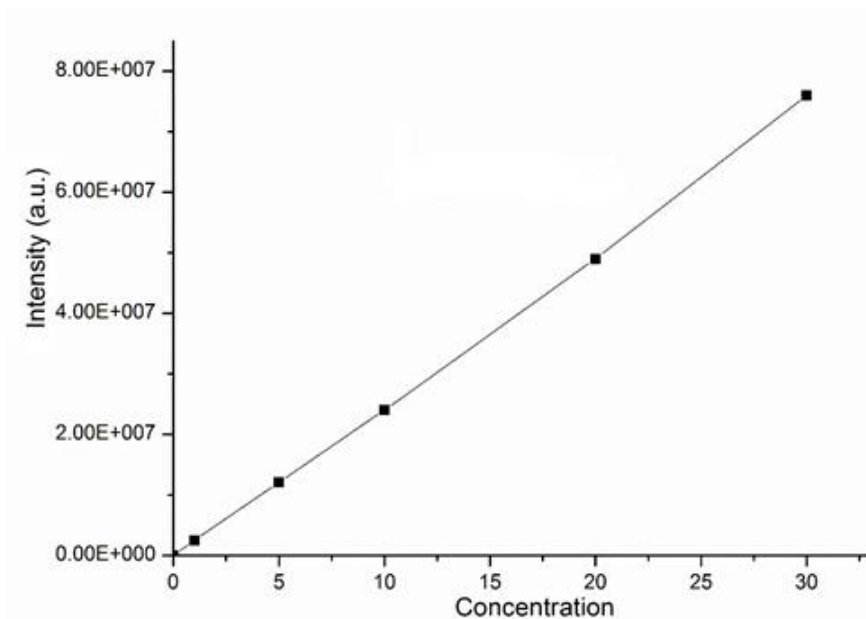


Figure 10: Calibration curve of absorbance vs. concentrations of phenol at $t=0$

3.11.1 Photolytic degradation

The influence of UV light was also examined without the catalyst on phenol photodegradation indicated very little catalytic activity, as the experiment was designed to determine the percentage of photolysis by UV illumination without the catalyst prior to the determination of the photocatalytic activity of SnO_2 . The results are explained in the coming Figures.

4 Results and discussion

4.1 Motivation for studying phenol and its byproducts

As it was discussed in the previous chapters that Phenol is an organic compound found in surface and ground water, which has an endless effect on the creatures and the environment. Some high concentration of phenol was also found in some processing food [12]. Phenol and phenolic compounds are assigned as priority pollutants by the Environmental Protection Agency [379]. In fact, a small concentration of these toxins can prevent the development of many living organisms [380, 381]. Studies have been indicated that phenol might link to other chemicals such as parabens, benzoic acids and others. The results show that the problems created by phenolic compounds in the wastewater would become worse in the future. Phenol was taken as a pollutant since it linked with so many other groups. Consequently, there is a requirement to abolish phenol and its compounds from the environment. If phenol removed from the solvent the other groups would be easily degraded. In this study, phenol was chosen as a model pollutant to represent the group of its byproducts identified during different analytical analysis for photocatalytic degradation study. Complete photocatalytic degradation of phenol and other six byproducts such as (HQ, BQ, Cat, Res, AA and 2-P) were studied, to show the excellent ability of the Nps synthesized.

This chapter examines the efficiency of the photocatalytic systems synthesized for photodegrading phenol and its intermediates. The chemical structure of phenol and its byproducts are shown in Figure 1.

Also in this work synthesized undoped SnO₂ and with differently doped ions photocatalyst were used. The photocatalytic activity of these Nps was examined by photodegradation of phenol in 3 different photocatalytic reactors explained in chapter III. The studied process composed of photocatalytic degradation in the presence of UV, sunlight, or visible light irradiation.

4.2 Characterization of the synthesis materials

The procedures used to explain the process of characterization were explained in chapter 3. In this section the comparison of results will be discussed with different techniques.

4.2.1 X-ray diffraction analysis (XRD)

Undoped and doped SnO₂ samples were examined by XRD, the average crystallite sizes were estimated from the Debye-Scherrer equation [382].

$$D = \frac{K\lambda}{\beta \cos\theta} \quad \text{Eq 12}$$

where D is the crystallite size, K is the Sherrer's constant (0.9), λ is the λ of Cu K α radiation (1.5418 Å), θ is the diffraction (Bragg's) angle, and β is the full width at half maximum (FWHM).

The lattice parameters 'a' and 'c' for the tetragonal structure ($a = b \neq c$, $\alpha = \beta = \gamma = 90^\circ$) can be calculated by the following expression [383],

$$\sin^2\theta = \frac{\lambda^2(h^2 + k^2)}{4a^2} + \frac{\lambda^2(l^2)}{4c^2} \quad \text{Eq 13}$$

where h, k and l are the Miller indices but variables (a and c) are the lattice constants.

The unit cell volume of the products is given by the formula.

$$V = a^2c \quad \text{Eq 14}$$

The XRD analysis for SnO₂/I Nps synthesized by sol-gel were done by placing the powder on the special glass provided through Miniflex 600 diffractometer

Each powder was prepared for XRD analysis using the technique explained in section 3.7.1.1, the powder was spread on the glass holder and placed on the magnetic recognition and the preparation method loaded. The XRD analysis was obtained after turning on the detector in continuous scan mode operated at 30 kV and a current of 15

mA. Diffractograms of the powder was recorded in 2θ scan configuration, in the range of $10\text{-}80^\circ 2\theta$ range at steps of 0.02° .

The XRD patterns of undoped SnO_2 , doped SnO_2/I 0.2 wt. % and SnO_2/I 1.0 wt. % samples synthesized by sol-gel process with the results are shown in Figure 11.

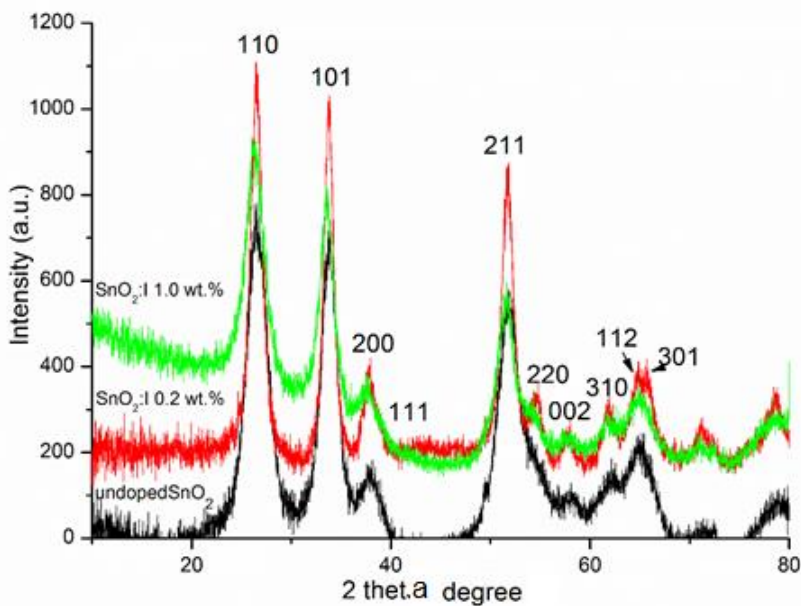


Figure 11: XRD patterns of undoped SnO_2 , SnO_2/I 0.2 wt. % and SnO_2/I 1.0 wt. % Nps synthesized by sol-gel process

Figure 11 indicates the presence of ten peaks which correspond to the SnO_2 crystal planes of 110, 101, 200, 111, 211, 220, 002, 310, 112, and 301 respectively. The results in Figure 11 matched the standard XRD file of SnO_2 (JCPDS-# 41-1445) (JCPDS abbreviation stands for Joint Committee on Powder Diffraction Standards) [161, 336, 338, 384-386], which are regarded as an attributive indication of the rutile SnO_2 structure.

The calculated crystallite sizes of the undoped, SnO_2/I 0.2 wt. %, and SnO_2/I 1.0 wt. % in the Figure were estimated by the FWHM of the most intense peak (110) using the Debye-Scherrer equation. The obtained SnO_2 crystallite sizes followed the well-known trend of crystallite size reduction, when the control SnO_2 showed 8.4 nm. But when

SnO₂ was doped with I, the crystallite size drastically reduced (SnO₂/I 0.2 wt. % it decreased to 8.0 nm; and 2.5 nm for SnO₂/I 1.0 wt. %).

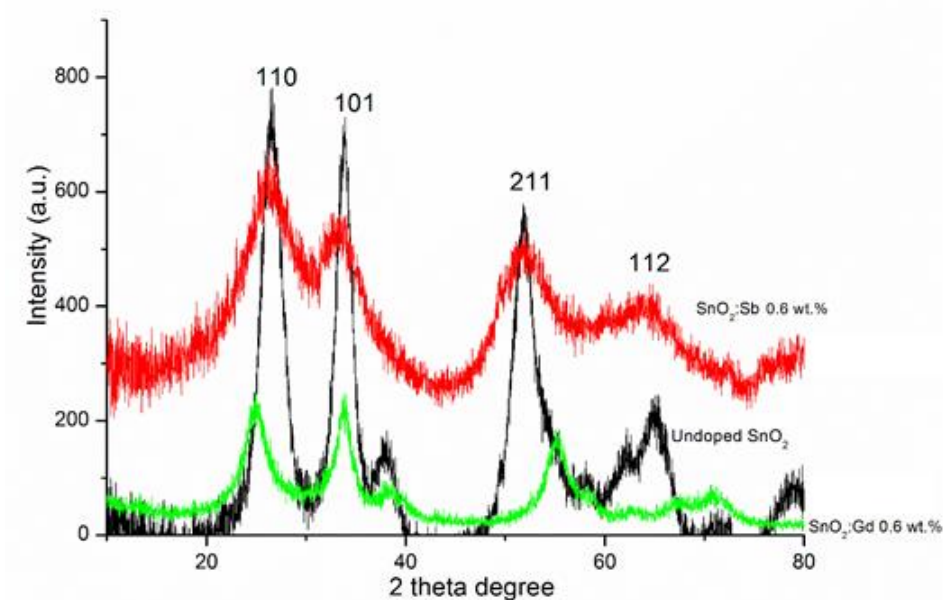


Figure 12: XRD patterns of undoped SnO₂, SnO₂/Gd 0.6 wt. % and SnO₂/Sb 0.6 wt. % Nps synthesized by sol-gel method.

SnO₂/Gd 0.6 wt. % and SnO₂/Sb 0.6 wt. % were both compared with undoped SnO₂ Nps. All the metals were synthesized by sol-gel and the powder were kept away of light and humid in a desiccator until characterized. The powder of each doped and undoped Nps was spread separately on the glass for the XRD measurement after the glass was cleaned and dried in the oven.

In Figure 12 the XRD patterns showed the undoped SnO₂, SnO₂/Gd 0.6 wt. %, and with SnO₂/Sb 0.6 wt. %. The crystallinity of each of the powder was characterized alone; no observable changes could be seen in the patterns between them.

In Figure 12 the obtained SnO₂ crystallite sizes followed the well-known trend of crystallite size reduction as in previous Figures, although, the control SnO₂ showed 8.4 nm, but when the Gd was doped with SnO₂ as SnO₂/Gd 0.6 wt. % the crystallite size

severely decreased to 3.2 nm. Again the crystallite size continued to significantly reduce down until it reached 1.8 nm for SnO₂/Sb 0.6 wt. %.

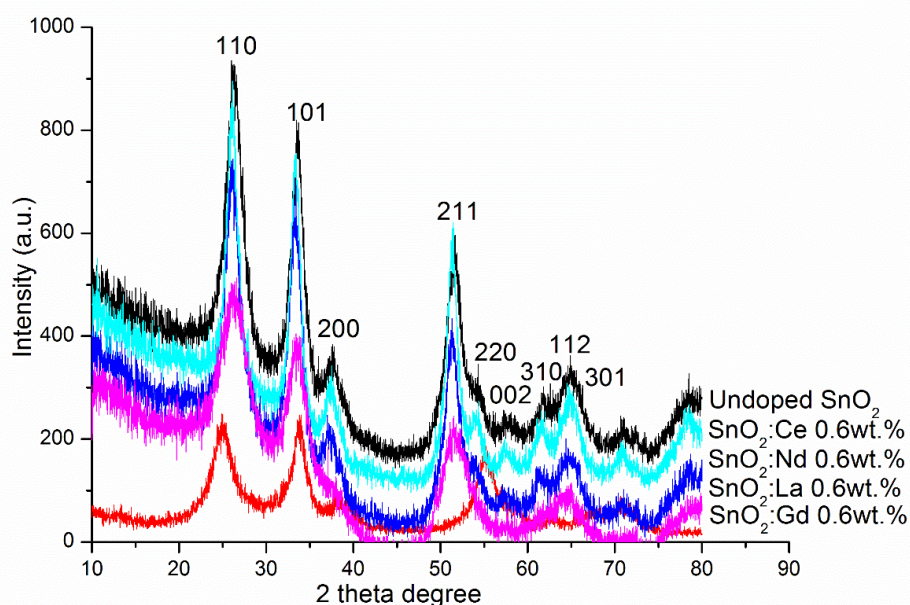


Figure 13: X-ray patterns of undoped SnO₂, SnO₂/Gd 0.6 wt. %, SnO₂/La 0.6 wt. % SnO₂/Nd 0.6 wt. % and SnO₂/Ce 0.6 wt. % Nps synthesized by sol-gel process.

In another analysis, all RE metals were compared with the control such as the undoped SnO₂, SnO₂/Gd 0.6 wt. %, SnO₂/La 0.6 wt. % SnO₂/Nd 0.6 wt. % and SnO₂/Ce 0.6 wt. %. Each of these samples spread alone on each glass holder provided for XRD as it described before and put in the XRD. The XRD patterns in Figure 13 indicated that the diffraction angles at $2\theta = 26.3^\circ, 33.6^\circ, 37.62^\circ, 51.68^\circ, 54.46^\circ, 57.7^\circ, 61.60^\circ, 65^\circ, 65.62^\circ$, that can be assigned to 110, 101, 200, 211, 220, 002, 310, 112, and 301 respectively, matched with the standard XRD file of the rutile phase of SnO₂ [161, 336, 338, 384-386].

No much difference could be gained in the XRD patterns between them and the previous patterns in Figure 11 and 12.

Although the previous Figures 11 and 12 followed the well-known trend of crystallite size reduction, as it followed and SnO₂ showed 8.4 nm, while Ce doped SnO₂ as (SnO₂/Ce 0.6 wt. %) decreased to 5.5 nm. When Nd was doped to SnO₂ as SnO₂/Nd 0.6 wt. % notably reduced to 4.1nm, on the other hand, as La was doped with SnO₂ the crystallite size extensively continued to reduce to 3.4 nm. With Sb doped SnO₂ it appreciably lessen to 1.8 nm for SnO₂/Sb 0.6 wt. %.

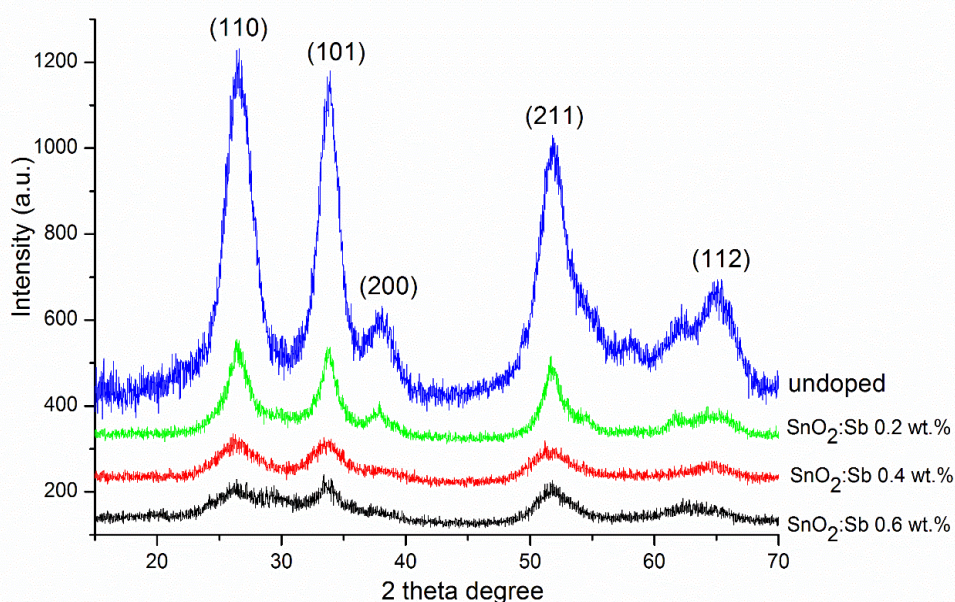


Figure 14: XRD patterns of undoped SnO₂, SnO₂/Sb 0.2 wt. %, SnO₂/Sb 0.4 wt. %, and SnO₂/Sb 0.6 wt. % Nps synthesized by sol-gel method.

The characterization of SnO₂ with different dopant ions, such as undoped SnO₂, SnO₂/Sb 0.2 wt. %, SnO₂/Sb 0.4 wt. %, and SnO₂/Sb 0.6 wt. % Nps was also analysed.

Figure 14 indicates the XRD pattern of undoped SnO₂ sample showed the presence of peaks as (110), (101), (200), (211) and (112) respectively. Matched with the standard XRD file of SnO₂ (JCPDS-# 41-1445) [161, 336, 338, 384-386], regarded as an attributive indication of rutile SnO₂ structure. The doped samples at differently SnO₂/Sb concentrations of 0.2, 0.4, and 0.6 wt. % showed no substantial differences in XRD

patterns compared to the undoped SnO₂. Again, Figure 14 showed that the crystalline size decreased with the increasing Sb doping wt. % onto SnO₂.

4.2.2 Crystallinity

The data obtained from the XRD analysis were compared to check how the doping affected the crystallinity. In Figure 15 the relation between crystallinity and the type of ions used for the doping process are outlined. The results indicate a decrease of crystallization size with an increasing amount of dopant used in the process (8.2 nm to 1.8 upon SnO₂/Sb 0.6 wt. %).

The crystallinity of the catalyst plays an important role for the overall efficiency of the photocatalytic degradation potential [387]. In Figure 15 the SnO₂ crystallite sizes obtained from the Debye-Scherrer equation considered the most intense (110) peak followed the crystallite size reduction.

Undoped material was found to have a crystallite size of 8.2 nm, while the crystallite size decreased when ions were present (5.5 for SnO₂/Ce 0.6 wt. % to 4.1 for SnO₂/Nd 0.6 wt. % to 3.4 for SnO₂/La 0.6 wt. % to 3.2 for SnO₂/Gd 0.6 wt. % to 2.5 for SnO₂/I 1.0 wt. % to 1.8 for SnO₂/Sb 0.6 wt. %).

It is clear from Figure 15 that the crystallite sizes of the mentioned samples above decreased as the dopant into SnO₂ increased. Decreasing the crystallinity of ions doped to SnO₂ is clear and consistent with the XRD results above.

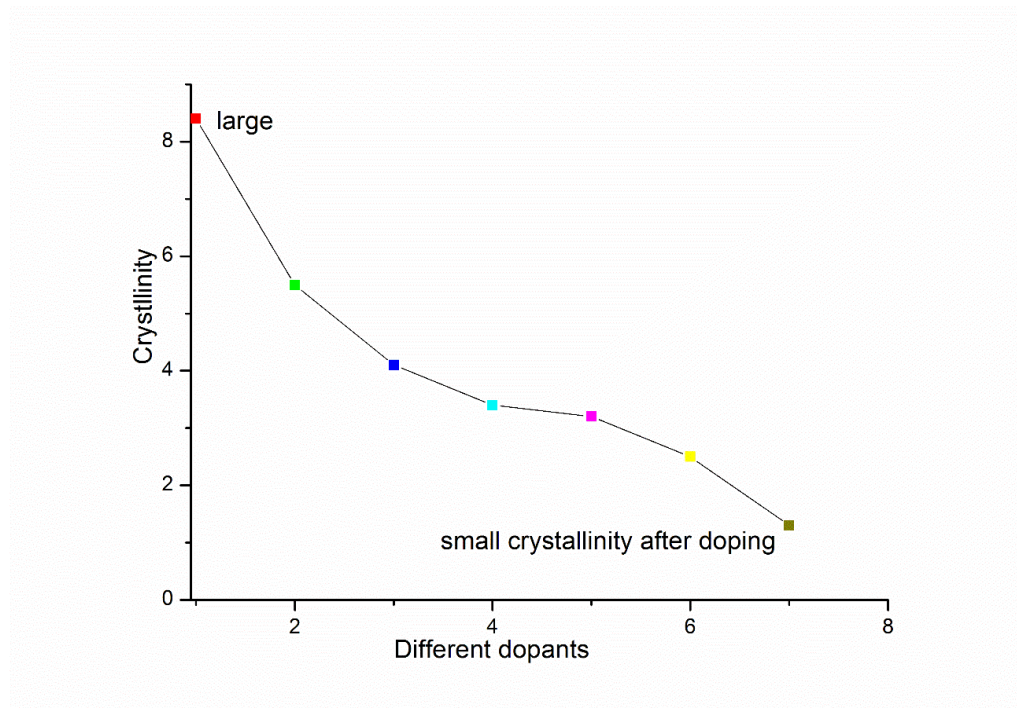


Figure 15: Crystallite size of undoped SnO₂, SnO₂/Ce 0.6 wt.%, SnO₂/Nd 0.6 wt.%, SnO₂/La 0.6 wt.%, SnO₂/Gd 0.6 wt.%, SnO₂/I 1.0 wt.% and SnO₂/Sb 0.6 wt.%, all these Nps were synthesized in the same way by sol-gel method and the parameters were same for the doping and the undoping.

Many researchers have shown that the crystalline decreased with the increasing doping on SnO₂. This configuration agrees with the understanding that incorporation of impurity atoms in SnO₂ reduces the crystallite sizes [320, 321]. In this study different doping to SnO₂ let the crystallite size of SnO₂-dopants to decrease as the concentration of the dopants to increase, these results agree with other study findings [388].

4.2.1 BET surface area

The BET specific surface area of the synthesized photocatalysts were analysed using a BET surface analyser (Nova[®] 2200) and with using nitrogen adsorption. Each 200-300 mg of the photocatalyst samples (undoped SnO₂, SnO₂/Ce 0.6 wt. %, SnO₂/Nd 0.6 wt.%, SnO₂/La 0.6 wt. %, SnO₂/Gd 0.6 wt. %, SnO₂/Sb 0.6 wt. % and SnO₂/I 1.0 wt.% were dried and degassed separately and alone in a sample tube at 300 °C for at least 3 h before adsorption.

The results were accumulated and analysed by using the 2200 Autosorb analyser software. The BET surface area of undoped SnO₂ Nps from gas adsorption studies was found to be 28 m² g⁻¹ smaller than the BET surface area of SnO₂/Gd 0.6 wt. % which increased to 58 m² g⁻¹, due to the reduction of the crystallite size as outlined in Table 15. Generally, heterogeneous catalysts with large surface areas are better suited as they allow increased adsorption of the reactants. Doping SnO₂ changed the crystal structure of the semiconductor. In addition, it created a reduction in crystal size and an enhancement in active surface area. Consequently, doping SnO₂ is an advantage since it fulfils a dual purpose, as it simultaneously alters the electronic properties of the metal oxide by narrowing the BG and enlarges the contact area between the catalyst and the pollutant [389]. This effect is observed in the following Table when a sample of SnO₂ was doped with different metals of variation concentrations. In all cases of the photocatalyst increased, resulted in higher catalytic activity. This steady increase continued up to a certain threshold which differs for each pollutant (depending on charge, size of the ion, and other factors).

Table 15: Calculated crystallite of different 0.6 % doped and undoped SnO₂ Nps from (110) peak using the Debye-Scherrer analysis

No.	Dopant	Size (nm)	Surface area (m ² /g)
1	Undoped	8.4	28
2	SnO ₂ /Ce (0.6 wt. %)	5.5	30
3	SnO ₂ /Nd (0.6 wt. %)	4.1	35
4	SnO ₂ /La (0.6 wt. %)	3.4	40
5	SnO ₂ /Gd (0.6 wt. %)	3.2	58
6	SnO ₂ /Sb (0.6 wt. %)	1.8	54
7	SnO ₂ /I (1.0 wt. %)	2.5	50

With 50 m² g⁻¹, the surface area of SnO₂/Sb 0.6 wt. % was found to be smaller than the surface area of SnO₂/Gd 0.6 wt. % which was found to be 58 m² g⁻¹. The surface area of the synthesized RE Nps with the other ions starting from undoped SnO₂, SnO₂/Ce 0.6

wt. %, SnO₂/Nd 0.6 wt. %, SnO₂/La 0.6 wt. %, SnO₂/Gd 0.6 wt. %, SnO₂/Sb 0.6 wt. % and SnO₂/I 1.0 wt. %. Nps are shown in Table 15 by having surface areas of 28, 30, 35, 40, 58, 54 and 50 m²/g respectively. Therefore, it is possible to notice that the doping of Gd/SnO₂ increased the specific surface area until it reached 58 m² g⁻¹. The increment in the surface area may be due to the reduction of the crystallite size as was explained above.

On the other hand, the crystallite size reduced from 8.4 nm for undoped SnO₂ Nps to 3.2 nm for the SnO₂/Gd 0.6 wt. % and 1.8 nm for the SnO₂/Sb 0.6 wt. % sample, which indicated that an increasing concentration of the dopant the diffraction peaks broadened due to the smaller crystalline sizes [390] as it was also noticed in the previous XRD Figures (11-14). Table 15 also includes the comparison of different doped crystalline sizes which were calculated from the broadening of the highest intensity (110) peak in the XRD patterns. Another notification with the crystallite sizes reduction upon doping with different ions as it was showed in the previous Figures. The specific surface area of undoped SnO₂ Nps from gas adsorption studies was found to be 28 m²g⁻¹, but increased to 58 m²g⁻¹ for the SnO₂/Gd 0.6 wt. % Nps and with SnO₂/Sb 0.6 wt. % Nps demonstrated about 54 m²g⁻¹, so it has nearly double the highest specific surface area of the undoped samples. Furthermore, Table 16 included the estimated crystallite size of undoped SnO₂ and different 0.6 wt. % ions doped SnO₂ Nps from the (110) peak using the Debye-Scherrer analysis [391].

Table 16: Calculated crystallite size of different SnO₂/Sb Nps from (110) peak using the Debye-Scherrer analysis

No.	Dopant	Size (nm)
1	Undoped	8.4
2	SnO ₂ /Sb (0.2 wt. %)	3.5
3	SnO ₂ /Sb (0.4 wt. %)	2.5
4	SnO ₂ /Sb (0.6 wt. %)	1.8
5	SnO ₂ /Sb (0.8 wt. %)	2.1

These results agreed well with the observations made from XRD results about the reduction in crystallite sizes of SnO₂: different ions Nps upon doping. An increased in the surface area was observed, which was attributed to the reduction in the grain size as it could be seen from Table 16. The analysis of crystallite sizes estimated from the broadening of highest intensity 110 peaks in the XRD pattern for undoped SnO₂, SnO₂/Sb 0.2 wt. %, SnO₂/Sb 0.4 wt.%, SnO₂/Sb 0.6 wt. % and SnO₂/Sb 0.8 wt. % having crystallite sizes of 8.4, 3.5, 2.5, 1.8 and 2.1 nm respectively. It was found that any further increment in the catalyst dosage slightly controlled the crystallite size or did not affect it any more. As it shown in the Table 16, with SnO₂/Sb 0.8 wt. % the crystallite size increased instead of getting smaller. The SnO₂ crystallite sizes obtained from the Debye Scherrer equation considered the most intense peak (110) followed the well-known trend of crystallite size reduction upon doping. Table 16 indicated that the reduction of the crystalline size increased with increasing concentration of the dopant. which agreed with the understanding that the incorporation of the impurity in SnO₂ reduced the crystallite sizes [392, 393] once more showed a reduction of crystallite sizes upon doping.

In addition, other researchers also supported our findings when they reported that doping SnO₂ with different ions increased its surface area as it shown below in Figure 16. Xia et al. [225] reported that the highest photocatalytic activity, good crystallization, and a high surface area were achieved with a 1:1 molar ratio of Cu and Sn, calcined at 500°C for 3 h.

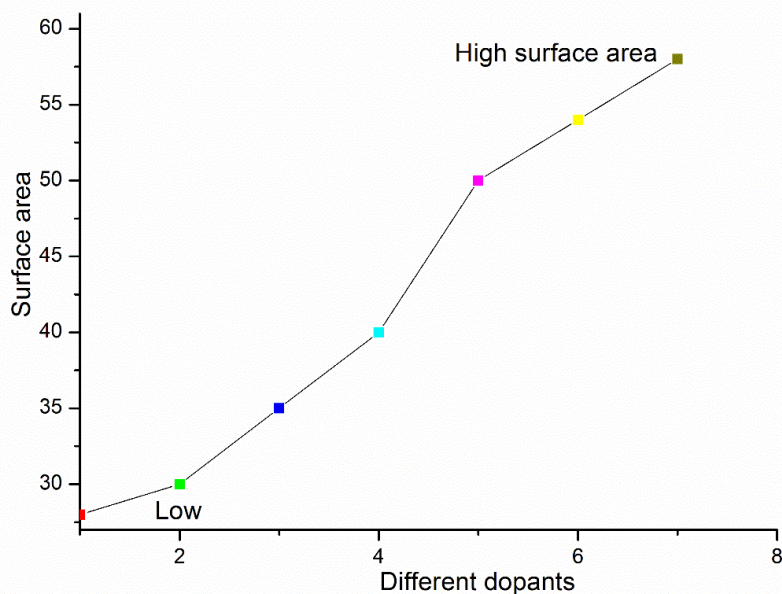


Figure 16: Surface area calculated of undoped SnO₂, SnO₂/Ce 0.6 wt. %, SnO₂/Nd 0.6 wt. %, SnO₂/La 0.6 wt. %, SnO₂/Gd 0.6 wt. %, SnO₂/I 1.0 wt. % and SnO₂/Sb 0.6 wt.%

In Figure 16 the SnO₂ specific surface area using the BET surface analyser, increased from 28 m²/g for undoped SnO₂ to 30 m²/g upon SnO₂/Ce 0.6 wt. % to 35 m²/g upon SnO₂/Nd 0.6 wt. % to 40 m²/g upon SnO₂/La 0.6 wt. % to 50 m²/g upon SnO₂/I 1.0 wt. % to 54 m²/g upon SnO₂/Sb 0.6 wt. % to 58 m²/g upon SnO₂/Gd 0.6 wt. %. The different doped SnO₂ ions showed a high surface area with doping. The Figure also shows that the surface area of the mentioned samples above increased with different dopants and were consistent with the XRD results above and also with the data seen in Table 16.

4.2.2 Electron microscopic analysis (SEM)

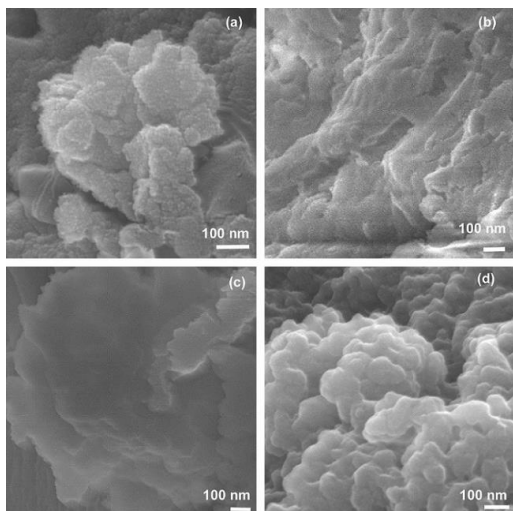


Figure 17: SEM images of a-undoped SnO₂, b-SnO₂/Nd 0.6 wt. %, c-SnO₂/Ce 0.6 wt. %, d-SnO₂/La 0.6 wt. % Nps synthesized by sol-gel method

The SEM morphology micrographs of different photocatalysts are shown above in Figure 17. The images of different powder samples were done with JEOL working at 30 kV. Images were taken up to about 50,000 magnifications or above, so the samples can be monitored at high resolution which can be achieved with the sub-100 nm resolution. Undoped SnO₂, SnO₂/Nd 0.6 wt. %, SnO₂/Ce 0.6 wt. % and SnO₂/La 0.6 wt. % powders were prepared separately for SEM sampling. The technique was by first coating the powder on a carbon tape. The coated carbon tape later put in the oven to dry at 60 °C. The SEM images are presented in Figure 17 as (Figure 17a, 17b, 17c, and 17d), indicated that the microstructures of the a-undoped SnO₂, b-SnO₂/Nd 0.6 wt. %, c-SnO₂/Ce 0.6 wt. %, and d-SnO₂/La 0.6 wt. % doped Nps respectively. Typically 50 nm sized agglomerates of Nps were observed. The 8.6–3.2 nm crystallite agglomerates to form the 50 nm powders.

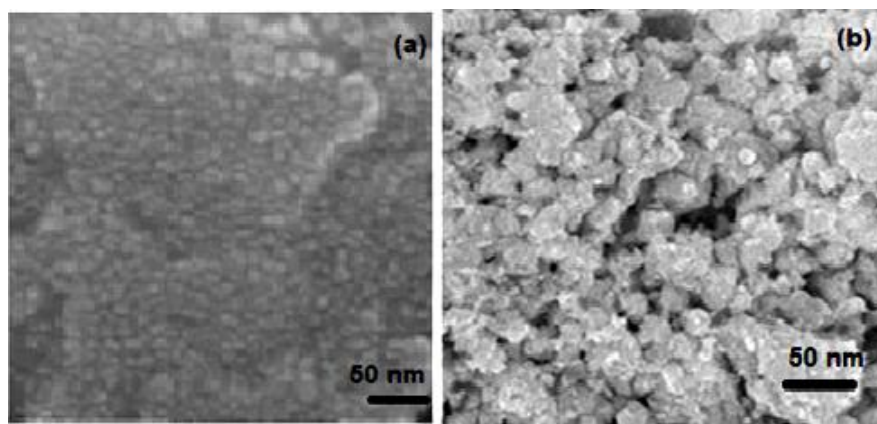


Figure 18: Typical SEM images of a-SnO₂/I 1.0 wt. % and b-SnO₂/Gd 0.6 wt. % Nps

In Figure 18 microstructures of SnO₂/I 1.0 wt. % and b-SnO₂/Gd 0.6 wt. % powders compared with Figure 17a as an undoped SnO₂. The samples treated exactly in the same way as discussed before with JEOL working at 30 kV. Images were taken at high resolution up to about 50,000 or above magnifications. SnO₂ and different doped powders were prepared separately as SnO₂/I 1.0 wt. % and b-SnO₂/Gd 0.6 wt. % Nps for SEM by first coating the powder on a carbon tape, later putting it in the oven to dry at 60 °C for about 10 min, until a carbon coat applied on SnO₂ powder. The SEM images are presented in Figure 18 it is clear from the images that in a-SnO₂/I 1.0 wt. % and in 18b-SnO₂/Gd 0.6 wt. % Nps, that upon doping I ion with the oxide the average grain size decreased. Gd doped SnO₂ also showed the same trend as it indicates in the Figure and noticed with I doping. The results agreed with what was observed from the calculation of crystallite sizes of both a-SnO₂/I 0.6 wt. % and b-SnO₂/Gd 0.6 wt. % Nps or from the XRD studies as it shown in Table 15.

Images from JEOL working at 30 kV were taken at high resolution up to about 50,000 magnifications or above. The SnO₂/Sb 0.6 wt. % powder, prepared exactly by the same way as the previous images have been treated.

In Figure 19 SnO₂/Sb 0.6 wt. % also showed the average grain size reduction which agreed in prior with the different images of Figure 17 and 18 and also in an agreement with the observations made from the calculation of crystallite size from XRD studies as noticed in Figure 11 and Tables 15 and 16.

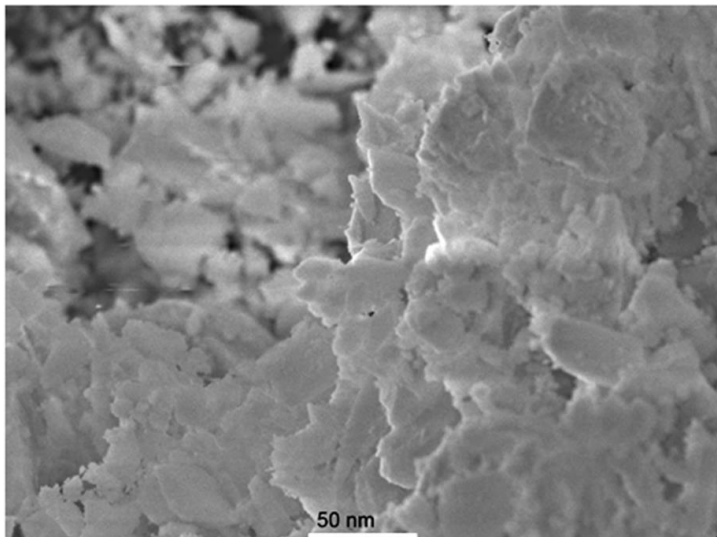


Figure 19: Typical SEM image of SnO₂/Sb 0.6 wt. % Nps synthesized by sol-gel process

4.2.3 Transmission microscopic analysis (TEM)

Samples of undoped SnO₂, SnO₂/Nd 0.6 wt. %, SnO₂/Ce 0.6 wt. % and SnO₂/La 0.6 wt. % Nps were prepared by crushing the powders separately and later spreading few particles of each catalyst in each special container with the alcohol and sonicating in (JAC, 210 KODO). Drops of the sample were deposited separately on Cu supporting grid with holy carbon supporting films. Later the grid was dried in the room temperature for analysis.

In some analysis, the samples were needed special treatment, diluted several times with high purity water and sonicated in (JAC, 210 KODO).

The high resolution (HR-TEM) images are shown in the following Figures. In fact, the crystallite sizes are comparable to what was calculated from the XRD Figures and from Tables 15 and 16. In these Tables the crystallite size is clearly seen to reduce in size upon doping, agreeing well with the earlier observations made from XRD and SEM analysis.

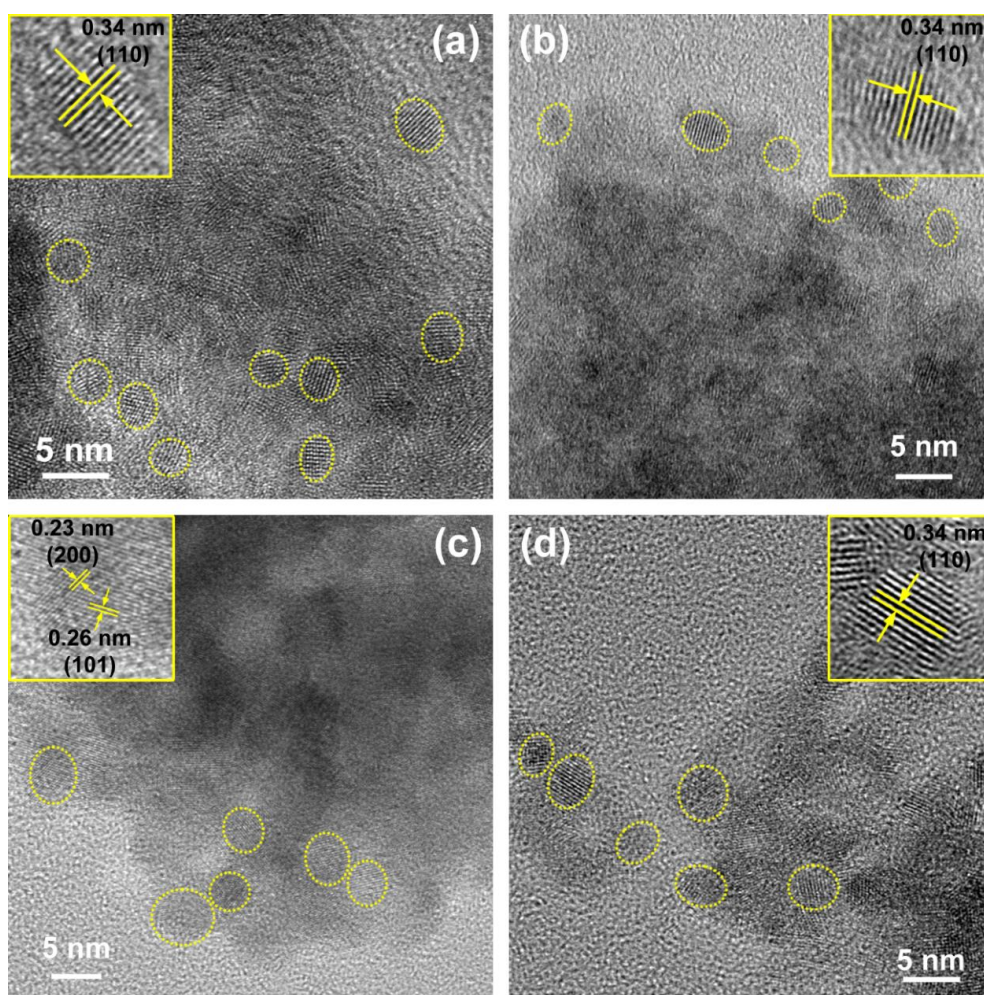


Figure 20: HR-TEM of a-undoped SnO₂, b-SnO₂/Nd 0.6 wt. %, c-SnO₂/Ce 0.6 wt. %, d-SnO₂/La 0.6 wt. % Nps

The HR-TEM of the a-undoped SnO₂ and b-SnO₂/Nd 0.6 wt. %, c-SnO₂/Ce 0.6 wt. %, d-SnO₂/La 0.6 wt. % Nps images are shown in Figures 20a, 20b, 20c and 20d respectively. These images confirm the observations made from SEM, XRD and gas adsorption analysis (BET) (see previous Figures) that upon doping with SnO₂ the average grain size decreases.

Morphology of SnO₂/Gd was also characterized by HR-TEM as in Figure 20.

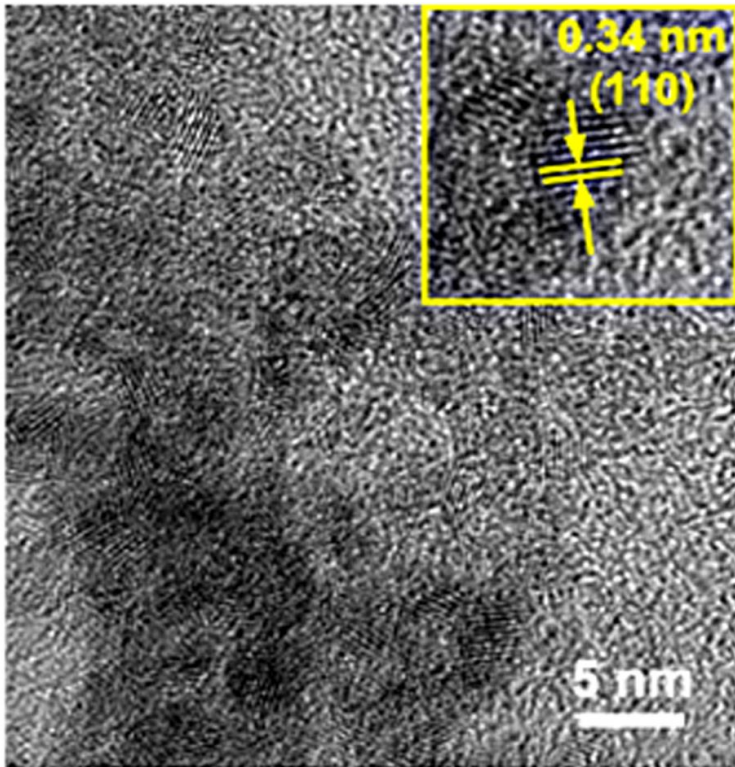


Figure 21: Typical HR-TEM of SnO₂/Gd 0.6 wt. % Nps synthesized by sol-gel process

Figure 21 shows the TEM image of SnO₂/Gd 0.6 wt. % Nps synthesized by sol-gel process. SnO₂/Gd 0.6 wt. % samples were prepared by crushing SnO₂/Gd 0.6 wt. % powders and later few particles of the powder were dispersed in the alcohol and sonicated. Drops of the sample were deposited on Cu supporting grid with holy carbon supporting films. Later the grid was dried in the room temperature. The average grain size of SnO₂ Nps was found to decrease which is in an agreement with the other observations made from previous characterization techniques.

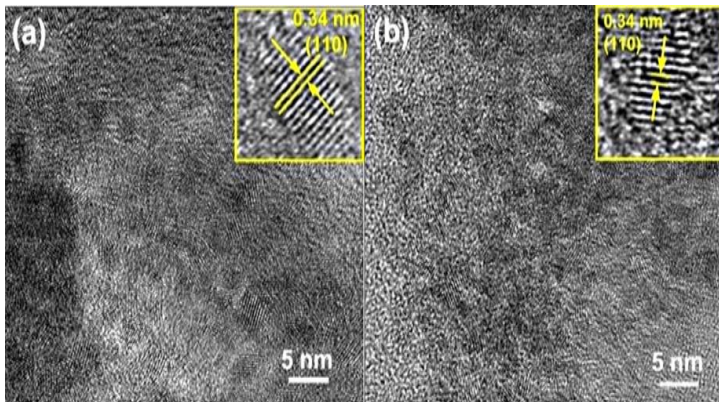


Figure 22: HR-TEM of (a) control SnO_2 (b) SnO_2/I , 1.0 wt. % Nps synthesized by sol gel process.

The micro structure of SnO_2/I 1.0 wt. % Nps was carried as it shown in Figure 22. HR-TEM images samples were prepared by crushing SnO_2/I 1.0 wt. % powders and dispersing them in the alcohol and let them to sonicated for some time. After the sonication, drops of the sample were deposited on Cu supporting grid with holy carbon supporting films. Exactly the same procedure followed as previously discussed, later the grid was dried.

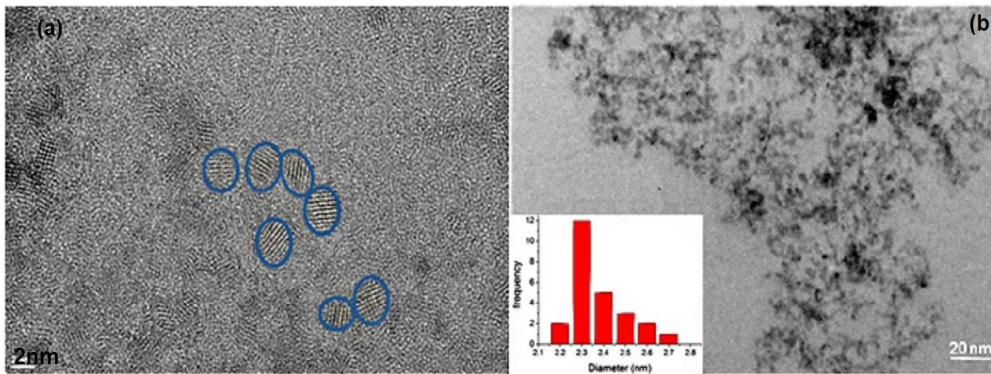


Figure 23: Typical HR-TEM of SnO_2/Sb 0.6 wt. % Nps synthesize by sol-gel

From the Figure it can be observed that the crystallite sizes are comparable to what was gained and observed and are clearly seen to reduce in size upon doping, again agreeing well with earlier statements made from the previous techniques.

In an estimation of nanocrystals size distribution from Figure 23 showed the size of SnO_2/Sb 0.6 wt. % samples. When the Nps were dispersed in alcohol, the image showed

similar average particle size of 2.3 nm for the SnO₂/Sb 0.6 wt. % samples as showed in (Figure 23 b). The size of the SnO₂/Sb 0.6 wt. % Nps was estimated from TEM analysis, also showed maximum percentage (12%) of particles having diameter 2.3 nm, while the overall diameter of the Nps was found in the range from 2.2 to 2.7 nm

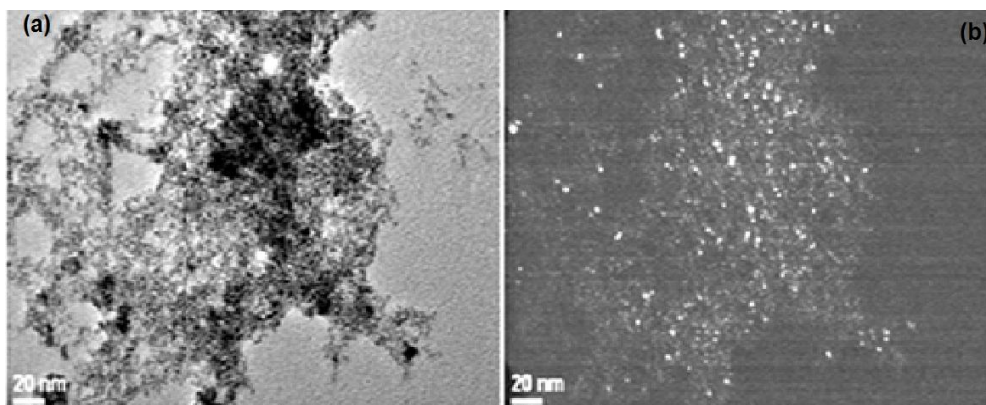


Figure 24: HR-TEM of SnO₂/Sb 0.6 wt. % Nps light field and dark field on images

In Figure 24 typical high resolution transmission electron micrograph of the same SnO₂/Sb 0.6 wt. % Nps synthesized by sol-gel process is shown in (24-a). The Figure was further verified using HR-TEM to show that the dark field imaging clearly showed the small nanocrystallites as it shown in (24-b).

4.3 Optical activity

In this section, the optical activity of SnO₂ and some doped SnO₂/Sb was compared. Typical optical absorption of undoped SnO₂, SnO₂/Sb 0.4 wt. % and SnO₂/Sb 0.6 wt. % dried samples were sonicated for some time and after collected from a suspension for each in aqueous media.

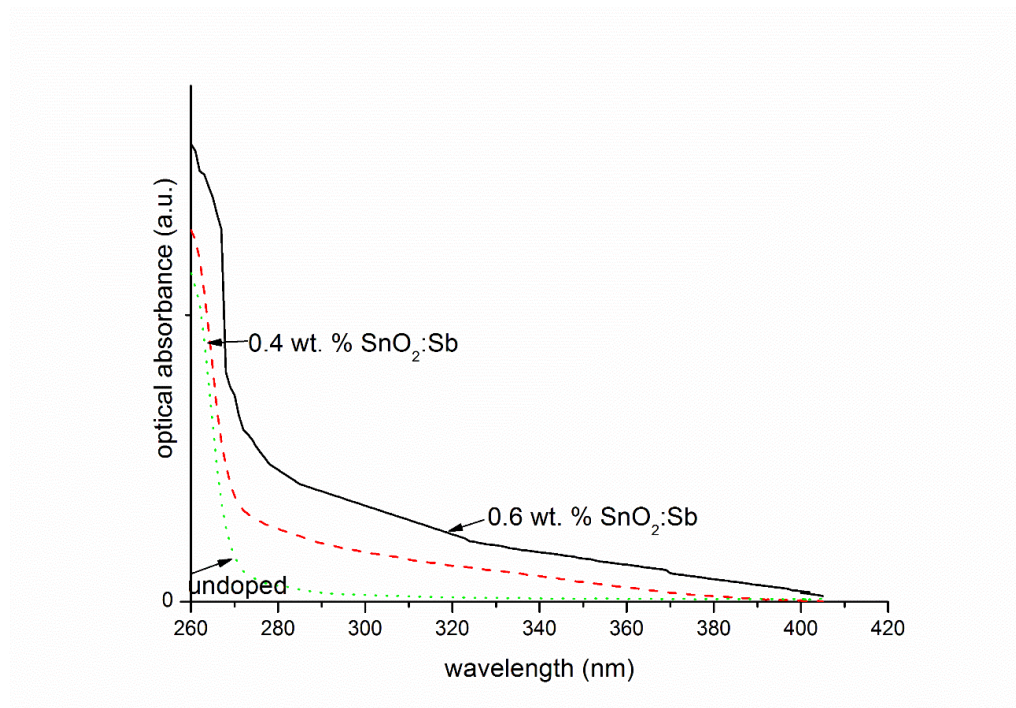


Figure 25: Optical absorption of SnO_2 , SnO_2/Sb 0.4 wt. %, and SnO_2/Sb 0.6 wt. % Nps

SnO_2 is the preferable material for photocatalytic processes due to its high photosensitivity, but its BG energy (3.6eV) limits its ability to absorb the high-energy UV portion of sunlight, which results in relatively low solar photocatalytic efficiency [213, 394, 395]. Therefore, electronic doping in the lattice sites of SnO_2 by Sb was attempted to change its absorption activity. Increasing the doping level concentration resulted in a variation in the absorption edge of the pure and doped SnO_2 Nps, shifted towards a longer λ , which is more predominant for the 0.6% Sb doped SnO_2 Nps, as shown in Figure 25.

This intense absorption in the region of red light has been assigned to the electronic transfer between two oxidation states [396].

Upon doping SnO_2 with Sb it helped to increase its optical activity. This is somewhat due to the enhanced optical absorption observed upon doping (as shown in the Figure 25). It can be observed from the optical spectra that upon doping, the absorption increased which is prominent in the SnO_2/Sb 0.4 wt. % and SnO_2/Sb 0.6 wt. % samples.

Many studies on TiO_2 about its optical absorption and photocatalytic improvement are based on the doping by anion or cation [397]. Since both regions show optical activity, it justified to study the suitability of phenol photodegradation under UV and visible light irradiation. In Publication I-IV, the enhancement of the optical absorption was observed upon doping with different ions.

Doping SnO_2 with RE metals also improved the photocatalytic activity of the particles. This is partially due to the enhance optical absorption observed upon doping (as shown in the Figure 26 below); which indicated that upon doping absorption increases which is prominent in the SnO_2/La samples

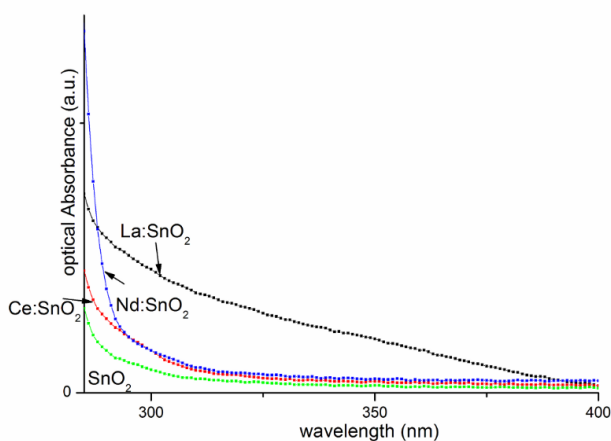


Figure 26: Typical optical absorption of undoped SnO_2 , 0.6 wt. %, Ce doped SnO_2 , 0.6 wt. %, Nd doped SnO_2 and 0.6 wt. %, La doped SnO_2 Nps dried samples collected from a suspension in aqueous media.

In Figure 27 below it is clear that upon doping SnO_2 with I, the photocatalytic activity of the Nps was improved which can be attributed to the increased optical absorption of the SnO_2/I Nps compared to the pure metal oxide (Figure 27).

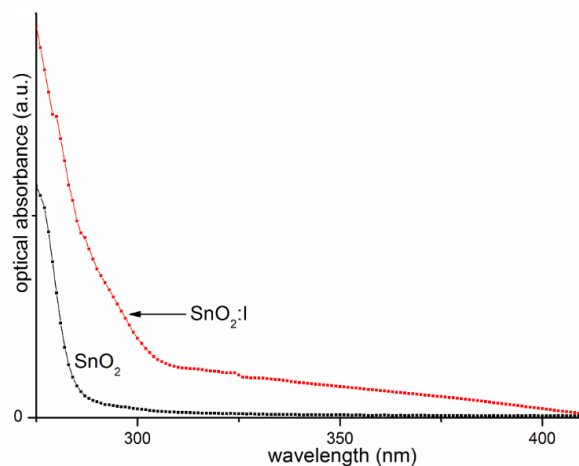


Figure 27: Optical absorption of undoped SnO₂, and 1.0 wt. %, I doped SnO₂ Nps

4.4 Parameters affecting phenol photodegradation in an aqueous solution dispersion of SnO₂

4.4.1 Effect of pH

During the phenol photodegradation formation of several byproducts occur which also lower the pH solution [47]. Many organic compounds are acidic nature when dissolved in solution, in addition, to the surface of the catalyst is also acidic. This behaviour let the pH to put a significant influence on the oxidation potential and determines the charges of the pollutant. In this study the pH is controlled before the irradiation and is not adjusted during the experiment. The effect of changing the pH from (3-8) on the photodegradation of phenol is shown in Figure 28. It is vital that the reaction is done under stable catalyst conditions. Phenol photodegradation showed stable results in the acidic media, no attempts were made to prepare phenol concentrations at higher basic media. It was noticed that all the SnO₂ Nps were insoluble at all pH ranges tested.

Figure 26, shows each 10 ppm phenol standard was adjusted with pH (3, 4, 5, 6, 7 and 8) was separately mixed in the reactor, while the other parameters were kept constant such as catalyst loading of (65 mg/50.00 mL) by using (SnO₂/Ce 0.6 wt. %), reaction

4.4 Parameters affecting phenol photodegradation in an aqueous solution dispersion of SnO₂ 137

time (2-3 h), sampling time (12-13), sample volume (250.00 mL) and inlet air flow 4 L/min.

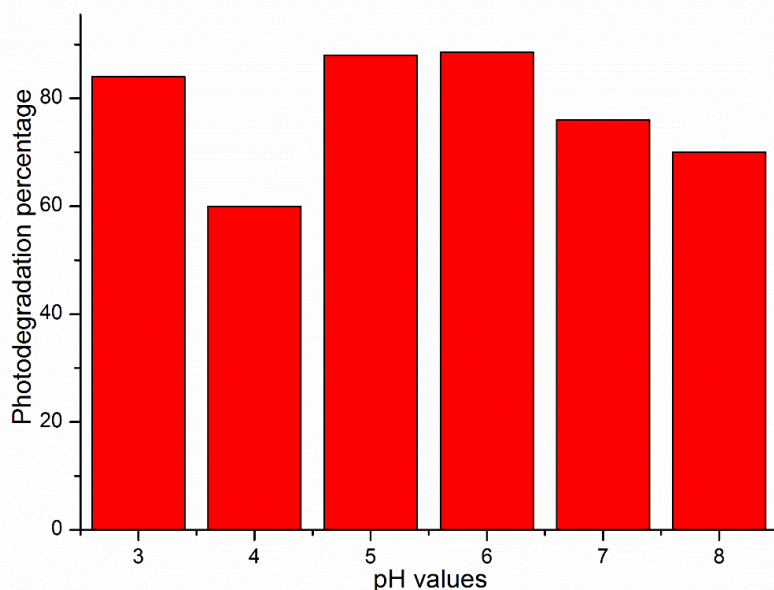


Figure 28: Effect of pH adjusted value on phenol photodegradation rate, (65 mg/50.00 mL) of (SnO₂/Ce 0.6 wt. %), under UV light irradiation, reaction time (2-3 h), sampling time (12-13), sample volume (250.00 mL) and inlet air flow 4 L/min.

Setting the pH of phenol solution at 3 enhanced the degradation rate to 84% but then decreased to 60% at the time of 150 min at pH 4. An increment was noticed in the phenol photodegradation rate in pH from 5-6, this increment reached to 89% at the same irradiation time. Acidic contaminant such as phenol can create an attraction between photocatalyst and phenol molecules, which can facilitate the adsorption of the phenol molecule on the SnO₂ surface resulting in the enhancement of phenol degradation [398]. SnO₂ may be acidic in nature and therefore the pH effect needs to be considered. The pH solution may affect the surface of the photocatalyst and increase the $\cdot\text{OH}$ and enhance its adsorption.

In addition, acidic conditions were more preferable for production of hydrogen peroxide which increase OH⁻ ions and the amount of $\cdot\text{OH}$ also increase. When the $\cdot\text{OH}$ increase,

the chance for $\cdot\text{OH}$ to react with phenol molecule increase and the result is increase in the photodegradation efficiency is noticed. In addition, more pH values (basic) initiate the formation of carbonate ions, these ions are known to be scavengers OH^- ions which decrease the photodegradation rate at alkaline values [53, 377]. Many scientists used lower pH ranges and were found to be beneficial for the degradation of phenolic compounds [399, 400]. Enhanced degradation of phenol under slightly acidic condition has been continuously done by scientists motivated in this subject [400]. On the other hand, if the pH of the reaction mixture falls under a certain threshold, the rate of the reaction mixture decreases considerably.

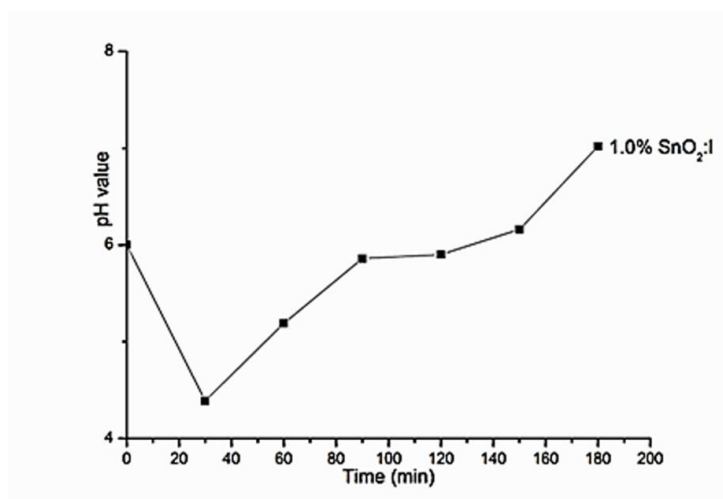


Figure 29: Effect of pH changes as a function of time for (65 mg/50.00 mL) SnO_2/I 1.0 wt. % Nps under UV light irradiation, reaction time (3 h), sampling time (12-13), sample volume (250.00 mL) and inlet air flow 4 L/min.

The effect of initial pH 5.7 of 10 ppm phenol solution with the (65 mg/50.00 mL) SnO_2/I 1.0 wt. % catalyst on the photodegradation of phenol was examined within 3 h reaction time as shown in Figure 29. In the beginning the pH decreased to a minimum pH 4.5, later raised up to values equal to or slightly higher than the initial pH, because more acidic byproducts were being formed and resulted. The phenol photodegradation depended on the formed intermediates and on the compounds mineralized until it rose again to reach pH 7. Many scientists noticed the same behaviour [262], as they shown that organic compounds can be degraded at medium pH and in acidic ranges [208, 399].

4.4 Parameters affecting phenol photodegradation in an aqueous solution dispersion of SnO₂ 139

It is known that the pH optimal degradation falls in between $pK_a < pH$, due to the increase in the electrostatic interaction between the anions of the weak acids and the cations catalyst surface other researchers reported that the photodegradation of chlorophenoxyacetic acid was increased when the pH of the reaction mixture was higher than its pK_a , but below the pH of the point of zero charge (pH_{zpc}) of the nanocomposite. Optimum electrostatic interaction of the deprotonated acid with the positively charged surface of the photocatalyst with higher reaction rates would be continued [401]. When an organic compound is neutral or protonated, its pH is lower than its pK_a value, however, the pH of the solution is greater than its pK_a value, the compound deionized or deprotonated and exists as negatively charge species [402]. The pK_a value is different for every organic dye and the point of zero charge varies for different photocatalysts, so careful control of the reaction mixture is needed and the settings must be optimized [403]

The formation of acidic binary hydroxyl compounds, such as Cat, BQ, HQ, during the photocatalytic degradation of phenol were considered to be the main reason for the pH cycle change. The $\cdot OH$ formed by redox reaction oxidized the conjugate structure of the phenyl ring, yielded carboxylic acids formed via ring cleavage to produce malonic acid, then short chain organic acids such as maleic, oxalic, acetic and formic acids, which lowered the solution pH [47]. Finally, upon continuous oxidation of the carboxylic acids these intermediates are consumed, returning the pH values to normal as initiated. Consequently, a cycle of pH changes occurred and the TOC is finally eliminated by the conversion of the intermediates to CO_2 and H_2O [404].

4.4.2 Effect of initial phenol concentration

The initial concentration of the model pollutant of 100 ppm (phenol) was prepared as explained in section 3.6.3. Initial concentration of the pollutant plays a significant role on the photodegradation process of organic compounds [405]. The photocatalytic degradation of phenol (5-50 ppm) was carried out to study and compare the final solution of phenol samples every 15-30 min within 2-3 h Figure 30.

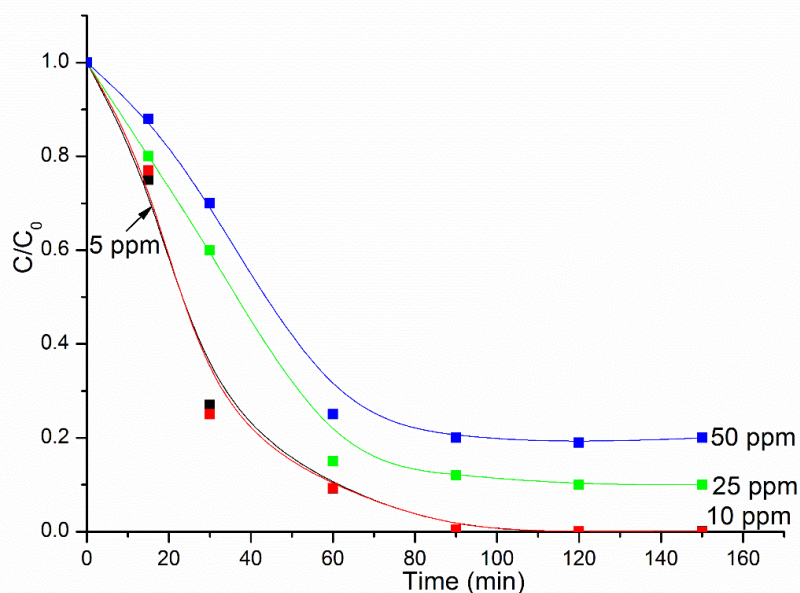


Figure 30: Effect of initial phenol concentration on the photodegradation process for phenol concentrations (5, 10, 25, 50 ppm), catalyst loading (65 mg/50.00 mL SnO₂/Gd 0.6 wt.%), under UV light irradiation, reaction time (2-3 h), sampling time, (12-13), sample volume (250.00 mL), pH of the reaction medium (5.7) and inlet air flow 4 L/min.

Four phenol standards (5, 10, 25, and 50) were prepared to study the effect on the initial pollutant concentration on the photocatalytic degradation efficiency of phenol solutions. Each standard was separately mixed in the reactor, while the other parameters were kept constant: catalyst loading (65 mg/50.00 mL SnO₂/Gd 0.6 wt.%), under UV light irradiation, reaction time (2-3 h), sampling time, (12-13), sample volume (250.00 mL), and pH of the reaction medium (5.7).

The results showed an enhancement in the photodegradation of phenol at 10 ppm but a slight reduction in the catalytic efficiency above 10 ppm. Temperature control in the reactor was set to be 25 °C. Usually, the photodegradation efficiency decreases with increasing contaminant concentration [406, 407]. The large amount of the contaminant will block the light penetration into the pollutant solution and also over supply the active sites. Inundate active sites mean fewer photons would be able to reach the catalyst surface. The lower photodegradation rate of phenol is because the absorbed light by

4.4 Parameters affecting phenol photodegradation in an aqueous solution dispersion of SnO₂ 141

phenol is more than the light absorbed by the SnO₂/Gd 0.6 wt. %. This means that not enough light is available to carry out the photodegradation process [370]. On continuously, more of phenol concentrations accumulate on the catalyst surface active site during the equilibrium absorption, this causes that absorption of $\cdot\text{OH}$ decreases so the amount of $\cdot\text{OH}$ and $\text{O}_2\cdot^-$ decreases. On incessantly of this process, the $\cdot\text{OH}$ decreases, so the chance for $\cdot\text{OH}$ to react with phenol molecules also diminishes. By the end of the route, this reduction lowers the photodegradation efficacy [377, 408]. When using high initial concentration, byproducts are formed and absorbed on the catalyst surface which also react with the oxidant species available [37]. In addition, the byproducts might react with the reducing species such as electrons, resulting in a lower rate of the photodegradation of the contaminant [37, 409]. The results indicated fast degradation of phenol at a concentration of 10 ppm but the degradation of phenol decreased when the initial concentration was above 15 ppm.

4.4.3 Effect of catalyst loading

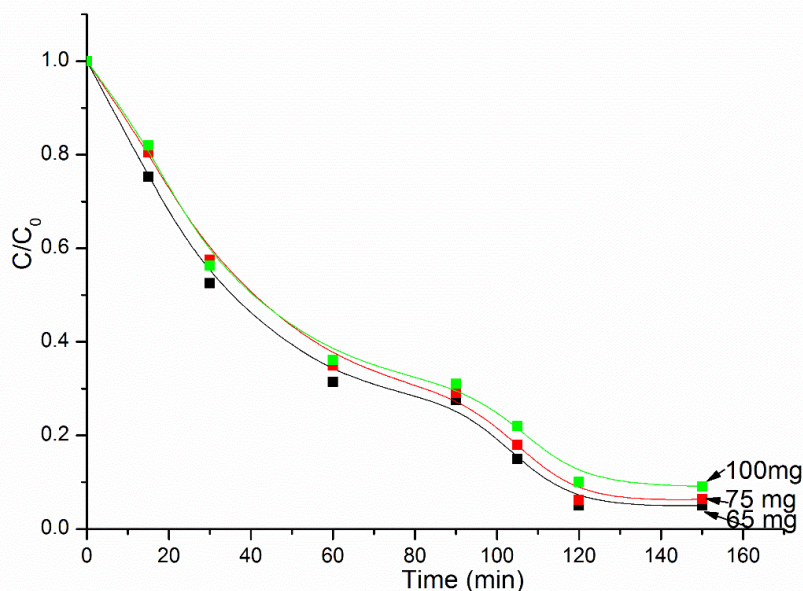


Figure 31: Effect of different catalysts loading 65 mg /50 mL, 75 mg/50 mL and 100 mg/50 mL on the photodegradation process by (0.6 wt. % SnO_2/Nd), each loading has 10 ppm phenol concentration, under UV light irradiation, reaction time (2-3 h), sampling time, (12-13), sample volume (250.00 mL), and pH of the reaction medium (5.7) and inlet air flow 4 L/min.

In this study the amount of catalyst loading by 0.6 wt. % SnO_2/Nd has been carried out. Three equal phenol standards each of 10 ppm with different catalyst loading were prepared such as (65, 75 and 100 mg each in 50 mL of solution) to study the effect of catalyst loading on the photocatalytic degradation efficiency of phenol solutions.

Each standard was separately mixed in the reactor, while the other parameters were kept constant under UV light irradiation, reaction time (2-3 h), sampling time, (12-13), sample volume (250.00 mL), pH of the reaction medium (5.7) and inlet air flow 4 L/min. The photocatalytic degradation of phenol exhibited best results from 56 to 75% at 150 min of irradiation time an increase in the loading decreases the removal rate, which decreases the activity of the catalyst as it shown in Figure 31. That's why 65 mg/50 mL catalyst was optimum dosage for undoped SnO_2 and doped SnO_2 ions and it was used in all the photocatalytic reactions in this study. Photocatalytic degradation rate increases

4.4 Parameters affecting phenol photodegradation in an aqueous solution dispersion of SnO₂ 143

with an increase in the weight of the catalyst up to an optimum loading, presumably by increasing in the surface area available for pollutant adsorption and the number of reaction sites [398, 410]. After the optimum conditions, it decreases, due to the result of light scattering and screening effects [411, 412]. It is also recognized by the optimum conditions loading, the quantity of hydroxyl and superoxide radicals will also increase, so it facilitates the degradation of different organic toxins. On the other hand, a decrease in the photodegradation was noticed at higher loading concentrations. As it mentioned, because increasing in the catalyst loading will prevent light passes through the solution, so it reduces the degradation on the pollutant [413].

4.4.4 Effect of air

It is noticed that air saturated solutions have higher degradation rate, compared to solutions under different conditions. Dissolved oxygen plays a significant role in producing peroxy radicals (superoxide anions) which take apart in producing $\cdot\text{HO}_2^-$ or eliminating to produce $\cdot\text{OH}$ and help to trap the excited CB electron recombination [205, 414]. When the photocatalytic experiments of phenol degradation were carried out without air flow, the results did not show a significant degradation. On the other hand, when all the experiments fixed up by a 4 L/min of an optimum air flow maximum of 90% and above of phenol photodegradation was achieved. For all photocatalytic experiments the inlet air flow of 4 L/min of used.

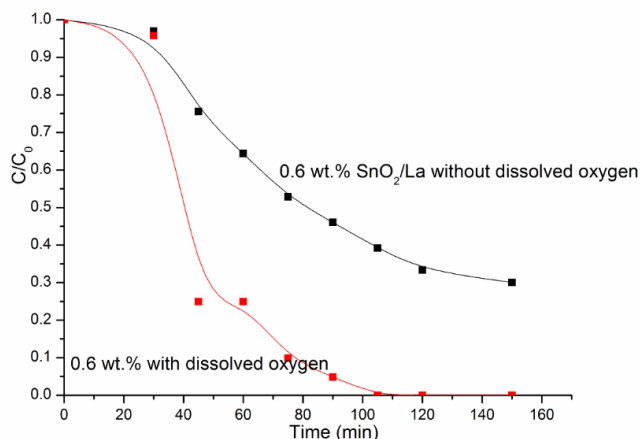


Figure 32: A comparative Figure for 0.6 wt. % of SnO₂/La for effect of dissolved oxygen and without dissolved oxygen at optimum conditions

4.4.5 Light intensity

Light irradiation has an important purpose in the photocatalytic reactions leads to determine the $e^- - h^+$ pairs and initiates the rate of photocatalysis [415]. In fact, the activation of the catalyst depends on irradiation with light of a certain λ is powerfully dependent on its intensity [209, 416-418]. Since SnO₂ has higher activation energy which equivalent to radiation with UV light, by choosing light intensity greater than the activation energy increases the efficiency of the photocatalyst. [419, 420]. When more radiations fall on the surface at higher irradiation intensities, produce more $\cdot\text{OH}$ and increase in the reaction rate of the photocatalytic removal [421-424]. Increase the incident light intensity may increase the excitation of e^- so enhance the degradation rate [425].

4.4.5.1 Light λ

Energy of photons is also of great importance since electrons jump up from CB to a VB by the help of energy's light. Energy of photons is related to its λ , but the overall energy is dependent on its intensity [71]. Because of energy quantization, excitation can only take place when photons of sufficient energy hit the surface of the photocatalyst. A radiation source who has different λ has an intense effect on the photocatalytic reaction

rate [426]. For UV irradiation, the corresponding electromagnetic radiation can be classified according to its emitting λ as UV-A, UV-B, UV-C and vacuum (V) UV. The UV-A range needs an excitation λ starting from 315-400 nm (for a BG 3.1 to 3.94 eV). The UV-B range requires an excitation λ starting from 280-315 nm (for a BG 3.94 to 4.43 eV). The germicidal UV-C range requires higher energy excitation λ from 100-280 nm (for a BG between 4.44 to 12.4 eV) [427]. VUV range $\lambda < 200$ nm and consider to be the most energetic λ between the UV spectrum. The VUV interrelates with O atoms even with minute amount of organic molecules. Due to the high energy these λ exist in vacuum [428].

Normally, the BG in SnO₂ with suitable dopants is smaller than 3.1 eV which renders possible the excitation of the photocatalyst with visible light and guarantees broad application of the semiconductor.

4.5 Photocatalytic degradation

To develop an easy photocatalytic method for phenol photodegradation under undoped SnO₂ and other metals doped SnO₂ catalysts.

The photocatalytic activity of 0.6 wt. % SnO₂/La Nps was observed by photodegradation of phenol (10 ppm) aqueous sample under different light irradiations is shown in Figure 33. Typically 65 mg photocatalyst powder was dispersed in 50 00 mL phenol solution and with the same other conditions such as time (2-3 h), sampling time, (12-13), sample volume (250.00 mL), pH of the reaction medium (5.7) and inlet air flow 4 L/min. The comparison for photocatalytic degradation efficiency of phenol with pure and doped Nps under UV and visible light irradiations showed that the undoped is less active. Generally, the doping Nps exhibited the maximum efficiency under UV against visible light. This observation confirmed that doping with La ions played an improvement role in the SnO₂ structure and increased the activity of SnO₂.

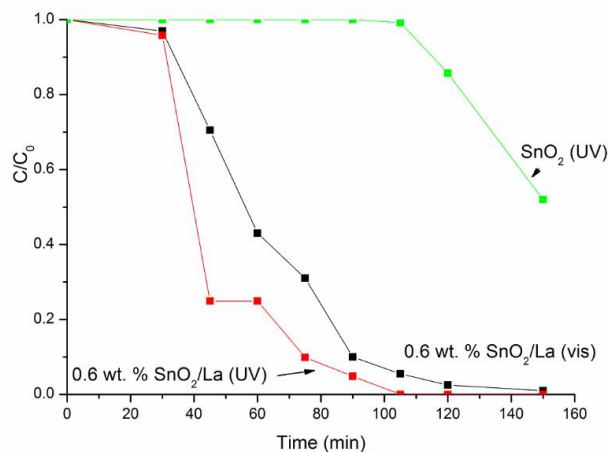


Figure 33: Comparison of photoactivity of 0.6 wt. % SnO₂/La Nps under UV and visible light irradiation at optimum conditions

The investigation was carried on to see the UV light effect with the dark conditions on the undoped SnO₂ and different Nd doped SnO₂. Photocatalytic degradation of 10 ppm of phenol concentration at pH 5.7 with the different experiments under UV light irradiations alone without the catalyst was low. The rest three experiments were done under UV irradiation with the catalyst and the other parameters were kept constant.

Figure 34 plots phenol concentrations in the aqueous sample after UV light illumination, in the presence of photolysis, undoped SnO₂, SnO₂/Nd 0.2 wt.% and SnO₂/Nd 0.6 wt.%.

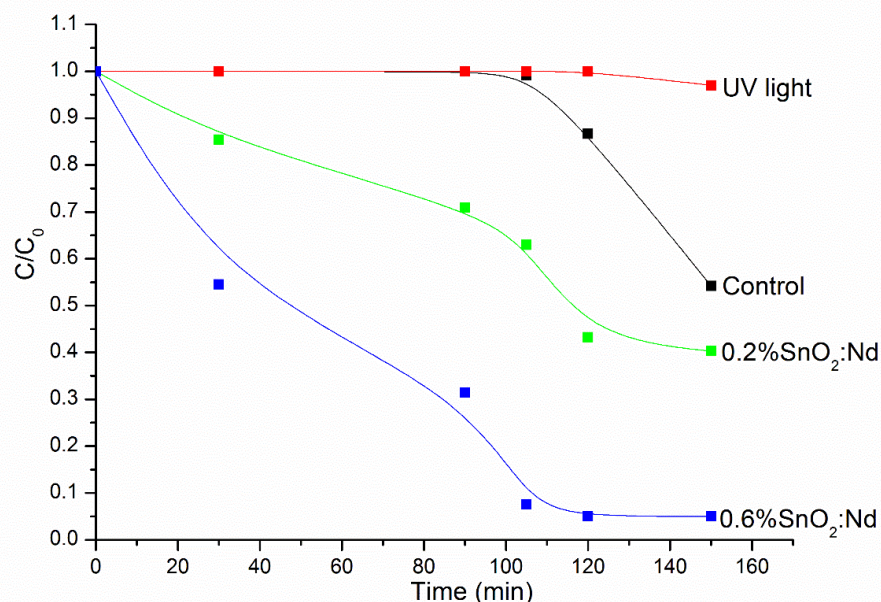


Figure 34: Decrease of phenol concentrations without catalyst UV only, with (65 mg/50.00 mL) of SnO₂ undoped (control), SnO₂/Nd 0.2 wt.% and SnO₂/Nd 0.6 wt.% under UV light irradiation, reaction time (2-3 h), sampling time, (12-13), sample volume (250.00 mL), pH of the reaction medium (5.7) and inlet air flow 4 L/min.

The UV light analysis without the catalyst (photolysis) on phenol photodegradation indicated very little catalytic activity. In the presence of SnO₂ catalyst alone (control) with the UV light, the increase in phenol photodegradation was greater when compared to the system containing UV light only without the catalyst which was almost negligible. The rate of photodegradation with control (undoped SnO₂) Nps was found to be 46%, improved upon doping with SnO₂/Nd 0.2 wt. % to 60% which increased to 95% with SnO₂/Nd 0.6 wt.% after 2.5 h irradiations. So, there was an improvement of about fourfold been observed with SnO₂/Nd 0.6 wt.% Nps.

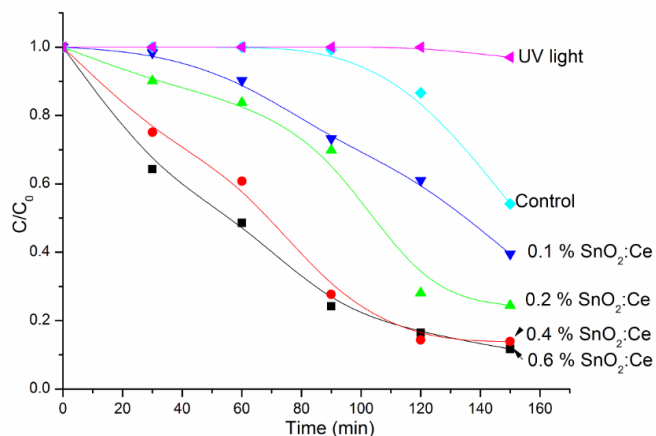


Figure 35: Decrease of phenol concentrations (each 10 ppm) upon (65 mg/50.00 mL) of SnO₂/Ce 0.1 wt.%, SnO₂/Ce 0.2 wt. %, SnO₂/Ce 0.4 wt. % and SnO₂/Ce 0.6 wt. % under UV light irradiation, reaction time (2-3 h), sampling time (12-13), sample volume (250.00 mL), pH of the reaction medium (5.7) and inlet air flow 4 L/min.

The UV-Vis spectra in Figure 35 plots phenol concentration in the aqueous sample after UV light illumination in the presence of a typical Ce doped SnO₂ Nps. The photocatalytic degradation of 10 ppm phenol at pH 5.7, with 65 mg/50 mL of SnO₂/Ce and with four different dopants as (0.1 wt. %, 0.2 wt. %, 0.4 wt. % and 0.6 wt. %) showed also enhancement in the photocatalytic activity but a little bit less efficiency than SnO₂/Nd activity. After 150 min of irradiation 88% of phenol was found to degrade upon using SnO₂/Ce 0.6 wt. %, but with SnO₂/Ce 0.4 wt. %, 86% of phenol photodegradation was clarified. On the other hand, 76% and 61% of phenol photodegradation was exhibited with SnO₂/Ce 0.2 wt. % and 0.1 wt.% respectively as it shown in Figure 35 above.

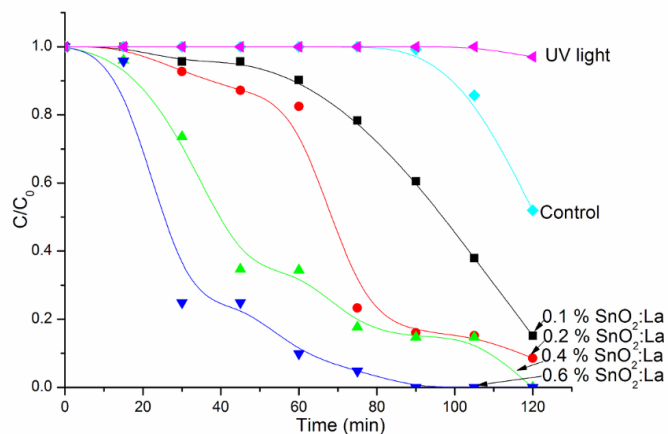


Figure 36: Decrease of phenol concentration (each 10 ppm), upon (65 mg/50.00 mL) of SnO₂/La 0.1 wt. %, SnO₂/La 0.2 wt.%, SnO₂/La 0.4 wt. % and SnO₂/La 0.6 wt. % under UV light irradiation, reaction time (2-3 h), sampling time (12-13), sample volume (250.00 mL), pH of the reaction medium (5.7) and inlet air flow 4 L/min

The UV-Vis spectra in Figure 36 plots phenol concentrations in the aqueous sample after UV light illumination in the presence of SnO₂/La Nps. The photocatalytic degradation experiments of 10 ppm phenol at pH 5.7 and with 65 mg/50 mL SnO₂/La, but with four different dopants as (0.1 wt. %, 0.2 wt. %, 0.4 wt. % and 0.6 wt. %) under UV light irradiation compared with the control. Regarding SnO₂/La the maximum rate of phenol photodegradation was achieved using SnO₂/La 0.6 wt. % reached to 100% photodegradation within 120 min of irradiation, which is almost the highest catalytic activity on phenol in aqueous solution during that photodegradation period with that catalyst. In fact, La doped SnO₂ samples were found to be the most photoactive, since 100 % of phenol was photodegraded for the same irradiation using SnO₂/La 0.4 wt. %, which also reached to 100% photodegradation and within 120 min of irradiation. In addition, SnO₂/La 0.2 and 0.1 wt. % indicated about 91% and 70% of phenol photodegradation rate respectively after 2.5 h.

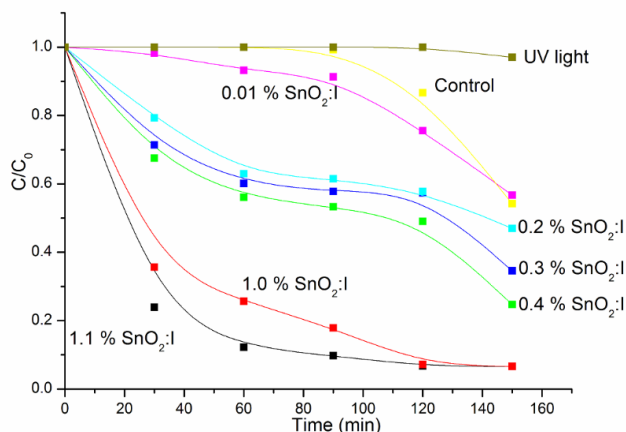


Figure 37: Decrease of phenol concentration each (10 ppm) with 65 mg/50 mL of SnO₂/I, (0.01, 0.1, 0.2, 0.3, 0.4, 0.1 and 1.1 wt.% under UV light irradiation reaction time (2-3 h), sampling time (12-13), sample volume (250.00 mL), pH of the reaction medium (5.7) and inlet air flow 4 L/min

The UV-Vis spectra in Figure 37 shows phenol concentration in the aqueous sample after UV light illumination in the presence of SnO₂/I Nps. The photocatalytic degradation experiments of 10 ppm phenol at pH 5.7 and with 65 mg/50 mL SnO₂/I, but with six different dopants as (0.01 wt.%, 0.2 wt.%, 0.3 wt.%, 0.4 wt.%, 1.0 wt.%, and 1.1 wt.%) under UV light irradiation.

The rate of phenol photodegradation with SnO₂/I 0.01 wt.% and with undoped SnO₂ Nps was found to be 43% and 46%, respectively, but improved upon doping with SnO₂/I 0.2 wt.% to 53% and increased to 75% with SnO₂/I 0.4 wt.% after 2.5 h. Further doping with SnO₂/I 1.1 wt. % did not improve the photodegradation efficiency. Regarding SnO₂/I the maximum rate of phenol photodegradation was achieved using SnO₂/I 1.0 wt. % reached to 93% photodegradation within 150 min of irradiation, which is almost the highest catalytic activity on phenol in aqueous solution during that photodegradation period with that catalyst.

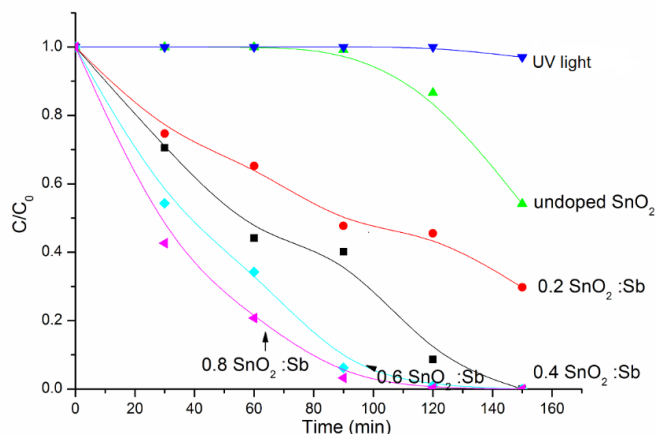


Figure 38: Decrease of phenol concentrations with undoped SnO₂ and SnO₂/Sb (0.2, 0.4, 0.6, 0.8 wt. %) under UV light irradiation with catalyst (65 mg/50.00 mL) reaction time (2-3 h), sampling time, (12-13), sample volume (250.00 mL), pH of the reaction medium (5.7) and inlet air flow 4 L/min

In Figure 38 shows the change in phenol concentration in the aqueous solution upon continued UV light illumination in the presence of doped and undoped SnO₂ Nps. When no catalysts were used, no significant reduction in phenol concentration was observed only about 2% decline was detected after 2.5 h due to the photolysis of phenol. With undoped SnO₂ Nps the photodegradation of phenol was occurred slowly in the initial 1 h with no significant degradation observed. Here it should be noted that during photocatalytic degradation, phenol molecules initially changed to form byproducts such as BQ, Cat and HQ, which upon subsequent oxidation transforms to mineral acids, CO₂ and H₂O. These byproducts formed at the beginning of the photocatalytic reactions also optically absorbed in the similar region as phenol, which would mask the degradation level of phenol in the UV/Vis spectroscopy. As a result, during the initial period of the photocatalytic degradation of phenol using undoped SnO₂ Nps showed non-significant variations in the optical absorption spectrum of phenol was observed as shown in Figure 38, although phenol was degraded by forming other intermediates. However, degradation of phenol was observed to begin immediately under UV light irradiation in the presence of doped SnO₂ Nps. Upon 120 min of UV irradiation, with 0.2 wt. % SnO₂/Sb samples, 55% of phenol photodegradation was observed, while 94% of phenol

degradation was achieved in the presence of 0.4 wt. % SnO_2/Sb . Further enhancement in the degradation process was shown to be about 100% of phenol disappearance when SnO_2/Sb 0.6 wt. % been used. This means that complete mineralization was achieved in the presence of SnO_2/Sb 0.6 wt. % Nps after 120 min.

4.5.1.1 Method development

To improve the photocatalytic efficiency of phenol photodegradation it is essential to practise the degradation under solar light irradiation for simplicity and to overcome the high expenses. In addition, solar light irradiation is an easy process; moreover, to unveil and utilize the UV radiation that is present in the solar spectrum. The natural sunlight as the light source has been used to further study the photocatalytic degradation of phenol.

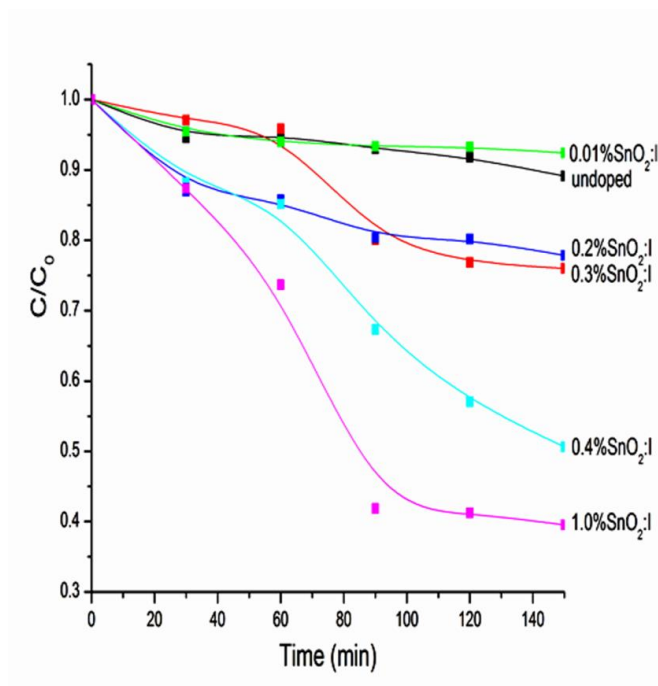


Figure 39: Comparison of the decrease of phenol concentrations degradation with 65 mg/50 mL of undoped SnO_2 and different SnO_2/I (0.01, 0.2, 0.3, 0.4, 1.0 wt.%) Nps, under solar light irradiation, reaction time (2-3 h), sampling time, (12-13), sample volume (250.00 mL), pH of the reaction medium (5.7) and inlet air flow 4 L/min

In Figure 39 no such photocatalytic activities were found in the samples doped with a very small amount as SnO_2/I 0.01 wt.% either by UV as it was explained earlier, or by

solar light irradiation as it is explained here in this section as it exhibited only about 10% photodegradation. The SnO_2/I 0.2 wt. % catalysts under solar light showed better activity than the control undoped SnO_2 samples. The reduction of phenol is about 45% in 2.5 h in the presence of SnO_2/I 0.4 wt. % but increased up to 61% with SnO_2/I 1.0 wt. % Nps under solar light irradiation as it shown in Figure 39.

4.5.2 Phenol photodegradation

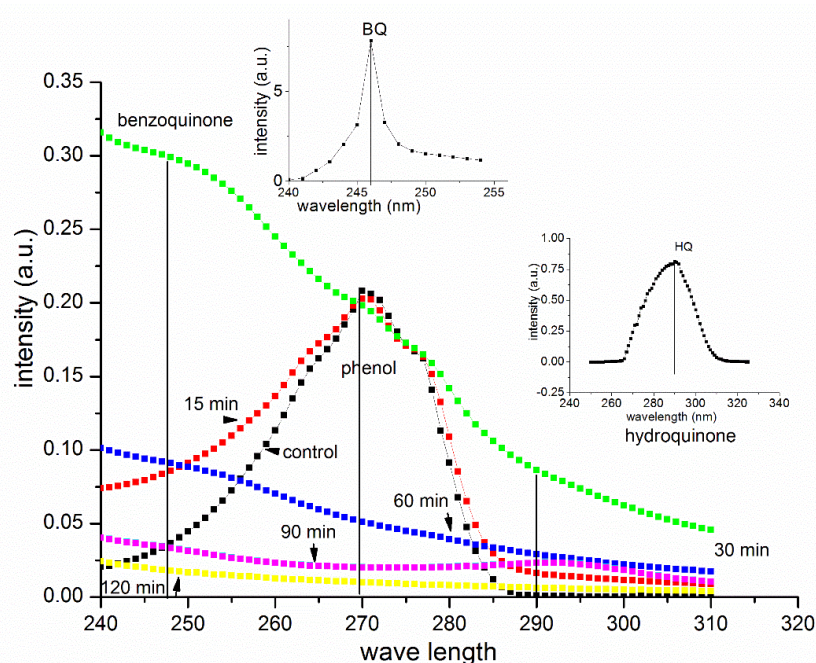


Figure 40: Spectra of phenol photodegradation and reduction in the intensity of 10 ppm phenol peak observed by UV-Vis spectrophotometry in the presence of 65 mg/50 mL of SnO_2/La 0.6 wt. % Nps, under UV light irradiation, reaction time (2-3 h), sampling time, (12-13), sample volume (250.00 mL), pH of the reaction medium (5.7) and inlet air flow 4 L/min.

Since La was the best photoactive, its photocatalytic activity SnO_2/La 0.6 wt. % was examined using phenol. The phenol typical absorption spectrum is characterized by a band at 269 nm attributed to absorption in the aromatic ring.

4.5.2.1 Under UV light irradiation

The UV-Vis spectra obtained for 10 phenol sample with 2 h at pH 5.7 and with SnO₂/La, 0.6 wt. % under UV light irradiation. The adsorption ability of the samples was tested, and it was found that after 30 min in dark conditions, very minimal changes in phenol adsorption were observed. In Figure 40 the absorption spectra of a 10 ppm phenol solution during illumination in the presence of SnO₂/La 0.6 wt. %. UV scans (240-320 nm) used also to investigate different phenol byproducts, also in the Figure the appearance of different phenol byproducts are emerged. Several studies have shown that phenol first undergone to BQ later the ring was opened to form other smaller byproducts such as carboxylic acids [262, 429]. A clear decrease from phenol absorbance band intensity was observed with increasing photoirradiation time within 15 min. An immediate increase at 290 nm absorbance presence of HQ band intensity and much more increase at 246 nm absorbance which is BQ band intensity. A decrease in the phenol absorbance band also noticed. This phenomenon can be associated with the degradation of phenol intermediates, HQ and BQ, respectively, within 15 min of photoirradiation. After 30 min of light irradiation, the phenol absorbance band reduced, but a concurrent increase and broadening of the 290 nm band and a rising increment with the broadening of the 246 nm band was observed. After 60 min of irradiation, the characteristic peak at 290 nm reduced, and the intensity of 246 nm peak decreased with the disappearance of the phenol peak. After 90 min of irradiation, it was clear that all phenol was degraded and also the formed intermediates are being further degraded. The degradation as observed from the optical spectroscopy point of view is different from the information gained using chromatography, as the extinction coefficients play an important part in the final optical absorption of the byproducts. Considering BQ, it was found that it absorbs nearly 10 times more than phenol around 269 nm, which is the peak absorption of phenol. Thus the formation of byproducts would mask the degradation level of phenol if only optical spectroscopy was used. The analysis in UV-Vis spectroscopy would not render a complete picture of the phenol degradation process, thus most of the subsequent discussions are much based on chromatographic studies.

Table 17: Comparison of phenol degradation after 2.5 h of irradiation with various dopants

Catalyst-Sample	% of Phenol photodegradation by UV-Vis at 120 °C analysis	% of Phenol photodegradation by UV-Vis at 150 °C analysis
No Catalyst	-	3%
Pure SnO ₂	13%	46%
0.01% SnO ₂ /I	24%	43%
0.1% SnO ₂ /Ce	39%	61%
0.1% SnO ₂ /La	60%	70%
0.2% SnO ₂ /I	42%	53%
0.2% SnO ₂ /Nd	57%	60%
0.2% SnO ₂ /La	85%	91%
0.2% SnO ₂ /Ce	72%	76%
0.2% SnO ₂ /Sb	55%	70%
0.3% SnO ₂ /I	43%	65%
0.4% SnO ₂ /Sb	94%	99%
0.4% SnO ₂ /I	51%	75%
0.4% SnO ₂ /La	100%	100%
0.4% SnO ₂ /Ce	86%	86%
0.6% SnO ₂ /Nd	95%	95%
0.6% SnO ₂ /La	100%	100%
0.6% SnO ₂ /Ce	84%	88%
0.6% SnO ₂ /Sb	100%	100%
1.0% SnO ₂ /I	93%	93%
1.1% SnO ₂ /I	93%	93%

Table 17 compares the photocatalytic degradation of phenol in the presence of various catalysts, where phenol photodegradation was measured using UV-Vis spectroscopy. In a control experiment, the photodegradation of phenol was examined without adding the catalyst, there was no significant reduction in the phenol concentration was observed and only 3% reduction was detected after 2.5 h. It is noticed from the Table 17 that at 120°C the photodegradation rate of phenol was 24% for SnO₂/I 0.01 wt. %, this was

higher than the photodegradation rate of the control 13% at 120°C, but raised for undoped SnO₂ to 46% at 150°C, and reduced for SnO₂/I 0.01 wt. % to 43%.

Under UV light irradiation technique, 86% of phenol photodegraded with SnO₂/Ce 0.6 wt. % samples after 120 min irradiation, but with SnO₂/Nd 0.6 wt.% it reached to 95% and gave about 100% with SnO₂/La 0.6 wt.%. Results of photocatalytic activity upon doping the catalyst with SnO₂/Nd 0.2 wt. %, showed 57%, enhanced to 95% with SnO₂/Nd 0.6 wt. % demonstrated an improved activity of about fourfold in Nd³⁺ doping.

4.5.2.2 Under solar light irradiation

Table 18: Comparison of phenol photodegradation after 2.5 h of solar irradiation

Catalyst	Phenol photodegradation
Undoped	11%
SnO ₂ /I 0.01 wt. %	8%
SnO ₂ /I 0.2 wt. %	22%
SnO ₂ /I 0.3 wt. %	24%
SnO ₂ /I 0.4 wt. %	50%
SnO ₂ /I 1.0 wt. %	61%
SnO ₂ /Sb 0.6 wt. %	95%

Table 18 shows a comparison of two used catalysts for 10 ppm phenol aqueous solution, at pH 5.7 photodegradation under solar light irradiation and inlet air flow 4 L/min. The results showed that the reduction of about 61% within less than 2.5 h with SnO₂/I 1.0 wt. %, but effectively >95% of phenol photodegradation reduction by doped SnO₂/Sb 0.6 wt. %. All the natural sunlight experiments were conducted on full sunny days, when the incident power of the sunlight was measured to be between 80 to 90 kW/m² and the other parameters kept fixed.

Figure 41 showed that within 150 min of visible light irradiation the 10 ppm phenol solution in water was photodegraded by 96-99%, thus demonstrating that SnO₂/Gd Nps are efficient visible light photocatalysts. Concerning with SnO₂/Gd 0.4 wt.%, 93% of phenol photodegraded at 120 min. but > 94% and 96% of phenol photodegraded with SnO₂/Gd 0.4 wt.% at 120 and 150 min or as it indicated in the Figure.

To explore the photocatalytic activity of undoped and doped SnO₂ Nps, the degradation of phenol under artificial UV, visible, and natural sunlight was investigated. The photocatalytic activity of SnO₂ was evaluated through comparison with undoped SnO₂ under the same experimental conditions. It is clearly observed from the previous Figures that the photocatalytic activity of the different doped SnO₂ is higher than the undoped SnO₂ under the UV, visible and sunlight irradiations.

SnO₂/Gd Nps showed 99% degradation of phenol under visible light irradiation more than undoped.

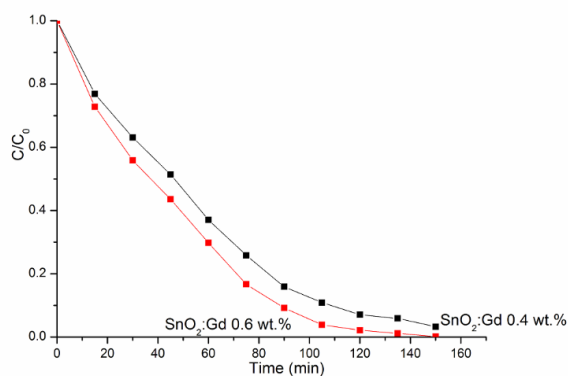


Figure 41: Comparison of the decrease of phenol concentrations degradation with 65 mg/50 mL of SnO₂/Gd 0.4 wt. % and SnO₂/Gd 0.6 wt. % Nps, under visible light irradiation, reaction time (2-3 h), sampling time, (12-13), sample volume (250.00 mL), pH of the reaction medium (5.7) and inlet air flow 4 L/min

4.5.2.3 Under visible light irradiation

Under UV irradiations the maximum percent photodegradation of phenol for undoped SnO₂ of 46% was observed after 150 min, whereas in the presence of 0.4 wt.% SnO₂ /La showed complete 100% photodegradation of phenol within 120 min only. SnO₂ /La was found to be the highest catalytic activity on phenol, the most photoactive, since 120 min of irradiation was needed to accomplish complete photodegradation of phenol.

The effectiveness of SnO₂/Gd is clearly observed for the photodegradation of phenol under visible light. About 99% degradation of phenol 10 mg/L was achieved after 150 min when 0.6 wt. % SnO₂/Gd was applied. Undoped SnO₂ showed only 15% of the same concentration of phenol degradation after 150 min of visible light.

4.6 TOC removal during phenol degradation (TOC)

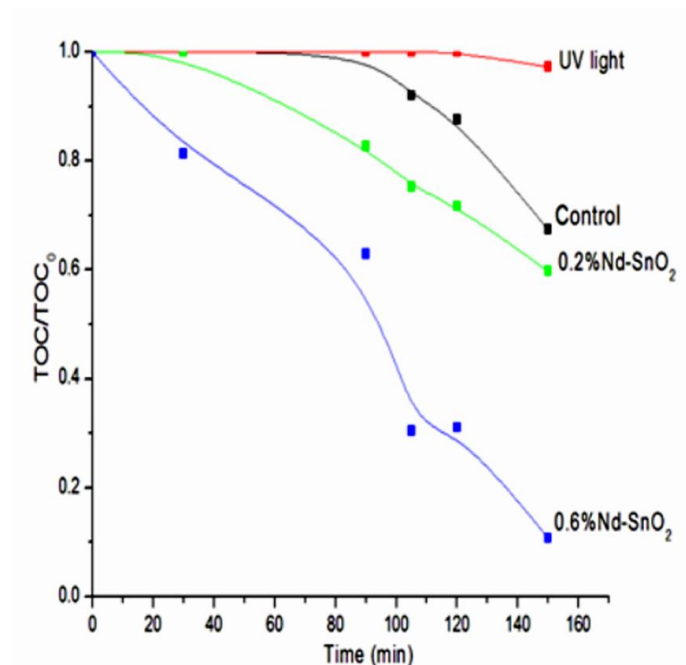


Figure 42: TOC removal from phenol solutions during 2.5 h of photocatalytic degradation by photolysis, undoped SnO₂, and SnO₂/Nd (0.2 and 0.6 wt. %), under UV light irradiation, reaction time (2-3 h), sampling time, (12-13), sample volume (250.00 mL), pH of the reaction medium (5.7) and inlet air flow 4 L/min

In order to determine the degree of mineralization reached during the photocatalyst experiments, the change of the total organic carbon (TOC) is measured. Nine to eleven samples in each test were collected at time intervals of 15 min up to 180 min and then analysed for TOC concentration.

TOC removal spectra of photolysis with UV light only, undoped and SnO₂/Nd (0.2 and 0.6 wt. %). A 10 ppm phenol solution with catalyst loading (65 mg/50.00 mL), reaction time (2-3 h), sampling time, (12-13) and sample volume (250.00 mL). It is obvious from Figure 42 that phenol degradation with SnO₂/Nd 0.2 wt. % is higher than the control, since it gave 28% of phenol mineralization in the presence of SnO₂/Nd 0.2 wt. % compared to 12%, but it jumped to 70% of TOC removal in the presence of SnO₂/Nd 0.6 wt. % and within 120 min of irradiation time. It can be seen from the Figure 43 that TOC reduced by increasing the time of UV irradiation.

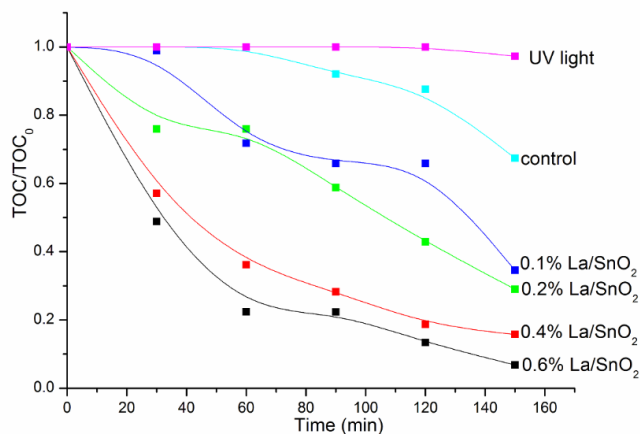


Figure 43: TOC removal from phenol solutions during 2.5 h of photocatalytic degradation by SnO₂/La (0.1 0.2 0.4 and 0.6 wt. %) under UV light irradiation, reaction time (2-3 h), sampling time, (12-13), sample volume (250.00 mL), pH of the reaction medium (5.7) and inlet air flow 4 L/min

TOC values remained high even after 150 min of irradiation time; the amount of phenol removal was about 40% and 89% for SnO₂/La 0.2 and 0.6 wt. % respectively.

TOC determined in high level even after the aromatic byproducts were totally removed [430]. It was also reported that the carboxylic acid are very difficult to be oxidized to CO₂ at the beginning of the reaction [431]. The results of TOC removal shown about 87% of TOC mineralization was observed to occur after 120 min irradiation with SnO₂/La 0.6 wt. %, while 93% mineralization was observed to occur after 150 min irradiation with the same catalyst.

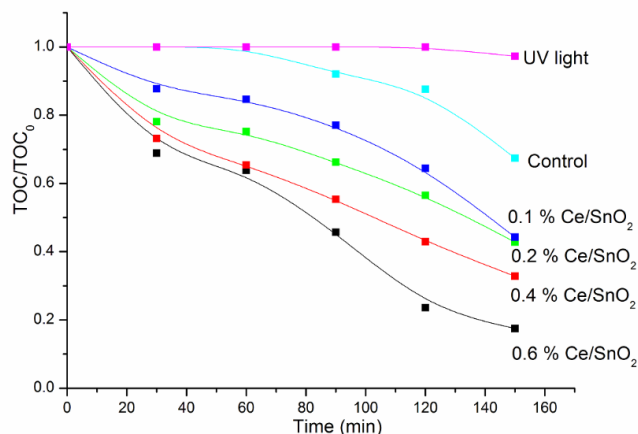


Figure 44: TOC removal from phenol solutions of 10 ppm concentrations during 2.5 h of photocatalytic degradation by SnO₂/Ce (0.1, 0.2, 0.4 and 0.6 wt. %) under UV light irradiation, reaction time (2-3 h), sampling time, (12-13), sample volume (250.00 mL), pH of the reaction medium (5.7) and inlet air flow 4 L/min

TOC values for catalyst changed during the study, which revealed that degradation of phenol was not complete at one stage and the formed organic compounds were still found in every stage until mineralized.

TOC values for catalysts were found to change during the study, which is understandable since degradation of phenol takes some time. It is well known that phenol photodegradation led to the formation of a mixture of byproducts such as Cat, BQ, Res, HQ, and some of the other intermediates as it shown in Figure 40, which further react with $\cdot\text{OH}$. Therefore, complete phenol degradation to TOC conversion is not easily detected upon a short irradiation time and with a small amount of catalyst. For Ce doped SnO₂ different doped SnO₂/Ce (0.1, 0.2, 0.4 and 0.6 wt. %), used to compare 10 ppm of phenol photodegradation up to 150 min of irradiation at pH 5.7, under UV light irradiation. With SnO₂/Ce 0.6 wt. % samples, after 150 min irradiation 83% of phenol was found to be removed, while 67%, 57% and 56% of phenol concentrations were removed at the same irradiation time with SnO₂/Ce 0.4, 0.2, and 0.1 wt. % respectively.

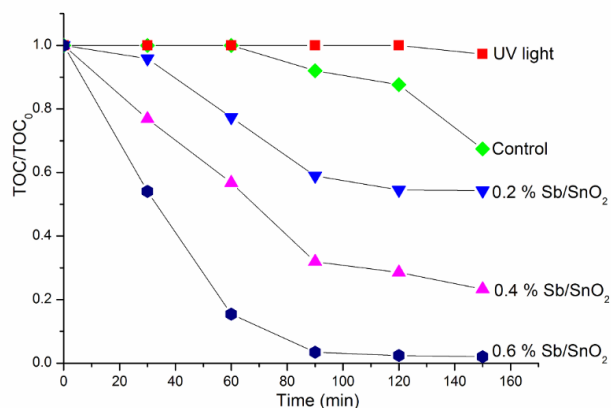


Figure 45: TOC removal from phenol solutions during 2.5 h of photocatalytic degradation by photolysis, SnO₂ [undoped (control)] SnO₂/Sb, (0.2, 0.4 and 0.6 wt. %) under UV light irradiation, reaction time (2-3 h), sampling time, (12-13), sample volume (250.00 mL), pH of the reaction medium (5.7) and inlet air flow 4 L/min

Figure 45 shows that with SnO₂/Sb 0.6 wt. % Nps, 99 % of TOC was found to be removed, for 10 ppm phenol at pH 5.7 after 150 min under UV light irradiation (8 W). 77 % of phenol removal achieved in the presence of SnO₂/Sb 0.4 wt. %, and 46% of phenol mineralization in the presence of SnO₂/Sb 0.2 wt. % during the same period. The fast reduction in TOC results after the 0.6 wt. % Sb doping indicated that the organic carbon is rapidly removed from the solution. For the undoped samples only 32% TOC was removed upon UV irradiation for 2 h as shown in Figure 45.

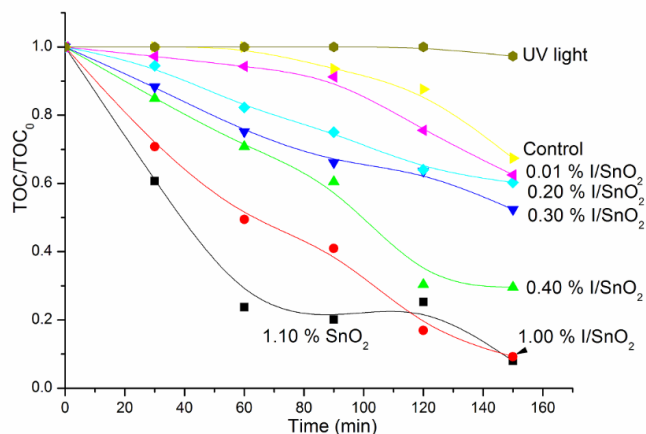


Figure 46: Comparison of the decrease of phenol degradation with undoped and SnO₂/I (0.01, 0.2, 0.3, 0.4, 1.0 and 1.1 wt.%) under UV light irradiation, reaction time (2-3 h), sampling time, (12-13), sample volume (250.00 mL), pH of the reaction medium (5.7) and inlet air flow 4 L/min

Figure 46 shows no change in TOC was observed when the UV irradiation was carried out without any photocatalyst with the parameters. A maximum rate of phenol removal 83% was achieved using SnO₂/I 1.0 wt. % Nps, but only 12% of TOC mineralization was achieved with control SnO₂ upon irradiation for 120 min. Mineralization of about 91% within 150 min by UV light irradiation with 1.0 wt. % catalysts, compared to only 33% TOC reduction observed with the control catalyst, which has almost the highest catalytic activity on phenol in water solution during the photodegradation period as it shown in Figure 46. On further doping did not show better improvement in photodegradation characteristics, because the relative density of SnO₂ decreases. Less activity in samples using SnO₂/I 1.1 wt. % would scatter the light to decrease the absorption by SnO₂ [385].

The comparison of rates with SnO₂/I 1.0 wt. % was about 91%, but with SnO₂/I 1.1 wt. % was about 92% with just more by 1% and SnO₂/I 0.4 wt. % gave a rate about 77% at 150 min irradiation time.

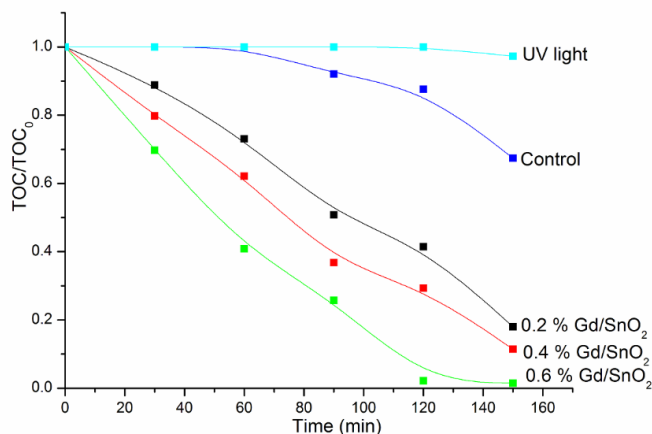


Figure 47: TOC removal from 10 ppm phenol solutions during 2.5 h of photodegradation upon 65 mg/50 mL of SnO₂/Gd (0.6, 0.4 and 0.2 wt.%), under solar light irradiation reaction time (2-3 h), sampling time, (12-13), sample volume (250.00 mL), pH of the reaction medium (5.7) and inlet air flow 4 L/min

Regarding to TOC removal in Figure 47, the process exhibited the highest mineralization rate indicated the combination of 65 mg/50 mL of SnO₂/Gd (0.6 wt. %) with solar light irradiation of 10 ppm phenol at pH 5.7. In this treatment, achievement of phenol removal reached to about > 95% of TOC reduction after 120 min of treatment. Complete mineralization was achieved after 150 min of treatment. The reduction in TOC generally followed the same trend observed above for phenol degradation as reported earlier with UV-Vis spectroscopy. In the case of lower SnO₂/Gd 0.2 wt. %, the TOC diminution was slower in the initial stages, attained a higher degree of mineralization, during the second h of treatment reached with TOC removal up to 82% after 150 min of irradiation. However, when SnO₂/Gd 0.4 wt. % was used, its degree of mineralization increased up to 89% after 150 min of photoirradiation. Upon doping with SnO₂/Gd, the TOC mineralization of phenol raised from 32% with the control SnO₂ to 99% with SnO₂/Gd 0.6 wt. %. From the previous results it can be reported that a threefold improvement in phenol removal was gained, when Gd was doped SnO₂ Nps at 150 min or as it showed in Figure 47.

Table 19 compares the photocatalytic degradation of phenol in the presence of various catalysts, measured using a TOC analyser. Percentages of TOC removal for I were as follows: After 120 min of irradiation with 1.0 wt. % SnO₂/I samples were about 83 %, while with 1.1 wt. % SnO₂/I only 75 % was achieved in the same irradiation time. After 150 min of irradiation with 1.1 wt. % SnO₂/I catalyst, 92% mineralization was observed, compared to 91.0% with 1.0 wt. % 67% with 0.4 wt. %, 46% of phenol mineralization was observed with 0.3 wt. % SnO₂/ I, and 33% with the undoped catalyst during the same period of irradiation.

Table 19: Comparison of photocatalytic performance of different doped SnO₂ Nps on phenol degradation

Catalyst-Sample	% of Phenol photodegradation by TOC removal at 120 °C	TOC removal at 150 °C
No Catalyst	-	3 %
Control	12%	32%
0.01% SnO ₂ /I	24%	38%
0.1% SnO ₂ /Ce	36%	56%
0.1% SnO ₂ /La	34%	65%
0.2% SnO ₂ /I	36%	40%
0.2% SnO ₂ /Nd	28%	40%
0.2% SnO ₂ /La	57 %	71%
0.2% SnO ₂ /Ce	44%	57%
0.2% SnO ₂ /Sb	46%	46%
0.3% SnO ₂ /I	37%	48%
0.4% SnO ₂ /Sb	72%	77%
0.4% SnO ₂ /I	70%	70%
0.4% SnO ₂ /La	81%	84%
0.4% SnO ₂ /Ce	57%	67%
0.6% SnO ₂ /Nd	70 %	89%
0.6% SnO ₂ /La	87%	93%
0.6% SnO ₂ /Ce	76%	83%
0.6 % SnO ₂ /Sb	98%	99%
1.0% SnO ₂ /I	83%	91%
1.1% SnO ₂ /I	75%	92%

A comparison of TOC removal with SnO₂/Ce 0.6 wt. % gave about 76%, but phenol degradation with SnO₂/Ce 0.6 wt. % gave 84% indicated about 8.0% lower of TOC removal than in UV-Vis degradation at 120 min. On the hand, a TOC removal of about 83% of phenol removal showed at 150 min compared to 88% of phenol degradation for the same catalyst which showed only 5% reduction at 150 min as it indicated in Table 19. Phenol removal evaluated from TOC measurements about 76% SnO₂/Ce 0.6 wt. % was 11% less when compared with SnO₂/La 0.6 wt. % as it showed about 87% after 2 h Table 19. This confirms that the synthesized Nps are an effective catalysts in degradation and mineralization of phenol upon UV irradiation light.

It was found from several studies reported that titania doped RE metal showed the highest photocatalytic activity because of its ability of higher absorption sites, increase of the surface area measured by BET, decrease of crystallite size which led to the prevention of $e^- - h^+$ recombination [238, 432].

4.7 Intermediate products of phenol photodegradation

4.7.1 HPLC separation technique

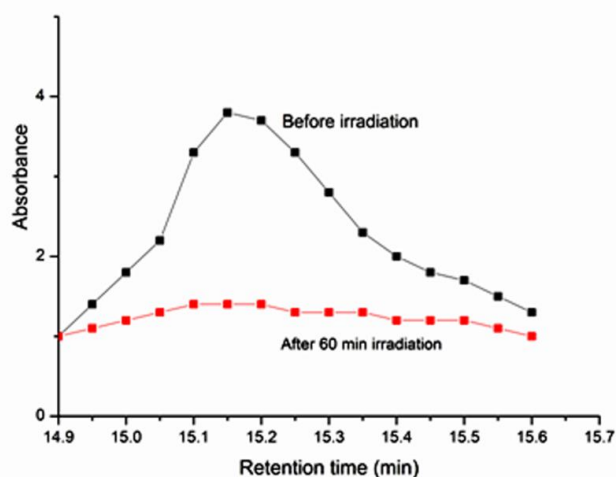


Figure 48: Spectra of 10 ppm phenol photodegradation before and after 60 min UV light irradiation upon 65 mg/50 mL of SnO₂/Ce 0.6 wt. %, reaction time (2-3 h), sampling time, (12-13), sample volume (250.00 mL), pH of the reaction medium (5.7) and inlet air flow 4 L/min

In fact, UV-Vis spectroscopy did not render a correct picture of the phenol degradation process, thus the rest subsequent discussions are based on chromatographic studies such as (HPLC, GC and CE).

Regarding HPLC is a technique of separation used for qualitative and quantitative analysis. Through the photocatalysis experiments, the pellucid and filtered solutions before and after irradiation were analyzed by liquid chromatography LC.

HPLC technique was applied to analyse the 10 ppm of phenol sample during the photodegradation process by SnO_2/Ce 0.6 wt. % Nps under UV light irradiation at pH 5.7 to set up the HPLC parameters for 1 h. It can be observed from Figure 48 that the phenol concentration in the aqueous reduced to zero. The results showed that phenol was effectively removed upon UV light irradiation when compared to the content of phenol by HPLC before irradiation as shown in Figure 49.

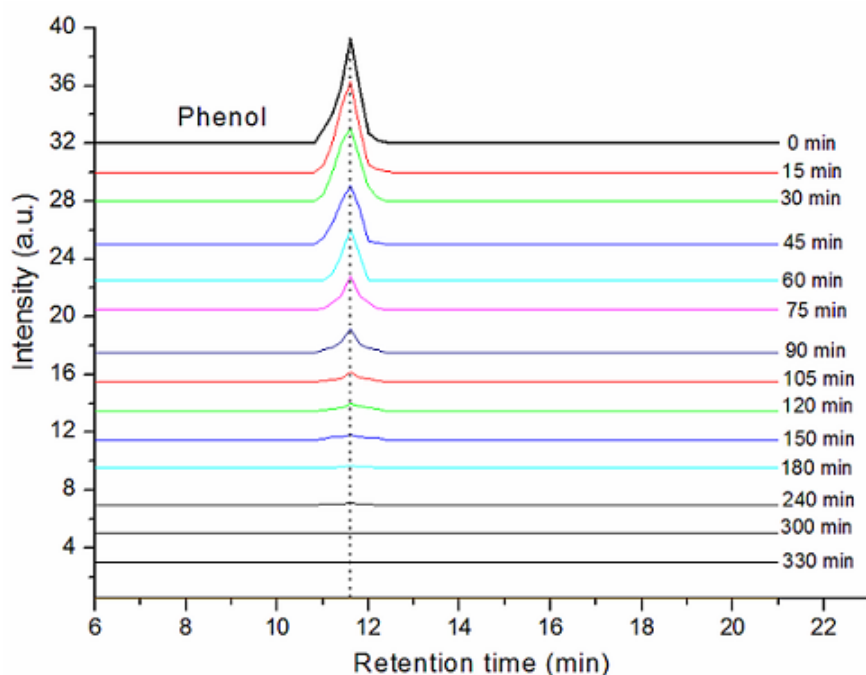


Figure 49: Comparison of the decrease of phenol concentrations with 0.6 wt. % SnO_2/Sb photocatalysis under solar light irradiation as measured by monitoring the phenol peak in HPLC

Figure 50 shows that phenol successfully degraded upon solar irradiation for 3 h, with the appearance of different fragments. Upon photodegradation of 10 ppm phenol

produced several aromatic intermediates observed in HPLC. The existence of carboxylic acid intermediates in the reaction was identified after 30 min of solar irradiation. These different fragments suggested that the structure of benzene ring was destroyed to form carboxylic acid intermediates through photochemical degradation by SnO₂/I 1.0 wt. % Nps as is shown in Figure 50.

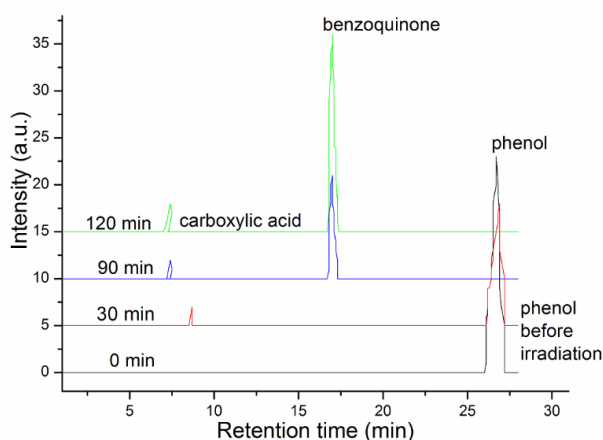


Figure 50: 10 ppm of phenol photodegradation analysed by HPLC upon effect of 65 mg/50 mL of SnO₂/I 1.0 wt. % Nps by solar irradiation light at (0, 30, 90 and 120 min), reaction time (2-3 h), sampling time (12-13), sample volume (250.00 mL), pH of the reaction medium (5.7) and inlet air flow 4 L/min

Intermediates such as Cat, Res and some acyclic compounds, like oxalic acid, formic acid, maleic acid and fumaric appeared but the results are not shown in this experiment. It was found that phenol was effectively degraded by solar light irradiated within 2.5 h. The results indicated that the synthesized I doped SnO₂ Nps is an effective catalyst in degradation and mineralization of phenol upon solar light irradiation.

In fact, the degradation of phenol in water, followed by the formation of many byproducts, some of the intermediates formed during phenol degradation in water could be even more toxic than phenol itself. Short-term exposure could cause irritation of the respiratory tract and muscle twitching, while longer term exposure could cause damage to the heart, kidneys, liver, and lungs.

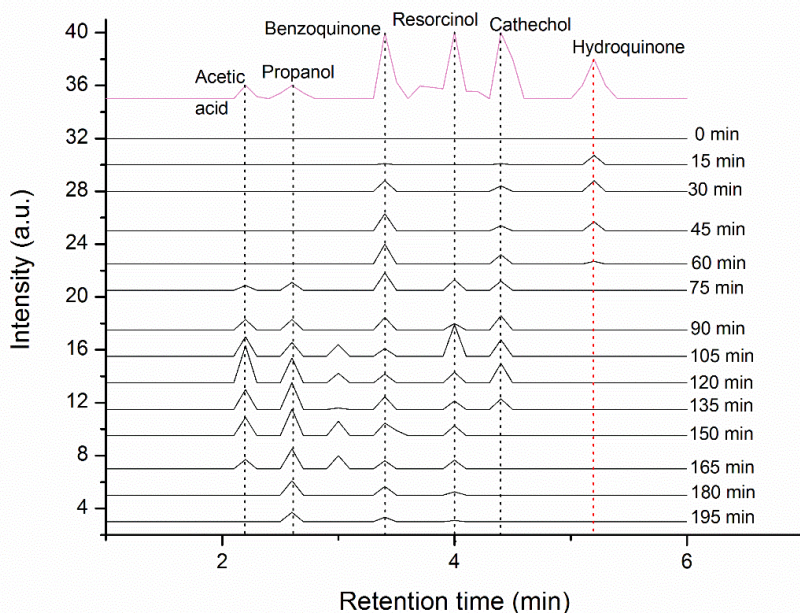


Figure 51: Evolution of different intermediates on 10 ppm phenol concentration detected by HPLC upon 65 mg/50 mL of SnO_2/Sb 0.6 wt. % under solar light irradiation, reaction time (2-3 h), sampling time (12-13), taken at (0, 15, 30, 45, 60, 75, 90, 105, 120, 135, 150, 165, and 180 minutes), sample volume (250.00 mL), pH of the reaction medium (5.7) and inlet air flow 4 L/min

There is plenty of evidences that phenol is first oxidized to BQ and later the ring is broken to form other intermediates [404]. Intermediates were obtained in the order of Cat, Res, and HQ. The identification and quantification of the byproducts may help in approximating and suggesting the reaction route. The main intermediates appearing in the samples, such as BQ, Res, Cat, HQ, AA, and 2-P were collected at different irradiation times as shown in Figure 51.

Several aromatic intermediates could be separated, such as BQ, Cat, Res and some acyclic compounds, including oxalic acid, formic acid, maleic acid and fumaric acid as it has been described above.

During the photocatalysis experiments process, results of 10 ppm phenol upon using 65 g/50 mL of SnO_2/Sb 0.6 wt. % Nps at pH 5.7 under solar light irradiations for 2.5

h. The observed formation of HQ, BQ, Cat, in the first 60 min of the photocatalytic experiment as shown in Figure 51, endorsed the photodegradation of phenol under the natural sunlight. At the beginning of the process, HQ and Cat will compete with each other to produce BQ, which can be degraded in the initial 30 min of the photocatalytic degradation. On the continuation of the photocatalytic process aliphatic intermediates such as (AA and 2-P) appeared in the reaction mixture after 60 min of the irradiation time. This appearance suggested that the structure of benzene ring was destroyed. This was proposed to form carboxylic acid intermediates through photocatalytic degradation of phenol by SnO₂/Sb 0.6 wt. % Nps.

4.7.1.1 Method development

As in publication 1 and 2 the analyses were carried out using different conditions according to the treated molecule and the studied step, but the separations of the intermediates were coming late which consume solutions, time and effort.

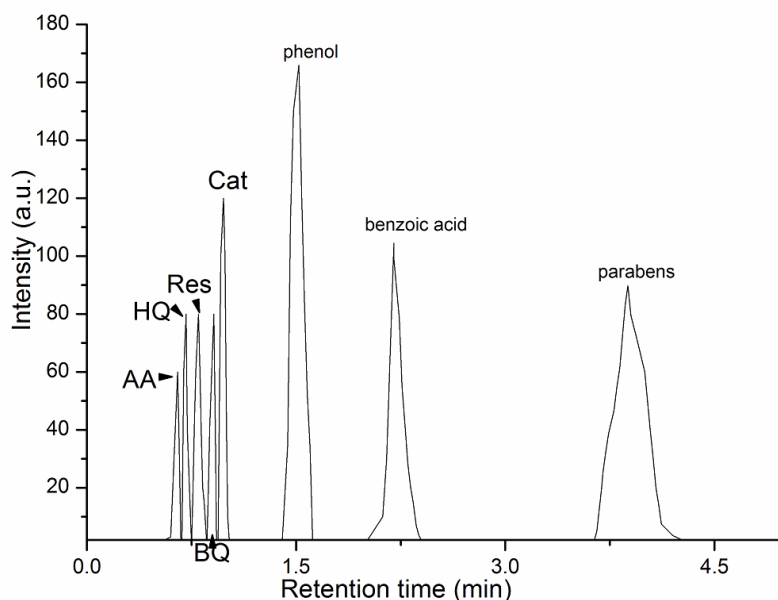


Figure 52: Separation of (10 ppm AA, 10 ppm HQ, 10 ppm Res, 10 ppm BQ, 10 ppm Cat, 10 ppm phenol, form 10 ppm benzoic acid and 10 ppm parabens (methyl paraben) mixtures observed by (HPLC) mobile phase (45% CH₃OH + 55% H₂O). Abbreviations; acetic acid; AA:hydroquinone; HQ: Resorcinol; Res: catechol; Cat.

When using HPLC, it is essential that the analyses remain repeatable and reliable and cost less effort either by using less chemicals or less time and less charge.

In this study, it was possible to separate phenol byproducts from the solutions during photocatalysis, using different techniques. The intermediates were quantified by HPLC using a simple reverse HPLC phase. The simple procedure was improved and the retention time was cut down from 25 min at the beginning of the experiment until reaching to 12 min and finally it was manageable to separate phenol samples with benzoic acids and parabens (methyl and ethyl parabens) in just less than 5 minutes as it is shown in Figure 52.

Thus, it was possible to save solvents, energy and time; this procedure took less than 5 minutes as shown in Figure 52. Since the running time was short, it took only 4 min. In

another run 10 ppm phenol was irradiated upon using 65 mg/50 mL of SnO₂/La 0.6 weight%. At pH 5.7 under solar light irradiation. Simple 50 x 4.6 mm monolithic column could separate parabens, benzoic acid, phenol, BQ, Cat, Res, HQ, AA, and 2-P from phenol photodegradation with other aliphatic and carboxylic acid intermediates (such as oxalic acid, formic acid maleic acid and fumaric acid, but the results of these rest intermediates are not shown). The waste from the mobile phase was also not plenty. The flow rate was 1 mL/minutes in the starting of the procedure and it was cut down to 0.4 which also save a lot of waste and time, so it was possible to reduce the waste and cut down the cost.

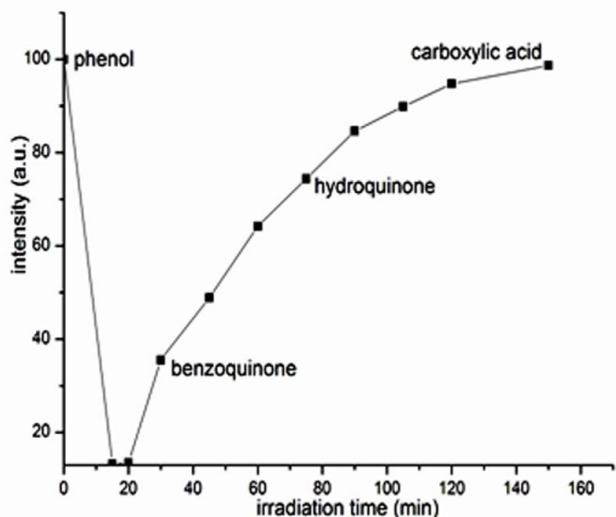


Figure 53: 10 ppm Phenol photodegradation before and after 150 min of 65 mg/50 mL of SnO₂/Gd 0.6 wt. % Nps, under visible light irradiations and optimized HPLC conditions and appearance of its different byproducts with the other parameters kept constants

Figure 53 shows the developments of the amount of different intermediates produced during the photocatalytic degradation of phenol by high performance liquid chromatography. Solar light irradiation upon 65 mg/50 mL of SnO₂/Gd 0.6 wt. % at pH 5.7 photocatalytic could be detected. A steady decline of 10 ppm phenol concentration upon photocatalytic degradation over an extended period of time could be observed. Figure 53 shows the development of different byproducts followed by BQ, HQ and later

carboxylic acid was recorded. There was an equilibrium between the degraded phenol and the phenol remained in the solution which determined the degradation phenomena. Actually, this trend appeared clearly in Fig 52 Solar light irradiation of 10 ppm upon using 65 mg/50 mL of SnO₂/La 0.6 wt. % at pH 5.7. Photocatalytic degradation of phenol detected maximum concentration of appearance of BQ followed by HQ, at the end of the analysis carboxylic acid was recorded. Intermediates obtained as in the order of Cat > Res > HQ > BQ as shown in Figure 54. The Res concentrations achieved were more than the HQ concentrations.

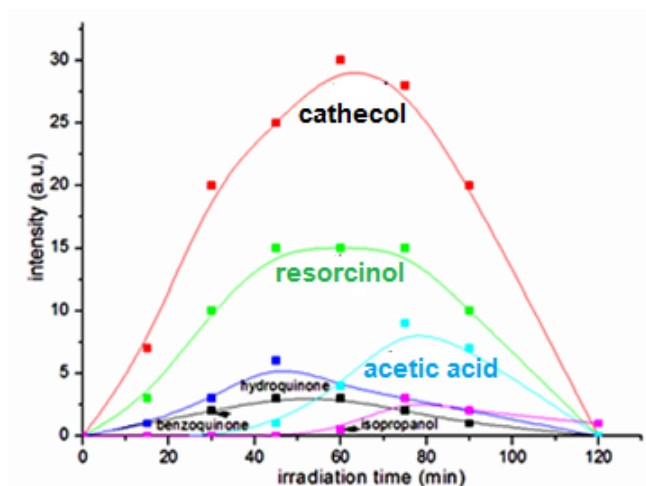


Figure 54: Evolution of phenol byproducts during phenol photo degradation in the presence of 65 mg/50 mL of SnO₂/La 0.6 wt. % Nps under solar light irradiation with the other parameters kept constant

According to the substitution rules, $\cdot\text{OH}$ radicals attack the aromatic ring with higher probability in position 1 (ortho) and position 4 (para) versus the OH group and the cleavage results from the reaction of the radicals formed by OH^- and O_2 . Upon continuous oxidation, by $\cdot\text{OH}$ radical and O_2 ultimately breaks the benzene ring. The cleavage of (C-C) bond leads to the formation of Cat or HQ, which then reacts with OH^- and forms BQ, and leads to the formation of aliphatic compounds and finally mineralizes to CO_2 and H_2O [433].

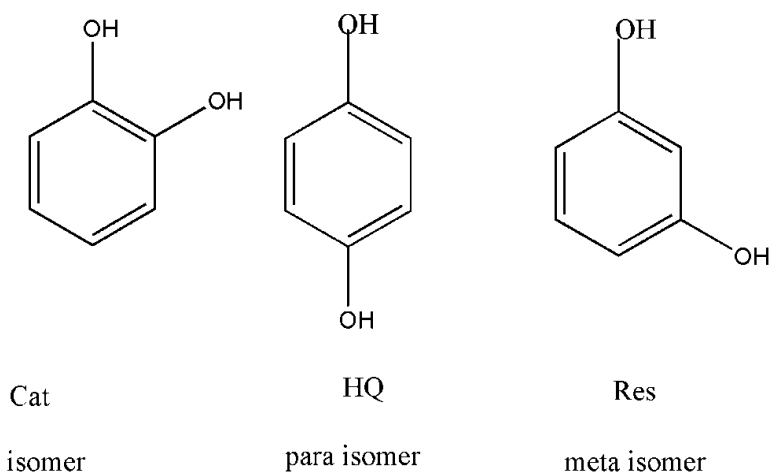


Figure 55: Examples of different phenol isomers
Abbreviations: Catechol:Cat;Hydroquinone:HQ;Resorcinol:Res

A reason for formation of Res could be regarded to the production of the OH^- since it is nonselective nature of attack. $\cdot\text{OH}$ effect is stronger to flow the substitution rule with high probability in 1, 4 or (ortho and para positions Figure 55) directing effect of the OH group of aromatic ring. Also a chance for ortho position attack is possible with the chance for (meta position) attack is also there, facilitating formation of Res. The existence of aliphatic intermediates in the reaction mixture was also checked and was found to appear after 3 min of retention time. This suggests that the structure of the benzene ring was destroyed to form carboxylic acid intermediates by photochemical oxidation.

The qualitative and quantitative analysis show the trends of six intermediates produced during the photocatalytic degradation of phenol.

4.7.2 COD photodegradation measurement

COD determines the photodegradation of phenol with its intermediates and also defines the oxygen equivalent of the organic content during the irradiation time. The experiment lets the quantity of phenol solution in terms of the total quantity of oxygen required for the mineralization of organic compound to CO_2 and H_2O . The results of COD rate removal effectiveness of phenol samples are shown and compared in (Figure 56 below) with HPLC results. The amount of organic compound recorded in the COD analysis

contains after every evaluation interval, with the byproducts growth during phenol photodegradation. COD content is presented, when 10 ppm of phenol photoactivated by 65 mg/50 mL SnO₂/Gd 0.6 wt. % under solar light irradiation for 2.5 h. The existence of phenol photodegradation was approved from the measurement of COD and compared with the results from the HPLC analysis. The photodegradation of the phenol sample was evaluated through COD analyses. The analysis showed that the quantity of organic material remained in the COD analysis, contained the amount of phenol endured after each test evaluation, with the intermediate created during phenol photodegradation.

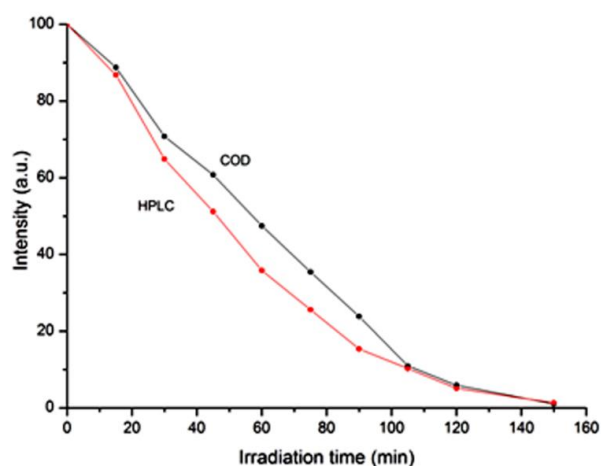


Figure 56: Comparison between the COD and the HPLC analysis during 2.5 h of phenol photodegradation by the same catalyst 65 mg/50 mL of SnO₂/Gd 0.6 wt. % for both analysis both under solar light irradiation with the other parameters kept constants

Phenol photodegradation was approved from the measurements of COD indicated that the COD concentration decreased with increasing irradiation time, showing that photodegradation of total phenol was possible in less than 3 h using SnO₂/Gd 0.6 wt. % and solar light irradiation. In addition, the assurance of phenol photodegradation was approved of COD results matched the phenol reduction observed during HPLC studies. The difference between COD results for the total organic compound remained compared with the HPLC results showed 65% in the first 60 min of irradiation time compared to HPLC 52%. This result dramatically reduced for COD to reach to 5%, which showed about 5% also for HPLC in the next 2 h of irradiation time. The results after 2.5 h showed

equal amounts about > 1% for each. The existence of the byproducts in phenol samples still remained even after phenol photodegradation [434].

4.7.3 GC Analysis technique

In order to study the effect of irradiation time on phenol photocatalytic degradation by GC, the standard solution of phenol was first subjected to UV or solar light and then extraction by SPE, after that all the samples and standards were subjected to separation through the GC.

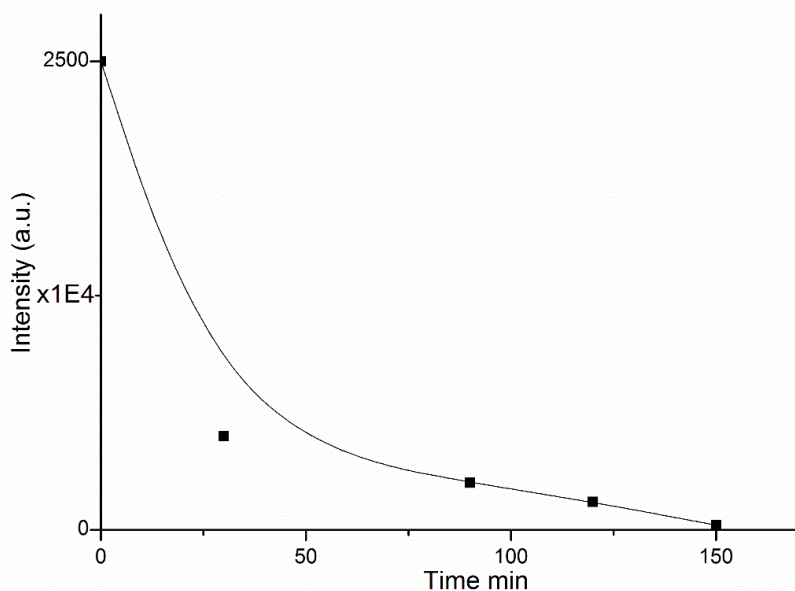


Figure 57: Reduction in the intensity of phenol peak observed by GC upon UV light irradiation degradation of phenol in the presence of 65 mg/50 mL of SnO₂/La 0.6 wt. % with the other parameters kept constants

In Figure 57 the 10 ppm phenol concentration in the aqueous sample after UV illumination from 0 to 60 min in the presence of a 65 mg/50 mL typical doped SnO₂/La 0.6 wt. % at pH 5.7. The average area changes for phenol were examined. In there it was found that after 120 min of UV light irradiation, the amount of 10 ppm phenol

concentration remained was under 5%. When the maximum illumination time reached 150 min of UV illumination, less than 1% of phenol detected.

In order to confirm the appearance of intermediates of the photochemical degradation process of phenol, samples were taken and analysed by GC technique. Two photoproducts were obviously measured in the photocatalysis BQ and Res.

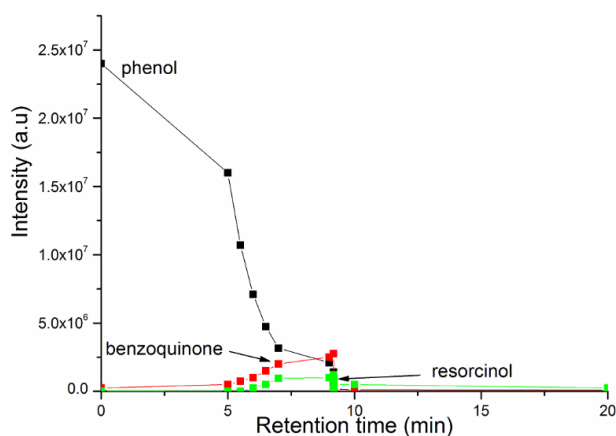


Figure 58: Reduction in the intensity of phenol peak observed by GC upon solar light degradation of phenol in the presence of 65 mg/50 mL of 1.0 wt. % SnO₂/I Nps with the other parameters kept constant

Figure 58 displays the trends of the amount of different byproducts during the photocatalytic degradation process of 10 ppm phenol upon SnO₂/I 1.0 wt. %. Throughout the same treatment period, for the first 90 min of irradiation, the formation of BQ was detected at 5 min of retention time, but Res was detected after 9 min of running time. Within 2 h, most of the phenol concentration was reduced and disappeared as it shown in Figure 58. Depending on the GC conditions applied, it was not possible to differentiate the formations of all phenol byproducts.

4.7.4 CE to monitor phenol and its byproducts

To get full knowledge about the separation of phenol and its byproducts, it is necessary to study the effect of irradiation time on phenol photocatalytic degradation by CE. In fact, to further confirm the results attained from the HPLC instrument analysis as seen

in Figure 54, the photochemical degradation process of phenol and its intermediates were analysed after photodegradation by CE technique. The separation efficiency is almost similar to HPLC analysis and therefore no extra further modification was needed. The photodegradation behaviour of 10 ppm phenol process was monitored to show its photocatalysis, by using 65 mg/50 mL of SnO_2/Gd 0.6 wt. % at pH 5.7 upon visible light illumination exposure.

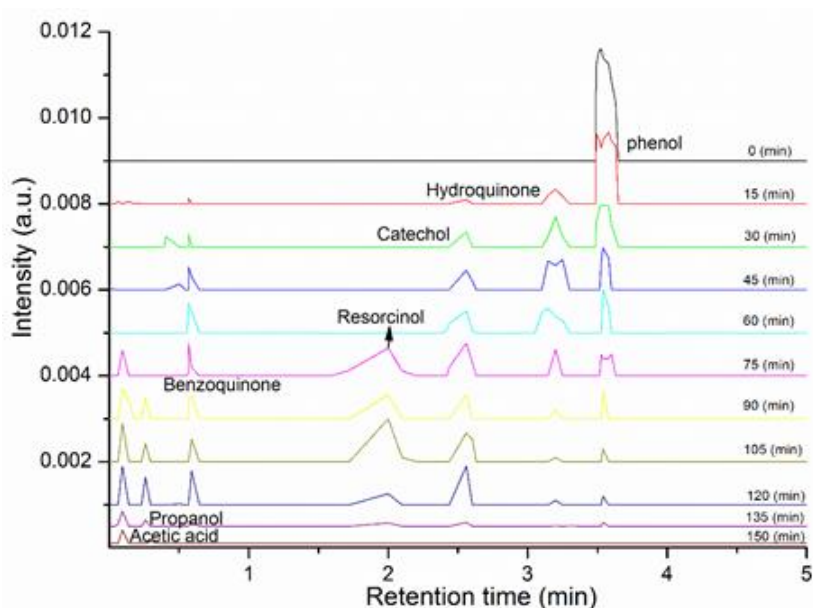


Figure 59: Different chemical byproducts produced from 10 ppm phenol photodegradation before its mineralization to CO_2 and H_2O as it analysed by CE under visible light irradiation upon 65 mg/50 mL of SnO_2/Gd 0.6 wt.% at pH 5.7 and with the other parameters kept constant

Figure 59 shows the movements of different intermediates produced during the photocatalytic degradation of phenol. The phenol pathway degraded into two main groups. Both groups are water soluble compounds. In the first group it was differentiated into quinones, and dicarboxylic acids as it was appeared in the second group. This confirmed the assumption of the formation of BQ and Cat in the first 15 min, later followed by the other intermediates. Analysis of Figure 59 also indicates that of the six byproducts, HQ was detected after 3 min of retention time, but Cat was detected after 2.5 min of running retention time, before the first intermediate. After 60 min of photocatalysis, the concentrations of phenol and some of its byproducts were found to

decrease slightly and they went on decreasing with extended irradiation times. The presence of three byproducts AA, 2-P and BQ, was detected before 1 min, but Res was observed at 2 min of retention time. These results are in agreement with the above observations from the HPLC studies to show that SnO₂/Gd 0.6 wt. % was also an effective visible light photocatalyst.

4.7.5 FTIR spectrum of phenol samples

The main target of this section in this study was to qualitatively monitor the evolution of CO₂ during photocatalytic degradation of phenol which indicates the complete mineralization of phenol. The FTIR spectra of the 10 ppm phenol solution at different stages of photocatalytic degradation under UV light irradiation with 65 mg/50 mL SnO₂/Sb 0.6 wt. % Nps at pH 5.7 are shown which clearly shows the CO₂ generation within 30 min indicated by 2 IR absorption. However, the results shown here cannot be correlated to the concentration of CO₂ that is formed during the reactions because this experiment did not carry out any quantitative analysis for CO₂. In fact, the FTIR analysis was conducted only to verify the complete mineralization of phenol during the photocatalytic process.

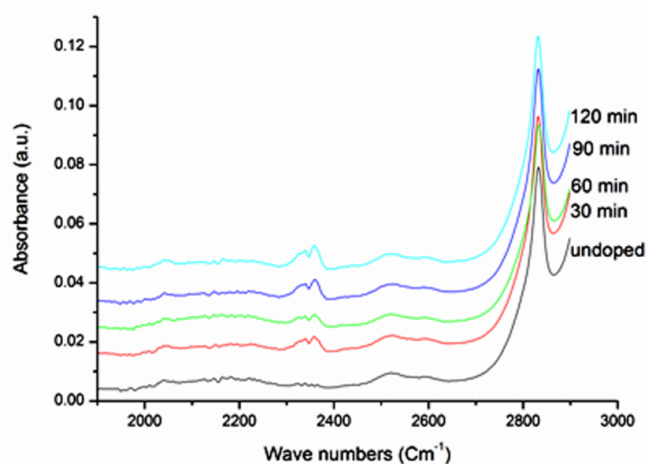


Figure 60: 10 ppm of phenol photodegradation upon 65 mg/50 mL of SnO₂/Sb 0.6 wt. % Nps at pH 5.7 which mineralized to CO₂ as indication observed by FTIR under UV light irradiation after 2 h with the other parameters kept constant

4.8 Degradation mechanism of phenol involving the O-H bond (Formation mechanism) 179

In order to clarify the byproducts of the photochemical oxidation of phenol, Figure 60 shows the FTIR spectrum of phenol irradiated at different periods at the same temperatures for 2 h only under UV light irradiation. The FTIR experiment was conducted only to verify the complete mineralization of phenol during the photocatalytic degradation process. In the Figure 60 the evolution of 2 bands, and CO₂ was identified during each photodegradation period. The presence of two bands at 2364 and 2324 cm⁻¹; specifies the mineralization peaks at different stages of the photocatalytic reactions. These results are clearly in accordance with other references showed earlier [435-437]. The presence of the two bands obviously specifies the availability of CO₂ in the early stage of phenol photodegradation.

4.8 Degradation mechanism of phenol involving the O-H bond (Formation mechanism)

In order to better understand the degradation mechanism, the major degradation byproducts were studied independently upon photoirradiation.

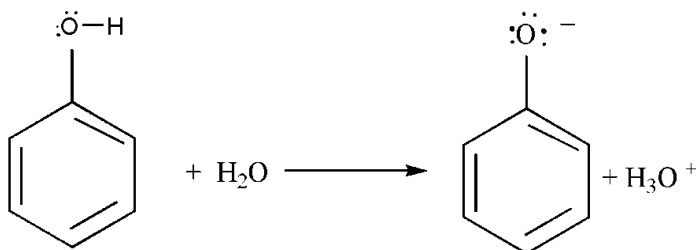


Figure 61: Possible formation of phenoxide ion in water from phenol

The reaction begins with the O-H group attached the aromatic (benzene) ring bonds breaking as it was explained earlier, giving up a proton or releasing a proton, thus forming an anion stabilized by the aromatic ring (phenoxide ion), as shown in Figure 61.

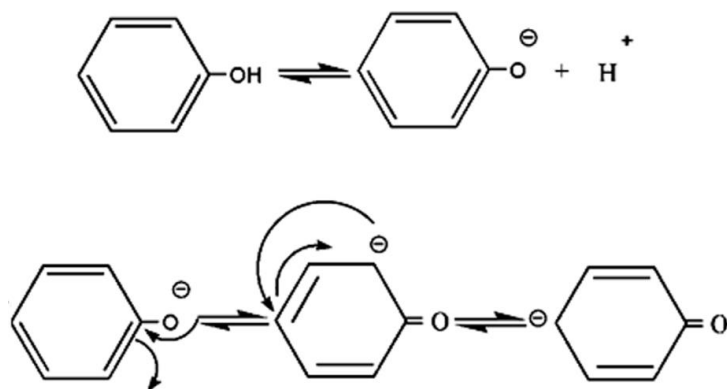


Figure 62: Possible degradation mechanism of phenol and resonance stability of phenoxide, and the formation of benzoquinone intermediate

Activation of the phenol by the generation of $\cdot\text{OH}$ will produce phenoxy radical which is in resonance with radical structures in the ortho and para positions as it shown in Figure 61 [438].

The three mesomeric forms of the radical are the initial formation of the different intermediates. These radicals can react with the $\cdot\text{OH}$ to form compounds such as HQ, BQ and Cat as it was explained earlier.

From the previous analysis it is shown that the photodegradation of phenol involves two stages, the first is the formation of the intermediate products, while the second is completion of the intermediates and the mineralization to CO_2 and H_2O . Results also confirmed the presence of Cat, BQ, Res and HQ with the continuous degradation peak of phenol. The presence of these intermediates decreased slightly over time.

Benzene ring is a stable structure, but the bond on the benzene ring can be potentially weakened when the $\cdot\text{OH}$ attacks the ring, resulting to the accumulation of one or more O-H group at the ortho or para position as it explained earlier.

Continuous photodegradation of phenol lead to the ring opening and the decomposing of phenolic structures to show up of diverse organic compounds. This reaction accounts to the continuous decrease in the values (measured by different instrumentations such as UV-Vis, HPLC, GC, CE, TOC and COD after only two h of photodegradation) and

4.8 Degradation mechanism of phenol involving the O-H bond (Formation mechanism) 181

the appearance of different intermediates until finally (AA) will form and mineralization of phenol.

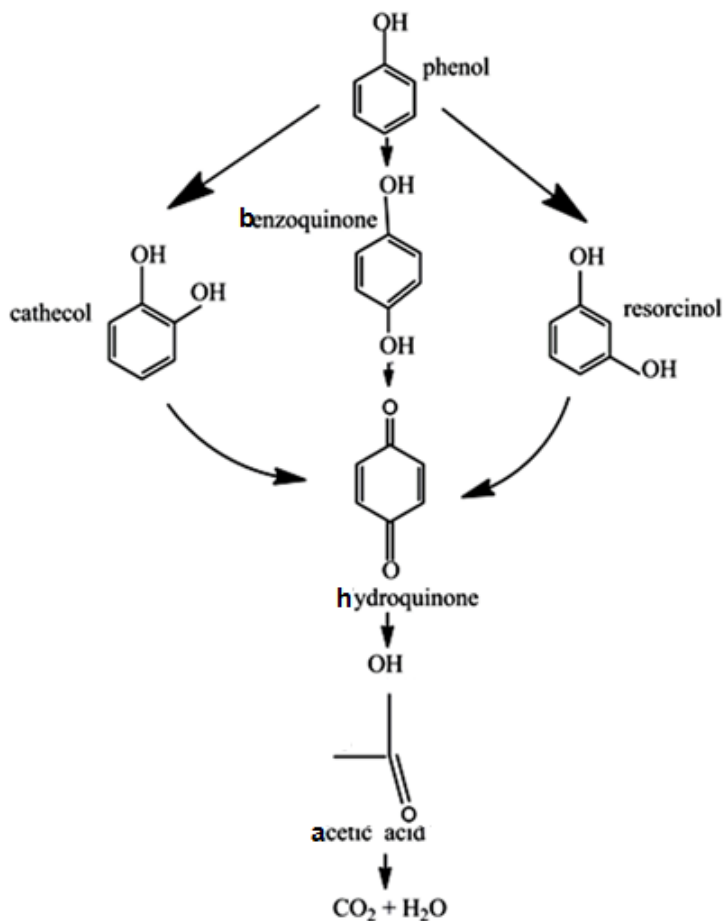


Figure 63: Different chemical photoproducts produced from phenol photodegradation before its mineralization by CO₂ and H₂O build up from results given by UV-Vis, HPLC, CE, GC and FTIR with the reports from the literature [190, 196]

Figure 63 shows the current experimental conditions following the observations made from HPLC, CE and other studies and with the reports in the literature [190, 196]. With the continuous effects of UV, solar or visible light irradiation hydrocarbon chains were mineralized completely to CO₂ and H₂O. The current experimental conditions are proposed in Figure 63, where the photocatalytic degradation of phenol involves the generation of intermediate compounds and a mineralization stage.

4.8.1 Hydroquinone (HQ)

During phenol degradation HQ appeared after 30 min, reaching its maximum after 45 min of photoirradiation at a rate of 0.0025 ppm/min, which was detected by UV-Vis spectrophotometry, in CE, and in HPLC. At 60 min of phenol photodegradation, HQ concentrations decreased sharply and further slow reduction was observed [439], followed by degradation to different short chain organic acids until all phenol was removed from the solution [440]. The concentration of HQ product obtained was moderate, but it is more toxic than phenol itself even at this low level [441]. The presence of HQ can lead to reasonably high value of ecotoxicity, consequently it is very important to follow the evolution of HQ in phenol photodegradation, until almost complete vanishing of the byproduct can be recorded [442]. It is shown from Figure 1 and 55 that HQ is a para directed product but it produced less than Res. HQ formation can be done from substitution at the position (C4) at the para carbon atom. Possibility for higher concentrations of ortho and para directing in aromatic electrophile substitution reactions could be assumed, but the results shown that concentrations of HQ were less produced than of Cat which is ortho directed and Res which is (meta) directed substitutions. The reason for this may be due to the nonselectivity nature of attack of the $\cdot\text{OH}$ in the aqueous media. This effect is much stronger than the ortho and para directing effect. Also possibility of ortho and meta positions present two new attack phenomena's as it been explained above.

4.8.2 Benzoquinone (BQ)

BQ was traced for the first 30 min of photodegradation and it was found to be lower than HQ. The formation rate of BQ was 0.0107 ppm/min, and the degradation rates were calculated from the reduction of the BQ peak at 0.00357 ppm/min. BQ showed maximum concentrations at 40 min and remained the same up to 60 min, after which its concentrations decreased gradually due to the photocatalytic degradation. The very low concentrations of BQ were detected by UV-Vis spectrophotometry, GC, and also by CE.

4.8 Degradation mechanism of phenol involving the O-H bond (Formation mechanism) 183

4.8.3 Catechol (Cat)

Higher concentrations of Cat were produced than any other byproduct, which may be related to the ortho directed properties group of phenol. Cat was formed within 15 min of phenol degradation; its concentration increased to a maximum of 0.7 ppm, and kept increasing until it reached 3 ppm after 45 min at a rate of 0.1249 ppm/min. After 75 min, the concentration of Cat decreased at a rate of 0.0292 ppm/min. Figure 45 shows that Cat was produced during all phenol degradation process. Cat possibility formation comes from substitution at the positions (C4) and (C6) at the carbon atom.

4.8.4 Resorcinol (Res)

Res appeared from the beginning, and its concentration increased from 0.3 ppm until it reached 1.5 ppm and became stable at that point, after 75 min at a rate of 0.0075 ppm/min. The almost stable concentration of Res production in the mixture analysis suggested that Cat would be produced by the same rate until all phenol could be removed from the solution. It was also noticed that Res concentrations were higher than HQ ones. It seems that the substitution rules of $\cdot\text{OH}$ radicals attacking the phenol molecule with higher probability in positions 1 and 4 (ortho and para directing effect) are weaker than the non-selective nature of attack of $\cdot\text{OH}$ group of the aromatic ring. Res possibility formation comes from substitution at the positions (C3) and (C3) at the carbon atom.

4.8.5 Acetic acid (AA)

AA appears more intractable to photodegradation, but this has no significance in conditions of ecotoxicity elevation. Ring opening of the byproducts leads to the formation of AA, and pH will also increase (results not shown). AA appeared in the reaction medium after 45 min at a rate of 0.0015 ppm/min.

4.8.6 Isopropanol (2-P)

2-P has a neutral pH level of approximately 7 (results from our previous analysis, not shown), and it is very similar to pure water. It seems that propionic acid competes with AA, which explains why traces of this compound sometimes appear before AA and on

other occasions after AA. 2-P appeared in the solution after 75 min at a rate of 0.0813 ppm/min.

4.9 Photocatalytic degradation of different aromatic compounds

In this study, the photodegradation of (phenol, BQ, HQ Cat, Res, AA, 2-P) was also investigated in the presence of SnO₂/La 0.6 wt. % Nps under solar light irradiation. On the degradation of each of these organic compounds evaluation, 10 ppm of each was compared with the photolysis and the control. Each of these separately put into the reactor with the other parameters were kept constant upon (65 mg/50 mL) of (SnO₂/La 0.6 wt. %) under solar light irradiation at pH 5.7 and the results are presented in Figure 64 shows comparison of photocatalytic activity of 65mg/50 mL of SnO₂/La 0.6 wt. % Nps under solar light irradiation on photodegradation of phenol, BQ, HQ Cat, Res, AA, 2-P at optimum condition as it was explained. There are oxygen vacancies in SnO₂ Nps which can donate oxygen [186] and play an important role in photocatalysis [443]. The influence of SnO₂/La 0.6 wt. % Nps on the degradation rate of phenol and the removal results of the intermediates in the aqueous solution show that phenol is highly eliminated more than the other byproducts.

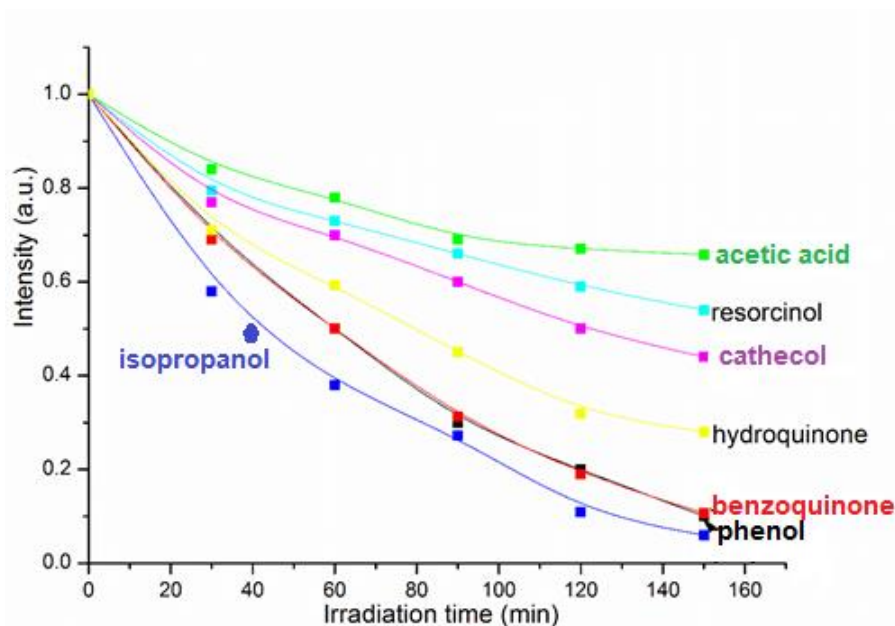


Figure 64: Degradation of 10 ppm phenol and its byproducts (2-P, phenol, BQ, HQ, Cat, Res, and AA) after 2.5 h treatment with SnO_2/La 0.6 wt. % under solar light irradiation, with the other parameters kept constant

Generally, the degradation efficiency of the phenol and its byproducts decreased significantly in the aqueous. The tendency of reduction was in the order of 2-P > phenol > BQ > HQ > Cat > Res and AA accomplishing degradation after 2.5 h of photocatalysis. This observation confirmed that the degradation rate of phenol was higher the other byproducts (HQ, Cat, Res and AA) but it was less than 2-P. 2-P is known to have a neutral pH level of approximately 7, which is very similar to pure water. The degradation rate of phenol is almost equal amount with BQ. In addition, Figure 64 indicated that the efficiency of AA degradation at optimum conditions under SnO_2/La 0.6 wt. % solar light irradiation was the lowest in comparison with the other byproducts. Consequently, photocatalysis also demonstrated to be quite effective in removing different kind of toxins from aqueous.

4.10 Kinetics of phenol degradation

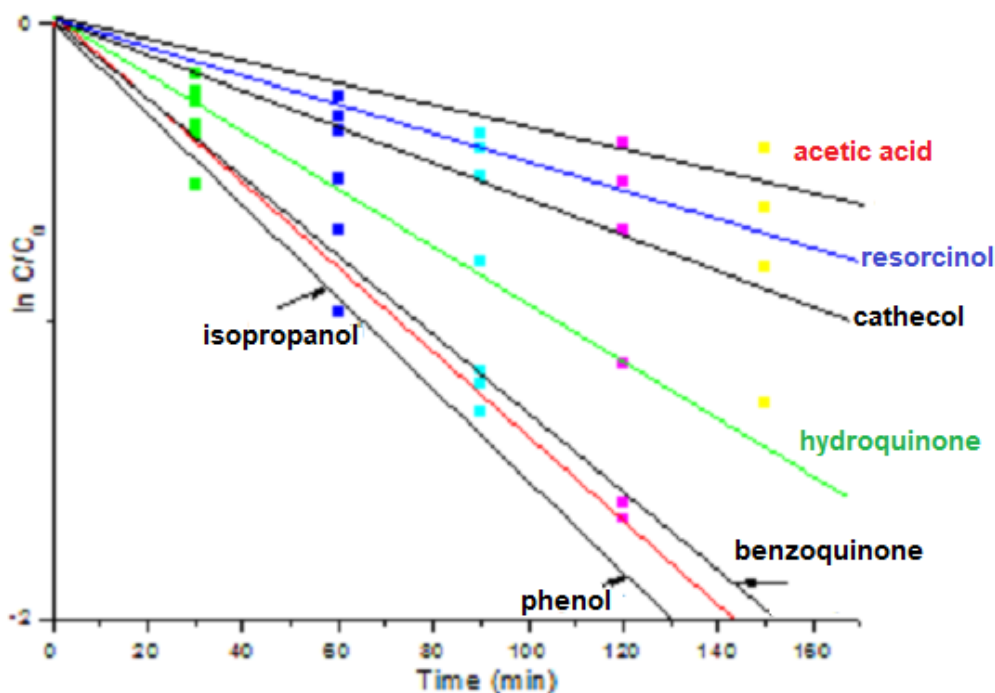


Figure 65: Kinetic study of photodegradation of phenol and its intermediates in the presence of 65 mg/50 mL of SnO₂/La 0.6 wt. % Nps under solar light irradiation with the other parameters kept constant

Moreover results shown that all calculated values of $\ln(C/C_0)$ (C_0 is the initial phenol concentration and C is the concentration of phenol at time t) in degradation of phenol under 65 mg/50 mL of SnO₂/La 0.6 wt. % Nps at pH 5.7 under solar light irradiation on origin pro gave linear curves. The overall degradation rate of phenol and its byproducts follows a linear model with the elapse of illumination time. This is well described by a pseudo-first order rate equation as can be seen in Figure 65, which means that the pseudo-first order kinetics relative to phenol and its byproducts is operative.

The rate of degradation of 2-P was rather similar to phenol, but AA one was much lower than phenol and 2-P. Slower degradation rates were also observed with Cat and Res Figure 65.

Table 20: Kinetic parameters of phenol and its byproducts degradation in photocatalysis by SnO₂/La nanoparticle

Organic molecule	Rate constant <i>K</i> (min ⁻¹)	R ²
Phenol	0.02228	0.9977
Propanol	0.02228	0.9961
Benzoquinone	0.0209	0.9952
Hydroquinone	0.017066	0.9834
Catechol	0.013839	0.9544
Resorcinol	0.013753	0.9158
Acetic acid	0.013412	0.9135

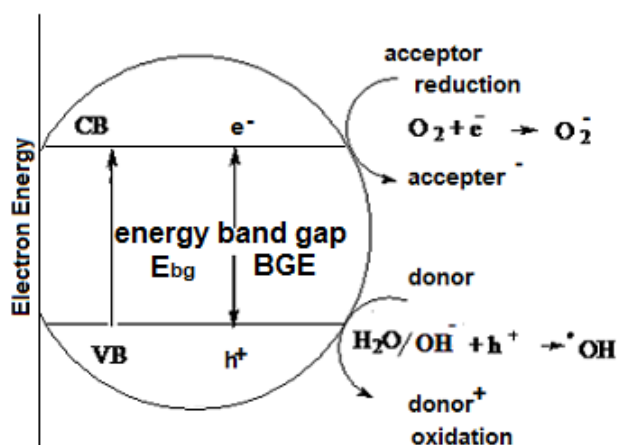
The pseudo-first order rate constants, *k*, estimated for photocatalytic degradation of 10 ppm phenol and 10 ppm of each byproduct such as (BQ, HQ Cat, Res, AA, 2-P) reacted separately with 0.065g/50 mL of SnO₂/La 0.6 wt. % in aerated system at pH 5.7 (optimum conditions) are summarized in Table 20. Pseudo-first order rate constants were obtained from linear transforms of the plot of ln C/C₀ as a function of time which comes from first order kinetic equation. The kinetics parameters of phenol and its byproducts are tabulated in Table 21. The best fit of the data to the first order plots at all contaminants studied, as indicated by the large amount of R² is an indication that degradation of phenol can be adequately described with first order kinetics. From the Table it can be determined that phenol degradation and its byproducts obtained hopefully results, which indicated that it was possible to degrade phenol to a very low amount, which showed again that photocatalysis is a promising technology to remove not only phenol but also its byproducts from water.

Table 21 also indicates the removal rates for TOC concentrations with 65 mg/50 mL SnO₂/I (0.01, 0.2, 0.03, 0.4, 1.0, and 1.1 wt. % nanoparticle), at optimum conditions which vary during the study, this variation is understandable since phenol takes time to become finally mineralized.

Table 21: Kinetic parameters of phenol degradation by SnO₂/I Nps

SnO ₂ /I wt. %	K (min ⁻¹)
Control	0.0028
0.01 wt. %	0.0032
0.2 wt. %	0.0036
0.3 wt. %	0.0049
0.4 wt. %	0.0096
1.0 wt. %	0.0224
1.1 wt. %	0.0277

From the Table it is observable that no appreciable change in photoactivity of SnO₂/I nanoparticle occurs for samples doped with lower than SnO₂/I 0.2 wt. %. The photocatalytic activity of phenol started to improve in samples with SnO₂/I 0.3 wt. % or higher dopant of SnO₂/I concentrations. As it is noticed from the Table 21 that the similar common tendency in the rate of removal of phenol concentrations in aqueous which indicated by TOC mineralization shows first order of kinetics. Although, the degradation rate started to increase later during the photodegradation of phenol, it is also noticeable from the Table that the overall rate of TOC removal was not a first-order process, maybe due to the formation of byproducts during phenol photodegradation which were degraded at different rates by the Nps.

Figure 66: Schematic presentation of the SnO₂ photocatalytic mechanism [207, 444]

Some degradation products were identified in this study, but the possible degradation mechanism of phenol starts by the generation of $\cdot\text{OH}$ and $\text{O}_2\cdot^-$ radicals [207, 444]. In water decontamination, the acceptor is an electron usually oxygen comes from aerated systems, but the donor is an electron comes from pollutants this explanation have been shown in equation 2 and explained there.

The mechanism and reaction outline for photocatalysis are followed above at Figure 64, $\cdot\text{OH}$ the reactive species responsible for forming the h^+ with absorbed H_2O and OH^- , and the $\text{O}_2\cdot^-$. In an aerated solution for O_2^- and H_2O_2 production of oxygen reduction is essential to support the charge transferring and driving the photocatalytic activity [135]. H_2O_2 is photodecomposed to $\cdot\text{OH}$ which reacts with the substrate [193].

5 Conclusions and future research

The synthesis of crystalline SnO₂ nanoparticle without and with doped ions such as Sb, I, La, Ce, Nd, and Gd by the simple sol-gel technique was demonstrated. The SnO₂ Nps showed excellent photocatalytic degradation of phenol from the solvent. The effect of various parameters such as catalyst loading, pollutant concentration, pH of the solution and sampling from the reactor was examined. Targeting the intermediates of phenol photodegradation gives crucial evidences about the substituent groups on the degradation rates of phenol. Also, it could give an idea when to expect the cleavage part and in which place. Photocatalytic mineralization of phenol was determined early within 15 min of irradiation. Byproducts such as HQ and Cat appeared through 15 min at a rate of 0.0025 and 0.175 ppm/min respectively as it quantitatively detected by UV-Vis, HPLC and CE. During the 30 min amount of time, the absorption band of CO₂ at 2364 and 2324 cm⁻¹ was also detected but qualitatively in the FTIR spectrum. Furthermore, the totally degradation of phenol achieved within 2.5 h in the presence of different doped SnO₂ Nps. Byproducts such as (Cat, Res, HQ, BQ, AA and 2-P) obtained upon the photocatalytic degradation of phenol, a degradation pathway is also proposed. BQ was found to form immediately upon photodegradation and all successive byproducts were formed through the degradation of BQ. The main aromatic intermediate formed of phenol photodegradation is Cat. Improvement of these simple techniques to utilize solar radiation more efficiently will provide more economic solutions to the problem of water purification and recovery. Cat, Res and HQ are three main aromatic compounds created from the photodegradation of phenol, followed by the opening of the aromatic ring to carboxylic acids. Carboxylic acids finally degrade to give complete mineralization.

High performance liquid chromatography, chemical electrophoresis, total organic carbon and chemical oxygen demand analysis during photodegradation of phenol and its byproducts will provide important and extensive information about the total mineralization. The presence of Nps caused a significant decrease in the COD concentration of the phenol, due to the increase in the surface area. Therefore, the

increase in the surface area due to doping of different ions to SnO₂ results in an increase in the active sites for better adsorption and hence better photocatalytic activity.

It was found that La, Gd and Sb were the best dopants, since they degraded practically > 98% of phenol within 2.5 h under either UV, solar or visible light irradiation, with the almost similar effect of each. Consequently Sb or Gd doped SnO₂ Nps are therefore promising candidates for photocatalytic oxidation processes and may have future potential for advanced water and wastewater treatments.

By continuous checking and testing the water samples would be a step forward in bridging the gap from the laboratory to the possibility of incorporation in the water treatment process because it could build important kinetic parameters needed for a system up scaling.

The results from the laboratory experiments for phenol degradation and its intermediates under UV, sunlight and visible light irradiation have directed to the following conclusion and future work.

- 1-The study of phenol photodegradation, Cat, Res, BQ, HQ, AA and 2-P in the photoreactor followed first order kinetics by SnO₂ doped catalysts.
- 2-Six intermediates are identified by phenol photodegradation process.
- 3-Results from phenol photodegradation showed that the intermediates obtained and formed are in the order of Cat >Res >HQ >BQ and later showed AA and 2-P. Only after phenol is completely photodegraded in the solution, then the rest of the intermediates are totally removed.

Future work should concentrate on the evaluation of different photocatalysts and different forms of photocatalytic materials for instance polymers, cellulose, thin films, and silica based support photocatalysis etc. Furthermore, phenol as an organic compound does not represent all the toxins but also inorganic compounds such as chromium and other toxins should be tested to remove from the environment and should be included in the degradation studies to allow evaluating the overall efficiency of the photocatalytic process and the applicability to real-life problems.

It would be preferable to test a large number of phenolic and more endocrine disrupting compounds. Further investigation could be tested with other toxins from actual polluted

waste water, such as municipal and pharmaceutical residues. To determine the effect of degrading other contaminants by this technique, this kind of treatment can be effective to treat hospital wastewater and others before transferring them to other places for final controlling.

The phenol photodegradation is experienced on a batch, but the implementation of this process is of interest. Therefore, it is an advantage to test the photocatalysis in a fixed bed placed in the reactor. However, in order to design an effective apparatus, the SnO₂ powder needs to be immobilized on a stationary phase, such as a silica or cellulose etc. Several groups have been active in this field and immobilized catalysts have been used in the photodegradation of organic pollutants.

5.1 Recommendations

For practical work if using UV light irradiation, the source of UV is mainly mercury vapour lamp which consumes a lot of energy for operating, has hazardous mercury, requires cooling and its lifetime is not long.

Photocatalytic processes have been carried out with less energetic form of radiation, namely visible light. This is advantage as visible light is less harmful to the human body. For this purpose, xenon lamps could be used instead of the more expensive mercury lamps the new nanoparticle catalysts should be a visible light activated. At the point solar irradiation, is a good low-cost alternative and an important light source for these kinds of materials.

The photocatalyst particles synthesized in this study were about 1-2 nm in size and it has some drawbacks:

- 1- In some cases solar light does not cover and reach the entire deep water surface.
- 2- Sedimentation of the Nps (catalyst powder) in the pollutant during the photocatalysis experiments takes longtime and also high cost to deal with.
- 3- The researcher during the analysis should be care full, due to the expected mobility and transferring of the powder during the experiment which may be harmful to his life.
- 4- The Nps are sometimes difficult to be applied for large scale application.

- 5- When the Nps are dispersed within the contaminant create problem of separation from the solution, need special technique for separation, cause reduction in efficiency at high catalyst concentrations because of turbidity as a result of screening effect of the photons of light by excess catalyst particles.
- 6- Further research is necessary to solve the loose powder problem, in fact, various substrates have been tried to support to hold oxide Nps so that to make easy final separation treatments. One of the best techniques used is the polymer-based support which helps in holding the photocatalyst Nps. In fact, this technique has many advantages and could be concluded as follows
 - i- It can be performed at a low cost and simple availability
 - ii- Can be prepared under simple thermal treatment
 - iii- It had been tested on other oxides as TiO_2 and showed to have a good affinity with catalysts and pollutants
 - iv- It has a high specific surface area as the Nps in this study.
 - v- The problem of the photocatalyst leaching will be avoided.
 - vi- Advantage of long term stability, with the easy use.

The development in photocatalytic synthesis of the polymer/catalyst hybrid composites including SnO_2 becomes a challenge.

6 References

- [1] A.K. Chakraborty, S. Ganguli, M.A. Kebede, Photocatalytic degradation of 2-propanol and phenol using Au loaded MnWO₄ nanorod under visible light irradiation, *J Clust Sci.* 23 (2012) 437-448.
- [2] X. Huang, M. Sillanpää, B. Duo, E.T. Gjessing, Water quality in the Tibetan Plateau: metal contents of four selected rivers, *Environ Pollution.* 156 (2008) 270-277.
- [3] X. Huang, M. Sillanpää, E.T. Gjessing, R.D. Vogt, Water quality in the Tibetan Plateau: major ions and trace elements in the headwaters of four major Asian rivers, *Sci Total Environ.* 407 (2009) 6242-6254.
- [4] S.H. Swan, Environmental phthalate exposure in relation to reproductive outcomes and other health endpoints in humans, *Environ. Res.* 108 (2008) 177-184.
- [5] A. Sambandam, The contribution of nanotechnology for removal of water pollutants, *Mater Sci Forum* 712 (2012) 24.
- [6] S. Kaneco, M.A. Rahman, T. Suzuki, H. Katsumata, K. Ohta, Optimization of solar photocatalytic degradation conditions of bisphenol A in water using titanium dioxide, *J Photoch Photobio A.* 163 (2004) 419-424.
- [7] E. El-Ashtoukhy, Y. El-Taweel, O. Abdelwahab, E. Nassef, Treatment of petrochemical wastewater containing phenolic compounds by electrocoagulation using a fixed bed electrochemical reactor, *Int. J. Electrochem. Sci.* 8 (2013) 1534-1550.
- [8] M. Rupnik, Negative impact of endocrine-disrupting compounds on human reproductive health, *Reprod Fert Develop.* 23 (2011) 403-416.
- [9] S. Vilhunen, H. Särkkä, M. Sillanpää, Ultraviolet light-emitting diodes in water disinfection, *Environ Sci Pollut Res.* 16 (2009) 439-442.
- [10] D.T. Sponza, Application of toxicity tests into discharges of the pulp-paper industry in Turkey, *Ecotox Environ Safe* 54 (2003) 74-86.
- [11] Rudel RA, Gray JM, Engel CL, Rawsthorne TW, Dodson RE, Ackerman JM, Rizzo J, Nudelman JL, B. JG., Food packaging and bisphenol A and bis(2-ethylhexyl) phthalate exposure: findings from a dietary intervention., *Environ Health Perspect.* 119 (2011) 914-920.
- [12] J. Michałowicz, W. Duda, Phenols - Sources and toxicity, *Pol J Environ Stud.* 16 (2007) 347-362.

- [13] R.L. Spehar, H.P. Nelson, M.J. Swanson, J.W. Renoos, Pentachlorophenol toxicity to amphipods and fathead minnows at different test pH values, *Environ Toxicol Chem.* 4 (1985) 389-397.
- [14] G.L. Phipps, G.W. Holcombe, J.T. Fiandt, Acute toxicity of phenol and substituted phenols to the fathead minnow, *B Environ Contam Tox.* 26 (1981) 585-593.
- [15] P. Hooda, A. Edwards, H. Anderson, A. Miller, A review of water quality concerns in livestock farming areas, *Sci Total Environ.* 250 (2000) 143-167.
- [16] X. Peng, Y. Yu, C. Tang, J. Tan, Q. Huang, Z. Wang, Occurrence of steroid estrogens, endocrine-disrupting phenols, and acid pharmaceutical residues in urban riverine water of the Pearl River Delta, South China, *Sci Total Environ.* 397 (2008) 158-166.
- [17] G.L. Phipps, G.W. Holcombe, J.T. Fiandt, Acute toxicity of phenol and substituted phenols to the fathead minnow, *Bull Environ Contam Toxicol.* 26 (1981) 585-593.
- [18] A. Fakhru'l-Razi, A. Pendashteh, L.C. Abdullah, D.R.A. Biak, S.S. Madaeni, Z.Z. Abidin, Review of technologies for oil and gas produced water treatment, *J Hazard Mater.* 170 (2009) 530-551.
- [19] W. Aktar, D. Sengupta, A. Chowdhury, Impact of pesticides use in agriculture: their benefits and hazards, *Interdiscip toxicol.* 2 (2009) 1-12.
- [20] P.S. Hooda, A.C. Edwards, H.A. Anderson, A. Miller, A review of water quality concerns in livestock farming areas, *Science of the Total Environment.* 250 (2000) 143-167.
- [21] D. Fatta-Kassinos, S. Meric, A. Nikolaou, Pharmaceutical residues in environmental waters and wastewater: current state of knowledge and future research, *Anal Bioanal Chem.* 399 (2011) 251-275.
- [22] J.-Q. Jiang, Z. Zhou, V. Sharma, Occurrence, transportation, monitoring and treatment of emerging micro-pollutants in waste water-a review from global views, *Microchem J.* 110 (2013) 292-300.
- [23] X. Peng, Y. Yu, C. Tang, J. Tan, Q. Huang, Z. Wang, Occurrence of steroid estrogens, endocrine-disrupting phenols, and acid pharmaceutical residues in urban riverine water of the Pearl River Delta, South China, *Sci Total Environ.* 397 (2008) 158-166.
- [24] J. Michalowicz, W. Duda, Phenols -- Sources and Toxicity, *Pol J Environ Stud.* 16 (2007) 347-362.

- [25] C. Valette, C. Andary, J. Geiger, J. Sarah, M. Nicole, Histochemical and cytochemical investigations of phenols in roots of banana infected by the burrowing nematode *Radopholus similis*, *Phytopathology*. 88 (1998) 1141-1148.
- [26] L. Ritter, K. Solomon, P. Sibley, K. Hall, P. Keen, G. Mattu, B. Linton, Sources, pathways, and relative risks of contaminants in surface water and groundwater: a perspective prepared for the Walkerton inquiry, *J Toxicol Environ Health*. 65 (2002) 1-142.
- [27] Y. Jiang, X. Cai, D. Wu, N. Ren, Biodegradation of phenol and m-cresol by mutated *Candida tropicalis*, *J Environ Sci*. 22 (2010) 621-626.
- [28] G. Busca, S. Berardinelli, C. Resini, L. Arrighi, Technologies for the removal of phenol from fluid streams: A short review of recent developments, *J Hazard Mater*. 160 (2008) 265-288.
- [29] S. Ahmed, M. Rasul, W.N. Martens, R. Brown, M. Hashib, Advances in heterogeneous photocatalytic degradation of phenols and dyes in wastewater: a review, *Water Air Soil Poll*. 215 (2011) 3-29.
- [30] R. Arasteh, M. Masoumi, A. Rashidi, L. Moradi, V. Samimi, S. Mostafavi, Adsorption of 2-nitrophenol by multi-wall carbon nanotubes from aqueous solutions, *Appl Surf Sci*. 256 (2010) 4447-4455.
- [31] G.P.P. Lima, F. Vianello, C.R. Corrêa, R.A. da Silva Campos, M.G. Borguini, Polyphenols in fruits and vegetables and its effect on human health, *Food and Nutrition sciences*. 5 (2014) 1065.
- [32] D.K. Mahmoud, M.A. Mohd, Langmuir model application on solid-liquid adsorption using agricultural wastes: Environmental application, *J Purity Utility Reac Environ*. 1 170-199.
- [33] U. European, the list of priority substances in the field of water policy and amending directive, council directive 2455/2001/ECC, *Official Journal of the European Communities* L331. 20 (2001) 1-5.
- [34] J. McMurry, *Organic Chemistry*, Brooks/Cole publishing, California, USA, 2012.
- [35] J. Huang, K. Huang, C. Yan, Application of an easily water-compatible hypercrosslinked polymeric adsorbent for efficient removal of catechol and resorcinol in aqueous solution, *Journal of Hazardous Materials*. 167 (2009) 69-74.

- [36] S. Suresh, V.C. Srivastava, I.M. Mishra, Adsorption of catechol, resorcinol, hydroquinone, and their derivatives: a review, *International Journal of Energy and Environmental Engineering*. 3 (2012) 1-19.
- [37] A. Sobczykński, Ł. Duczmal, W. Zmudziński, Phenol destruction by photocatalysis on TiO₂: an attempt to solve the reaction mechanism, *Journal of Molecular Catalysis A: Chemical*. 213 (2004) 225-230.
- [38] A. Mokriani, D. Ousse, S. Esplugas, Oxidation of aromatic compounds with UV radiation/ozone/hydrogen peroxide, *Water Science and Technology*. 35 (1997) 95-102.
- [39] G. Busca, S. Berardinelli, C. Resini, L. Arrighi, Technologies for the removal of phenol from fluid streams: a short review of recent developments, *Journal of Hazardous Materials*. 160 (2008) 265-288.
- [40] B.-D. Lee, M.-J. Lee, Prediction of Hydroxyl Substitution Site (s) of Phenol, Monochlorophenols and 4-Chloronitrobenzene by Atomic Charge Distribution Calculations, *Bull Korean Chem Soc*. 30 (2009) 787-790.
- [41] N. Raghavan, S. Steenken, Electrophilic reaction of the hydroxyl radical with phenol. Determination of the distribution of isomeric dihydroxycyclohexadienyl radicals, *J Am Chem Soc*. 102 (1980) 3495-3499.
- [42] Z. Wu, M. Zhou, Partial degradation of phenol by advanced electrochemical oxidation process, *Environl sci technol*. 35 (2001) 2698-2703.
- [43] J. Huang, K. Huang, C. Yan, Application of an easily water-compatible hypercrosslinked polymeric adsorbent for efficient removal of catechol and resorcinol in aqueous solution, *J Hazard Mater*. 167 (2009) 69-74.
- [44] S. Suresh, V.C. Srivastava, I.M. Mishra, Adsorption of catechol, resorcinol, hydroquinone, and their derivatives: a review, *Int Energ Environ Eng*. 3 (2012) 1-19.
- [45] Li, Yin, W. Chen, Wang, Solubility of Hydroquinone in Different Solvents from 276.65 K to 345.10 K, *J Chem Eng Data* 51 (2006) 127-129.
- [46] A. Sobczykński, Ł. Duczmal, W. Zmudziński, Phenol destruction by photocatalysis on TiO₂: an attempt to solve the reaction mechanism, *J Mol Catal A- Chem*. 213 (2004) 225-230.
- [47] C. Comninellis, C. Pulgarin, Anodic oxidation of phenol for waste water treatment, *J Appl Electrochem*. 21 (1991) 703-708.

- [48] V.S. de Sucre, A.P. Watkinson, Anodic oxidation of phenol for waste water treatment, *Can J Chem Eng.* 59 (1981) 52-59.
- [49] H. Sharifian, D. Kirk, Electrochemical oxidation of phenol, *J Electrochem Soc.* 133 (1986) 921-924.
- [50] N. Pradeep, S. Anupama, K. Navya, H. Shalini, M. Idris, U. Hampannavar, Biological removal of phenol from wastewaters: a mini review, *Appl Water Sci.* 5 (2015) 105-112.
- [51] F.A. Caliman, M. Gavriescu, Pharmaceuticals, personal care products and endocrine disrupting agents in the environment—a review, *Clean Soil Air Water.* 37 (2009) 277-303.
- [52] S. Bismo, K. Sutrasno, N. Saksono, E. Karamah, A. Rahardjo, Some aspects of lake water treatment to produce clean water using intergration processes of adsorption, filtration and ozonation, *World Appl Sci J.* 7 (2009) 472-478.
- [53] F. Akbal, A.N. Onar, Photocatalytic degradation of phenol, *Environ Monit Assess.* 83 (2003) 295-302.
- [54] J. Sun, X. Li, Y. Quan, Y. Yin, S. Zheng, Effect of long-term organic removal on ion exchange properties and performance during sewage tertiary treatment by conventional anion exchange resins, *Chemosphere.* 136 (2015) 181-189.
- [55] H. Zhou, D.W. Smith, Advanced technologies in water and wastewater treatment, *J Environ Eng Sci.* 1 (2002) 247-264.
- [56] C. Comninellis, A. Kapalka, S. Malato, S.A. Parsons, I. Poulios, D. Mantzavinos, Advanced oxidation processes for water treatment: advances and trends for R&D, *J Chem Technol Biot.* 83 (2008) 769-776.
- [57] A. Stasinakis, Use of selected advanced oxidation processes (AOPs) for wastewater treatment—a mini review, *Global Nest J.* 10 (2008) 376-385.
- [58] J.M. Poyatos, M. Muño, M. Almecija, J. Torres, E. Hontoria, F. Osorio, Advanced oxidation processes for wastewater treatment: state of the art, *Water Air Soil Pollut.* 205 (2010) 187-204.
- [59] S. Parsons, Advanced oxidation processes for water and wastewater treatment, IWA publishing 2004.

- [60] S. Li, Z. Ma, J. Zhang, Y. Wu, Y. Gong, A comparative study of photocatalytic degradation of phenol of TiO₂ and ZnO in the presence of manganese dioxides, *Catalysis Today*. 139 (2008) 109-112.
- [61] R. Maciel, G. Sant'Anna, M. Dezotti, Phenol removal from high salinity effluents using Fenton's reagent and photo-Fenton reactions, *Chemosphere*. 57 (2004) 711-719.
- [62] W.H. Glaze, J.-W. Kang, D.H. Chapin, The chemistry of water treatment processes involving ozone, hydrogen peroxide and ultraviolet radiation, *Ozone-Sci Eng* 9(1987) 335-352.
- [63] P.R. Gogate, A.B. Pandit, A review of imperative technologies for wastewater treatment I: oxidation technologies at ambient conditions, *Adv Environ Res*. 8 (2004) 501-551.
- [64] A. Matilainen, M. Sillanpää, Removal of natural organic matter from drinking water by advanced oxidation processes, *Chemosphere*. 80 (2010) 351-365.
- [65] S. Esplugas, J. Gimenez, S. Contreras, E. Pascual, M. Rodríguez, Comparison of different advanced oxidation processes for phenol degradation, *Water Res*. 36 (2002) 1034-1042.
- [66] S. Esplugas, J. Gimenez, S. Contreras, E. Pascual, M. Rodríguez, Book 2002, pp. 1034-1042.
- [67] R. Maciel, G. Sant'Anna, M. Dezotti, Phenol removal from high salinity effluents using Fenton's reagent and photo-Fenton reactions, *Chemosphere*. 57 (2004) 711-719.
- [68] E.E. Bamuza-Pemu, Photocatalytic degradation of phenolic compounds and algal metabolites in water, 2014.
- [69] S.K. Kansal, M. Singh, D. Sud, Studies on photodegradation of two commercial dyes in aqueous phase using different photocatalysts, *J Hazard Mater*. 141 (2007) 581-590.
- [70] U.G. Akpan, B.H. Hameed, Parameters affecting the photocatalytic degradation of dyes using TiO₂-based photocatalysts: A review, *J Hazard Mater*. 170 (2009) 520-529.
- [71] D.S. Bhatkhande, V.G. Pangarkar, A.A.C.M. Beenackers, Photocatalytic degradation for environmental applications – a review, *J ChemTechnol Biot* 77 (2002) 102-116.
- [72] C. Jimmy, Photochemical growth of nanoporous SnO₂ at the air–water interface and its high photocatalytic activity, *J Mater Chem*. 20 (2010) 5641-5645.

- [73] A. Fujishima, Electrochemical photolysis of water at a semiconductor electrode, *Nature*. 238 (1972) 37-38.
- [74] B. Ohtani, Photocatalysis A to Z—What we know and what we do not know in a scientific sense, *J Photoch Photobio C*. 11 (2010) 157-178.
- [75] J.-M. Herrmann, Heterogeneous photocatalysis: fundamentals and applications to the removal of various types of aqueous pollutants, *Catal Today*. 53 (1999) 115-129.
- [76] F. Vatansever, C. Ferraresi, M.V.P. de Sousa, R. Yin, A. Rineh, S.K. Sharma, M.R. Hamblin, Can biowarfare agents be defeated with light?, *Virulence*. 4 (2013) 796-825.
- [77] P.W. Brickner, R.L. Vincent, M. First, E. Nardell, M. Murray, W. Kaufman, The application of ultraviolet germicidal irradiation to control transmission of airborne disease: bioterrorism countermeasure, *Public Health Rep*. 118 (2003) 99.
- [78] S. Vilhunen, H. Särkkä, M. Sillanpää, Ultraviolet light-emitting diodes in water disinfection, *Environ Sci Pollut R*. 16 (2009) 439-442.
- [79] E. Repo, S. Rengaraj, S. Pulkka, E. Castagnoli, S. Suihkonen, M. Sopanen, M. Sillanpää, Photocatalytic degradation of dyes by CdS microspheres under near UV and blue LED radiation, *Sep Purif Technol*. 120 (2013) 206-214.
- [80] S.H. Vilhunen, M.E. Sillanpää, Ultraviolet light emitting diodes and hydrogen peroxide in the photodegradation of aqueous phenol, *J Hazard Mater*. 161 (2009) 1530-1534.
- [81] S.L. Miller, J. Linnes, J. Luongo, Ultraviolet germicidal irradiation: future directions for air disinfection and building applications, *Photoch Photobio*. 89 (2013) 777-781.
- [82] T.L. Thompson, J.T. Yates, Surface Science Studies of the Photoactivation of TiO₂ New Photochemical Processes, *Chem Rev*. 106 (2006) 4428-4453.
- [83] N.S. Lewis, Toward Cost-Effective Solar Energy Use, *Science*. 315 (2007) 798-801.
- [84] A. Kudo, Y. Miseki, Heterogeneous photocatalyst materials for water splitting, *Chem Soc Rev*. 38 (2009) 253-278.
- [85] A.L. Linsebigler, G. Lu, J.T. Yates, Photocatalysis on TiO₂ Surfaces: Principles, Mechanisms, and Selected Results, *Chem Rev*. 95 (1995) 735-758.
- [86] I. Kondarides Dimitris, encyclopaedia of life support systems (EOLSS), (2005).

- [87] R. van Eldik, C.D. Hubbard, *Advances in Inorganic Chemistry*, Elsevier Science 2009.
- [88] M. Batzill, U. Diebold, *The surface and materials science of tin oxide*, *Prog Surf Sci.* 79 (2005) 47-154.
- [89] E. Morais, L.V.d.A. Scalvi, L. Ravaro, M.S. Li, E. Floriano, *Optical and Transport Properties of Rare-earth Trivalent Ions Located at Different Sites in Sol-gel SnO₂*, *J Phys: , IOP Publishing, Conference Series*, 2010, pp. 012005.
- [90] D.-H. Kim, G.-W. Lee, Y.-C. Kim, *Interaction of zinc interstitial with oxygen vacancy in zinc oxide: An origin of n-type doping*, *Solid State Commun.* 152 (2012) 1711-1714.
- [91] K.G. Godinho, A. Walsh, G.W. Watson, *Energetic and Electronic Structure Analysis of Intrinsic Defects in SnO₂*, *The Journal of Physical Chemistry C.* 113 (2009) 439-448.
- [92] E. Mete, D. Uner, O. Gülseren, Ş. Ellialtıođlu, *Pt-incorporated anatase TiO₂ (001) surface for solar cell applications: First-principles density functional theory calculations*, *Phys Rev B.* 79 (2009) 125418.
- [93] J. Robertson, S. Clark, *Limits to doping in oxides*, *Phys Rev B.* 83 (2011) 075205.
- [94] J. Yu, L. Qi, M. Jaroniec, *Hydrogen production by photocatalytic water splitting over Pt/TiO₂ nanosheets with exposed (001) facets*, *J Phys Chem C.* 114 (2010) 13118-13125.
- [95] S. Millesi, R. Lo Nigro, M. Pedroni, A. Speghini, A. Gulino, *Photoexcited Porphyrins Functionalizing TiO₂ and SnO₂ Nanocrystals*, *J Phys Chem C.* 119 (2015) 23743-23751.
- [96] M. Zhang, G. Sheng, J. Fu, T. An, X. Wang, X. Hu, *Novel preparation of nanosized ZnO–SnO₂ with high photocatalytic activity by homogeneous co-precipitation method*, *Mater Lett.* 59 (2005) 3641-3644.
- [97] H. Xia, H. Zhuang, T. Zhang, D. Xiao, *Visible-light-activated nanocomposite photocatalyst of Fe₂O₃/SnO₂*, *Mater Lett.* 62 (2008) 1126-1128.
- [98] L. Zhang, J. Liu, C. Tang, J. Lv, H. Zhong, Y. Zhao, X. Wang, *Palygorskite and SnO₂–TiO₂ for the photodegradation of phenol*, *Appl Clay Sci.* 51 (2011) 68-73.

- [99] S.Y. Yang, W. Choi, H. Park, TiO₂ Nanotube Array Photoelectrocatalyst and Ni–Sb–SnO₂ Electrocatalyst Bifacial Electrodes: A New Type of Bifunctional Hybrid Platform for Water Treatment, *ACS Appl Mater Interf.* 7 (2015) 1907-1914.
- [100] G. Colon, M. Maicu, M.s. Hidalgo, J. Navio, Cu-doped TiO₂ systems with improved photocatalytic activity, *Appl Catal B- Environ.* 67 (2006) 41-51.
- [101] V. Kruefu, H. Ninsonti, N. Wetchakun, B. Inceesungvorn, P. Pookmanee, S. Phanichphant, Photocatalytic degradation of phenol using Nb-loaded ZnO nanoparticles, *Eng J.* 16 (2012) 91-100.
- [102] A. Hagfeldt, M. Graetzel, Light-induced redox reactions in nanocrystalline systems, *Chem Rev.* 95 (1995) 49-68.
- [103] J. Coey, M. Venkatesan, C. Fitzgerald, Donor impurity band exchange in dilute ferromagnetic oxides, *Nat mate.* 4 (2005) 173-179.
- [104] D. Liu, L. Li, Y. Gao, C. Wang, J. Jiang, Y. Xiong, The Nature of Photocatalytic “Water Splitting” on Silicon Nanowires, *Angewandte Chemie International Edition.* 54 (2015) 2980-2985.
- [105] B. Neppolian, H.C. Choi, S. Sakthivel, B. Arabindoo, V. Murugesan, Solar/UV-induced photocatalytic degradation of three commercial textile dyes, *J Hazard Mater* 89 (2002) 303-317.
- [106] I.K. Konstantinou, T.A. Albanis, Photocatalytic transformation of pesticides in aqueous titanium dioxide suspensions using artificial and solar light: intermediates and degradation pathways, *Appl Catal B-Environ.* 42 (2003) 319-335.
- [107] S. Senthilkumaar, K. Porkodi, R. Vidyalakshmi, Photodegradation of a textile dye catalyzed by sol–gel derived nanocrystalline TiO₂ via ultrasonic irradiation, *J Photoch Photobio A.* 170 (2005) 225-232.
- [108] D. Ravelli, D. Dondi, M. Fagnoni, A. Albini, Photocatalysis. A multi-faceted concept for green chemistry, *Chem Soc Rev.* 38 (2009) 1999-2011.
- [109] N. Hafizah, I. Sopyan, Nanosized TiO₂ Photocatalyst Powder via Sol-Gel Method: Effect of Hydrolysis Degree on Powder Properties, *Int J Photoenergy.* 2009 (2009) 8.
- [110] X. Fu, H. Zhang, S. Niu, Q. Xin, Synthesis and luminescent properties of SnO₂: Eu nanopowder via polyacrylamide gel method, *J Solid State Chem.* 178 (2005) 603-607.

- [111] H. Wang, F. Sun, Y. Zhang, L. Li, H. Chen, Q. Wu, J.C. Yu, Photochemical growth of nanoporous SnO₂ at the air-water interface and its high photocatalytic activity, *J Mater Chem.* 20 (2010) 5641-5645.
- [112] M. Kaneko, I. Okura, *Photocatalysis: Science and Technology*, Springer Berlin Heidelberg 2010.
- [113] K. Hara, T. Horiguchi, T. Kinoshita, K. Sayama, H. Sugihara, H. Arakawa, Highly efficient photon-to-electron conversion with mercurochrome-sensitized nanoporous oxide semiconductor solar cells, *Sol Energ Mat Solar C.* 64 (2000) 115-134.
- [114] M.R. Hoffmann, S.T. Martin, W. Choi, D.W. Bahnemann, Environmental applications of semiconductor photocatalysis, *Chem Rev.* 95 (1995) 69-96.
- [115] Z. Yang, L. Lv, Y. Dai, Z. Xu, D. Qian, Synthesis of ZnO–SnO₂ composite oxides by CTAB-assisted co-precipitation and photocatalytic properties, *Appl Sur Sci.* 256 (2010) 2898-2902.
- [116] D.J. Grimshaw, L.D. Gudza, J. Stilgoe, How Can Nanotechnologies Fulfill the Needs of Developing Countries?, in: E.S. Cozzens, J. Wetmore (Eds.) *Nanotechnology and the Challenges of Equity, Equality and Development*, Springer Netherlands, Dordrecht, 2011, pp. 379-391.
- [117] W.A. Goddard III, D. Brenner, S.E. Lyshevski, G.J. Iafrate, *Handbook of nanoscience, engineering, and technology*, CRC press 2007.
- [118] A.S. Arico, P. Bruce, B. Scrosati, J.-M. Tarascon, W. Van Schalkwijk, Nanostructured materials for advanced energy conversion and storage devices, *Nat Mat.* 4 (2005) 366-377.
- [119] Y. Ogo, H. Hiramatsu, K. Nomura, H. Yanagi, T. Kamiya, M. Hirano, H. Hosono, p-channel thin-film transistor using p-type oxide semiconductor, SnO, *Appl Phys Lett* 93 (2008) 2113.
- [120] Y. Hu, K. Xu, L. Kong, H. Jiang, L. Zhang, C. Li, Flame synthesis of single crystalline SnO nanoplatelets for lithium-ion batteries, *Chem Eng J.* 242 (2014) 220-225.
- [121] C.R. Martin, Nanomaterials: A membrane-based synthetic approach, *Science.* 266 (1994) 1961-1966.
- [122] B.B. Lakshmi, C.J. Patrissi, C.R. Martin, Sol–Gel Template Synthesis of Semiconductor Oxide Micro- and Nanostructures, *Chem Mater.* 9 (1997) 2544-2550.

- [123] J. Zhu, Z. Lu, S. Aruna, D. Aurbach, A. Gedanken, Sonochemical synthesis of SnO₂ nanoparticles and their preliminary study as Li insertion electrodes, *Chem Mater.* 12 (2000) 2557-2566.
- [124] B.G. Pawar, D.V. Pinjari, S.S. Kolekar, A.B. Pandit, S.H. Han, Effect of Sintering Temperatures on the Synthesis of Nanospheres, *Chem Eng* 2012 (2012) 7.
- [125] Z. He, J. Zhou, Synthesis, characterization, and activity of tin oxide nanoparticles: influence of solvothermal time on photocatalytic degradation of rhodamine B, *Mod Res Catal.* 2 (2013) 13.
- [126] N. Bajpai, S. Khan, R. Kher, N. Brahme, S. Dhoble, Sol gel synthesis and photoluminescence study of Eu³⁺ doped SnO₂, *Recent Res Sci Technol.* 4 (2012).
- [127] G. Zhang, C. Xie, S. Zhang, S. Zhang, Y. Xiong, Defect chemistry of the metal cation defects in the p- and n-doped SnO₂ nanocrystalline films, *J Phys Chem C.* 118 (2014) 18097-18109.
- [128] K.C. Sanal, M.K. Jayaraj, Growth and characterization of tin oxide thin films and fabrication of transparent p-SnO/n-ZnO p-n hetero junction, *Mater Sci Eng-B.* 178 (2013) 816-821.
- [129] C. Ahn, J.-M. Triscone, J. Mannhart, Electric field effect in correlated oxide systems, *Nature.* 424 (2003) 1015-1018.
- [130] A. Heller, Chemistry and Applications of Photocatalytic Oxidation of Thin Organic Films, *Accounts Chem Res.* 28 (1995) 503-508.
- [131] J.-Y. Luo, L.-J. Chen, Y.-J. Zhao, P. He, Y.-Y. Xia, The effect of oxygen vacancies on the structure and electrochemistry of LiTi₂(PO₄)₃ for lithium-ion batteries: A combined experimental and theoretical study, *J Power Sources.* 194 (2009) 1075-1080.
- [132] A. Diallo, E. Manikandan, V. Rajendran, M. Maaza, Physical & enhanced photocatalytic properties of green synthesized SnO₂ nanoparticles via *Aspalathus linearis*, *Journal of Alloys and Compounds.* 681 (2016) 561-570.
- [133] D.A. Gaal, J.T. Hupp, Thermally activated, inverted interfacial electron transfer kinetics: High driving force reactions between tin oxide nanoparticles and electrostatically-bound molecular reactants, *Journal of the American Chemical Society.* 122 (2000) 10956-10963.
- [134] J. Bellingham, W. Phillips, C. Adkins, Intrinsic performance limits in transparent conducting oxides, *Journal of Materials Science Letters.* 11 (1992) 263-265.

- [135] A. Fujishima, T.N. Rao, Recent advances in heterogeneous TiO₂ photocatalysis, *J Chem Sci.* 109 (1997) 471-486.
- [136] K.S. Yoo, N.W. Cho, H.S. Song, H.J. Jung, Surface morphology and gas-sensing characteristics of SnO₂-x thin films oxidized from Sn films, *Sensor Actuat B-Chem* 25 (1995) 474-477.
- [137] K. Mishra, K. Johnson, P. Schmidt, Electronic structure of antimony-doped tin oxide, *Phys Rev B.* 51 (1995) 13972.
- [138] Y.-J. Lin, C.-J. Wu, The properties of antimony-doped tin oxide thin films from the sol-gel process, *Surf Coat Tech.* 88 (1997) 239-247.
- [139] C. Goebbert, R. Nonninger, M.A. Aegerter, H. Schmidt, Wet chemical deposition of ATO and ITO coatings using crystalline nanoparticles redispersable in solutions, *Thin Solid Films.* 351 (1999) 79-84.
- [140] S. Shanthi, C. Subramanian, P. Ramasamy, Growth and characterization of antimony doped tin oxide thin films, *Journal of crystal growth.* 197 (1999) 858-864.
- [141] T. Nütz, U.Z. Felde, M. Haase, Wet-chemical synthesis of doped nanoparticles: Blue-colored colloids of n-doped SnO₂:Sb, *Journal of Chemical physics.* 110 (1999).
- [142] J. Rockenberger, U. Zum Felde, M. Tischer, L. Tröger, M. Haase, H. Weller, Near edge X-ray absorption fine structure measurements (XANES) and extended X-ray absorption fine structure measurements (EXAFS) of the valence state and coordination of antimony in doped nanocrystalline SnO₂, *J Chem Phys.* 112 (2000) 4296-4304.
- [143] P. Moseley, Solid state gas sensors, *Meas Sci Technol.* 8 (1997) 223-237.
- [144] N. Yamazoe, N. Miura, Some basic aspects of semiconductor gas sensors, *Chemical sensor technology.* 4 (1992) 19-42.
- [145] Z. Chen, M. Wu, C.-H. Shek, C.L. Wu, J.K. Lai, Multifunctional tin dioxide materials: advances in preparation strategies, microstructure, and performance, *Chem Commun.* 51 (2015) 1175-1184.
- [146] D.M. Poojary, A.I. Bortun, L.N. Bortun, A. Clearfield, Structural Studies on the Ion-Exchanged Phases of a Porous Titanosilicate, Na₂Ti₂O₃SiO₄.2H₂O, *Inorg Chem.* 35 (1996) 6131-6139.
- [147] C. Goebbert, M.A. Aegerter, D. Burgard, R. Nass, H. Schmidt, Ultrafiltration conducting membranes and coatings from redispersable, nanoscaled, crystalline SnO₂:Sb particles, *J Mater Chem.* 9 (1999) 253-258.

- [148] K. Anandan, V. Rajendran, Influence of dopant concentrations (Mn= 1, 2 and 3mol%) on the structural, magnetic and optical properties and photocatalytic activities of SnO₂ nanoparticles synthesized via the simple precipitation process, *Superlattice Microst.* 85 (2015) 185-197.
- [149] M. Dou, C. Persson, Comparative study of rutile and anatase SnO₂ and TiO₂: Band-edge structures, dielectric functions, and polaron effects, *J Appl Phys* 113 (2013) 083703.
- [150] H. Yu, S. Wang, C. Xiao, B. Xiao, P. Wang, Z. Li, M. Zhang, Enhanced acetone gas sensing properties by aurelia-like SnO₂ micro-nanostructures, *Cryst Eng Comm.* 17 (2015) 4316-4324.
- [151] S. Saleh, A. Ibrahim, S. Mohamed, Structural and Optical Properties of Nanostructured Fe-Doped SnO₂, *Acta Physica Polonica, A.* 129 (2016).
- [152] T. Entradas, J.F. Cabrita, S. Dalui, M.R. Nunes, O.C. Monteiro, A.J. Silvestre, Synthesis of sub-5 nm Co-doped SnO₂ nanoparticles and their structural, microstructural, optical and photocatalytic properties, *Mater Chem Phys* 147 (2014) 563-571.
- [153] R. Abe, M. Higashi, K. Sayama, Y. Abe, H. Sugihara, Photocatalytic activity of R₃MO₇ and R₂Ti₂O₇ (R= Y, Gd, La; M= Nb, Ta) for water splitting into H₂ and O₂, *J Phys Chem B* 110 (2006) 2219-2226.
- [154] O. Madelung, U. Rössler, M. Schulz, Tin dioxide (SnO₂) crystal structure, lattice parameters, thermal expansion, *Non-Tetrahedrally Bonded Elements and Binary Compounds I*, Springer Berlin Heidelberg, Berlin, Heidelberg, 1998, pp. 1-2.
- [155] J.A. Toledo-Antonio, R. Gutiérrez-Baez, P.J. Sebastian, A. Vázquez, Thermal stability and structural deformation of rutile SnO₂ nanoparticles, *J Solid State Chem.* 174 (2003) 241-248.
- [156] Q. Zhao, Z. Zhang, T. Dong, Y. Xie, Facile synthesis and catalytic property of porous tin dioxide nanostructures, *J Phys Chem B.* 110 (2006) 15152-15156.
- [157] M. Dimitrov, T. Tsoncheva, S. Shao, R. Köhn, Novel preparation of nanosized mesoporous SnO₂ powders: Physicochemical and catalytic properties, *Appl Catal B- Environ.* 94 (2010) 158-165.
- [158] F. Gu, S.F. Wang, M.K. Lü, G.J. Zhou, D. Xu, D.R. Yuan, Photoluminescence Properties of SnO₂ Nanoparticles Synthesized by Sol-Gel Method, *J Phys Chem B* 108 (2004) 8119-8123.

- [159] A. Kenyon, Recent developments in rare-earth doped materials for optoelectronics, *Prog Quantum Electron.* 26 (2002) 225-284.
- [160] H. Chen, L. Hu, X. Fang, L. Wu, General Fabrication of Monolayer SnO₂ Nanonets for High-Performance Ultraviolet Photodetectors, *Adv Funct Mater.* 22 (2012) 1229-1235.
- [161] P.D.F.N.J.-.-I. data).
- [162] Y. Zhao, Y. Huang, Q. Wang, K. Wang, M. Zong, L. Wang, W. Zhang, X. Sun, Preparation of hollow Zn₂SnO₄ boxes for advanced lithium-ion batteries, *Rsc Advances.* 3 (2013) 14480-14485.
- [163] I.A. Courtney, J. Dahn, Key factors controlling the reversibility of the reaction of lithium with SnO₂ and Sn₂BPO₆ Glass, *Journal of the Electrochemical Society.* 144 (1997) 2943-2948.
- [164] O. Madelung, U. Rössler, M. Schulz, Tin dioxide (SnO₂) crystal structure, lattice parameters, thermal expansion 1998.
- [165] M. Batzill, U. Diebold, The surface and materials science of tin oxide, *Prog Surf Science.* 79 (2005) 47-154.
- [166] Ben Mills (Public Domain). Rutile structure, 07.01.2016.
<<https://en.wikipedia.org/wiki/Rutile#/media/File:Rutile-unit-cell-3D-balls.png>>.
- [167] Y. Du, N. Zhang, C. Wang, Photo-catalytic degradation of trifluralin by SnO₂-doped Cu₂O crystals, *Catal Commun.* 11 (2010) 670-674.
- [168] S. Chaisitsak, Nanocrystalline SnO₂:F thin films for liquid petroleum gas sensors, *Sensor.* 11 (2011) 7127-7140.
- [169] A. Bhattacharjee, M. Ahmaruzzaman, Photocatalytic-degradation and reduction of organic compounds using SnO₂ quantum dots (via a green route) under direct sunlight, *Rsc Advances.* 5 (2015) 66122-66133.
- [170] M. Morimitsu, Y. Ozaki, S. Suzuki, M. Matsunaga, Effects of surface modification with platinum and ruthenium on temperature and humidity dependence of SnO₂-based CO gas sensors, *Sensor Actuat B-Chem.* 67 (2000) 184-188.
- [171] Y.-S. Choe, New gas sensing mechanism for SnO₂ thin-film gas sensors fabricated by using dual ion beam sputtering, *Sensor Actuat B-Chem.* 77 (2001) 200-208.

- [172] B.-Y. Wei, M.-C. Hsu, P.-G. Su, H.-M. Lin, R.-J. Wu, H.-J. Lai, A novel SnO₂ gas sensor doped with carbon nanotubes operating at room temperature, *Sensor Actuat B-Chem.* 101 (2004) 81-89.
- [173] H. Wang, Y. Li, M. Yang, Fast response thin film SnO₂ gas sensors operating at room temperature, *Sensor Actuat B-Chem.* 119 (2006) 380-383.
- [174] G. Korotcenkov, B. Cho, Thin film SnO₂-based gas sensors: film thickness influence, *Sensor Actuat B-Chem.* 142 (2009) 321-330.
- [175] I. Kocemba, J. Rynkowski, The influence of catalytic activity on the response of Pt/SnO₂ gas sensors to carbon monoxide and hydrogen, *Sensor Actuat B-Chem.* 155 (2011) 659-666.
- [176] Z. Dai, J. Gole, J. Stout, Z. Wang, Tin oxide nanowires, nanoribbons, and nanotubes, *J Phys Chem B.* 106 (2002) 1274-1279.
- [177] S.K. Tammina, B.K. Mandal, Tyrosine mediated synthesis of SnO₂ nanoparticles and their photocatalytic activity towards Violet 4 BSN dye, *Journal of Molecular Liquids.* 221 (2016) 415-421.
- [178] N. Rajesh, J. Kannan, T. Krishnakumar, S. Leonardi, G. Neri, Sensing behavior to ethanol of tin oxide nanoparticles prepared by microwave synthesis with different irradiation time, *Sensors and Actuators B: Chemical.* 194 (2014) 96-104.
- [179] S. Goldsmith, E. Çetinörgü, R. Boxman, Modeling the optical properties of tin oxide thin films, *Thin Solid Films.* 517 (2009) 5146-5150.
- [180] R. Gupta, K. Ghosh, R. Patel, S. Mishra, P. Kahol, Highly conducting and transparent tin-doped CdO thin films for optoelectronic applications, *Materials Letters.* 62 (2008) 4103-4105.
- [181] K. Bouras, J.-L. Rehspringer, G. Schmerber, H. Rinnert, S. Colis, G. Ferblantier, M. Balestrieri, D. Ihiwakrim, A. Dinia, A. Slaoui, Optical and structural properties of Nd doped SnO₂ powder fabricated by the sol-gel method, *J Mater Chem C* 2(2014) 8235-8243.
- [182] G. Xi, J. Ye, Ultrathin SnO₂ nanorods: Template- and surfactant-free solution phase synthesis, growth mechanism, optical, gas-Sensing, and surface adsorption properties, *Inorg Chem* 49 (2010) 2302-2309.
- [183] A. Azam, A.S. Ahmed, M.S. Ansari, M. Shafeeq M, A.H. Naqvi, Study of electrical properties of nickel doped SnO₂ ceramic nanoparticles, *J Alloy Compd.* 506 (2010) 237-242.

- [184] X. Fang, J. Yan, L. Hu, H. Liu, P.S. Lee, Thin SnO₂ Nanowires with Uniform Diameter as Excellent Field Emitters: A Stability of More Than 2400 Minutes, *Adv Functional Mater.* 22 (2012) 1613-1622.
- [185] N. Yongvanich, P. Visuttipitukkul, P. Leksuma, V. Vutcharaammat, P. Sangwanpanit, Sinterability and microstructure of Bi-added SnO₂ nanomaterials by precipitation method, *J Met Mater Min.* 20 (2010) 67-72.
- [186] N. Li, K. Du, G. Liu, Y. Xie, G. Zhou, J. Zhu, F. Li, H.-M. Cheng, Effects of oxygen vacancies on the electrochemical performance of tin oxide, *J Mater Chem A* 1(2013) 1536-1539.
- [187] W. Bergermayer, I. Tanaka, Reduced SnO₂ surfaces by first-principles calculations, *Appl Phys Lett.* 84 (2004) 909-911.
- [188] A.A. Yawalkar, D.S. Bhatkhande, V.G. Pangarkar, A.A. Beenackers, Solar-assisted photochemical and photocatalytic degradation of phenol, *J Chem Technol Biot* 76 (2001) 363-370.
- [189] B.H. Bielski, D.E. Cabelli, R.L. Arudi, A.B. Ross, Reactivity of HO₂/O⁻ 2 radicals in aqueous solution, *Journal of physical and chemical reference data.* 14 (1985) 1041-1100.
- [190] U.I. Gaya, A.H. Abdullah, Heterogeneous photocatalytic degradation of organic contaminants over titanium dioxide: a review of fundamentals, progress and problems, *Journal of Photochemistry and Photobiology C: Photochemistry Reviews.* 9 (2008) 1-12.
- [191] J.-M. Herrmann, Heterogeneous photocatalysis: fundamentals and applications to the removal of various types of aqueous pollutants, *Catalysis Today.* 53 (1999) 115-129.
- [192] K.-i. Okamoto, Y. Yamamoto, H. Tanaka, A. Itaya, Kinetics of heterogeneous photocatalytic decomposition of phenol over anatase TiO₂ powder, *B Chem Soc JPN.* 58 (1985) 2023-2028.
- [193] S. Tunesi, M. Anderson, Influence of chemisorption on the photodecomposition of salicylic acid and related compounds using suspended titania ceramic membranes, *J Phys Chem-us* 95 (1991) 3399-3405.
- [194] N. Li, K. Du, G. Liu, Y. Xie, G. Zhou, J. Zhu, F. Li, H.-M. Cheng, Effects of oxygen vacancies on the electrochemical performance of tin oxide, *Journal of Materials Chemistry A.* 1 (2013) 1536-1539.

- [195] G. Liu, H.G. Yang, X. Wang, L. Cheng, H. Lu, L. Wang, G.Q. Lu, H.-M. Cheng, Enhanced Photoactivity of Oxygen-Deficient Anatase TiO₂ Sheets with Dominant {001} Facets, *The Journal of Physical Chemistry C*. 113 (2009) 21784-21788.
- [196] Z. He, C. Wang, H. Wang, F. Hong, X. Xu, J. Chen, S. Song, Increasing the catalytic activities of iodine doped titanium dioxide by modifying with tin dioxide for the photodegradation of 2-chlorophenol under visible light irradiation, *J Hazard Mater*. 189 (2011) 595-602.
- [197] Y. Cong, J. Zhang, F. Chen, M. Anpo, D. He, Preparation, photocatalytic activity, and mechanism of nano-TiO₂ co-doped with nitrogen and iron (III), *J Phys Chem C*. 111 (2007) 10618-10623.
- [198] S. Kamble, S. Sawant, V. Pangarkar, Photocatalytic mineralization of phenoxyacetic acid using concentrated solar radiation and titanium dioxide in slurry photoreactor, *Chem Eng Res Design*. 84 (2006) 355-362.
- [199] S. Wu, H. Cao, S. Yin, X. Liu, X. Zhang, Amino Acid-Assisted Hydrothermal Synthesis and Photocatalysis of SnO₂ Nanocrystals, *J Phys Chem C* 113 (2009) 17893-17898.
- [200] G. Sangami, N. Dharmaraj, UV-visible spectroscopic estimation of photodegradation of rhodamine-B dye using tin (IV) oxide nanoparticles, *Spectrochim Acta A*. 97 (2012) 847-852.
- [201] E. Haritha, S.M. Roopan, G. Madhavi, G. Elango, N.A. Al-Dhabi, M.V. Arasu, Green chemical approach towards the synthesis of SnO₂ Nps in argument with photocatalytic degradation of diazo dye and its kinetic studies, *Journal of Photochemistry and Photobiology B: Biology*. 162 (2016) 441-447.
- [202] G.-B. Hong, C.-J. Jiang, Synthesis of SnO₂ nanoparticles using extracts from *Litsea cubeba* fruits, *Materials letters*. 194 (2017) 164-167.
- [203] V. Štengl, S. Bakardjieva, N. Murafa, Preparation and photocatalytic activity of rare earth doped TiO₂ nanoparticles, *Mater Chem Phys*. 114 (2009) 217-226.
- [204] S. Tojo, T. Tachikawa, M. Fujitsuka, T. Majima, Iodine-doped TiO₂ photocatalysts: correlation between band structure and mechanism, *J Phys Chem C*. 112 (2008) 14948-14954.
- [205] K. Kovács, S. He, V. Mile, T. Csay, E. Takács, L. Wojnárovits, Ionizing radiation induced degradation of diuron in dilute aqueous solution, *Chem Cent J*. 9 (2015) 1-10.

- [206] V.M. Cristante, S.M.A. Jorge, J.P.S. Valente, M.J. Saeki, A.O. Florentino, P.M. Padilha, TiO₂ films organofunctionalized with 2-aminothiazole ligand and adsorbed Pd(II) ions applied in the photocatalytic degradation of phenol in an aqueous medium, *Thin Solid Films*. 515 (2007) 5334-5340.
- [207] M.N. Chong, B. Jin, C.W.K. Chow, C. Saint, Recent developments in photocatalytic water treatment technology: A review, *Water Res.* 44 (2010) 2997-3027.
- [208] S.G. Anju, S. Yesodharan, E.P. Yesodharan, Zinc oxide mediated sonophotocatalytic degradation of phenol in water, *Chem Eng J.* 189–190 (2012) 84-93.
- [209] A.E. Cassano, O.M. Alfano, Reaction engineering of suspended solid heterogeneous photocatalytic reactors, *Catal Today*. 58 (2000) 167-197.
- [210] H. Peelaers, E. Kioupakis, C.G. Van de Walle, Fundamental limits on optical transparency of transparent conducting oxides: Free-carrier absorption in SnO₂, *Appl Phys Lett*. 100 (2012) 011914.
- [211] N.R. Srinivasan, R. Bandyopadhyaya, Sn_xTi_{1-x}O₂ solid-solution-nanoparticle embedded mesoporous silica (SBA-15) hybrid as an engineered photocatalyst with enhanced activity, *Faraday Discussions*. 186 (2016) 353-370.
- [212] C. Xiong, K.J. Balkus Jr, Mesoporous molecular sieve derived TiO₂ nanofibers doped with SnO₂, *J Phys Chem C*. 111 (2007) 10359-10367.
- [213] K. Vinodgopal, P.V. Kamat, Enhanced rates of photocatalytic degradation of an azo dye using SnO₂/TiO₂ coupled semiconductor thin films, *Environ sci technol.* 29 (1995) 841-845.
- [214] L.-R. Hou, C.-Z. Yuan, Y. Peng, Synthesis and photocatalytic property of SnO₂/TiO₂ nanotubes composites, *J Hazard Mater*. 139 (2007) 310-315.
- [215] Y.-F. Tu, S.-Y. Huang, J.-P. Sang, X.-W. Zou, Synthesis and photocatalytic properties of Sn-doped TiO₂ nanotube arrays, *J Alloy Compd.* 482 (2009) 382-387.
- [216] M.F. Abdel-Messih, M.A. Ahmed, A.S. El-Sayed, Photocatalytic decolorization of Rhodamine B dye using novel mesoporous SnO₂-TiO₂ nano mixed oxides prepared by sol-gel method, *J Photoch Photobio A*. 260 (2013) 1-8.
- [217] Z. Wen, G. Wang, W. Lu, Q. Wang, Q. Zhang, J. Li, Enhanced photocatalytic properties of mesoporous SnO₂ induced by low concentration ZnO doping, *Cryst Growth Design*. 7 (2007) 1722-1725.

- [218] Z. Zhang, C. Shao, X. Li, L. Zhang, H. Xue, C. Wang, Y. Liu, Electrospun Nanofibers of ZnO–SnO₂ Heterojunction with High Photocatalytic Activity, *J Phys Chem C*. 114 (2010) 7920-7925.
- [219] Cun Wang, Bo-Qing Xu, Xinming Wang, J. Zhao, Preparation and photocatalytic activity of ZnO/TiO₂/SnO₂ mixture, *J Solid State Chem*. 178 (2005) 3500-3506.
- [220] J. Liqiang, F. Honggang, W. Baiqi, W. Dejun, X. Baifu, L. Shudan, S. Jiazhong, Effects of Sn dopant on the photoinduced charge property and photocatalytic activity of TiO₂ nanoparticles, *Appl Catal B-Environ* 62 (2006) 282-291.
- [221] R. Bhosale, S. Pujari, G. Muley, B. Pagare, A. Gambhire, Visible-light-activated nanocomposite photocatalyst of Cr₂O₃/SnO₂, *J Nano Chem*. 3 (2013) 1-7.
- [222] M. Niu, F. Huang, L. Cui, P. Huang, Y. Yu, Y. Wang, Hydrothermal synthesis, structural characteristics, and enhanced photocatalysis of SnO₂/α-Fe₂O₃ semiconductor nanoheterostructures, *Acs Nano*. 4 (2010) 681-688.
- [223] M. Shahid, I. Shakir, S.-J. Yang, D.J. Kang, Facile synthesis of core–shell SnO₂/V₂O₅ nanowires and their efficient photocatalytic property, *Mater Chem Phys*. 124 (2010) 619-622.
- [224] K. Li, Y. Wang, S. Wang, B. Zhu, S. Zhang, W. Huang, S. Wu, A comparative study of CuO/TiO₂-SnO₂, CuO/TiO₂ and CuO/SnO₂ catalysts for low-temperature CO oxidation, *J Nat Gas Chem*. 18 (2009) 449-452.
- [225] H.-l. Xia, H.-s. Zhuang, T. Zhang, D.-c. Xiao, Photocatalytic degradation of Acid Blue 62 over CuO-SnO₂ nanocomposite photocatalyst under simulated sunlight, *J Environ Sci*. 19 (2007) 1141-1145.
- [226] Y.C. Zhang, Z.N. Du, K.W. Li, M. Zhang, D.D. Dionysiou, High-Performance Visible-Light-Driven SnS₂/SnO₂ Nanocomposite Photocatalyst Prepared via In situ Hydrothermal Oxidation of SnS₂ Nanoparticles, *ACS Applied Materials & Interfaces*. 3 (2011) 1528-1537.
- [227] E.L. Foletto, S. Battiston, G.C. Collazzo, M.M. Bassaco, M.A. Mazutti, Degradation of Leather Dye Using CeO₂–SnO₂ Nanocomposite as Photocatalyst Under Sunlight, *Water Air Soil Poll*. 223 (2012) 5773-5779.
- [228] Y. Liu, P. Zhang, B. Tian, J. Zhang, Core–Shell Structural CdS@ SnO₂ Nanorods with Excellent Visible-Light Photocatalytic Activity for the Selective Oxidation of Benzyl Alcohol to Benzaldehyde, *ACS appl Mater Inter*. 7 (2015) 13849-13858.

- [229] M. Sun, Q. Zhao, C. Du, Z. Liu, Enhanced visible light photocatalytic activity in BiOCl/SnO₂: heterojunction of two wide band-gap semiconductors, *RSC Advances*. 5 (2015) 22740-22752.
- [230] A. Erkan, U. Bakir, G. Karakas, Photocatalytic microbial inactivation over Pd doped SnO₂ and TiO₂ thin films, *J Photoch Photobio A*. 184 (2006) 313-321.
- [231] S. Kim, S.-J. Hwang, W. Choi, Visible light active platinum-ion-doped TiO₂ photocatalyst, *J Phys Chem B*. 109 (2005) 24260-24267.
- [232] P.G. Harrison, C. Bailey, W. Azelee, Modified Tin(IV) Oxide (M/SnO₂M=Cr, La, Pr, Nd, Sm, Gd) Catalysts for the Oxidation of Carbon Monoxide and Propane, *J Catal*. 186 (1999) 147-159.
- [233] A.-W. Xu, Y. Gao, H.-Q. Liu, The preparation, characterization, and their photocatalytic activities of rare-earth-doped TiO₂ nanoparticles, *J Catal*. 207 (2002) 151-157.
- [234] J. Reszczyńska, T. Grzyb, J.W. Sobczak, W. Lisowski, M. Gazda, B. Ohtani, A. Zaleska, Lanthanide co-doped TiO₂: The effect of metal type and amount on surface properties and photocatalytic activity, *Applied Surface Science*. 307 (2014) 333-345.
- [235] E.R. Leite, I.T. Weber, E. Longo, J.A. Varela, A New Method to Control Particle Size and Particle Size Distribution of SnO₂ Nanoparticles for Gas Sensor Applications, *Advanced Materials*. 12 (2000) 965-968.
- [236] I. Weber, A. Maciel, P.N. Lisboa-Filho, E. Longo, E. Leite, C. Paiva-Santos, Y. Maniette, W.H. Schreiner, Effects of synthesis and processing on supersaturated rare earth-doped nanometric SnO₂ powders, *Nano Letters*. 2 (2002) 969-973.
- [237] E.R. Leite, A.P. Maciel, I.T. Weber, P.N. Lisboa-Filho, E. Longo, C.O. Paiva-Santos, A.V.C. Andrade, C.A. Pakoscimas, Y. Maniette, W.H. Schreiner, Development of Metal Oxide Nanoparticles with High Stability Against Particle Growth Using a Metastable Solid Solution, *Advanced Materials*. 14 (2002) 905-908.
- [238] J. Reszczyńska, T. Grzyb, J.W. Sobczak, W. Lisowski, M. Gazda, B. Ohtani, A. Zaleska, Visible light activity of rare earth metal doped (Er³⁺, Yb³⁺ or Er³⁺/Yb³⁺) titania photocatalysts, *Applied Catalysis B: Environmental*. 163 (2015) 40-49.
- [239] J. Hays, A. Punnoose, R. Baldner, M.H. Engelhard, J. Peloquin, K. Reddy, Relationship between the structural and magnetic properties of Co-doped SnO₂ nanoparticles, *Phys Rev B*. 72 (2005) 075203.

- [240] J. del-Castillo, V. Rodríguez, A. Yanes, J. Méndez-Ramos, Energy transfer from the host to Er^{3+} dopants in semiconductor SnO_2 nanocrystals segregated in sol-gel silica glasses, *J Nanopart Res.* 10 (2008) 499-506.
- [241] S.-S. Chang, M.S. Jo, Luminescence properties of Eu-doped SnO_2 , *Ceram Int.* 33 (2007) 511-514.
- [242] T. Tachikawa, T. Ishigaki, J.-G. Li, M. Fujitsuka, T. Majima, Defect-Mediated Photoluminescence Dynamics of Eu^{3+} -Doped TiO_2 Nanocrystals Revealed at the Single-Particle or Single-Aggregate Level, *Angew Chem Int Edit.* 47 (2008) 5348-5352.
- [243] C. Piguet, J.C.G. Buezli, G. Bernardinelli, G. Hopfgartner, A.F. Williams, Self-assembly and photophysical properties of lanthanide dinuclear triple-helical complexes, *J Am Chem Soc.* 115 (1993) 8197-8206.
- [244] F. Gu, S.F. Wang, C.F. Song, M.K. Lü, Y.X. Qi, G.J. Zhou, D. Xu, D.R. Yuan, Synthesis and luminescence properties of SnO_2 nanoparticles, *Chem Phys Lett.* 372 (2003) 451-454.
- [245] F. Gu, S.F. Wang, M.K. Lü, Y.X. Qi, G.J. Zhou, D. Xu, D.R. Yuan, Luminescent characteristics of Eu^{3+} in SnO_2 nanoparticles, *Opt Mater.* 25 (2004) 59-64.
- [246] H. Coelho-Júnior, J. Aquino, F. Aragón, P. Hidalgo, R. Cohen, L. Nagamine, J. Coaquira, S. Da Silva, H. Brito, Doping effects on the structural, magnetic, and hyperfine properties of Gd-doped SnO_2 nanoparticles, *J Nanopart Res.* 16 (2014) 1-9.
- [247] J. Gouteron, D. Michel, A. Lejus, J. Zarembowitch, Raman spectra of lanthanide sesquioxide single crystals: correlation between A and B-type structures, *J Solid State Chem.* 38 (1981) 288-296.
- [248] H. Nakane, A. Noya, S. Kuriki, G. Matsumoto, Dielectric properties of europium oxide films, *Thin Solid Films.* 59 (1979) 291-293.
- [249] M. Jayaraj, C. Vallabhan, Dielectric and optical properties of europium oxide films, *Thin Solid Films.* 177 (1989) 59-67.
- [250] Y. Feng, Y.-H. Cui, J. Liu, B.E. Logan, Factors affecting the electro-catalytic characteristics of Eu doped SnO_2/Sb electrode, *J Hazard Mater.* 178 (2010) 29-34.
- [251] T. Jinkawa, G. Sakai, J. Tamaki, N. Miura, N. Yamazoe, Relationship between ethanol gas sensitivity and surface catalytic property of tin oxide sensors modified with acidic or basic oxides, *J Mol Catal A-Chem.* 155 (2000) 193-200.

- [252] N. Carreño, amp, x, L.V, H.V. Fajardo, A.P. Maciel, A. Valentini, F.M. Pontes, L.F.D. Probst, E.R. Leite, E. Longo, Selective synthesis of vinyl ketone over SnO₂ nanoparticle catalysts doped with rare earths, *J Mol Catal A-Chem.* 207 (2004) 91-96.
- [253] J.S. Reed, *Principles of ceramics processing*, (1995).
- [254] S. Matsushima, T. Maekawa, J. Tamaki, N. Miura, N. Yamazoe, Role of additives on alcohol sensing by semiconductor gas sensor, *Chem Lett.* (1989) 845-848.
- [255] N. Carreno, A. Maciel, E. Leite, P.N. Lisboa-Filho, E. Longo, A. Valentini, L. Probst, C. Paiva-Santos, W. Schreiner, The influence of cation segregation on the methanol decomposition on nanostructured SnO₂, *Sensor Actuat B-Chem.* 86 (2002) 185-192.
- [256] P.G. Harrison, B.M. Maunders, Tin oxide surfaces. Part 12.—A comparison of the nature of tin (IV) oxide, tin (IV) oxide–silica and tin (IV) oxide–palladium oxide: surface hydroxyl groups and ammonia adsorption, *J Chem Soc Faraday T 1: Phys Chem Condensed Phases.* 80 (1984) 1341-1356.
- [257] F.B. Li, X.Z. Li, M.F. Hou, K.W. Cheah, W.C.H. Choy, Enhanced photocatalytic activity of Ce³⁺–TiO₂ for 2-mercaptobenzothiazole degradation in aqueous suspension for odour control, *Applied Catalysis A: General.* 285 (2005) 181-189.
- [258] J.M. López, A.L. Gilbank, T. García, B. Solsona, S. Agouram, L. Torrente-Murciano, The prevalence of surface oxygen vacancies over the mobility of bulk oxygen in nanostructured ceria for the total toluene oxidation, *Applied Catalysis B: Environmental.* 174 (2015) 403-412.
- [259] C. Liu, X. Tang, C. Mo, Z. Qiang, Characterization and activity of visible-light-driven TiO₂ photocatalyst codoped with nitrogen and cerium, *J Solid State Chem.* 181 (2008) 913-919.
- [260] S.K. Muduli, S. Wang, S. Chen, C.F. Ng, C.H.A. Huan, T.C. Sum, H.S. Soo, Mesoporous cerium oxide nanospheres for the visible-light driven photocatalytic degradation of dyes, *Beilstein Journal of Nanotechnology.* 5 (2014) 517-523.
- [261] L. Singh, M.N. Luwang, S. Srivastava, Luminescence and photocatalytic studies of Sm³⁺ ion doped SnO₂ nanoparticles, *New J Chem.* 38 (2014) 115-121.
- [262] Y.-H. Cui, Y.-J. Feng, J. Liu, N. Ren, Comparison of various organic compounds destruction on rare earths doped Ti/Sb-SnO₂ electrodes, *J Hazar Mater.* 239–240 (2012) 225-232.
- [263] C.-M. Fan, Y. Peng, Q. Zhu, L. Lin, R.-X. Wang, A.-W. Xu, Synproportionation Reaction for the Fabrication of Sn²⁺ Self-Doped SnO_{2-x} Nanocrystals with Tunable

Band Structure and Highly Efficient Visible Light Photocatalytic Activity, *J Phys Chem-US* 117 (2013) 24157-24166.

[264] F. Gu, S.F. Wang, M.K. Lü, G.J. Zhou, D. Xu, D.R. Yuan, Photoluminescence properties of SnO₂ nanoparticles synthesized by sol-gel method, *J Phys Chem B*. 108 (2004) 8119-8123.

[265] S. Kumar, P. Chauhan, V. Kundu, Sol-gel synthesis, structural, morphological and optical properties of Se-doped SnO₂ nanoparticles, *J Mater Sci- Mater Electron*. 1-6.

[266] G. Oldfield, T. Ung, P. Mulvaney, Au@SnO₂ Core-Shell Nanocapacitors, *Advanced Materials*. 12 (2000) 1519-1522.

[267] W. Wu, L. Liao, S. Zhang, J. Zhou, X. Xiao, F. Ren, L. Sun, Z. Dai, C. Jiang, Non-centrosymmetric Au-SnO₂ hybrid nanostructures with strong localization of plasmonic for enhanced photocatalysis application, *Nanosc*. 5 (2013) 5628-5636.

[268] H. You, R. Liu, C. Liang, S. Yang, F. Wang, X. Lu, B. Ding, Gold nanoparticle doped hollow SnO₂ supersymmetric nanostructures for improved photocatalysis, *J Mater Chem A*. 1 (2013) 4097-4104.

[269] S.A. Ansari, M.M. Khan, M.O. Ansari, J. Lee, M.H. Cho, Visible light-driven photocatalytic and photoelectrochemical studies of Ag-SnO₂ nanocomposites synthesized using an electrochemically active biofilm, *Rsc Advances*. 4 (2014) 26013-26021.

[270] C. Liu, L. Fang, X. Zu, W. Zhou, The magnetism and photoluminescence of nickel-doped SnO₂ nano-powders, *Physica Scripta*. 80 (2009) 065703.

[271] W. Wu, L. Liao, S. Zhang, J. Zhou, X. Xiao, F. Ren, L. Sun, Z. Dai, C. Jiang, Non-centrosymmetric Au-SnO₂ hybrid nanostructures with strong localization of plasmonic for enhanced photocatalysis application, *Nanoscale*. 5 (2013) 5628-5636.

[272] A.M. Abdel Hakeem, Structure and magnetic properties of Sn_{1-x}MnxO₂, *J Magn Mater*. 324 (2012) 95-99.

[273] L. Zhang, S. Ge, Y. Zuo, J. Wang, J. Qi, Ferromagnetic properties in undoped and Cr-doped SnO₂ nanowires, *Scripta Materialia*. 63 (2010) 953-956.

[274] J. Coey, A. Douvalis, C. Fitzgerald, M. Venkatesan, Ferromagnetism in Fe-doped SnO₂ thin films, arXiv preprint cond-mat/0401293. (2004).

- [275] J. Mazloom, F.E. Ghodsi, H. Golmojeh, Synthesis and characterization of vanadium doped SnO₂ diluted magnetic semiconductor nanoparticles with enhanced photocatalytic activities, *J Alloy Compd.* 639 (2015) 393-399.
- [276] Q.-R. Zhao, Controllable synthesis and catalytic activity of SnO₂ nanostructures at room temperature, *T Nonferr Metal Soc.* 19 (2009) 1227-1231.
- [277] C. Fitzgerald, M. Venkatesan, A. Douvalis, S. Huber, J. Coey, T. Bakas, SnO₂ doped with Mn, Fe or Co: room temperature dilute magnetic semiconductors, *J Appl Phys.* 95 (2004) 7390-7392.
- [278] G.A. Prinz, Magneto-electronics, *Science.* 282 (1998) 1660-1663.
- [279] Q.-R. Zhao, Controllable synthesis and catalytic activity of SnO₂ nanostructures at room temperature, *T Nonferr Metal Soc.* 19 (2009) 1227-1231.
- [280] M.R. Fadavieslam, Effect of Sb doping on the structural, electrical, and optical properties of SnO₂ thin films prepared through spray pyrolysis, *Journal of Materials Science: Materials in Electronics.* 27 (2016) 4943-4950.
- [281] G. Zhang, C. Xie, S. Zhang, S. Zhang, Y. Xiong, Defect Chemistry of the Metal Cation Defects in the p- and n-Doped SnO₂ Nanocrystalline Films, *J Phys Chem C* 118 (2014) 18097-18109.
- [282] Y. Wang, I. Djerdj, B. Smarsly, M. Antonietti, Antimony-Doped SnO₂ Nanopowders with High Crystallinity for Lithium-Ion Battery Electrode, *Chemistry of Materials.* 21 (2009) 3202-3209.
- [283] M. Kojima, H. Kato, M. Gatto, Blackening of tin oxide thin films heavily doped with antimony, *Philosophical Magazine B.* 68 (1993) 215-222.
- [284] C.A. Vincent, The nature of semiconductivity in polycrystalline tin oxide, *Journal of the Electrochemical Society.* 119 (1972) 515-518.
- [285] Y. Li, J. Liu, J. Liang, X. Yu, D. Li, Tunable Solar-Heat Shielding Property of Transparent Films Based on Mesoporous Sb-Doped SnO₂ Microspheres, *ACS applied materials & interfaces.* 7 (2015) 6574-6583.
- [286] K.H. Kim, S.W. Lee, D.W. Shin, C.G. Park, Effect of antimony addition on electrical and optical properties of tin oxide film, *Journal of the American Ceramic Society.* 77 (1994) 915-921.
- [287] Y. Nakanishi, Y. Suzuki, T. Nakamura, Y. Hatanaka, Y. Fukuda, A. Fujisawa, G. Shimaoka, Coloration of SnSbO thin films, *Applied Surface Science.* 48 (1991) 55-58.

- [288] B. Correa-Lozano, C. Comninellis, A. De Battisti, Electrochemical properties of Ti/SnO₂-Sb₂O₅ electrodes prepared by the spray pyrolysis technique, *J Appl Electrochem.* 26 (1996) 683-688.
- [289] S.K. Johnson, L.L. Houk, J. Feng, R. Houk, D.C. Johnson, Electrochemical incineration of 4-chlorophenol and the identification of products and intermediates by mass spectrometry, *Environ Sci Technol.* 33 (1999) 2638-2644.
- [290] Y. Feng, X.Y. Li, Electro-catalytic oxidation of phenol on several metal-oxide electrodes in aqueous solution, *Water Res.* 37 (2003) 2399-2407.
- [291] M. Behtash, P.H. Joo, S. Nazir, K. Yang, Electronic structures and formation energies of pentavalent-ion-doped SnO₂: First-principles hybrid functional calculations, *J Appl Phys.* 117 (2015) 175101.
- [292] M. Seo, Y. Akutsu, H. Kagemoto, Preparation and properties of Sb-doped SnO₂/metal substrates by sol-gel and dip coating, *Ceram Int.* 33 (2007) 625-629.
- [293] S. Assia, O. Ratiba, M. El Mahdi, K. Mohamed, Optical reflectance of pure and doped tin oxide: From thin films to poly-crystalline silicon/thin film device, *Int J Biol Chem Eng.* 2 (2009) 48-50.
- [294] C. Borrás, C. Berzoy, J. Mostany, B. Scharifker, Oxidation of p-methoxyphenol on SnO₂-Sb₂O₅ electrodes: Effects of electrode potential and concentration on the mineralization efficiency, *J appl Electrochem.* 36 (2006) 433-439.
- [295] Y.H. Wang, K.Y. Chan, X.Y. Li, S.K. So, Electrochemical degradation of 4-chlorophenol at nickel-antimony doped tin oxide electrode, *Chemosphere.* 65 (2006) 1087-1093.
- [296] V. Casey, M.I. Stephenson, A study of undoped and molybdenum doped, polycrystalline, tin oxide thin films produced by a simple reactive evaporation technique, *J Phys D-Appl Phys.* 23 (1990) 1212.
- [297] S. Zhuang, X. Xu, Y. Pang, H. Li, B. Yu, J. Hu, Variation of structural, optical and magnetic properties with Co-doping in Sn_{1-x}CoxO₂ nanoparticles, *J Magn Magn Mater* 327 (2013) 24-27.
- [298] S. Ogale, R. Choudhary, J. Buban, S. Lofland, S. Shinde, S. Kale, V. Kulkarni, J. Higgins, C. Lanci, J. Simpson, High temperature ferromagnetism with a giant magnetic moment in transparent Co-doped SnO_{2-δ}, *Phys Rev Lett.* 91 (2003) 077205_077201-077205_077204.

- [299] Q. Zhao, D. Ju, X. Deng, J. Huang, B. Cao, X. Xu, Morphology-modulation of SnO₂ Hierarchical Architectures by Zn Doping for Glycol Gas Sensing and Photocatalytic Applications, *Scientific Reports*. 5 (2015) 7874.
- [300] H. Huang, S. Tian, J. Xu, Z. Xie, D. Zeng, D. Chen, G. Shen, Needle-like Zn-doped SnO₂ nanorods with enhanced photocatalytic and gas sensing properties, *Nanotechnology*. 23 (2012) 105502.
- [301] L. Fang, X. Zu, Z. Li, S. Zhu, C. Liu, W. Zhou, L. Wang, Synthesis and characteristics of Fe³⁺-doped SnO₂ nanoparticles via sol-gel-calcination or sol-gel-hydrothermal route, *J Alloy Compd*. 454 (2008) 261-267.
- [302] M. Davis, F. Hung-Low, W.M. Hikal, L.J. Hope-Weeks, Enhanced photocatalytic performance of Fe-doped SnO₂ nanoarchitectures under UV irradiation: synthesis and activity, *J Mater Sci*. 48 (2013) 6404-6409.
- [303] X. Wei, R. Georgescu, N. Ali, I. Morjan, T. George, F. Dumitrache, R. Birjega, M. Chipara, R. Skomski, D. Sellmyer, On the Synthesis and Physical Properties of Iron Doped SnO₂ Nanoparticles, *J Nanosci Nanotechnol*. 12 (2012) 9299-9301.
- [304] H. Yang, X. Song, X. Zhang, W. Ao, G. Qiu, Synthesis of vanadium-doped SnO₂ nanoparticles by chemical co-precipitation method, *Mater Lett*. 57 (2003) 3124-3127.
- [305] S. Kumar, P. Chauhan, V. Kundu, Sol-gel synthesis, structural, morphological and optical properties of Se-doped SnO₂ nanoparticles, *Journal of Materials Science: Materials in Electronics*. 27 (2016) 3103-3108.
- [306] P.G. Harrison in: P.G. Harrison (Ed.), *Chemistry of Tin*, Blackie, Glasgow (1989) (Chapter 12).
- [307] G.C. Bond, L.R. Molloy, M.J. Fuller, Oxidation of carbon monoxide over palladium-tin (IV) oxide catalysts: An example of spillover catalysis, *J Chem Soc Chem Commun*. (1975) 796-797.
- [308] M.M. Reddy, A. Chandorkar, E-beam deposited SnO₂, Pt-SnO₂ and Pd-SnO₂ thin films for LPG detection, *Thin Solid Films*. 349 (1999) 260-265.
- [309] S. Gupta, R. Roy, M.P. Chowdhury, A. Pal, Synthesis of SnO₂/Pd composite films by PVD route for a liquid petroleum gas sensor, *Vacuum*. 75 (2004) 111-119.
- [310] M.V. Vaishampayan, R.G. Deshmukh, I. Mulla, Influence of Pd doping on morphology and LPG response of SnO₂, *Sensor Actuat B-Chem*. 131 (2008) 665-672.

- [311] D. Amalric-Popescu, F. Bozon-Verduraz, SnO₂-supported palladium catalysts: activity in deNO_x at low temperature, *Catal Lett.* 64 (2000) 125-128.
- [312] N. Kamiuchi, T. Mitsui, N. Yamaguchi, H. Muroyama, T. Matsui, R. Kikuchi, K. Eguchi, Activation of Pt/SnO₂ catalyst for catalytic oxidation of volatile organic compounds, *Catal Today.* 157 (2010) 415-419.
- [313] A. Diéguez, A. Vilà, A. Cabot, A. Romano-Rodríguez, J.R. Morante, J. Kappler, N. Bârsan, U. Weimar, W. Göpel, Influence on the gas sensor performances of the metal chemical states introduced by impregnation of calcinated SnO₂ sol-gel nanocrystals, *Sensor Actuat B-Chem* 68 (2000) 94-99.
- [314] K. Sekizawa, H. Widjaja, S. Maeda, Y. Ozawa, K. Eguchi, Low temperature oxidation of methane over Pd catalyst supported on metal oxides, *Catal Today.* 59 (2000) 69-74.
- [315] Y. Feng, R. Yao, L. Zhang, Synthesis and sensitivity properties of Pd-doped tin oxide nanoparticles dispersed in mesoporous silica, *Mater Chem Phys.* 89 (2005) 312-315.
- [316] P. Favennec, H. L'haridon, M. Salvi, D. Moutonnet, Y. Le Guillou, Luminescence of erbium implanted in various semiconductors: IV, III-V and II-VI materials, *Electron Lett.* 25 (1989) 718-719.
- [317] S.-S. Chang, D.K. Park, Novel Sn powder preparation by spark processing and luminescence properties, *Mater Sci Eng-B.* 95 (2002) 55-60.
- [318] F. Gu, S.F. Wang, M.K. Lü, X.F. Cheng, S.W. Liu, G.J. Zhou, D. Xu, D.R. Yuan, Luminescence of SnO₂ thin films prepared by spin-coating method, *J Cryst Growth.* 262 (2004) 182-185.
- [319] J. Jeong, S.-P. Choi, C.I. Chang, D.C. Shin, J.S. Park, B. Lee, Y.-J. Park, H.-J. Song, Photoluminescence properties of SnO₂ thin films grown by thermal CVD, *Solid State Commun.* 127 (2003) 595-597.
- [320] A. Cirera, A. Vila, A. Cornet, J. Morante, Properties of nanocrystalline SnO₂ obtained by means of a microwave process, *Mater Sci Eng-C.* 15 (2001) 203-205.
- [321] S. Majumder, S. Hussain, S. Das, R. Bhar, A. Pal, Silicon doped SnO₂ films for liquid petroleum gas sensor, *Vacuum.* 82 (2008) 760-770.
- [322] B. Thomas, S. Benoy, K.K. Radha, Influence of Cs doping in spray deposited SnO₂ thin films for LPG sensors, *Sensor Actuat B-Chem.* 133 (2008) 404-413.

- [323] H. Jin, Y. Xu, G. Pang, W. Dong, Q. Wan, Y. Sun, S. Feng, Al-doped SnO₂ nanocrystals from hydrothermal systems, *Mater Chem Phys.* 85 (2004) 58-62.
- [324] P.G. Harrison, E.W. Thornton, Tin oxide surfaces. Part 4.—Infrared study of the adsorption of oxygen and carbon monoxide+ oxygen mixtures on tin (IV) oxide, and the adsorption of carbon dioxide on ammonia-pretreated tin (IV) oxide, *J Chem Soc Faraday T 1: Phys Chem Condensed Phases.* 74 (1978) 2597-2603.
- [325] S. Rehman, R. Ullah, A. Butt, N. Gohar, Strategies of making TiO₂ and ZnO visible light active, *J Hazard Mater.* 170 (2009) 560-569.
- [326] C. Wen, Y.-J. Zhu, T. Kanbara, H.-Z. Zhu, C.-F. Xiao, Effects of I and F codoped TiO₂ on the photocatalytic degradation of methylene blue, *Desalination.* 249 (2009) 621-625.
- [327] X. Hong, Z. Wang, W. Cai, F. Lu, J. Zhang, Y. Yang, N. Ma, Y. Liu, Visible-Light-Activated Nanoparticle Photocatalyst of Iodine-Doped Titanium Dioxide, *Chemistry of Materials.* 17 (2005) 1548-1552.
- [328] Z. Banyamin, P. Kelly, G. West, J. Boardman, Electrical and Optical Properties of Fluorine Doped Tin Oxide Thin Films Prepared by Magnetron Sputtering, *Coatings.* 4 (2014) 732.
- [329] C. Guillén, J. Herrero, TCO/metal/TCO structures for energy and flexible electronics, *Thin Solid Films.* 520 (2011) 1-17.
- [330] O.I. Velikokhatnyi, P.N. Kumta, Ab-initio study of fluorine-doped tin dioxide: A prospective catalyst support for water electrolysis, *Physica B: Condensed Matter.* 406 (2011) 471-477.
- [331] V. Kumar, A. Govind, R. Nagarajan, Optical and Photocatalytic Properties of Heavily F--Doped SnO₂ Nanocrystals by a Novel Single-Source Precursor Approach, *Inorg Chem.* 50 (2011) 5637-5645.
- [332] G. Liu, C. Sun, X. Yan, L. Cheng, Z. Chen, X. Wang, L. Wang, S.C. Smith, G.Q.M. Lu, H.-M. Cheng, Iodine doped anatase TiO₂ photocatalyst with ultra-long visible light response: correlation between geometric/electronic structures and mechanisms, *J Mater Chem.* 19 (2009) 2822-2829.
- [333] Ç. Kılıç, A. Zunger, Origins of coexistence of conductivity and transparency in SnO₂, *Phys Rev Lett.* 88 (2002) 095501.
- [334] R.G. Gordon, Criteria for choosing transparent conductors, *MRS B.* 25 (2000) 52-57.

- [335] H. Seema, K.C. Kemp, V. Chandra, K.S. Kim, Graphene–SnO₂ composites for highly efficient photocatalytic degradation of methylene blue under sunlight, *Nanotechnology*. 23 (2012) 355705.
- [336] K. Melghit, K. Bouziane, One step aqueous solution preparation of nanosize iron-doped tin oxide from SnO₂· xH₂O gel, *Mater Sci Eng-B*. 128 (2006) 58-62.
- [337] K. Melghit, K. Bouziane, One step aqueous solution preparation of nanosize iron-doped tin oxide from SnO₂· xH₂O gel, *Materials Science and Engineering: B*. 128 (2006) 58-62.
- [338] K. Melghit, K. Bouziane, Low-Temperature Preparation and Magnetic Properties of V-Doped SnO₂ Nanoparticles, *Je Am Ceram Soc*. 90 (2007) 2420-2423.
- [339] J.F. Wager, Transparent electronics, *Science*. 300 (2003) 1245-1246.
- [340] B. Cheng, J.M. Russell, W. Shi, L. Zhang, E.T. Samulski, Large-scale, solution-phase growth of single-crystalline SnO₂ nanorods, *Journal of the American Chemical Society*. 126 (2004) 5972-5973.
- [341] A. Kay, M. Grätzel, Dye-sensitized core-shell nanocrystals: improved efficiency of mesoporous tin oxide electrodes coated with a thin layer of an insulating oxide, *Chemistry of Materials*. 14 (2002) 2930-2935.
- [342] T. Krishnakumar, R. Jayaprakash, V. Singh, B. Mehta, A. Phani, Synthesis and characterization of tin oxide nanoparticle for humidity sensor applications, *Journal of Nano Research, Trans Tech Publ*, 2009, pp. 91-101.
- [343] T. Krishnakumar, R. Jayaprakash, M. Parthibavarman, A. Phani, V. Singh, B. Mehta, Microwave-assisted synthesis and investigation of SnO₂ nanoparticles, *Materials Letters*. 63 (2009) 896-898.
- [344] A.A. Firooz, A.R. Mahjoub, A.A. Khodadadi, Preparation of SnO₂ nanoparticles and nanorods by using a hydrothermal method at low temperature, *Materials Letters*. 62 (2008) 1789-1792.
- [345] J. Kaur, S.C. Roy, M. Bhatnagar, Highly sensitive SnO₂ thin film NO₂ gas sensor operating at low temperature, *Sensor Actuat B-Chem*. 123 (2007) 1090-1095.
- [346] G. Neri, A. Bonavita, G. Micali, N. Donato, F.A. Deorsola, P. Mossino, I. Amato, B. De Benedetti, Ethanol sensors based on Pt-doped tin oxide nanopowders synthesised by gel-combustion, *Sensors and Actuators B: Chemical*. 117 (2006) 196-204.

- [347] H.-C. Chiu, C.-S. Yeh, Hydrothermal synthesis of SnO₂ nanoparticles and their gas-sensing of alcohol, *J Phys Chem C*. 111 (2007) 7256-7259.
- [348] X. Zhou, W. Fu, H. Yang, D. Ma, J. Cao, Y. Leng, J. Guo, Y. Zhang, Y. Sui, W. Zhao, Synthesis and ethanol-sensing properties of flowerlike SnO₂ nanorods bundles by poly (ethylene glycol)-assisted hydrothermal process, *Materials Chemistry and Physics*. 124 (2010) 614-618.
- [349] Y. Wang, X. Jiang, Y. Xia, A Solution-Phase, Precursor Route to Polycrystalline SnO₂ Nanowires That Can Be Used for Gas Sensing under Ambient Conditions, *Journal of the American Chemical Society*. 125 (2003) 16176-16177.
- [350] A. Ayeshamariam, S. Ramalingam, M. Bououdina, M. Jayachandran, Preparation and characterizations of SnO₂ nanopowder and spectroscopic (FT-IR, FT-Raman, UV-Visible and NMR) analysis using HF and DFT calculations, *Spectrochim Acta A*. 118 (2014) 1135-1143.
- [351] R.S. Sonawane, B.B. Kale, M.K. Dongare, Preparation and photo-catalytic activity of Fe-TiO₂ thin films prepared by sol-gel dip coating, *Mater Chem Phys*. 85 (2004) 52-57.
- [352] E. Michel, D. Chaumont, D. Stuerger, SnO₂ thin films prepared by dip-coating from microwave synthesized colloidal suspensions, *Journal of colloid and interface science*. 257 (2003) 258-262.
- [353] Y.-T. Yu, P. Dutta, Synthesis of Au/SnO₂ core-shell structure nanoparticles by a microwave-assisted method and their optical properties, *J Solid State Chem*. 184 (2011) 312-316.
- [354] A.Z. Adamyan, Z.N. Adamian, V.M. Aroutiounian, Preparation of SnO₂ films with thermally stable nanoparticles, *Sensors*. 3 (2003) 438-442.
- [355] S. Ilican, Y. Caglar, M. Caglar, Preparation and characterization of ZnO thin films deposited by sol-gel spin coating method, *J Optoelectron Adv M*. 10 (2008) 2578-2583.
- [356] P. Belleville, C. Bonnin, J.-J. Priotton, Room-temperature mirror preparation using sol-gel chemistry and laminar-flow coating technique, *J sol-gel sci technol*. 19 (2000) 223-226.
- [357] V. Senthilkumar, P. Vickraman, M. Jayachandran, C. Sanjeeviraja, Structural and electrical studies of nano structured Sn_{1-x}Sb_xO₂ (x = 0.0, 1, 2.5, 4.5 and 7 at%) prepared by co-precipitation method, *J Mater Sci: Mater Electron*. 21 (2010) 343-348.

- [358] A. Bouaine, N. Brihi, G. Schmerber, C. Ulhaq-Bouillet, S. Colis, A. Dinia, Structural, Optical, and Magnetic Properties of Co-doped SnO₂ Powders Synthesized by the Coprecipitation Technique, *J Phys Chem C*. 111 (2007) 2924-2928.
- [359] Z. Maolin, S. Guoying, F. Jiamo, A. Taicheng, W. Xinming, H. Xiaohong, Novel preparation of nanosized ZnO–SnO₂ with high photocatalytic activity by homogeneous co-precipitation method, *Mater Lett*. 59 (2005) 3641-3644.
- [360] Ö. Acarbaş, E. Suvacı, A. Doğan, Preparation of nanosized tin oxide (SnO₂) powder by homogeneous precipitation, *Ceramics International*. 33 (2007) 537-542.
- [361] S. Wu, C. Li, W. Wei, H. Wang, Y. Song, Y. Zhu, I. Lu, Nd-doped SnO₂: characterization and its gas sensing property, *J Rare Earths*. 28, Supplement 1 (2010) 171-173.
- [362] X. Yang, L. Wang, Synthesis of novel hexagon SnO₂ nanosheets in ethanol/water solution by hydrothermal process, *Materials Letters*. 61 (2007) 3705-3707.
- [363] T. Sahm, L. Mädler, A. Gurlo, N. Barsan, S.E. Pratsinis, U. Weimar, Flame spray synthesis of tin dioxide nanoparticles for gas sensing, *Sensors and Actuators B: Chemical*. 98 (2004) 148-153.
- [364] K. Melghit, A.K. Mohammed, I. Al-Amri, Chimie douce preparation, characterization and photocatalytic activity of nanocrystalline SnO₂, *Mater Sci Eng-B*. 117 (2005) 302-306.
- [365] J. Gopalakrishnan, Chimie Douce Approaches to the Synthesis of Metastable Oxide Materials, *Chemistry of Materials*. 7 (1995) 1265-1275.
- [366] S.H. Ng, D. Dos Santos, S.Y. Chew, D. Wexler, J. Wang, S. Dou, H.K. Liu, Polyol-mediated synthesis of ultrafine tin oxide nanoparticles for reversible Li-ion storage, *Electrochemistry communications*. 9 (2007) 915-919.
- [367] D. Qu, P. Yan, J. Chang, D. Yan, J. Liu, G. Yue, R. Zhuo, H. Feng, Nanowires and nanowire–nanosheet junctions of SnO₂ nanostructures, *Materials Letters*. 61 (2007) 2255-2258.
- [368] H. Yang, Y. Hu, A. Tang, S. Jin, G. Qiu, Synthesis of tin dioxide nanoparticles by mechanochemical reaction, *J Alloy Compd* 363 (2003) 271-274.
- [369] F. Legendre, S. Poissonnet, P. Bonnaille, Synthesis of nanostructured SnO₂ materials by reactive ball-milling, *Journal of Alloys and Compounds*. 434–435 (2007) 400-404.

- [370] X. Yang, R. Zou, F. Huo, D. Cai, D. Xiao, Preparation and characterization of Ti/SnO₂-Sb₂O₃-Nb₂O₅/PbO₂ thin film as electrode material for the degradation of phenol, *Journal of Hazardous Materials*. 164 (2009) 367-373.
- [371] V. Vidhu, D. Philip, Biogenic synthesis of SnO₂ nanoparticles: Evaluation of antibacterial and antioxidant activities, *Spectrochimica Acta Part A: Molecular and Biomolecular Spectroscopy*. 134 (2015) 372-379.
- [372] T.K. Tseng, Y.S. Lin, Y.J. Chen, H. Chu, A review of photocatalysts prepared by sol-gel method for VOCs removal, *Int j mol sci*. 11 (2010) 2336-2361.
- [373] I.A. Rahman, V. Padavettan, Synthesis of silica nanoparticles by sol-gel: size-dependent properties, surface modification, and applications in silica-polymer nanocomposites—a review, *Journal of Nanomaterials*. 2012 (2012) 8.
- [374] A. Novinrooz, P. Sarabadani, J. Garousi, Characterization of pure and antimony doped SnO₂ thin films prepared by the sol-gel technique, *Iran. J. Chem. Chem. Eng.* Vol. 25 (2006).
- [375] A. Jitianu, Y. Altindag, M. Zaharescu, M. Wark, New SnO₂ nano-clusters obtained by sol-gel route, structural characterization and their gas sensing applications, *J sol-gel sci technol*. 26 (2003) 483-488.
- [376] J. Chatelon, C. Terrier, J. Roger, Influence of elaboration parameters on the properties of tin oxide films obtained by the sol-gel process, *J sol-gel sci technol*. 10 (1997) 55-65.
- [377] N. Kashif, F. Ouyang, Parameters effect on heterogeneous photocatalysed degradation of phenol in aqueous dispersion of TiO₂, *Journal of Environmental Sciences*. 21 (2009) 527-533.
- [378] S. Ragupathy, K. Raghu, P. Prabu, Synthesis and characterization of TiO₂ loaded cashew nut shell activated carbon and photocatalytic activity on BG and MB dyes under sunlight radiation, *Spectrochim Acta A*. 138 (2015) 314-320.
- [379] Y. Yu, Z. Hu, Y. Wang, H. Gao, Magnetic SN-functionalized diatomite for effective removals of phenols, *International Journal of Mineral Processing*. 162 (2017) 1-5.
- [380] A. Barrios-Martinez, E. Barbot, B. Marrot, P. Moulin, N. Roche, Degradation of synthetic phenol-containing wastewaters by MBR, *Journal of Membrane Science*. 281 (2006) 288-296.

- [381] S.M. Cordova-Rosa, R.I. Dams, E.V. Cordova-Rosa, M.R. Radetski, A.X.R. Corrêa, C.M. Radetski, Remediation of phenol-contaminated soil by a bacterial consortium and *Acinetobacter calcoaceticus* isolated from an industrial wastewater treatment plant, *Journal of Hazardous Materials*. 164 (2009) 61-66.
- [382] A. Malik, S. Hameed, M.J. Siddiqui, M.M. Haque, M. Muneer, Influence of Ce Doping on the Electrical and Optical Properties of TiO₂ and Its Photocatalytic Activity for the Degradation of Remazol Brilliant Blue R, *Int J Photoenergy*. 2013 (2013) 9.
- [383] N. Shanmugam, T. Sathya, G. Viruthagiri, C. Kalyanasundaram, R. Gobi, S. Ragupathy, Photocatalytic degradation of brilliant green using undoped and Zn doped SnO₂ nanoparticles under sunlight irradiation, *Appl Surf Sci*. 360, Part A (2016) 283-290.
- [384] O. Lupan, L. Chow, G. Chai, A. Schulte, S. Park, H. Heinrich, A rapid hydrothermal synthesis of rutile SnO₂ nanowires, *Mater Sci Eng-B*. 157 (2009) 101-104.
- [385] W.-C. Lin, Y.-J. Lin., Effect of Vanadium(IV)-Doping on the Visible Light-Induced Catalytic Activity of Titanium Dioxide Catalysts for Methylene Blue Degradation *Environ Eng Sci* 29 (2012) 447-452.
- [386] A. Das, V. Bonu, A.K. Prasad, D. Panda, S. Dhara, A.K. Tyagi, The role of SnO₂ quantum dots in improved CH₄ sensing at low temperature, *J Mater Chem C*. 2 (2014) 164-171.
- [387] A. Sarkar, A.B. Ghosh, N. Saha, D.N. Srivastava, P. Paul, B. Adhikary, Enhanced photocatalytic performance of morphologically tuned Bi₂S₃ Nps in the degradation of organic pollutants under visible light irradiation, *Journal of Colloid and Interface Science*. 483 (2016) 49-59.
- [388] J. Jiang, Y. Lu, B. Kramm, F. Michel, C.T. Reindl, M.E. Kracht, P.J. Klar, B.K. Meyer, M. Eickhoff, Nitrogen incorporation in SnO₂ thin films grown by chemical vapor deposition, *physica status solidi (b)*. (2016).
- [389] C. Terrier, J.P. Chatelon, R. Berjoan, J.A. Roger, Sb-doped SnO₂ transparent conducting oxide from the sol-gel dip-coating technique, *Thin Solid Films*. 263 (1995) 37-41.
- [390] Q. Zhao, D. Ju, X. Deng, J. Huang, B. Cao, X. Xu, Morphology-modulation of SnO₂ Hierarchical Architectures by Zn Doping for Glycol Gas Sensing and Photocatalytic Applications, *Sci Rep*. 5 (2015).

- [391] G.L. Hornyak, J. Dutta, H. Tibbals, A. Rao, Introduction to nanoscience, CRC Press ISBN-10: 14200480582008.
- [392] Y. Wang, L. Zhang, S. Li, P. Jena, Polyol-mediated synthesis of ultrafine TiO₂ nanocrystals and tailored physiochemical properties by Ni doping, *J Phys Chem C*. 113 (2009) 9210-9217.
- [393] G.A. Alanko, A. Thurber, C.B. Hanna, A. Punnoose, Size, surface structure, and doping effects on ferromagnetism in SnO₂, *J Appl Phys*. 111 (2012) 07C321.
- [394] O. Fouad, A. Ismail, Z. Zaki, R. Mohamed, Zinc oxide thin films prepared by thermal evaporation deposition and its photocatalytic activity, *Appl Catal B-Environ*. 62 (2006) 144-149.
- [395] A.A. Ismail, H. Bouzid, Synthesis of mesoporous ceria/titania thin films for self-cleaning applications, *J colloid interf sci*. 404 (2013) 127-134.
- [396] C. Terrier, J. Chatelon, R. Berjoan, J. Roger, Sb-doped SnO₂ transparent conducting oxide from the sol-gel dip-coating technique, *Thin Solid Films*. 263 (1995) 37-41.
- [397] A. Kubačka, M. Fernández-García, G. Colón, Advanced nanoarchitectures for solar photocatalytic applications, *Chemical Reviews*. 112 (2011) 1555-1614.
- [398] S. Ahmed, M.G. Rasul, R. Brown, M.A. Hashib, Influence of parameters on the heterogeneous photocatalytic degradation of pesticides and phenolic contaminants in wastewater: A short review, *J Environ Manage*. 92 (2011) 311-330.
- [399] C. Wu, X. Liu, D. Wei, J. Fan, L. Wang, Photosonochemical degradation of Phenol in water, *Water Res*. 35 (2001) 3927-3933.
- [400] S. Anju, S. Yesodharan, E. Yesodharan, Zinc oxide mediated sonophotocatalytic degradation of phenol in water, *Chem Eng J*. 189 (2012) 84-93.
- [401] A.H. Abdullah, L.K. Mun, Z. Zainal, M.Z. Hussein, Photodegradation of Chlorophenoxyacetic Acids by ZnO/r-Fe₂O₃ Nanocatalysts: A Comparative Study, *Intl J Chem*. 5 (2013) p56.
- [402] D. Perrin, pKa Prediction for Organic Acids and Bases, Springer Science & Business Media 2013.
- [403] C. Trellu, E. Mousset, Y. Pechaud, D. Huguenot, E.D. van Hullebusch, G. Esposito, M.A. Oturan, Removal of hydrophobic organic pollutants from soil

washing/flushing solutions: A critical review, *Journal of hazardous materials*. 306 (2016) 149-174.

[404] Y. Feng, Y. Cui, B. Logan, Z. Liu, Performance of Gd-doped Ti-based Sb-SnO₂ anodes for electrochemical destruction of phenol, *Chemosphere*. 70 (2008) 1629-1636.

[405] S.-S. Hong, C.-S. Ju, C.-G. Lim, B.-H. Ahn, K.-T. Lim, G.-D. Lee, A photocatalytic degradation of phenol over TiO₂ prepared by sol-gel method, *Journal of Industrial and Engineering Chemistry*. 7 (2001) 99-104.

[406] A.R. Khataee, M. Zarei, Photocatalysis of a dye solution using immobilized ZnO nanoparticles combined with photoelectrochemical process, *Desalination*. 273 (2011) 453-460.

[407] S. Rabindranathan, S. Devipriya, S. Yesodharan, Photocatalytic degradation of phosphamidon on semiconductor oxides, *J Hazard Mater*. 102 (2003) 217-229.

[408] I.K. Konstantinou, T.A. Albanis, TiO₂-assisted photocatalytic degradation of azo dyes in aqueous solution: kinetic and mechanistic investigations: A review, *Appl Catal B-Environ*. 49 (2004) 1-14.

[409] Y. Zhang, K. Yu, G. Li, D. Peng, Q. Zhang, F. Xu, W. Bai, S. Ouyang, Z. Zhu, Synthesis and field emission of patterned SnO₂ nanoflowers, *Mater Lett*. 60 (2006) 3109-3112.

[410] M. Barakat, H. Schaeffer, G. Hayes, S. Ismat-Shah, Photocatalytic degradation of 2-chlorophenol by Co-doped TiO₂ nanoparticles, *Appl Catal B-Environ*. 57 (2005) 23-30.

[411] S. Lathasree, A.N. Rao, B. SivaSankar, V. Sadasivam, K. Rengaraj, Heterogeneous photocatalytic mineralisation of phenols in aqueous solutions, *J Mol Catal A-Chem*. 223 (2004) 101-105.

[412] L. Wei, C. Shifu, Z. Wei, Z. Sujuan, Titanium dioxide mediated photocatalytic degradation of methamidophos in aqueous phase, *J Hazard Mater*. 164 (2009) 154-160.

[413] S.K. Pardeshi, A.B. Patil, A simple route for photocatalytic degradation of phenol in aqueous zinc oxide suspension using solar energy, *Sol Energy*. 82 (2008) 700-705.

[414] C.v. Sonntag, P. Dowideit, X. Fang, R. Mertens, X. Pan, M.N. Schuchmann, H.-P. Schuchmann, The fate of peroxy radicals in aqueous solution, *Water Sci Technol*. 35 (1997) 9-15.

- [415] M.J. Hansen, W.A. Velema, M.M. Lerch, W. Szymanski, B.L. Feringa, Wavelength-selective cleavage of photoprotecting groups: strategies and applications in dynamic systems, *Chemical Society Reviews*. 44 (2015) 3358-3377.
- [416] D. Bahnemann, Photocatalytic water treatment: solar energy applications, *Sol Energy*. 77 (2004) 445-459.
- [417] A. Mills, S.K. Lee, Semiconductor Photocatalysis, in: S. Parkins (Ed.) *Advanced Oxidation Processes for Water and Wastewater Treatment*, IWA Publishing 2004, pp. 137-166.
- [418] S. Taishi, Y. Tetsuya, Y. Shunya, M. Atsumi, A New Characterization Method of Photocatalytic Activity in Semiconductor Photocatalysts, *Jpn J Appl Phys*. 40 (2001) 4007.
- [419] M. Mahalakshmi, S. Vishnu Priya, B. Arabindoo, M. Palanichamy, V. Murugesan, Photocatalytic degradation of aqueous propoxur solution using TiO₂ and H β zeolite-supported TiO₂, *Journal of Hazardous Materials*. 161 (2009) 336-343.
- [420] D.F. Ollis, Solar-assisted photocatalysis for water purification: issues, data, questions, *Photochemical conversion and storage of solar energy*, Springer 1991, pp. 593-622.
- [421] M. Mahalakshmi, B. Arabindoo, M. Palanichamy, V. Murugesan, Photocatalytic degradation of carbofuran using semiconductor oxides, *J Hazard Mater*. 143 (2007) 240-245.
- [422] R. Pourata, A.R. Khataee, S. Aber, N. Daneshvar, Removal of the herbicide Bentazon from contaminated water in the presence of synthesized nanocrystalline TiO₂ powders under irradiation of UV-C light, *Desalination*. 249 (2009) 301-307.
- [423] W. Liu, S. Chen, W. Zhao, S. Zhang, Study on the photocatalytic degradation of trichlorfon in suspension of titanium dioxide, *Desalination*. 249 (2009) 1288-1293.
- [424] M. Faramarzpour, M. Vossoughi, M. Borghei, Photocatalytic degradation of furfural by titania nanoparticles in a floating-bed photoreactor, *Chem Eng J*. 146 (2009) 79-85.
- [425] K. Mehrotra, G.S. Yablonsky, A.K. Ray, Kinetic Studies of Photocatalytic Degradation in a TiO₂ Slurry System: Distinguishing Working Regimes and Determining Rate Dependences, *Industrial & Engineering Chemistry Research*. 42 (2003) 2273-2281.

- [426] O. Legrini, E. Oliveros, A.M. Braun, Photochemical processes for water treatment, *Chem Rev.* 93 (1993) 671-698.
- [427] A.-G. Rincón, C. Pulgarin, Use of coaxial photocatalytic reactor (CAPHORE) in the TiO₂ photo-assisted treatment of mixed *E. coli* and *Bacillus* sp. and bacterial community present in wastewater, *Catal Today.* 101 (2005) 331-344.
- [428] T.D. Cutler, J.J. Zimmerman, Ultraviolet irradiation and the mechanisms underlying its inactivation of infectious agents, *Anim Health Res Rev.* 12 (2011) 15-23.
- [429] E.E. Bamuza-Pemu, E. Chirwa, Profile of aromatic intermediates of titanium dioxide mediated degradation of phenol, *Chem Eng.* 35 (2013) 1333.
- [430] L. Zhang, T. Kanki, N. Sano, A. Toyoda, Pathways and Kinetics on Photocatalytic Destruction of Aqueous Phenol, *Environmental monitoring and assessment.* 115 (2006) 395-403.
- [431] A. Santos, P. Yustos, A. Quintanilla, S. Rodríguez, F. García-Ochoa, Route of the catalytic oxidation of phenol in aqueous phase, *Applied Catalysis B: Environmental.* 39 (2002) 97-113.
- [432] D. Jun, W. Qi, S. ZHONG, G. Xin, L. Jiao, G. Haizhi, W. ZHANG, P. Hailong, Z. Jianguo, Effect of hydroxyl groups on hydrophilic and photocatalytic activities of rare earth doped titanium dioxide thin films, *Journal of Rare Earths.* 33 (2015) 148-153.
- [433] A. Mohedano, V. Monsalvo, J. Bedia, J. Lopez, J. Rodriguez, Highly stable iron catalysts from sewage sludge for CWPO, *J Environ Chem Eng.* 2 (2014) 2359-2364.
- [434] K.-i. Okamoto, Y. Yamamoto, H. Tanaka, M. Tanaka, A. Itaya, Heterogeneous photocatalytic decomposition of phenol over TiO₂ powder, *Bulletin of the Chemical Society of Japan.* 58 (1985) 2015-2022.
- [435] W. Xie, Z. Gao, K. Liu, W.-P. Pan, R. Vaia, D. Hunter, A. Singh, Thermal characterization of organically modified montmorillonite, *Thermochim Acta.* 367 (2001) 339-350.
- [436] W. Xie, Z. Gao, W.-P. Pan, D. Hunter, A. Singh, R. Vaia, Thermal degradation chemistry of alkyl quaternary ammonium montmorillonite, *Chem Mater.* 13 (2001) 2979-2990.
- [437] H. Zou, C. Yi, L. Wang, H. Liu, W. Xu, Thermal degradation of poly (lactic acid) measured by thermogravimetry coupled to Fourier transform infrared spectroscopy, *J Therm Anal Calorim.* 97 (2009) 929-935.

- [438] A.M. Peiró, J.A. Ayllón, J. Peral, X. Doménech, TiO₂-photocatalyzed degradation of phenol and ortho-substituted phenolic compounds, *Appl Catal B-Environ.* 30 (2001) 359-373.
- [439] A. Turki, C. Guillard, F. Dappozze, Z. Ksibi, G. Berhault, H. Kochkar, Phenol photocatalytic degradation over anisotropic TiO₂ nanomaterials: Kinetic study, adsorption isotherms and formal mechanisms, *Appl Catal B-Environ.* 163 (2015) 404-414.
- [440] J. Reszczyńska, T. Grzyb, J.W. Sobczak, W. Lisowski, M. Gazda, B. Ohtani, A. Zaleska, Visible light activity of rare earth metal doped (Er³⁺, Yb³⁺ or Er³⁺/Yb³⁺) titania photocatalysts, *Appl Catal B-Environ.* 163 (2015) 40-49.
- [441] A. Santos, P. Yustos, S. Gomis, G. Ruiz, F. Garcia-Ochoa, Reaction network and kinetic modeling of wet oxidation of phenol catalyzed by activated carbon, *Chem Eng Sci.* 61 (2006) 2457-2467.
- [442] C. Belver, J. Bedia, J.J. Rodriguez, Titania–clay heterostructures with solar photocatalytic applications, *Appl Catal B-Environ.* 176–177 (2015) 278-287.
- [443] G. Liu, H.G. Yang, X. Wang, L. Cheng, H. Lu, L. Wang, G.Q. Lu, H.-M. Cheng, Enhanced photoactivity of oxygen-deficient anatase TiO₂ sheets with dominant {001} facets, *J Phys Chem C.* 113 (2009) 21784-21788.
- [444] M. Pelaez, N.T. Nolan, S.C. Pillai, M.K. Seery, P. Falaras, A.G. Kontos, P.S.M. Dunlop, J.W.J. Hamilton, J.A. Byrne, K. O'Shea, M.H. Entezari, D.D. Dionysiou, A review on the visible light active titanium dioxide photocatalysts for environmental applications, *Appl Catal B-Environ.* 125 (2012) 331-349.

Publication I

A. M. Al-Hamdi, M. Sillanpää, J. Dutta

**Photocatalytic degradation of phenol in aqueous solution by
rare-earth-doped SnO₂ nanoparticles**

Reprinted with permission from

Journal of Material Science

Vol. 49, pp. 5151-5159, 2014

© 2014, Springer

Photocatalytic degradation of phenol in aqueous solution by rare earth-doped SnO₂ nanoparticles

Abdullah M. Al-Hamdi · Mika Sillanpää · Joydeep Dutta

Received: 19 November 2013 / Accepted: 3 April 2014 / Published online: 22 April 2014
Springer Science+Business Media New York 2014

Abstract The influence of heterogeneous semiconductors on the photodegradation of phenol in water was investigated using doped tin dioxide (SnO₂) nanoparticles. Photocatalysts of SnO₂ were synthesized with lanthanum (La), cerium (Ce), and neodymium (Nd) dopants. These photocatalysts were synthesized from tin tetrachloride by sol–gel method with different dopant concentrations, and its photocatalytic degradation was investigated up to 0.8 % under UV-A light in aqueous suspensions. The photocatalytic oxidation reactions were studied by varying photocatalyst composition, light intensity, reaction time, pH of the reaction medium, and phenol concentration. It was found that the photocatalytic activity of rare earth-doped SnO₂ for phenol decomposition under UV light irradiation was considerably higher than that of pure SnO₂ nanoparticles. The experimental results also indicate that more than 95 % phenol was effectively oxidized in the presence of an aqueous suspension of La: SnO₂ nanoparticles within 120 min of UV light irradiation.

Introduction

Water pollution by different hazardous compounds is becoming an increasing global concern [1–3]. Phenols, dyes, pharmaceuticals, parabens, endocrine-disrupting compounds, phthalates, and benzoic acids [4, 5] are commonly encountered organic pollutants in toxic waste discharged in industrial effluents [6, 7]. The accumulation of these toxic pollutants can affect human life and sustainable development [8–10].

The improper treatment and inappropriate disposal of these toxic carcinogenic compounds pose a considerable threat to the environment [11].

Phenol is released into the air and water as a result of industrial activities [12]. Studies have shown that the greatest potential source of exposure to phenol is the occupational setting, since phenols used in manufacturing processes evaporate into the surrounding sea or water bodies [13–15]. The degradation of phenol by titanium dioxide (TiO₂) photocatalysts has received a great deal of recent attention from a number of researchers [16] as TiO₂ oxidizes organic molecules completely at a low energy cost [17–19]. Many researchers reported that TiO₂, zinc oxide (ZnO), and SnO₂ are the most active catalysts in the degradation of dyes, phenols, and pesticides [20–22]. Furthermore, these semiconductors have been recognized as preferable materials for photocatalytic processes due to their high photosensitivity, nontoxic nature, low cost, and chemical stability [23–27]. In the photocatalytic oxidation process, organic pollutant is decomposed in the presence of a wide-band gap semiconductor that can promote reactions in the presence of UV light without being consumed in the overall reaction [27]. The band gap of TiO₂, ZnO, and SnO₂ are 3.2, 3.3, and 3.6 eV, respectively [28–30]. SnO₂ is relatively less studied compared to the other two

Electronic supplementary material The online version of this article (doi:10.1007/s10853-014-8223-2) contains supplementary material, which is available to authorized users.

A. M. Al-Hamdi · M. Sillanpää
Laboratory of Green Chemistry, Lappeenranta University of
Technology, Sammonkatu 12, 50130 Mikkeli, Finland e-mail:
abdullah.al.hamdi@lut.fi

M. Sillanpää
e-mail: mika.sillanpaa@lut.fi

J. Dutta
Chair in Nanotechnology, Water Research Center,
Sultan Qaboos University, 123 Al-Khouth,
P.O. Box 17, Musqat, Sultanate of Oman
e-mail: dutta@squ.edu.om

semiconductors for photocatalytic applications [31]. Recent interest has developed in the synthesis of SnO₂ nanoparticles of different sizes [32–34]. Incorporation of rare earth metal ions into the SnO₂ matrix could introduce defects lowering the effective optical gap and hence leading to a better photoactivity [35]. Several reports suggest the successful incorporation of dopants in titania to increase its photocatalytic efficiency [36–38]. Sol–gel synthesis is a simple process based on hydrolysis and condensation of a metal salt to form hydroxide or metal oxides [34–41]. It is a simple technique that allows possible control of dopant ions during particle synthesis. Several studies of SnO₂ doping with different metals to produce nanocrystals have been reported in recent years [42–44]. One of the most useful properties of SnO₂ for many applications is that the stoichiometric surfaces with Sn⁴⁺ can be easily reduced to Sn²⁺ which dramatically changes the surface electronic structure of the material. Reduction of the surface leads to the formation of Sn 5S-derived surface states that lie deep within the band gap and also cause a lowering of the work function. Another interesting aspect of SnO₂ surface is with respect to the oxygen atoms that reside there, whereby energetically favorable reconstructions of the SnO₂ (110) and (101) surfaces result in surface oxygen deficiency [45, 46]. The surface of SnO₂ then acts as a sink for vacancies. Reconstruction of the SnO₂ surface is possible and gives rise to a host of different surface situations. This ability to make the crystal structure oxygen deficient, SnO_{2-x}, renders it suitable for enhanced catalytic activities of adsorbed surface species [47]. Doping occurs by moving the Fermi energy to the band edge leading to the spontaneous formation of compensating defects if the formation energy of the defect falls to zero at that Fermi energy [48, 49]. Sparse information is available in the literature regarding the SnO₂-R (R = rare earth) system. Some authors have compared photocatalytic activities of different rare earth metal ions (La, Ce, Er, Pr, Gd, Nd, and Sm) doped into TiO₂ and reported enhanced photocatalytic activities [50]. It is well known that the catalytic properties of semiconductor oxides are strongly related to their acid/base characteristics [51, 52]. While SnO₂ is predominantly acidic oxide (isoelectronic point, iep = 4–7), the rare oxides are mostly basic (ex iep_{La2O3} = 10–12 and iep_{Y2O3} = 11) [53]. It has been reported that catalytic activity is related to electronegativity of the cations present in the system (and thus the acid–base characteristics). For example, rare earth dopants from redox couple (Ce³⁺/Ce⁴⁺) allow the shift from RO_x to R₂O_{x/2} (like CeO₂ to Ce₂O₃) under oxidizing and reducing conditions. Also, rare earth metals, which incompletely occupied 4f and empty 5d orbitals, imbibe the easy formation of labile oxygen vacancies with the relatively high mobility of bulk oxygen species [54].

In this work, we report the doping of sol–gel-synthesized SnO₂ particles with different types of rare earth dopants, namely lanthanum, cerium, and neodymium. We also report the photocatalytic degradation of phenol by mineralization using these rare earth-doped SnO₂ nanoparticles.

Experimental

Materials

Analytical-grade tin (IV) chloride (SnCl₄, Sigma-Aldrich, Purity: 99 %), lanthanum nitrate hexahydrate (La (NO₃)₃ 6H₂O, Fluka), cerium (III) chloride anhydrous (CeCl₃, Sigma-Aldrich, 99 %), ammonium Cerium (IV) nitrate ((NH₄)₂Ce (NO₃)₆, Sigma-Aldrich, 99 %), neodymium (III) nitrate hexahydrate (Nd (NO₃)₃ 6H₂O, Sigma-Aldrich, 99 %), ethanol (C₂H₅OH, ETAX Aa Merck Absolute), phenol (C₆H₅OH, Sigma-Aldrich, 99 %), sulfuric acid (H₂SO₄, Sigma-Aldrich, 99 %), hydrochloric acid (HCl, Sigma-Aldrich, 99 %), sodium hydroxide pellets (NaOH, Sigma-Aldrich, 99 %), methanol (CH₃OH, Sigma-Aldrich, 99 % HPLC grade), and sodium chloride (NaCl, BDH 99 % Analar grade) were used in the experimental studies. Double-deionized water with a high purity from Ultra Clear Water SG was used for the preparation of all solutions.

Photocatalyst preparation

Synthesis of pure and doped SnO₂ nanoparticles

Nanoparticles containing various molar compositions of SnO₂ were chemically synthesized by the sol–gel method, according to the following procedure:

Pure SnO₂ was prepared using 5.225 ml of SnCl₄ mixed in 100.00 ml absolute ethanol and used as a precursor for SnO₂ synthesis for control experiments. The mixture was continuously stirred for 2 h at room temperature, until a colorless solution was obtained. The solution then was condensed in a round-bottomed flask at 80 LC, and the temperature was kept stable during the process. A colorless solution of tin alkoxide was obtained after heating the mixture at 80 LC under vacuum conditions [39]. After refluxing, the resultant solution was gelled into an open heated dish at 30 LC, and the mixture turned into a sol. This transparent colloidal suspension was stored for about 5–6 days in the ambient. The gel was then dried at 80 LC for 7 h. Finally, the powder was heated at 200 LC for 7 h until it calcined. For the species containing lanthanum, cerium, and neodymium, 0.1, 0.2, 0.4, 0.6, and 0.8 % concentrations of each doped to SnO₂ were mixed and dissolved separately in ethanol. Later, a series of samples were synthesized in the same way by changing the

concentration of tin tetrachloride and the percentage amount of the dopant. Each of these dopants was added slowly, upon vigorous stirring of the total solution containing pure tin tetrachloride after the condensing process. They were then subjected to dissolution in ethanol and synthesis by the same process used for undoped SnO₂ as explained above.

Photocatalytic experiments

Photocatalytic reactor

The photoreactor was a cylindrical Pyrex-glass container with a 250-ml capacity, 50-mm internal diameter, and 300-mm height. A 8-W medium-pressure mercury lamp (Osaka, Japan) was used to emit an intensity of about 80 W m⁻², and the reaction temperature was kept at 25 °C by cooling with water.

Experimental procedure

To investigate the effects of different dopants on the photocatalytic activity of SnO₂, oxidative photodegradation of phenol was chosen to evaluate the photocatalytic activity of synthesized nanoparticles. The study of degradation of phenol in water was carried out at 25 °C using the water-cooled cylindrical glass batch photoreactor of 250 ml volume. The experimental conditions were varied as follows: The amount of catalyst powder (photocatalyst) was kept at 0.065 g in 50.00 ml; the initial concentration of the pollutant was varied from 5 to 100 ppm, and the pH of the solution was adjusted by the addition of 0.5 M NaOH to fix pH at 4. 10 mg/l; phenol solution was used to carry out photocatalytic experiments. Before each test, the mixture was kept in the dark for 30 min under constant magnetic stirring to ensure that the adsorption–desorption equilibrium was reached before illumination. The sample was then taken out at the end of the dark adsorption period, prior to turning the light on. When the lamp was turned on, the irradiation time varied from 2 to 3 h; aliquots of the suspensions were collected and removed from the reactor every 15 or 30 min. At the given time intervals, the photocatalyst particles were removed from the samples first by centrifugation (4,000 rpm, 5 min) using Eppendorf Centrifuge (system model 5810R) and then filtered through 0.2-µm Millipore filters.

Characterization

To study the surface morphology of the prepared SnO₂ and doped SnO₂ samples, scanning electron microscopy (SEM) was carried out with JEOL (Japan) (JSM-5600LY) working at 30 kV and high-resolution transmission electron

microscopy (HRTEM) was carried out with JEOL (Japan) (JEM 2100F) working at 200 kV. Surface area of the samples was measured using Acorn Area—Particle Surface Area Analyzer from Xigo Nanotools analyzer unit, which works based on nuclear magnetic resonance (NMR) technique. The crystalline phase of the synthesized SnO₂ and doped SnO₂ catalysts was analyzed by X-ray powder diffraction (XRD) using a MiniFlex 600 diffractometer (Rikagu, Japan) with Cu K radiation (wave-length = 1.54 Å). Diffractograms of powders were recorded in 2θ configuration from 10–80° at an increment of 0.02°.

Analytical methods

The change in phenol concentration in each photodegraded solution was monitored by two sets of measurements. Firstly, the maximum absorbance of phenol was measured at $k_{\text{max}} = 270$ nm in an ultraviolet–visible (UV–Vis) spectrometer (Perkin Elmer Lambda 45). Secondly, the total organic carbon was determined by a Total Organic Carbon Analyzer (TOC-VCPH Shimadzu) equipped with an auto sampler (ASI-V Shimadzu). Prior to the TOC determination, the solution was filtered through a syringe filter of 0.2 µm pore size to remove photocatalysts.

High-performance liquid chromatography analysis (HPLC)

Phenol photodegradation products were analyzed using high-performance liquid chromatography which contained a P580 high-precision pump from Dionex (Germering, Germany), which fulfilled the requirement for a measured delivery rate of the mobile phase. The injector was a Rheodyne (Cotati) 8125 valve fitted with a 20-µl loop. The analysis was carried out using a C18 column (5 µm) maintained at room temperature. After elution from the column, the eluent passed through a Dionex UVD 170S diode array detector set at 245 nm for phenol. The mobile phase for the HPLC separation was prepared by mixing methanol with water (45:55) and then adjusting the pH at 3.0 by adding sulfuric acid (H₂SO₄). The mobile phase was degassed in an ultrasonic bath and then passed through a Millipore filtration apparatus (0.2 µm). Photodegraded Phenol and control samples were eluted at a flow rate of 1 ml/min.

Gas chromatography

Solid-phase extraction (SPE) columns Chromabond C18 ec (octadecyl-modified silica, Macherey–Nagel) had a volume of 3 ml and 500 mg. Columns were first conditioned with three column volumes of methanol (CH₃OH) and two column volumes of 0.01 M hydrochloric acid (HCl). For

the treatment, 200 mg NaCl was added for every 1 ml of sample. HCl (1 M) was used to adjust pH to 2.0. 2.5 ml sample of phenol was pipetted to SPE column slowly at a flow rate of 0.5 ml/min. Sample was washed twice with

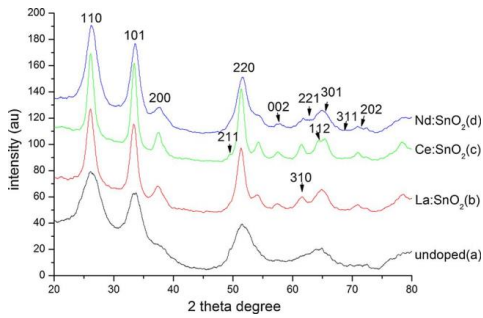


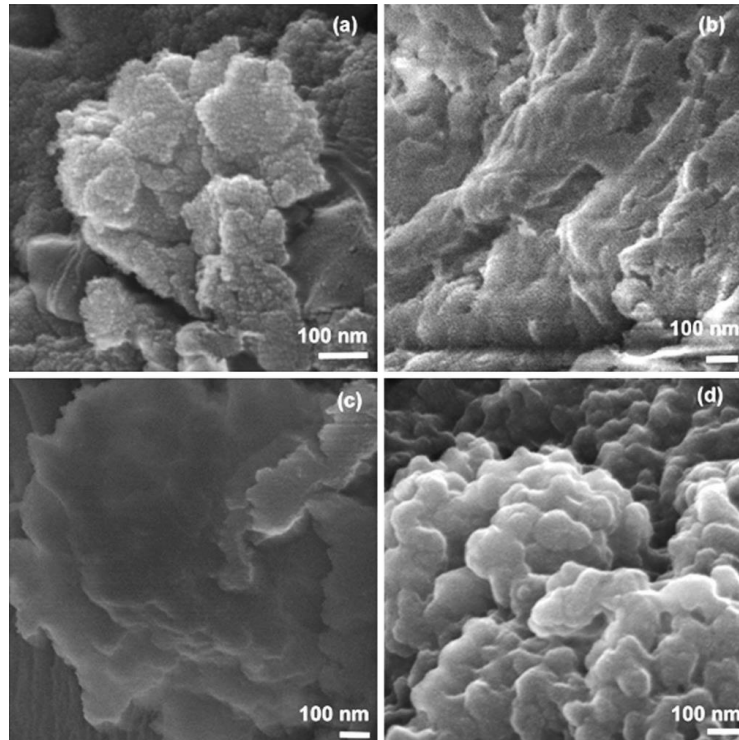
Fig. 1 X-ray diffraction (XRD) patterns of typical samples a undoped tin dioxide particles and b lanthanum-doped tin dioxide particles, c cerium-doped tin dioxide particles and d neodymium-doped tin dioxide particles synthesized by sol-gel process

500 μ l of 0.01 M HCl and dried under vacuum for 10 min. Elution was performed with 3 x 500 μ l of methanol. Gas chromatography (Agilent 6890 GC) coupled with mass spectrometry (GC/MS) was used for the determination of phenol concentration. The analysis was carried out using HP-5 (Agilent, 5 % phenyl methyl siloxane, capillary 30 m x 320 μ m nominal) column. Injection mode was splitless, and the volume was 1 μ l. Injector and detector temperatures were maintained at 300 $^{\circ}$ C. Helium was used as a carrier gas with a flow of 1.2 ml/min. Oven temperature was varied at 20 $^{\circ}$ C/min up to 260 $^{\circ}$ C and thereafter at 15 $^{\circ}$ C/min to 300 $^{\circ}$ C.

Table 1 Estimated crystallite size of 0.8 % rare earth-doped SnO₂ samples from (110) peak using the Debye-Scherrer analysis

Dopant	Crystal size (nm)
Undoped	4.2
La: SnO ₂	8.6
Ce: SnO ₂	7.6
Nd: SnO ₂	6.3

Fig. 2 Typical scanning electron micrograph of SnO₂ nanoparticles synthesized by sol-gel process



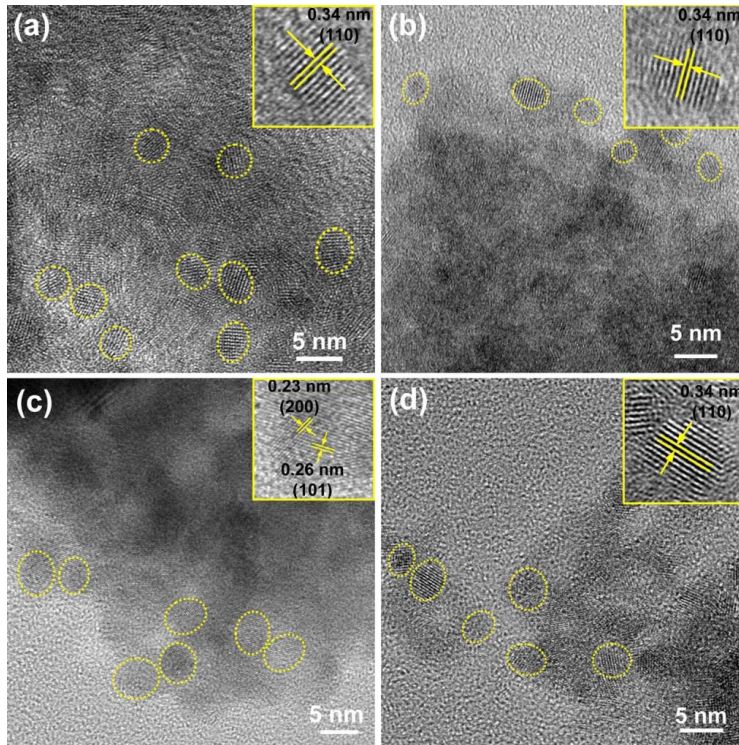


Fig. 3 Typical high-resolution transmission electron micrograph of SnO₂ nanoparticles synthesized by sol-gel process

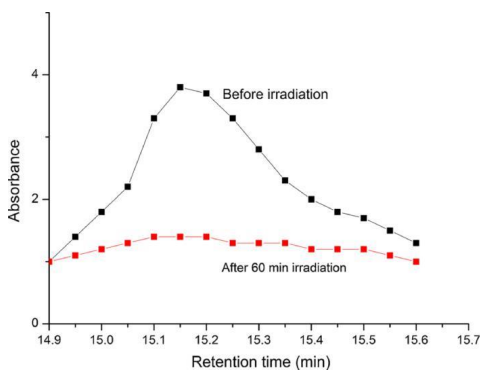


Fig. 4 Spectra of phenol photodegradation before and after 60 min light irradiation by cerium-doped tin dioxide under optimized HPLC conditions

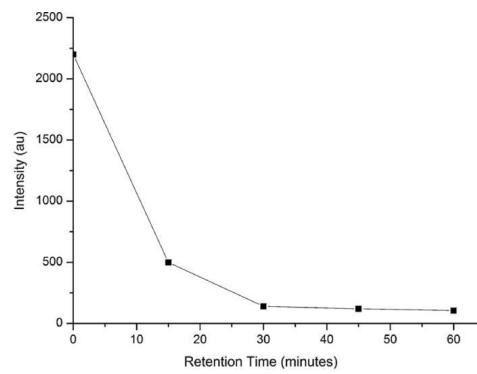


Fig. 5 Reduction in the intensity of phenol peak observed by gas chromatograph upon UV degradation of phenol in the presence of 0.6 wt% La: SnO₂

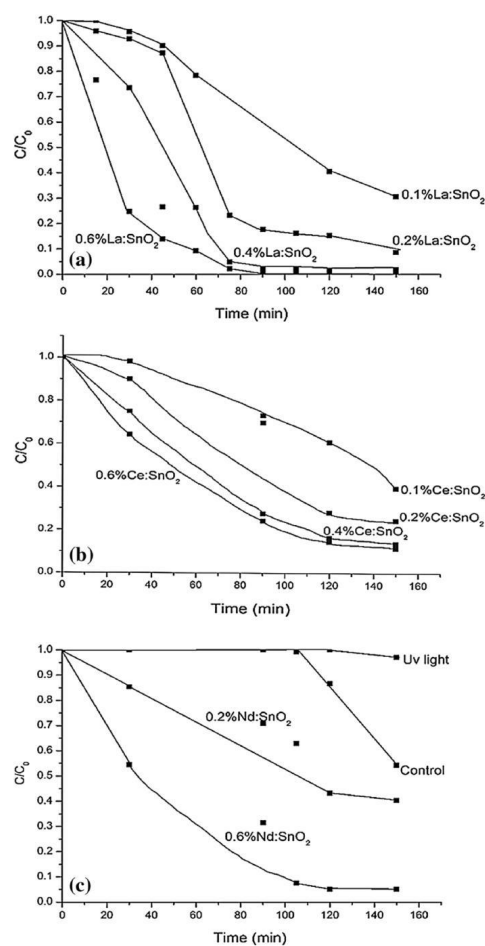


Fig. 6 Comparison of the decrease of phenol concentration with different a La-doped-SnO₂, b Ce-doped-SnO₂, and c Nd-doped-SnO₂ photocatalysts under UV light irradiation as measured by monitoring the phenol peak in UV-Vis spectrometry

Results and discussion

Undoped and doped SnO₂ samples were examined by XRD as shown in Fig. 1. The XRD pattern showed the presence of twelve peaks corresponding to SnO₂ crystal planes of (110), (101), (200), (211), (220), (002), (310), (221), (301), (112), (311), and (202), respectively. This result matches well with the standard XRD file of SnO₂ (JCPDS-#41-1445) regarded as an attributive indication of rutile SnO₂ structure [55–58]. The level of doping influences the

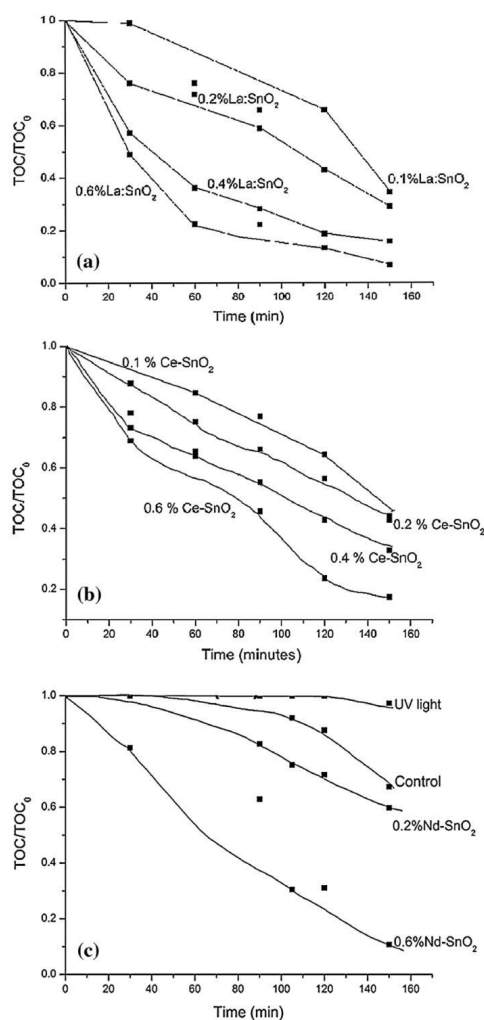


Fig. 7 Total organic carbon (TOC) removal from phenol solutions during 2 h of photocatalytic degradation by different a La-doped SnO₂, b Ce-doped-SnO₂, and c Nd-doped-SnO₂ under UV light irradiation

broadening of the main peaks and changes the intensity. In Table 1, we have summarized the value of the crystallite size estimated from the Debye–Scherrer equation considering the most intense (110) peak and found the crystallite size from 4 to 8.6 nm.

In Fig. 2, we have shown the microstructure of the SnO₂ and doped nanoparticles. Typically 50-nm-sized

agglomerates of nanoparticles were observed. The 4–8.6-nm crystallites agglomerate to form the 50-nm particles as observed by SEM, in order to find a better insight, we carried out high-resolution HRTEM as shown in Fig. 3. The crystallite sizes are comparable to what was estimated from the XRD (Table 1). The surface area of the synthe-sized nanoparticles was found to be between 27 and 35 m²/g (results not shown).

Photocatalytic degradation of phenol

During the photocatalysis experiments, the pellucid solutions before and after irradiation were analyzed by HPLC. It was found as shown that phenol was effectively removed upon UV irradiation when compared to the content of phenol by HPLC before irradiation, as shown in Fig. 4.

In Fig. 5, we have plotted the phenol concentration in the aqueous sample after UV illumination in the presence of a typical doped SnO₂ (Nd:SnO₂). It can be observed the phenol content in the solution reduces to zero level after only 30 min of UV irradiation in the presence of the photocatalyst.

With Ce³⁺-doped SnO₂ samples, after 120 min irradiation, 86 % of phenol was found to degrade upon using 0.4 wt% Ce: SnO₂ catalyst (Fig. 6). After 120 min irradiation, 57 % of phenol was found to degrade upon using 0.2 wt% Nd: SnO₂ catalyst, while 24 % of phenol was removed when undoped SnO₂ catalyst was used. Upon doping the catalyst with 0.6 wt% Nd, the photocatalytic activity was found to increase from 57 to 95 %. Thus, a fourfold improvement in photocatalytic activity of phenol was observed when Nd-doped nanoparticles were used

upon 120 min UV light irradiation. However, out of all the three dopants, La-doped SnO₂ samples were found to be most photoactive, since 100 % of phenol was photodegraded for the same irradiation time.

TOC removal in phenol degradation

In order to determine the degree of mineralization reached during the photocatalyst experiments, nine to ten samples in each test were collected at time intervals of 15 min up to 150 min and then analyzed for TOC concentration. No change in TOC was observed when the irradiation was done without the presence of any photocatalyst. The maximum TOC mineralization after 120 min irradiation was observed to occur when 0.6 wt% La-doped SnO₂ samples were used (86 % degradation), while only 12 % TOC mineralization was achieved with undoped SnO₂ upon UV irradiation for the same time. 93 % mineralization was observed after 150 min of UV irradiation with 0.6 wt% La-doped SnO₂ catalyst, compared to only 33 % TOC mineralization observed with the undoped catalyst. The reduction in TOC generally followed the trend observed in the phenol removal as reported earlier (UV-Vis spectroscopy).

It can also be seen from Fig. 7 that 71 % of TOC removal was achieved in the presence of 0.6 wt% Nd-doped SnO₂ within 120 min of irradiation time, while 28 % of phenol mineralization was observed in the pre-sence of 0.2 wt% Nd-SnO₂ during the same period.

TOC values for catalyst were found to change during the study, which is understandable since degradation of phenol takes time until being finally mineralized.

Fig. 8 Different chemical photoproducts expected from phenol photodegradation before its mineralization by CO₂ and water reported by different researchers [59–61]

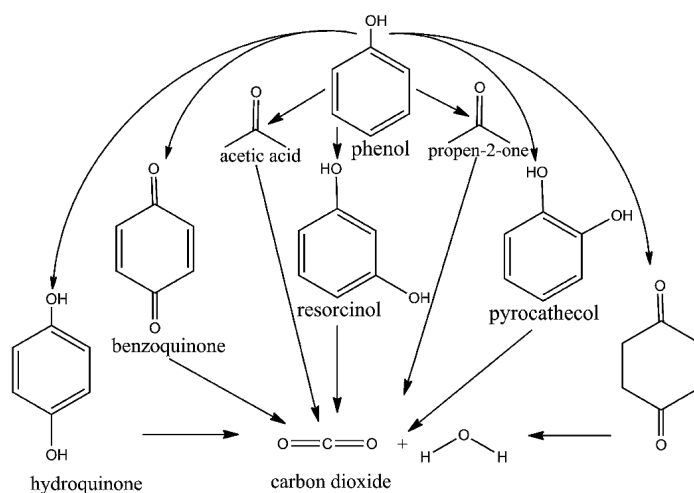


Table 2 Comparison of phenol degradation after 2 h of irradiation

Catalyst sample	% Of phenol photodegradation by TOC detection	% Of phenol photodegradation by UV-Vis analysis
No catalyst	–	–
Pure SnO ₂	12.4	13.4
0.1 % Ce–SnO ₂	35.6	39
0.1 % La–SnO ₂	34.1	62.1
0.2 % Nd–SnO ₂	28.0	56.7
0.2 % La–SnO ₂	57.1	84.8
0.2 % Ce–SnO ₂	43.5	71.9
0.4 % La–SnO ₂	81.3	100
0.4 % Ce–SnO ₂	57.1	85.6
0.6 % Nd–SnO ₂	70.8	94.9
0.6 % La–SnO ₂	86.6	100
0.6 % Ce–SnO ₂	76.3	83.5

It is well known that phenol degradation leads to the formation of a mixture of byproducts such as catechol, benzoquinone, resorcinol, and hydroquinone as shown in Fig. 8 which further reacts with hydroxyl radicals [59–61]. Therefore, 100 % phenol degradation to TOC conversion is not easily detected upon a short irradiation time and with a small amount of catalyst. In Table 2, we have shown the comparison of the photocatalytic degradation of phenol in the presence of various catalysts, where phenol degradation was measured using TOC analyzer and UV-Vis spectroscopy.

Conclusions

A series of La-, Ce-, and Nd-doped tin dioxide samples were prepared by the sol-gel method and investigated for phenol degradation under UV irradiation. The results show that phenol undergoes more effective photodegradation with doped than with undoped SnO₂ photocatalysts. The experiments demonstrated that phenol was effectively degraded by more than 95 % within 120 min in the presence of rare earth-doped SnO₂ nanoparticles. According to the TOC levels, phenol mineralization showed a similar tendency to remove organic compound to that observed by the dissociation of phenol using UV-Vis spectrometry. Rare earth-doped SnO₂ is thus promising for photocatalytic oxidation process and may have a future potential for advanced water and wastewater treatment. Improvement on these simple techniques to utilize solar radiation more efficiently could provide more economic solutions to the problem of water purification and recovery.

Acknowledgements Authors would like to thank partial financial support from the Chair in Nanotechnology Programme of the Research Council of Oman and the College of Science (Chemistry Department) for giving this opportunity to carry out the research at Sultan Qaboos University.

References

- Chakraborty AK, Ganguli S, Kebede AM (2012) Photocatalytic degradation of 2-propanol and phenol using Au loaded MnWO₄ nanorod under visible light irradiation. *J Clust Sci* 23:437–448
- Huang X, Sillanpää M, Gjessing ET, Vogt RD (2009) Water quality in the Tibetan Plateau: major ions and trace elements in the headwaters of four major Asian rivers. *Sci Total Environ* 407:6242–6254
- Huang X, Sillanpää M, Duo B, Gjessing ET (2008) Water quality in the Tibetan Plateau: metal contents of four selected rivers. *Environ Pollut* 156:270–277
- Sambandam A (2012) The contribution of nanotechnology for removal of water pollutants. *Mater Sci Forum* 712:1–24
- Kaneco SK, Rahman AM, Suzuki T, Katsumata H, Kiyohisa O (2004) Optimization of solar photocatalytic degradation conditions of bisphenol A in water using titanium dioxide. *J Photo-chem Photobiol A* 163:419–424
- Vilhunen SH, Sillanpää M, MET (2009) Ultraviolet emitting diodes and hydrogen peroxide in the photodegradation of aqueous phenol. *J Hazard Mater* 161:419–424
- Sponza TD (2003) Application of toxicity tests into discharges of the pulp-paper industry in Turkey. *Ecotoxicol Environ Saf* 24:74–86
- Rudel RA (2011) Food packing and bisphenol A bis (2-ethylhexyl) phthalate exposure: findings from a dietary intervention. *Environ Health Perspect* 119:914–920
- Abdelouahab N, Aimmek Y, Takser L (2011) Polybrominated diphenyl ethers and sperm quality. *Reprod Toxicol* 4:546–550
- Duty MS, Singh PN, Silva JM, Barr BD, Brock WJ, Ryan L, Herrick FR, David CC, Hausler R (2003) The relation between environmental exposure to phthalates and DNA damage in human sperm using the neutral comet assay. *Environ Health Perspect* 111:1164–1169
- Ezeonu SC, Tagbo R, Anike NE, Oje AO, Onwurah ENI (2012) Biotechnological tools for environmental sustainability: prospects and challenges for environments in Nigeria: a standard review. *Biotechnol Res Int* 2012:450802. doi:10.1155/2012/450802
- Michalowicz J, Duda W (2007) Phenols-sources and toxicity. *Pol J Environ Stud* 3:347–362
- Vieira I, Sonnier M, Cresteil T (1996) Toxicological profile for phenol. *J Pharmacol Exp Ther* 88:400–413
- Toxicological Review of Phenol (2002) U.S. Environmental Protection Agency, September
- Toxicological Profile of Phenol (2008) U.S. Department of Health and Human Services, Public Health Service, Agency for Toxic Substances and Disease Registry, September
- Hafizah N, Sopyan L (2009) Nanosized TiO₂ photocatalyst powder via sol-gel method: effect of hydrolysis degree on powder
- Mahmoudi NM, Armani M, Lymae NY, Gharanjig K (2007) Photocatalytic degradation of agricultural N-heterocyclic organic pollutants using immobilized nanoparticles of titania. *J Hazard Mater* 145:65–71
- Chiou CH, Wu CY, Juang RS (2008) Photocatalytic degradation of phenol and m-nitrophenol using irradiated TiO₂ in aqueous solutions. *Sep Purif Technol* 62:559–564
- Laoufi NA, Tassalit D, Bentahar F (2008) The degradation of phenol in water solution by TiO₂ photocatalysis in a helical reactor. *Global Nest J* 10:404–414
- Ahmed S, Rasul GM, Martens NW, Brown R, Hasib AM (2010) Advances in heterogeneous photocatalytic degradation of phenols and dyes in waste water. *Water air soil poll* 215:3–29
- Zhang L, Liu J, Tang C, Lv J, Zhang H, Zhao Y, Wang X (2011) Palygorskite and SnO₂-TiO₂ for the photodegradation of phenol. *Appl Clay Sci* 1:68–73

22. Kruefu V, Ninsonti H, Wetchakun N, Inceesungvorn B, Pookmanee P, Phanichpant S (2012) Photocatalytic degradation of phenol using Nb-doped ZnO nanoparticles. *Eng J Can* 163:90–99
23. Neppolian B, Choi HC, Sakthivel S, Arabindoo B, Murugesan V (2002) Solar/UV- induced photocatalytic degradation of three commercial textile dyes. *J Hazard Mater* 89:303–317
24. Konstantinou IK, Albanis TA (2003) Photocatalytic transformation of pesticides in aqueous titanium dioxide suspension using artificial and solar light: intermediates and degradation pathways. *Appl Catal B* 42:319–335
25. Senthilkumaar S, Porkodi K, Vidyakshmi R (2005) Photodegradation of a textile dye catalyzed by sol-gel derived nanocrystalline TiO₂ via ultrasonic irradiation. *J Photochem Photobiol* 170:225–232
26. Lakshmi BB, Patrissi CP, Martin CR (1977) Sol-gel template synthesis of semiconductor oxide micro and nanostructures. *Chem Mater* 9:2544–2550
27. Hara K, Horiguchi T, Khinoshita T, Sayama K, Sugihara H, Arakawa H (2000) Highly efficient photon-to-electron conversion with mercurochrome-sensitized nanoporous oxide semiconductor solar cells. *Sol Energ Mater Sol C* 64:115–134
28. Hagfeldt A, Gratzel M (1995) Light induced redox reactions in nanocrystalline systems. *Chem Rev* 95:49–68
29. Yates JT Jr, Thompson TL, Tracy L (2006) Surface science studies of the photoactivation of TiO₂-new photochemical processes. *Chem Rev* 106:4428–4453
30. Coey JMD, Venkatesan M, Fitzgerald CB (2005) Donor impurity band exchange in dilute ferromagnetic oxides. *Nature Mater* 4:173–179
31. Diebold U (2003) The surface science of titanium dioxide. *Surf Sci Rep* 48:53–229
32. Ullah R, Dutta J (2008) Photocatalytic degradation of organic dyes with manganese-doped ZnO nanoparticles. *J Hazard Mater* 156:194–200
33. El-Bahy MZ, Ismail AA, Mohamed MR (2009) Enhancement of titania by doping rare earth for photodegradation of organic dye (Direct Blue). *J Hazard Mater* 166:138–143
34. Tec CM, Mohamed AR (2011) Roles of titanium dioxide and ion doped titanium dioxide on photocatalytic degradation of organic pollutants (phenolic compounds and dyes) in aqueous solutions: a review. *J Alloy Compd* 509:1648–1660
35. Strengl V, Bakardjieva S, Murafa N (2009) Preparation and photocatalytic activity of rare earth doped TiO₂ nanoparticles. *Mater Chem Phys* 114:217–226
36. Bharat GP, Dipak VP, Sanjay SK, Aniruddha BP, Sung HH (2012) Effect of sintering temperatures on the synthesis of SnO₂ nanospheres. *ISRN Chem Eng* 5402:946–989
37. Novinrooz AP, Sarabadani A, Garousi J (2006) Characterization of pure and antimony doped SnO₂ thin films prepared by the sol-gel technique. *Iran J Chem Eng* 25:31–38
38. Hadj B, Messaoud C (2011) Synthesis and characterization of pure and alkali catalysis metals doped tin dioxide. *Afr J Basic Appl Sci* 5:228–234
39. Tseng KT, Lin SY, Chen JY, Chu H (2010) A review of photocatalysts prepared by sol-gel method for VOCs removal. *Int J Mol Sci* 11:2336–2361
40. Norris DJ, Efron AL, Erwin SC (2008) Doped nanocrystals. *Science* 319:1776–1779
41. Chandra BA, Thangadurai P, Ramasamy S (2006) Grain size dependent electrical studies on nanocrystalline SnO₂. *Mater Chem Phys* 95:72–78
42. Sadeh A, Sladkevich S, Gelman F, Prikhodchenko P, Baumberg I, Berezin O, Lev O (2007) Sol-gel-derived composite antimony-doped tin oxide-coated clay-silicate semitransparent and conductive electrodes. *Anal Chem* 79:5188–5195
43. Yu W, Idalia R, Jorg JSA (2007) Optical band gap and photoconductance of electrospun tin oxide nanofibres. *J Appl Phys* 102:093517-5
44. Chinnappa L, Ranichandran K, Periathambi T, Muruganatham G, Sriram S, Sakthivel B (2012) Influence of solvent volume on solar cell related electrical and optical properties of antimony doped tin oxide films synthesized using a low-cost spray technique. *J Appl Sci* 12:1651–1655
45. Batzill M, Diebold U (2005) The surface and materials science of tin oxide. *Prog Surf Sci* 79:47–154
46. Bergermayor W, Tanaka I (2004) Reduced SnO₂ surfaces by first principles calculations. *Appl Phys Lett* 84:909–911
47. Yoo KS, Cho NW, Song HS, Jung HJ (1995) Surface morphology and gas sensing characteristics of SnO_{2-x} thin films oxidized from Sn films. *Sensor Actuator B* 24–25:474–477
48. Robertson J, Clark SJ (2011) Limits to doping in oxides. *Phys Rev B* 8:075205
49. Shukla S, Seal S (2004) Encyclopedia and nanotechnology. *Nanosci Nanotechnol Lett* 10:1–16
50. Aw XYG, Hq L (2002) The preparation characterization and their photocatalytic activities of rare earth doped TiO₂ nanoparticles. *J Catal* 207:151–157
51. Jinkawa T, Sakai G, Tamaki N, Yamazoe N (2000) Relationship between ethanol gas sensitivity and surface catalytic property of tin oxide sensors modified with acidic or basic oxides. *J Mol Catal A* 155:193–200
52. Carren'o NLV, Fajardo HV, Maciel AP, Valentini A, Pontes FM, Probst LFD, Leite ER, Longo E (2004) Selective synthesis of vinyl ketone over SnO₂ nanoparticle catalysts doped with rare earths. *J Mol Catal A* 207:89–94
53. Reed JS (1995) Principle of ceramics processing. Wiley, New York
54. Liu CH, Tang C, Zh M, Qiang J (2008) Characterization and activity of visible-light-driven TiO₂ photocatalyst codoped with nitrogen and cerium. *J Solid State Chem* 181:913–919
55. Melghit K, Bouziane K (2006) One step aqueous solution preparation of nanosize iron-doped tin oxide from SnO₂ xH₂O gel. *Mater Sci Eng B* 128:58–62
56. Melghit K, Bouziane K (2007) Low temperature preparation and magnetic properties of V-doped SnO₂ nanoparticles. *J Am Ceram Soc* 8:2420–2423
57. Joint Committee on Powder Diffraction Standards, powder diffraction (File No. JCPDS-41-1445) (ICSD data)
58. Lin W-C, Lin Y-J (2012) Effect of vanadium (IV)-doping on the visible light-induced catalytic activity of titanium dioxide catalysts for methylene blue degradation. *J Environ Eng Sci* 29:447–452
59. He X, Wang C, Wang H, Hong F, Xu X, Chen J, Son S (2011) Increasing the catalytic of iodine for the photodegradation of 2-chlorophenol under visible light irradiation. *J Hazard Mater* 189:595–602
60. Kamble PS, Sawant BS, Pangarkar GV (2006) Photocatalytic mineralization of phenoxyacetic acid using concentrated solar radiation and titanium dioxide in slurry photoreactor. *Chem Eng Res Des* 84:355–362
61. Fan C, Xue P, Sun Y (2006) Preparation of nano-TiO₂ doped with cerium and its photocatalytic activity. *J Rare Earth* 24:309–313

Publication II

A. M. Al-Hamdi, M. Sillanpää, J. Dutta

Photocatalytic degradation of phenol by iodine doped tin oxide nanoparticles under UV and sunlight irradiation

Reprinted with permission from
Journal of Alloys and Compounds
Vol. 618, pp. 366-371, 2015
© 2015, Elsevier



Photocatalytic degradation of phenol by iodine doped tin oxide nanoparticles under UV and sunlight irradiation


 Abdullah M. Al-Hamdi^a, Mika Sillanpää^a, Joydeep Dutta^{b,†}
^a Laboratory of Green Chemistry, Lappeenranta University of Technology, Sammonkatu 12, 50130 Mikkeli, Finland ^b Chair in Nanotechnology, Water Research Center, Sultan Qaboos University, P.O. Box 17, 125 Al-Khoudh, Oman

article info

Article history:
 Received 12 May 2014
 Received in revised form 11 August 2014
 Accepted 12 August 2014 Available online 20 August 2014

Keywords:
 Tin oxide
 Sol–gel process
 Nanoparticle
 Photocatalysis
 Phenol degradation
 Visible light

abstract

Iodine doped tin oxide (SnO₂:I) nanoparticles were prepared by sol–gel synthesis and their photocatalytic activities with phenol as a test contaminant were studied. In the presence of the catalysts, phenol degradation under direct sunlight was comparable to what was achieved under laboratory conditions. Photocatalytic oxidation reactions were studied by varying the catalyst loading, light intensity, illumination time, pH of the reactant and phenol concentration. Upon UV irradiation in the presence of SnO₂:I nanoparticles, phenol degrades very rapidly within 30 min, forming carboxylic acid which turns the solution acidic. Phenol degradation rate with 1% iodine doped SnO₂ nanoparticles is at least an order of magnitude higher compared to the degradation achieved through undoped SnO₂ nanoparticles under similar illumination conditions.

© 2014 Elsevier B.V. All rights reserved.

1. Introduction

Phenols, bisphenols A, dyes, pharmaceuticals, parabens, endocrine disrupting compounds, phthalates and benzoic acids are all severe environmental pollutants [1–3] that are introduced into the environment from chemical and pharmaceutical industries [4]. Advanced oxidative processes (AOPs) are one of the most effective technologies suitable for the treatment of organic pollutants to harmless end products. The reactions are activated through the generation of very reactive species such as hydroxyl radicals. Significant progress has been made in recent years in synthesizing nanoparticles as environmental purification photocatalysts [5,6]. Many researchers reported that titanium dioxide (TiO₂), zinc oxide (ZnO) and tin dioxide (SnO₂) are the most active catalysts for the degradation of dyes, phenols and pesticides [7–11]. In addition, these semiconductors have been recognized as preferable materials for photocatalytic processes due to their photosensitivity, non-toxicity, low cost and high chemical stability [7,12,13].

Several studies have been carried out on the application of TiO₂ and ZnO for mineralization of organics [14–18]. A new class of activated iodine doped TiO₂ was found to enhance photocatalytic oxidation of phenol under UV and visible light illumination [19]. In another work, catalytic activity of iodine doped titanium dioxide

was enhanced by modifying with tin dioxide [20]. The light response range and photo-efficiency of TiO₂ is limited because of its wide band gap [18,21]. It has been reported that TiO₂ doped with non-metals extends the absorption wavelengths from UV to visible region that enhances visible light photocatalytic activity [22,23]. TiO₂ nanoparticles and co-doped with iodine and fluorine showed better degradation of organic compounds under visible light irradiation [24]. It has been reported that iodine atoms prefer to be doped near TiO₂ surface due to strong I–O repulsion [25]. In iodine-doped TiO₂ nanoparticles, the recombination of e[−]–h⁺ pairs are inhibited since the doped I sites not only trap electrons, but also facilitates electron transfer to the surface adsorbed species, thus enhancing photocatalytic activity [26]. Continuous states consisting of 5p and/or 5s orbitals of I⁵ and O 2p orbitals of the valence band are favorable for efficient trapping of holes at the I-induced states in TiO₂ nanoparticles.

Tin oxide or stannic oxide (SnO₂) is considered as a promising semiconductor photocatalyst, which is usually n-type with tetragonal crystal structure and a band gap of around 3.6 eV [27], rendering it transparent in the visible region up to the edge of the ultraviolet region of the solar spectra [28]. In spite of large scale utilization of (SnO₂) powders in different applications, and many reports devoted to its preparation techniques, the investigation of the surface science of (SnO₂) indicated that tin dioxide is comparatively unexplored for photocatalytic applications [29]. As the rutile structure of TiO₂ matches the rutile phase of SnO₂ [30],

† Corresponding author. Tel.: +968 2414 3266; fax: +968 24413532.
 E-mail address: dutta@squ.edu.om (J. Dutta).

it should be possible to introduce iodine ions in SnO₂ crystals in a wet-chemical process.

Among various synthesis techniques, the sol–gel process for tin oxide preparation has numerous advantages [31,32]. Several studies on doping of tin dioxide nanocrystals with different metals have been reported in recent years [33,34]. Anionic or cationic doping of wide band gap semiconductor photocatalysts has been conducted to improve their visible light absorption characteristics [35,36]. The oxygen deficient crystal structure, SnO_{2-x}, leads to an enhancement of catalytic activities of adsorbed surface species [35]. The conduction band edge in n-type oxides like SnO₂ are deep below vacuum level and are thus relatively easy to dope as it is controlled by the compensation of native defects. Doping occurs by moving the Fermi energy to the band edge leading to the spontaneous formation of compensation defects if the formation energy of the defect falls to zero at the Fermi energy. Upon doping SnO₂ with iodine, the Fermi energy will be shifted towards the conduction band, which would eventually lead to an efficient transfer of photo-induced electrons from the conduction band to the SnO₂ surface [35–37].

The goal of this study was to synthesize nanosized doped and undoped tin dioxide particles by sol–gel process with different iodine concentrations. Photocatalytic properties of SnO₂:I nanoparticles were studied through the degradation and mineralization of phenol in water upon illumination with UV light and upon direct exposure to sunlight. This simple technique to synthesize iodine doped tin dioxide nanoparticles could allow its wide-scale use for the degradation of phenol and other toxic organic compounds.

2. Experimental

2.1. Materials

Analytical-grade tin (IV) chloride (SnCl₄, Sigma Aldrich, Purity: 99.99%), iodine (I₂, Sigma Aldrich, 99.9%), ethanol, (C₂H₅OH, ETAX Aa Merck Absolute), phenol (C₆H₅OH, Sigma Aldrich, Purity: 99.99%), p-Benzoquinone (O=C₆H₂O, BDH, AnalaR 99%), resorcinol (C₆H₄(OH)₂, BDH, AnalaR 99%), acetic acid (C₂H₄O₂, Sigma Aldrich, 99.9%), benzoic acid (C₆H₅COOH, BDH, AnalaR 99%), sulfuric acid (H₂SO₄, Sigma Aldrich, 99%), hydrochloric acid (HCl, Sigma Aldrich, 99%), sodium hydroxide pellets (NaOH, Sigma Aldrich, 99%), and methanol (CH₃O, Sigma Aldrich, 99% HPLC grade), sodium chloride (NaCl, BDH, 99% AnalaR grade) were used in the experimental studies. Double deionized water from Ultra Clear Water SG was used for the preparation of all aqueous solutions.

2.2. Photocatalyst preparation

2.2.1. Synthesis of pure and doped-SnO₂ nanoparticles

SnO₂ nanoparticles containing different percentages of iodine ions in the starting solution were synthesized by sol–gel technique by the following procedure: 5.225 ml of SnCl₄ mixed in 100 ml absolute ethanol, and used as precursor for synthesizing SnO₂ nanoparticles. The mixture was continuously stirred for 2 h at room temperature, until a colorless solution was obtained. The solution was then condensed in a round bottom flask kept at a constant temperature of 80 °C. A colorless solution of tin alkoxide was obtained after heating the mixture at 80 °C under vacuum conditions [24]. For the synthesis of iodine doped tin dioxide nanoparticles, different concentrations of iodine were mixed and dissolved separately in ethanol and added to the precursor solution. A turbid colloidal solution of tin alkoxide was obtained, after adding aqueous ammonia (25%) into the condensed solution upon continuous stirring until a pH value of 8 was reached [24]. After refluxing, the resultant solution was poured into an open heated plate kept at 30 °C. This transparent colloidal suspension was left for about 5–6 days until it gelled completely. The gel was then dried at 80 °C for 7 h. Finally, the obtained powder was air-annealed at 200 °C for 7 h.

2.2.2. Characterization

Optical absorption spectra were recorded in colloidal suspension in a double beam spectrophotometer (Perkin Elmer, Lambda 45). To study the surface morphology of the prepared SnO₂ and SnO₂:I samples, scanning electron microscopy (SEM) was carried out with JEOL (Japan) (JSM-5600LY) working at 30 kV. The crystalline phase of the synthesized SnO₂ and SnO₂:I powder was analyzed by X-ray powder diffraction (XRD) using a MiniFlex 600 diffractometer (Rikagu, Japan) with Cu K α radiation (wavelength = 1.54 Å). Diffractograms of powders were recorded in 2 θ scan configuration, in the 10–80° 2 θ range, with the data collected at steps of

0.02°. 200–300 mg of sample was degassed at 300 °C for 3 h under nitrogen (N₂) flow followed by a six point N₂ adsorption carried out at p/p₀ of 1–5 in a Nova 2200 analyzer. The surface area was determined by the Nova 2200 analyzer software using the Brunauer–Emmett–Teller (B.E.T.) method.

2.3. Photocatalysis experiments

2.3.1. Photocatalytic reactors

The photoreactor was a cylindrical Pyrex-glass container of 250 ml capacity, 50 mm internal diameter and 300 mm in height. 8 W medium pressure mercury lamp (Osaka, Japan) with an emission of about 80 W/m² was used for irradiation of the samples and the reaction temperature was controlled at 25 °C by cooling with water. A second photoreactor for the solar photocatalysis experiments was constructed using a borosilicate glass container of 250 ml capacity, 100 mm internal diameter and 200 mm in height where sunlight was directed axially at the center of the reactor.

2.4. Experimental procedures

To investigate the effects of different dopants on the photocatalytic activity of SnO₂, oxidative photodegradation of phenol was chosen to evaluate the photocatalytic activity of synthesized nanoparticles. The study of degradation of phenol in water was carried out at 25 °C using the water-cooled cylindrical glass batch photoreactor. The experimental conditions were varied as follows: the amount of catalyst powder (photocatalyst) was kept constant at 0.065 g in 50 ml of the test contaminant (aqueous phenol solution). 10 mg/l aqueous solution of phenol was used to carry out photocatalytic experiments. Prior to each test, the mixture was kept in the dark for 30 min under constant magnetic stirring to ensure that the adsorption–desorption equilibrium was reached before illuminating the samples. At the end of the adsorption period (in dark conditions), prior to turning the light on, reference samples were collected for analysis. The irradiation times varied from 2 to 5 h. Aliquots of the suspensions were collected and removed from the reactor every 15 or 30 min. At given time intervals, from the collected samples, photocatalyst particles were removed first by centrifugation (4000 rpm, for 5 min) using Eppendorf Centrifuge (model 5810R) followed by filtration through a 0.2 μ m Millipore filter.

2.5. Analytical methods

The change in phenol concentration in each photodegraded solution was monitored by two sets of measurements. The maximum absorbance of phenol was measured at λ_{max} = 270 nm in an ultraviolet–visible (UV–Vis) spectrometer (Perkin Elmer Lambda 45). Also, the total organic carbon was determined by a Total Organic Carbon Analyzer (TOC-VCPH Shimadzu) equipped with an auto sampler (ASI-V Shimadzu).

2.6. High performance liquid chromatography analysis (HPLC)

Phenol photodegradation products were analyzed using high performance liquid chromatography (HPLC) which contained a P580 high-precision pump from Dionex (Germering, Germany), which fulfilled the requirement for a measured delivery rate of the mobile phase. The injector was a Rheodyne (Cotati) 8125 valve fitted with a 20 μ l loop. The analysis was carried out using a C18 column (5 μ m) maintained at room temperature. After elution from the column, the eluent passed through a Dionex UVD 170S diode array detector set at 245 nm. The mobile phase for the HPLC separation was prepared by mixing methanol with water 45:55 and then adjusting the pH at 3.0 by adding sulphuric acid (H₂SO₄). The mobile phase was degassed in an ultrasonic bath, and then passed through a Millipore filtration apparatus (0.2 μ m). Photodegraded Phenol and control samples were eluted at a flow rate of 0.5 ml/min.

2.7. Gas chromatography

Solid phase extraction (SPE) columns of chromabond C18 ec (octadecyl-modified silica, Macherey–Nagel) weighing 500 mg had a volume of 3 ml. Columns were first conditioned with three column volumes of methanol (CH₃OH) and two column volumes of 0.01 M hydrochloric acid (HCl) [36]. For extracting the phenolic compounds from the degraded mixture, 200 mg NaCl was added for every 1 ml of sample. HCl (1 M) was used to adjust pH to 2. 2.5 ml sample of phenol was then pipetted to SPE column slowly at a flow rate of 0.5 ml/min. Samples were washed twice with 500 μ l of 0.01 M HCl and dried in vacuum for 10 min. Elution was carried out with 3 500 μ l of methanol. Gas chromatography (Agilent 6890 GC) coupled with mass spectrometry (GC/MS) was used for the determination of phenol concentration. The analysis was carried out using HP-5 (Agilent, 5% phenyl methyl siloxane, capillary 30 m 320 μ m nominal) column. Injection mode was split less, and the volume was 1 μ l. Injector and detector temperatures were maintained at 300 °C. Helium was used as a carrier gas with a flow of 1.2 ml/min. Oven temperature was varied at 20 °C/min up to 260 °C and thereafter at 15 °C/min to 300 °C.

3. Results and discussion

3.1. Undoped and iodine doped SnO₂ nanoparticles

Undoped and doped SnO₂ nanoparticle samples were examined by XRD as shown in Fig. 1. The XRD pattern of SnO₂ samples show the presence of (1 1 0), (1 0 1), (1 1 1), (2 1 1), (2 2 0), (0 0 2), (3 1 0), (1 1 2) and (3 0 1) respectively, matching with the standard XRD file of SnO₂ (JCPDS-#41-1445), regarded as an attributive indication of rutile SnO₂ structure [37–40]. The SnO₂ crystallite sizes obtained from the Debye Scherrer equation considering the most intense peak (1 1 0) follows the well-known trend of crystallite size reduction upon doping and was found to reduce from 8.4 nm for undoped SnO₂ particles to 2.5 nm for the 1 wt.% SnO₂:I samples. In Table 1 we have shown the crystallite sizes which were estimated from the broadening of (1 1 0) peak of XRD patterns. The specific surface area of undoped SnO₂ particles from gas adsorption studies was found to be 28 m² g⁻¹, which increased to 50 m² g⁻¹ for the 1 wt.% iodine doped tin oxide samples, again indicating a reduction of crystallite sizes upon doping.

Typical electron micrographs (SEM) of the photocatalysts are shown in Fig. 2. It is also clear from Fig. 2(a) and (b) that upon iodine doping the average grain size decreases in agreement with what we observed from the estimation of crystallite size from XRD studies (Table 1). In order to get a better insight, we carried out high resolution HRTEM as shown in Fig. 3 where the crystallite size is clearly seen to reduce in size upon doping, agreeing well with the earlier observations made from the SEM and XRD analysis.

3.2. Photocatalytic degradation of phenol

During the photocatalysis experiments, the clear solutions before and after different irradiation times were analyzed by HPLC. It was found as shown in Fig. 4, that phenol was effectively degraded upon solar irradiation for 3 h, with the emergence of fragments observed in HPLC. The main intermediate such as p-benzoquinone appeared at 16 min retention time and is clearly visible in the HPLC results. According to the substitution rules, OH radicals attack the phenol molecule with higher probability in 1 and 4 positions versus OH group of the aromatic ring. The existence of aliphatic intermediates in the reaction mixture was also checked and was found to appear after 6 min retention time, which suggest that the structure of benzene ring was destroyed to form carboxylic acid intermediates through photochemical oxidation by SnO₂:I nanoparticles. As it can be observed in Fig. 4,

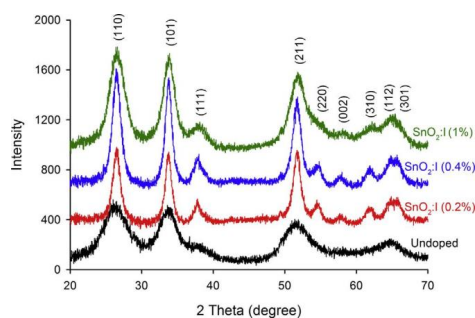


Fig. 1. X-ray diffraction (XRD) patterns of typical samples undoped, 0.2 wt.%, 0.4 wt.% and 1.0 wt.% iodine doped tin dioxide particles synthesized by sol-gel process.

Table 1

Estimated crystallite size of different I doped SnO₂ nano-particles from (1 1 0) peak using the Debye–Scherrer analysis.

Dopant	Crystal size (nm)
Undoped	8.4
SnO ₂ :I (0.2%)	8.0
SnO ₂ :I (0.4%)	7.4
SnO ₂ :I (1%)	2.5

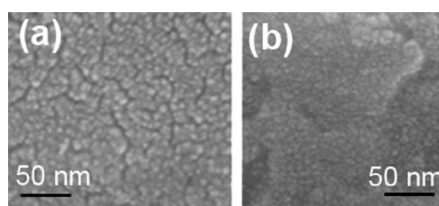


Fig. 2. Typical scanning electron micrograph of (a) undoped and (b) iodine doped tin dioxide nanoparticles synthesized by sol-gel process.

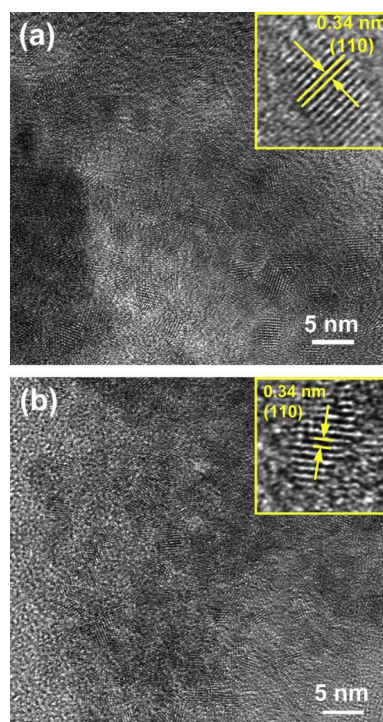


Fig. 3. Typical high resolution transmission electron micrograph of SnO₂ nanoparticles synthesized by sol-gel process (a) undoped (b) 1% iodine doped.

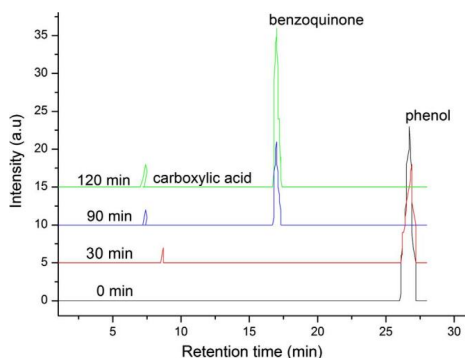


Fig. 4. Spectra of phenol photodegradation before and after 120 min by iodine doped tin dioxide nanoparticles under optimized HPLC conditions.

the maximum concentration of intermediates appear after 2 h of solar irradiation of phenol in the presence of SnO₂:I nanoparticles.

In order to identify the byproducts of the photochemical oxidation process of phenol, GC–MS was used. Fig. 5 shows the trends of the amount of different intermediates during the photocatalytic degradation process. In the same treatment period, for the first 90 min irradiation, the formation of p-benzoquinone was detected at 5 min retention time, but resorcinol was detected after nine minutes running time. Within 150 min, most of the phenol was found to be removed as it can be seen from Fig. 5.

The rate of photodegradation under UV light with undoped SnO₂ nanoparticles was found to be 46% which improved upon using 0.2 and 0.4 wt.% SnO₂:I nanoparticles to 53% and 75% respectively. A maximum rate of phenol removal was achieved using 1.0 wt.% SnO₂:I powders, reaching to 93.4% degradation within 150 min of UV light irradiation, which has almost the highest catalytic activity on phenol in water solution during the photodegradation period, as shown in Fig. 6. Further doping of SnO₂ nanoparticles did not improve the photodegradation characteristics.

Fig. 7 shows the photocatalytic degradation rates as a function of irradiation time with different wt.% SnO₂:I nanoparticles under solar light irradiation. In Fig. 7, no significant difference in photo-catalytic activities were found between samples doped with very small amount of iodine (0.01%) and the undoped samples. The

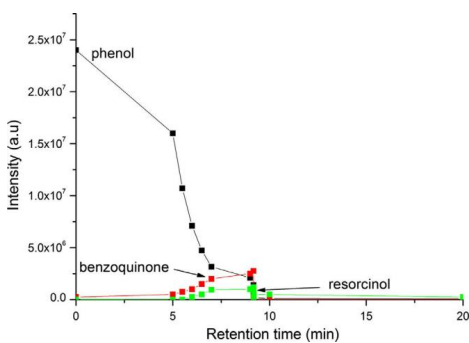


Fig. 5. Reduction in the intensity of phenol peak observed by gas chromatograph upon solar light degradation of phenol in the presence of 1.0 wt.% iodine doped SnO₂ nanoparticles. The appearance of phenol intermediates are drawn in the figure.

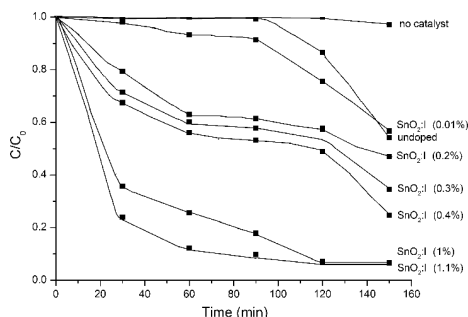


Fig. 6. Comparison of the decrease of phenol degradation with undoped SnO₂ and different SnO₂:I under UV light irradiation as measured by monitoring the phenol peak (at 270 nm) by UV–Vis spectrometry.

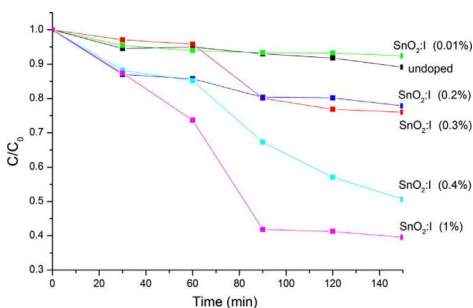


Fig. 7. Comparison of the decrease of phenol degradation with undoped SnO₂ and different SnO₂:I under solar light irradiation measured by monitoring the phenol peak (at 270 nm) by UV–Vis spectrometry.

0.2 wt.% iodine doped SnO₂ exhibits better photodegradation efficiency than the undoped SnO₂ nanoparticles. The reduction of phenol is about 45% in 2 h in the presence of 0.4 wt.% SnO₂:I nanoparticles. 1.0 wt.% SnO₂:I powders under solar light irradiation shows that phenol concentration degraded by up to 60% within 2 h.

In Fig. 8 we show that upon doping SnO₂ with iodine photocatalytic activity of the particles were improved which can be attributed to the increased optical absorption of the SnO₂:I nanoparticles (Fig. 9). In order to establish the reusability of the photocatalysts, we carried out stability test with 1.0 wt.% SnO₂:I nanoparticles over multiple cycles, each with 6 h of solar light irradiation. The nanoparticles were carefully removed from the degraded phenol solution and then reintroduced in fresh phenol solution for another cycle. We observed that at least for the first three cycles the particles yield comparable photocatalytic activity (Table 2).

From Table 3, we can observe that no appreciable change in photoactivity of SnO₂:I nanoparticle occurs for samples doped with lower than 0.2 wt.% iodine. Photocatalytic activity started to improve in samples with 0.3 wt.% iodine or higher dopant concentration.

3.3. Total organic carbon

In order to determine the degree of mineralization reached during the photocatalysis experiments, nine to ten samples in each

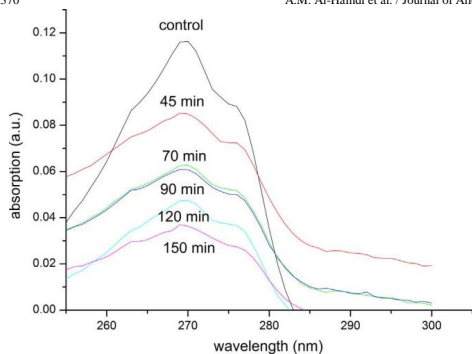


Fig. 8. UV-Vis spectra of phenol obtained at different times during the photoirradiation with AM 1.5 solar light at 0 min (control), 45 min, 90 min, 120 min and 150 min, respectively.

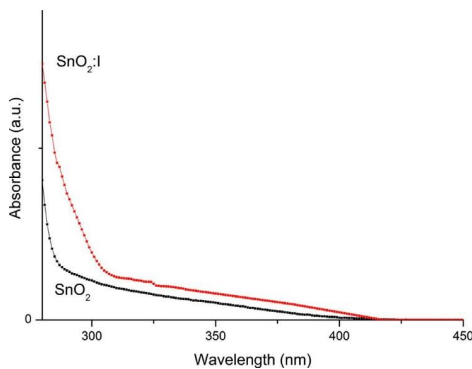


Fig. 9. Typical optical absorption of undoped SnO₂, 1.0 wt.% I-doped SnO₂, dried samples collected from a suspension in aqueous media.

Table 2

Degradation of phenol by 1 wt.% I-doped SnO₂ for 6 h during each cycle (note: fresh phenol sample was added after every 6 h).

Cycle number	1	2	3	4	5
Phenol degradation (%)	64.14	63.83	63.57	51.25	33.04

test were collected at a time interval of 15 min during 150 min of photo-irradiation and then analyzed for TOC concentration. No change in TOC was observed when the UV irradiation was carried out without any photocatalyst. The maximum TOC mineralization after 120 min UV irradiation was observed to occur when 1.1 wt.% SnO₂:I samples were used (83% degradation), while only 12% TOC mineralization was achieved with undoped SnO₂ upon irradiation for 120 min. 92% mineralization was observed after 150 min of UV irradiation with 1.1 wt.% SnO₂:I catalysts, compared to only 33% TOC mineralization observed with the undoped catalyst (Fig. 10). 67% of TOC removal was achieved in the presence of 0.4 wt.% SnO₂:I within 150 min of UV irradiation, while 48% of phenol mineralization was observed in the presence of 0.3 wt.% SnO₂:I

Iodine content (%)	Rate constant (min ⁻¹)
0.00	0.004
0.01	0.004
0.2	0.004
0.3	0.005
0.4	0.007
1.0	0.011
1.1	0.009

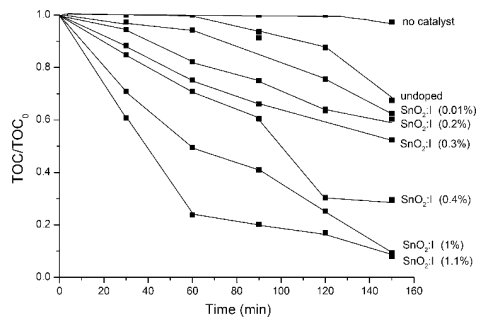


Fig. 10. Total organic carbon (TOC) removal from phenol solutions during 2 h of photocatalytic degradation by different SnO₂:I under UV light irradiation as measured by monitoring the phenol peak (at 270 nm) in UV-Vis spectrometry.

during the same period. The reduction in TOC generally followed the same trend observed in the phenol removal as discussed earlier (using UV-Vis spectroscopy).

The pH of phenol concentrations during degradation initially decreased, but then increased to values equal to or slightly higher than the initial pH (Fig. 11). Binary hydroxyl compounds catechol, benzoquinone, hydroquinone are formed during photocatalytic degradation of phenol. The OH radical formed by redox reaction oxidizes the conjugate structure of the phenyl ring yielding carboxylic acids formed via ring cleavage to give malonic acid, then short-chain organic acids such as, maleic, oxalic, acetic and formic acids. Finally upon continuous oxidation the carboxylic acids are converted to carbon dioxide (CO₂) and water (H₂O). It has been reported that the initial pH of aqueous phenol solution (5.5–6.0)

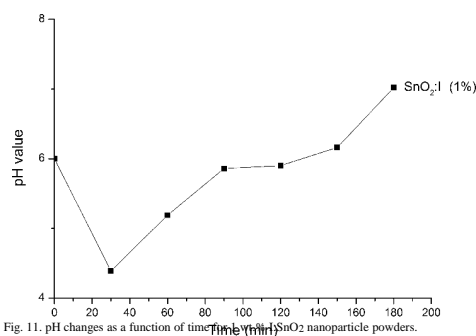


Fig. 11. pH changes as a function of time for SnO₂:I nanoparticle powders.

decrease to 3.5 upon continued photo-irradiation [41]. pKa of phe-nol is around 9 and thus an aqueous solution is mildly acidic as observed from the pH of the starting solution (pH 5.7) as shown in Fig. 11. Upon UV irradiation in the presence of SnO₂:I nanoparticles, phenol degrades very rapidly within 30 min (Fig. 6), with the appearance of carboxylic acid as observed in the HPLC measurements (Fig. 4). The expected carboxylic acid byproducts are strongly acidic (pKa 3–5) and thus the pH of the phenolic solution decreases to 4.35 upon light irradiation for 30 min in the presence of SnO₂:I nanoparticles. Upon subsequent removal of carboxylic acids to CO₂ and water by mineralization, the solution gets less acidic as is observed in Fig. 11 [42].

In an earlier work we have reported the rare earth doped tin dioxide nanoparticles and their effect on photocatalysis. Halide atoms like fluorine, chlorine and bromine are extensively studied for application as dopants of metal oxides like SnO₂, but iodine is relatively new and has not been studied in detail. The goal of this work was to find an optimum condition for the synthesis of iodine doped tin oxide nanoparticles which can improve photocatalytic degradation. From our earlier report (rare earth doped tin dioxide nanoparticles) [43], we find that iodine doping indeed improves the photocatalytic behavior of tin dioxide.

4. Conclusions

The addition of iodine to tin dioxide improved the photocatalytic performance of nanoparticle powders. Based on the doping technique used here, it was found that performance of the nanoparticles was optimized using 1.0 wt.% SnO₂:I. At the higher iodine doping levels no appreciable improvement in phenol degradation was found. Introducing iodine atoms enhances pollutant degradation by changing the concentration of oxygen vacancies in the SnO₂ crystal lattice. Improvement of these simple techniques to utilize solar radiation more efficiently could provide more economic solutions for the degradation of organic compounds like phenol from water.

Acknowledgements

Authors would like to thank partial financial support from the Chair in Nanotechnology programme of the Research Council of Oman and the College of Science for giving this opportunity to carry out the research at Sultan Qaboos University.

References

- [1] S.H. Swan, *Environ. Res.* 108 (2008) 177–184.
- [2] S. Anandan, *Mater. Sci. Forum* 712 (2012) 1–24.

- [3] S. Kaneco, M.A. Rahman, T. Suzuki, H. Katsumata, K. Ohta, *J. Photochem. Photobiol. A* 163 (2004) 419–424.
- [4] J. Michalowicz, W. Duda, *Pol. J. Environ. Stud.* 3 (2007) 347–362.
- [5] N. Chantarat, Y.W. Chen, S.H. Hsu, C.C. Lin, M.C. Chiang, S.Y. Chen, *J. Solid State Sci. Technol.* 2 (2013) Q131–Q135.
- [6] T. Bora, J. Dutta, *J. Nanosci. Nanotechnol.* 14 (2014) 613–626.
- [7] H. Jiang, Q. Wang, S. Zang, J. Li, X. Wang, *J. Alloys Comp.* 600 (2014) 34–42.
- [8] S. Ahmed, M.G. Rasul, W. Martens, R. Brown, M.A. Hashib, *Water Air Soil Poll.* 215 (2011) 3–29.
- [9] L. Zhang, J. Liu, C. Tang, J. Lv, H. Zhong, Y. Zhao, X. Wang, *Appl. Clay Sci.* 51 (2011) 68–73.
- [10] V. Kruefu, H. Ninsonti, N. Wetchakun, B. Inceesungvorn, P. Pookmanee, S. Phanichphant, *Eng. J.* 16 (2012) 90–99.
- [11] S. Senthilkumar, K. Porkodi, R. Vidyakshmi, *J. Photochem. Photobiol. A* 170 (2005) 225–232.
- [12] D. Liang, C. Cui, H. Hu, Y. Wang, S. Xu, B. Ying, P. Li, B. Lu, H. Shen, *J. Alloys Comp.* 582 (2014) 236–240.
- [13] U. Diebold, *Surf. Sci. Rep.* 48 (2003) 53–229.
- [14] C.M. Teh, A.R. Mohamed, *J. Alloys Comp.* 509 (2011) 1648–1660.
- [15] C. Karunakaran, R. Dhanalakshmi, *Int. J. Chem. Kinet.* 41 (2009) 275–283.
- [16] N. Philippidis, S. Sotiropoulos, A. Efsthathiou, I. Poullos, *J. Photochem. Photobiol. A* 204 (2009) 129–136.
- [17] R. Ullah, J. Dutta, *J. Hazard. Mater.* 156 (2008) 194–200.
- [18] S.K. Kansal, S. Sood, A. Umar, S.K. Mehta, *J. Alloys Comp.* 581 (2013) 392–397.
- [19] X. Hong, Z. Wang, W. Cai, F. Lu, J. Zhang, Y. Yang, N. Ma, Y. Liu, *Chem. Mater.* 17 (2005) 1548–1552.
- [20] Z. He, C. Wang, H. Wang, F. Hong, X. Xu, J. Chen, S. Song, *J. Hazard. Mater.* 189 (2011) 595–602.
- [21] R. Pan, Y. Wu, Z. Li, Z. Fang, *Appl. Surf. Sci.* 292 (2014) 886–891.
- [22] Y.F. Tu, S.Y. Huang, J.P. Sang, X.W. Zou, *J. Alloys Comp.* 482 (2009) 382–387.
- [23] S. In, A. Orlov, R. Berg, F. Garcia, S. Pedrosa-Jimenez, M.S. Tikhov, D.S. Wright, R.M. Lambert, *J. Am. Chem. Soc.* 129 (2007) 13790–13791.
- [24] C. Wen, Y.J. Zhu, T. Kanbara, H.Z. Zhu, C.F. Xiao, *Desalination* 249 (2009) 621–625.
- [25] G. Liu, C. Sun, X. Yan, L. Cheng, Z. Chen, X. Wang, L. Wang, S.C. Smith, G.Q. Lu, H.M. Cheng, *J. Mater. Chem.* 19 (2009) 2822–2829.
- [26] S. Tojo, T. Tachikawa, M. Fujitsuka, T. Majima, *J. Phys. Chem. C* 112 (2008) 14948–14954.
- [27] Z. Zhu, J. Zhou, H. Liu, Z. He, X. Wang, *J. Nanomater. Mol. Nanotechnol.* 1 (2) (2012) 1–5.
- [28] Q.R. Zhao, *Trans. Nonferrous Met. Soc. China* 19 (2009) 1227–1231.
- [29] M. Batzill, U. Diebold, *Prog. Surf. Sci.* 79 (2005) 47–154.
- [30] D.Y. Torres, R.C. Perez, G.T. Delgado, O.Z. Angel, *J. Mater. Sci.* 22 (2011) 684–689.
- [31] K. Vijayarangamuthu, S. Rath, *J. Alloys Comp.* 610 (2014) 706–712.
- [32] Y.C. Zhang, Z.N. Du, K.W. Li, M. Zhang, D.D. Dionysiou, *J. Appl. Mater. Interfaces* 3 (2011) 1528–1537.
- [33] A.K. Sinha, M. Pradhan, S. Sarkar, T. Pal, *Environ. Sci. Technol.* 47 (2013) 2339–2345.
- [34] A.A. Zhukova, M.N. Rumyantseva, V.B. Zaytsev, A.V. Zaytseva, A.M. Abakumov, A.M. Gaskov, *J. Alloys Comp.* 565 (2013) 6–10.
- [35] K.S. Yoo, N.W. Cho, H.S. Song, H.J. Jung, *Sens. Actu. B. – Chem.* 25 (1995) 474–477.
- [36] S.H. Vilhunen, M.E.T. Sillanpää, *J. Hazard. Mater.* 161 (2009) 1530–1534.
- [37] A. Das, V. Bonu, A.K. Prasad, D. Panda, S. Dhara, A.K. Tyagi, *J. Mater. Chem. C* 2 (2014) 164–171.
- [38] K. Melghit, K. Bouziane, *Mater. Sci. Eng. B* 128 (2006) 58–62.
- [39] K. Melghit, K. Bouziane, *J. Am. Ceram. Soc.* 90 (2007) 2420–2423.
- [40] R. Liu, Y. Huang, A. Xiao, H. Liu, *J. Alloys Comp.* 503 (2010) 103–110.
- [41] A. Mills, S. Morris, R. Davies, *J. Photochem. Photobiol. A* 70 (1993) 183–191.
- [42] Y. Feng, Y. Cui, B. Logan, Z. Liu, *Chemosphere* 70 (2008) 1629–1636.
- [43] A. Al-Hamdi, M. Sillanpää, J. Dutta, *J. Mater. Sci.* 49 (2014) 5151–5159.

Publication III

A. M. Al-Hamdi, M. Sillanpää, Tanujjal Bora, J. Dutta

Efficient photocatalytic degradation of phenol in aqueous solution by SnO₂/Sb nanoparticles.

Reprinted with permission from

Applied Surface Science

Vol. 42, pp 229-236, 2016

© 2016, Elsevier



Efficient photocatalytic degradation of phenol in aqueous solution by SnO₂:Sb nanoparticles



Abdullah M. Al-Hamdi^{a,b,c,*}, Mika Sillanpää^a, Tanujjal Bora^c, Joydeep Dutta^{c,d}

^a Laboratory of Green Chemistry, Lappeenranta University of Technology, Sammonkatu 12, 50130 Mikkeli, Finland^b

Chemistry Department, Sultan Qaboos University, P.O. Box 17, 123 Al-Khoudh, Oman

^c Chair in Nanotechnology, Water Research Center, Sultan Qaboos University, P.O. Box 17, 123 Al-Khoudh, Oman

^d Functional Materials Division, ICT, KTH Royal Institute of Technology, Isafjordsgatan 22, SE-164 40 Kista/Stockholm, Sweden

article info

Article history:

Received 19 November 2015
Received in revised form 8 February 2016
Accepted 15 February 2016 Available online 22 February 2016

Keywords:

Tin dioxide nanoparticles
Phenol degradation
Photocatalysis
Antimony
Doping

abstract

Photodegradation of phenol in the presence of tin dioxide (SnO₂) nanoparticles under UV light irradiation is known to be an effective photocatalytic process. However, phenol degradation under solar light is less effective due to the large band gap of SnO₂. In this study antimony (Sb) doped tin dioxide (SnO₂) nanoparticles were prepared at a low temperature (80 °C) by a sol–gel method and studied for its photo-catalytic activity with phenol as a test contaminant. The catalytic degradation of phenol in aqueous media was studied using high performance liquid chromatography and total organic carbon measurements. The change in the concentration of phenol affects the pH of the solution due to the by-products formed during the photo-oxidation of phenol. The photoactivity of SnO₂:Sb was found to be a maximum for 0.6 wt.% Sb doped SnO₂ nanoparticles with 10 mg L⁻¹ phenol in water. Within 2 h of photodegradation, more than 95% of phenol could be removed under solar light irradiation.

© 2016 Elsevier B.V. All rights reserved.

1. Introduction

Endocrine disrupting chemicals such as phenols, bisphenols A, dyes, pharmaceuticals, parabens, phthalates, and benzoic acid [1–3] are found in our environment and this causing increasing global concern [4,5] and could link to human reproductive abnormalities [6]. Sources of phenol pollution in water has been found in waste from the refining of oil and coal tar industries [7] and the distillation of wood or coal [8], phenolic chemicals used in livestock dips [9], and discharges of domestic sewage [10] and even from rotting of vegetation.

Metal oxide semiconductor photocatalysts have attracted a lot of attention because of their usefulness in environment protection. The band gap of titanium dioxide (TiO₂), zinc oxide (ZnO) and tin dioxide (SnO₂) are 3.2 eV, 3.3 eV and 3.6 eV, respectively rendering these photocatalysts active under UV light activation [11]. SnO₂ nanoparticles are relatively less studied [12], but is highly suitable photocatalyst as it is chemically highly stable [13]. In fact, SnO₂ has been shown to be an active photocatalyst mate-

rial for the degradation of many organic compounds [14]. In metal oxides, upon irradiation with an appropriate light energy, the free electrons are excited to the empty conduction bands leaving positively charged holes in the valence band, resulting in the formation of electron–hole pairs (e⁻–h⁺) [15]. As the band gap of SnO₂ is 3.6 eV, most of the photocatalytic activities of this semiconductor have been limited to the UV light region [16]. It is well known that UV irradiation requires a high energy source of light, which is expensive and hazardous, a reason why solar irradiation for photocatalytic processes needs to be developed. Modifications of SnO₂ are required in order to broaden the photoresponse to longer wavelengths. Doping metal oxides by transition metals lead to the formation of energy states below the conduction band effectively increasing visible light absorption in materials [17–19]. Further, the doping of SnO₂-based nanomaterials offers a convenient way to tailor their electrical, optical and microstructural properties [20].

Antimony (Sb) is one of the most common n-type dopant for SnO₂, popularly used for preparing n-type SnO₂ thin films [21]. As SnO₂ is a n-type semiconductor [22], pentavalent Sb⁵⁺ ions can replace tetravalent Sn⁴⁺ sites. It has been reported that Sb doping of SnO₂ leads to the formation of donor levels in the bulk, shifting the Fermi level toward the conduction band (CB) edge. Substitution of Sn⁴⁺ by Sb⁵⁺ is found to be dominant at lower Sb doping concentrations (typically less than 2 wt.%) due to their similar ionic radii (Sn⁴⁺ ~0.071 nm and Sb⁵⁺ ~0.065 nm), resulting in an increase

* Corresponding author at: Laboratory of Green Chemistry, Lappeenranta University of Technology, Sammonkatu 12, 50130 Mikkeli, Finland.

E-mail addresses: Abdullah.AlHamdi@lut.fi,

alhamdi@sq.edu.om (A.M. Al-Hamdi).

<http://dx.doi.org/10.1016/j.apsusc.2016.02.123>

0169-4332/© 2016 Elsevier B.V. All rights reserved.

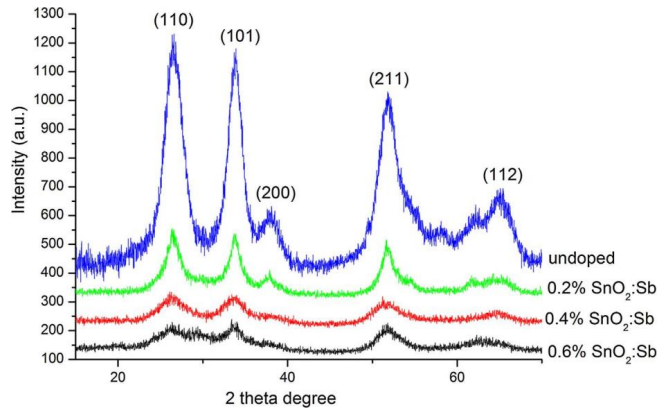


Fig. 1. X-ray diffraction (XRD) patterns of typical undoped tin dioxide nanoparticles and (0.2, 0.4, 0.6 wt.%) antimony doped tin dioxide nanoparticles synthesized by sol-gel process.

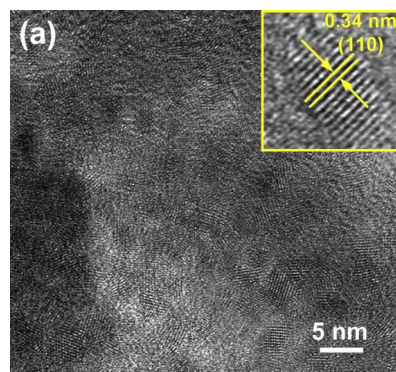


Fig. 2. Typical high resolution transmission electron micrograph of 0.6% antimony doped tin dioxide nanoparticles synthesized by sol-gel process.

in the conductivity of SnO_2 [23–25]. However at higher Sb doping levels, reduction in the conductivity, optical transparency, and crystallinity were reported due to the precipitation of antimony oxides [26], reduction in Sb^{5+} states to Sb^{3+} states resulting in the lowering of n-type conductivity due to the formation of the acceptor sites [27].

In this study, we have synthesized SnO_2 :Sb nanoparticles by sol-gel process at room temperature, which is suitable for large scale production. The synthesis process is simple and relatively inexpensive, that is based on the hydrolysis and condensation of metal ions to form metal oxide [28], providing a control on the size and the shape of nanoparticles [29,30]. The prepared samples were characterized and its photocatalytic performance was studied by degrading phenol under ultraviolet and solar irradiation using different analytical techniques.

2. Experimental

2.1. Materials

Analytical-grade tin(IV) chloride (SnCl_4 , Sigma-Aldrich, Purity: 99.99%), antimony (III) chloride, (SbCl_3 , Fluka, 99%), ethanol ($\text{C}_2\text{H}_5\text{OH}$, ETAX Aa Merck Absolute), phenol ($\text{C}_6\text{H}_5\text{OH}$, Sigma-Aldrich, Purity: 99.99%), p-benzoquinone ($\text{O}=\text{C}_6\text{H}_4=\text{O}$, BDH, AnalaR 99.0%), resorcinol ($\text{C}_6\text{H}_4(\text{OH})_2$, BDH, AnalaR 99.0%), acetic acid ($\text{C}_2\text{H}_4\text{O}_2$, Sigma-Aldrich, 99.9%), benzoic acid ($\text{C}_6\text{H}_5\text{COOH}$, BDH, AnalaR 99.0%), catechol ($\text{C}_6\text{H}_4(\text{OH})_2$, Sigma-Aldrich, 99.0%), ethyl paraben ($\text{C}_9\text{H}_{10}\text{O}_3$, Sigma-Aldrich, 99.0%), sulfuric acid (H_2SO_4 , Sigma-Aldrich, 99.0%), hydrochloric acid (HCl, Sigma-Aldrich, 99.0%), sodium hydroxide pellets (NaOH, Sigma-Aldrich, 99.0%), methanol (CH_3OH , Sigma-Aldrich, 99% HPLC grade) and sodium chloride (NaCl, BDH 99% AnalaR grade) were used in the experimental studies. Double deionized water from Ultra Clear Water SG was used for the preparation of all the solutions.

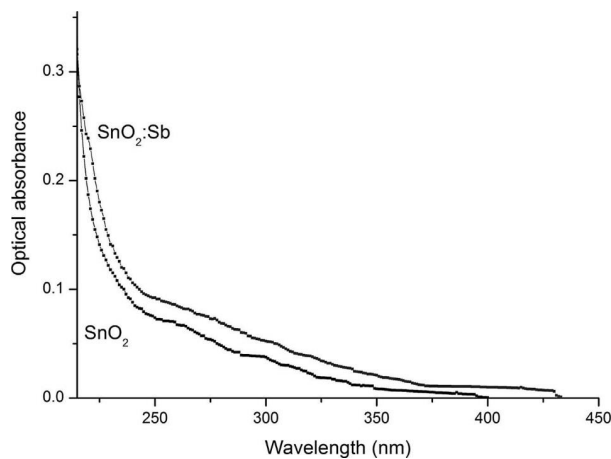


Fig. 3. Typical optical absorption of undoped SnO_2 , and 0.6 wt.% Sb doped SnO_2 nanoparticles suspensions in aqueous media.

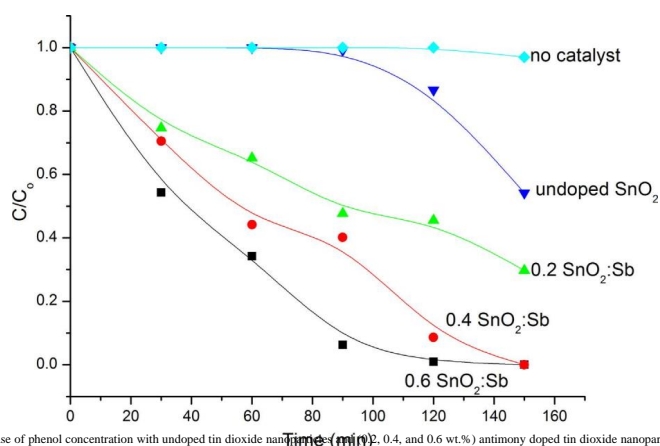


Fig. 4. Comparison of the decrease of phenol concentration with undoped tin dioxide nanoparticles, 0.2, 0.4, and 0.6 wt.% antimony doped tin dioxide nanoparticles under UV light irradiation as measured by monitoring the phenol peak in UV–vis spectrometry.

2.2. Photocatalyst preparation

2.2.1. Synthesis of pure and doped- SnO_2 nanoparticles

SnO_2 nanoparticles containing different percentages of Sb ions in the starting solution were synthesized by sol–gel technique, according to the following procedure:

3.8825 ml of SnCl_4 mixed with 50 ml absolute alcohol (ethanol) and 50 ml ultra-pure water in a round bottom flask and used as a precursor for synthesizing undoped SnO_2 nanoparticles. The mixture was subjected to vigorous stirring for 3 h at room temperature, until a colorless solution was obtained. For the synthesis of SnO_2 :Sb nanoparticles, different concentration of Sb such as (0.2%, 0.4%, 0.6) were mixed and dissolved separately in ethanol and added to the precursor solution. A turbid colloidal solution of tin alkoxide started to appear after adding 25% aqueous ammonia drop by drop into

the solution under continuous stirring until a pH value of 8 was reached. The sol was left for 48 h, for aging in air until the gel was formed. Filtration and successive washing with ultra-pure water was repeated several times to remove both ammonia and chloride ions until all chloride ions had been removed (by examining the filtrate solution using aqueous silver nitrate solution). Later a series of samples were synthesized in the same way by changing the concentration of tin tetrachloride and the percentage amount of the required dopant. Each dopant was added carefully and under vigorous stirring to the total solution containing pure tin tetrachloride. They were then subjected to dissolution in ethanol and synthesis by the same process used for undoped tin dioxide as explained above.

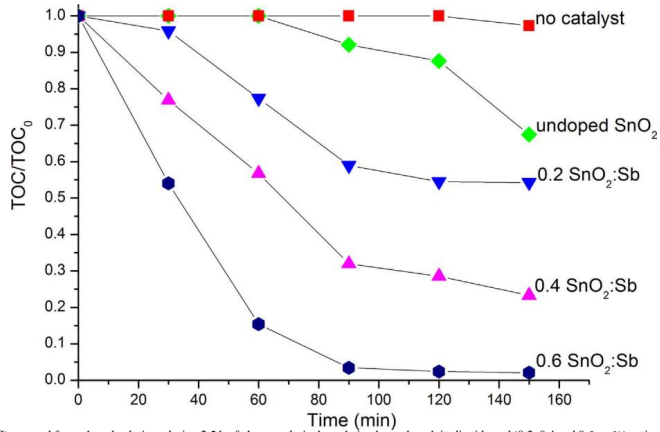


Fig. 5. Total organic carbon (TOC) removal from phenol solutions during 2.5 h of photocatalytic degradation by undoped tin dioxide and (0.2, 0.4 and 0.6 wt.%) antimony doped tin dioxide nanoparticles under UV light irradiation.

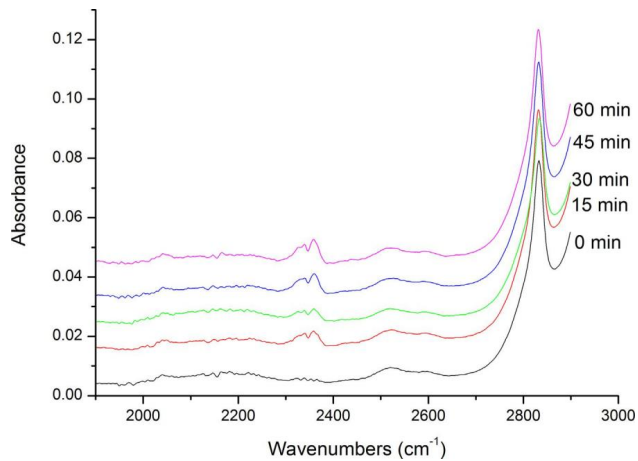


Fig. 6. Evolution of CO₂ as an indication of complete mineralization of phenol molecules during 1 h photocatalytic degradation under UV light irradiation observed by FTIR.

2.2.2. Material characterization

Optical absorption spectra were recorded in colloidal suspension in a double beam spectrometer (PerkinElmer, Lambda 45). To study the surface morphology of the prepared SnO₂ and SnO₂:Sb samples, high resolution transmission electron microscopy (HRTEM) were carried out with JEOL (Japan) (JEM 2100F) working at 200 kV. The crystalline phase of the synthesized SnO₂ and SnO₂:Sb nanoparticles were analyzed by X-ray powder diffraction (XRD) using a MiniFlex 600 diffractometer (Rikagu, Japan) with Cu K radiation (wavelength = 1.54 Å). Diffractograms of powders were recorded in 2 scan configuration, in the 10–90° 2θ range, with the data collected at steps of 0.02°. 200–300 mg of sample was degassed at 300 °C for 3 h under nitrogen (N₂) flow followed by a six point N₂ adsorption carried out at p/p₀ of 1–5 in a Nova[®] 2200 analyzer. Surface area was determined by gas adsorp-

tion technique using Nova[®] 2200 (Brunauer–Emmett–Teller (BET) method).

2.3. Photocatalytic experiments

2.3.1. UV photocatalytic reactor

The photoreactor was a cylindrical pyrex-glass container with a 250 ml capacity, 50 mm internal diameter and 300 mm height. An 8 W medium pressure mercury lamp (Osaka, Japan) was used as UV light source with an intensity of about 80 W/m² and the reaction temperature was kept at 25 °C by cooling with water.

2.3.2. Degradation using natural sunlight

In this case the photoreactor was a borosilicate glass container with a 250 ml capacity, 100 mm internal diameter and 200 mm

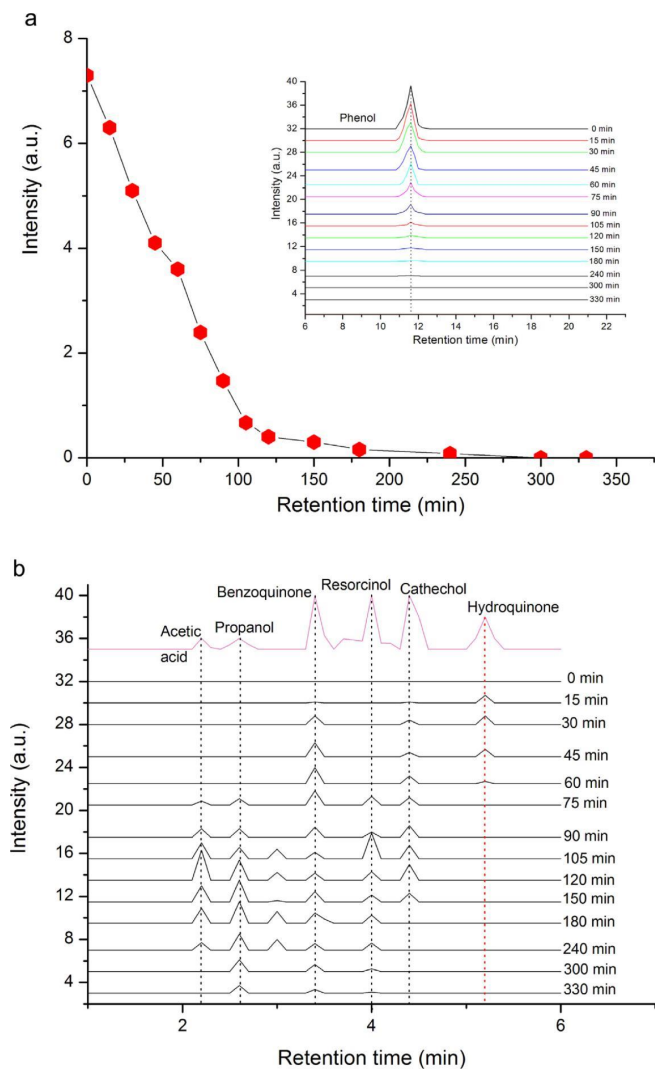


Fig. 7. (a) Comparison of the decrease of phenol concentration with 0.6 wt.% Sb doped SnO₂ photocatalysts under solar light irradiation as measured by monitoring the phenol peak in HPLC. Inset shows the chromatogram of phenol at different stages of degradation. (b) Evolution of different intermediate byproducts detected by HPLC during the photocatalytic degradation of phenol under solar light irradiation with 0.6 wt.% Sb doped SnO₂ nanoparticles as photocatalysts.

height. Sunlight was directed axially at the center of the photoreactor. The photoreactor was kept in open area in order to avoid reflected sunlight from the surrounding. All the natural sunlight experiments were conducted on full sunny days during 10:00–15:00 h when the incident power of the sunlight was measured to be between 80 to 90 kW/m².

2.4. Experimental procedure

To investigate the effects of different concentrations of dopants on the photocatalytic activity of SnO₂, phenol was chosen as a test contaminant. The study of the degradation of phenol in water was carried out at 25 °C using a water-cooled cylindrical glass batch photoreactor of 250 ml volume. The experimental conditions were varied as follows: the amount of catalyst powder (photocatalyst)

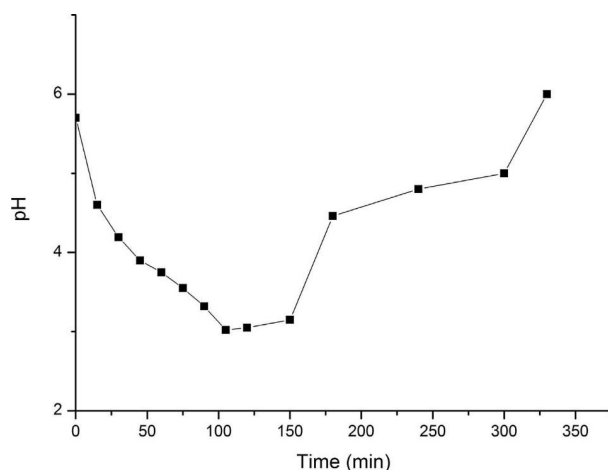


Fig. 8. pH changes in the phenol aqueous solution as a function of photocatalysis time for 0.6 wt.% Sb doped SnO₂ nanoparticle powders.

was kept at 0.065 g in 50.00 ml; the initial concentration of the pollutant was varied from 5 to 100 ppm and the pH of the solution was adjusted by the addition of 0.5 N NaOH to fix the pH at 5.7. 10 mg/l phenol solution was used to carry out photocatalytic experiments. Before each test, the mixture was kept in the dark for 30 min under constant magnetic stirring to ensure that the adsorption–desorption equilibrium was reached before illumination. The sample was then taken out at the end of the dark adsorption period, prior to turning the lights on or before exposing to sunlight. When the lamp was turned on, the irradiation time varied from 2–3 h; aliquots of the suspensions were collected and removed from the reactor every 15 or 30 min. At the given time intervals, the photocatalyst particles were removed from the samples first by centrifugation (4000 rpm, for 5 min) using Eppendorf Centrifuge (system model 5810R) and then filtered through a 0.2 μm Millipore filter.

2.5. Analytical methods

The change in phenol concentration in each photodegraded solution was monitored by two sets of measurements. The optical absorption of SnO₂ and absorbance of phenol was measured at $\lambda_{max} = 270$ nm in UV–vis spectrometer (PerkinElmer, Lambda 45). Total organic carbon was determined by a Total Organic Carbon Analyzer (TOC-VCPH Shimadzu) equipped with an auto sampler (ASI-V Shimadzu). Prior to the TOC determination, the solution was filtered through a syringe filter of 0.2 μm pore size to remove photocatalysts from the solution.

2.6. High performance liquid chromatography analysis (HPLC)

Phenol photodegradation products were analyzed using high performance liquid chromatography (HPLC) which contained a P580 high-precision pump from Dionex (Germering, Germany), which fulfilled the requirement for a measured delivery rate of the mobile phase. The injector was a Rheodyne (Cotati) 8125 valve fitted with a 20 l loop. The analysis was carried out using a C18 column (5 m) maintained at room temperature. After elution from the column, the eluent passed through a Dionex UVD 170S diode array detector set at 245 nm for phenol. The mobile phase for the

Table 1

Estimated crystallite size of doped and undoped SnO₂ nanoparticles from XRD pattern using the Debye–Scherrer equation.

Sample	Size (nm)
Undoped	8.4
SnO ₂ :Sb (0.2%)	3.5
SnO ₂ :Sb (0.4%)	2.5
SnO ₂ :Sb (0.6%)	1.8

HPLC separation was prepared by mixing methanol with water 45:55 and then adjusting the pH at 3.0 by adding sulfuric acid (H₂SO₄). The mobile phase was degassed in an ultrasonic bath, and then passed through a Millipore filtration apparatus (0.2 μm). Photodegraded phenol and control samples were eluted at a flow rate of 1 ml/min.

3. Results and discussion

3.1. Characterization of Sb-doped SnO₂ nanoparticles

The XRD pattern of undoped sample shows the presence of (1 1 0), (1 0 1), (2 0 0), (2 2 0), (3 1 0), (3 0 1) and (2 0 2) respectively, matching with the standard XRD file of SnO₂ (JCPDS-#41-1445) which matches with rutile SnO₂ structure [31–34]. The doped samples also show the SnO₂ phases and no substantial differences in XRD patterns could be observed since we doped the crystallites with marginal Sb concentrations (0.2, 0.4, and 0.6%) (Fig. 1). However, the SnO₂ crystallite sizes obtained from the Debye Scherrer equation considering the most intense peak (1 1 0) peak follows the well-known trend of crystallite size reduction upon doping and was found to reduce from 8.4 nm for undoped SnO₂ particles to 1.8 nm for the 0.6 wt.% SnO₂:Sb samples. In Table 1 we have shown the crystallite sizes which were estimated from the broadening of highest intensity (1 1 0) peak in the XRD patterns. The size of the doped SnO₂ nanoparticles was further verified using transmission electron microscopy (TEM), which showed similar average particle size of 2.3 nm for the 0.6 wt.% SnO₂:Sb samples (Fig. 2). The size of the 0.6 wt.% Sb doped SnO₂ nanoparticles was estimated from TEM analysis, which showed maximum percentage (12%) of par-

ticles having diameter 2.3 nm, while the overall diameter of the nanoparticles was found in the range from 2.2 to 2.7 nm. The specific surface area of undoped SnO₂ particles from gas adsorption studies was found to be 28 m² g⁻¹, which increased until 54 m² g⁻¹ for the 0.6 wt.% Sb doped tin oxide samples due to the reduction in the crystallite sizes.

UV–vis absorption spectra were measured for pure and doped SnO₂ nanoparticles and the spectra are shown in Fig. 3. Upon Sb doping the absorption edge of the doped SnO₂ nanoparticles was observed to shift toward longer wavelengths suggesting more light absorption due to the doping.

3.2. Photocatalytic degradation of phenol

3.2.1. Under UV light irradiation

In Fig. 4 we have plotted the change in phenol concentration in the aqueous solution upon continued UV light illumination in the presence of doped and undoped SnO₂ nanoparticles. When no catalysts were used, no significant reduction in phenol concentration was observed and only about 2% reduction was detected after 2.5 h due to the photolysis of phenol under the UV light irradiation. With undoped SnO₂ nanoparticles the degradation of phenol was also found to occur slowly and in the initial 1 h with no significant degradation observed. Here it should be noted that during photocatalytic degradation, phenol molecules initially transform to form by-products such as benzoquinone, catechol and hydroquinone, which upon subsequent oxidation transforms to mineral acids, CO₂ and H₂O. These by-products formed at the beginning of the photocatalytic reactions also optically absorb in the similar region as phenol, which would mask the degradation level of phenol in the UV/vis spectroscopy. As a result during the initial period of the photocatalytic degradation of phenol using undoped SnO₂ nanoparticles no significant variations in the optical absorption spectrum of phenol was observed as shown in Fig. 4, although phenol was degrading by forming other intermediates. However, degradation of phenol was observed to begin immediately under UV light irradiation in the presence of doped SnO₂ nanoparticles. Upon 150 min of UV irradiation, 46% of phenol was found to degrade in the presence of undoped SnO₂ nanoparticles. With 0.2 wt.% Sb doped SnO₂ samples, after 120 min irradiation, 54% of phenol photodegradation was observed, while 91% of phenol degradation was achieved in the presence of 0.4 wt.% Sb doped SnO₂ within 120 min of irradiation time. Further increase in the degradation process was observed (99% of phenol disappearance) when doping concentration was increased to 0.6 wt.%. Complete mineralization was achieved in the presence of 0.4% and 0.6% Sb doped SnO₂ nanoparticles after 150 and 120 min of UV irradiation respectively.

In order to determine the degree of mineralization reached during the photocatalysis experiments, samples were analyzed for TOC concentration. With the 0.6% SnO₂:Sb nanoparticles, 97% of TOC was found to be removed within 120 min, while 71% and 45% removal was found with 0.4% and 0.2% SnO₂:Sb samples respectively. For the undoped samples only 12% TOC was removed upon UV irradiation for 2 h as shown in Fig. 5. The reduction in TOC was found to follow the same trend as observed in the phenol degradation in Fig. 4. Using FTIR spectroscopy it was also found that the mineralization process starts early during the photocatalytic degradation process which continues till all phenol molecules are converted to CO₂ and water, which are the final by-products of the mineralization process. In Fig. 6 the FTIR spectra of the phenol solution at different stages of photocatalytic degradation with the 0.6% SnO₂:Sb nanoparticles are shown which clearly shows the CO₂ generation within 15 min indicated by two IR absorption bands centering at 2364 and 2324 cm⁻¹ [35–37].

3.2.2. Under natural solar light irradiation

In order to utilize the UV radiation that is present in the solar further study the photocatalytic degradation of phenol. In addition to that we have used the HPLC technique to analyze the phenol solution during the degradation process in order to have better insight on the mineralization process of phenol under natural sunlight. For these experiments we have chosen the 0.6 wt.% SnO₂:Sb nanoparticles for which maximum degradation of phenol was observed under UV irradiation.

Upon exposure to natural sunlight, phenol was found to degrade effectively as indicated by the reduction in the intensity of the phenol peak observed in the HPLC chromatogram at retention time 11.7 min. Fig. 7a shows the degradation kinetics of phenol under the natural sunlight, where almost 95% phenol was found to degrade within 120 min, showing almost similar photocatalytic activity by the 0.6% SnO₂:Sb nanoparticles observed under UV irradiation. It has been reported that during the photocatalysis process, phenol is first oxidized to benzoquinone followed by catechol, resorcinol, and hydroquinone, and later the ring is broken to form other aliphatic acids [37,38]. According to the substitution rule, OH[•] radicals attack the phenol molecules with higher probability in 1 and 4 positions versus OH⁻ group of the aromatic ring, to produce catechol or hydroquinone and either one of them will attack OH to produce benzoquinone. Upon investigation using the HPLC technique, we have observed generation of benzoquinone, catechol and hydroquinone in the first 60 min of the photocatalytic process, as shown in Fig. 7b, confirming the oxidation of phenol under the natural sunlight. At the very initial stage, hydroquinone and catechol will compete with each other to produce benzoquinone, which can be detected in the first 30 min of the photocatalytic oxidation. On the continuous oxidation aliphatic intermediates in the reaction mixture was found to appear (acetic acids and propanol) after 60 min, which suggests that the structure of benzene ring was destroyed as it was proposed to form carboxylic acid intermediates through photochemical oxidation of phenol by SnO₂:Sb nanoparticles.

The evolution of the intermediates during the photocatalytic degradation of phenol under solar light was also followed by measuring the pH of the reaction mixture. pK_a of phenol is around 9 and thus an aqueous solution is mildly acidic as observed from the pH of the starting solution pH ~5.7, as shown in Fig. 8, which then observed to decrease continuously to acidic pH reaching close to pH 3 in 120 min. This reduction in the pH value can be attributed to the formation of carboxylic acid intermediates during the initial period of the degradation process. Up to about 150 min pH was found to be almost stable, after which it started to rise again due to the subsequent removal of carboxylic acids to form CO₂ and water leading to complete mineralization of phenol.

4. Conclusions

SnO₂:Sb nanoparticles were synthesized by using simple sol–gel process and used to investigate photocatalytic degradation of phenol in aqueous solution. Sb doping was increased from 0.2 wt.% to 0.6 wt.% which showed higher surface area (54 m²/g) than the undoped nanoparticles (28 m²/g). Doping SnO₂ with Sb also resulted shifting in the physicochemical and optical features of the samples toward more favorable state for photocatalytic degradation of organic compounds. Photocatalytic activity of the undoped and doped samples were studied under both UV irradiation and natural sunlight, which showed efficient degradation of phenol demonstrating almost 95% reduction in phenol concentration within 2 h of light exposure. The results from this study suggest that the SnO₂:Sb nanoparticles can be a promising candidate for practical application in the field of photocatalysis.

Acknowledgements

Authors would like to thank partial financial support from the Chair in Nanotechnology Programme of the Research Council of Oman and the College of Science (Chemistry department) for giving this opportunity to carry out the research at Sultan Qaboos University.

References

- [1] Anandan, The contribution of nanotechnology for removal of water pollutants, *Mater. Sci. Forum* 712 (2012) 1–24.
- [2] S. Kaneco, M.A. Rahman, T. Suzuki, H. Katsumata, K. Ohta, Optimization of solar photocatalytic degradation conditions of bisphenol A in water using titanium dioxide, *J. Photochem. Photobiol. A* 163 (2004) 419–424.
- [3] S.H. Swan, Environmental phthalate exposure in relation to reproductive outcomes and other health endpoints in humans, *Environ. Res.* 108 (2008) 177–184.
- [4] X. Huang, M. Sillanpää, B. Duo, E.T. Gjessing, Water quality in the Tibetan plateau: metal contents of four selected rivers, *Environ. Pollut.* 156 (2008) 270–277.
- [5] X. Huang, M. Sillanpää, E.T. Gjessing, R.D. Vogt, Water quality in the Tibetan plateau: major ions and trace elements in the headwaters of four major Asian rivers, *Sci. Total Environ.* 407 (2009) 6242–6254.
- [6] E.S.Z. El-Ashtouky, Y.A. El-Taweel, O. Abdelwahab, E.M. Nassef, Treatment of petrochemical wastewater containing phenolic compounds by electrocoagulation using a fixed bed electrochemical reactor, *Int. J. Electrochem. Sci.* 8 (2013) 1534–1550.
- [7] G. Phipps, G. Holcombe, J. Fianid, Acute toxicity of phenol and substituted phenols to the fathead minnow, *Bull. Environ. Contam. Toxicol.* 26 (1981) 585–593.
- [8] J. Michalowicz, W. Duda, Phenols—sources and toxicity, *Pol. J. Environ. Stud.* 16 (2007) 347–362.
- [9] P.S. Hooda, A.C. Edwards, H.A. Anderson, A. Miller, A review of water quality concerns in livestock farming areas, *Sci. Total Environ.* 250 (2000) 143–167.
- [10] X. Peng, Y. Yu, C. Tang, J. Tan, Q. Huang, Z. Wang, Occurrence of steroid estrogens, endocrine-disrupting phenols, and acid pharmaceutical residues in urban riverine water of the Pearl River Delta, South China, *Sci. Total Environ.* 397 (2008) 158–166.
- [11] A. Hagfeld, M. Gratzel, Light-induced redox reactions in nanocrystalline systems, *Chem. Rev.* 95 (1995) 49–68.
- [12] U. Diebold, The surface science of titanium dioxide, *Surf. Sci. Rep.* 48 (2003) 53–229.
- [13] R.K. Nath, S.S. Nath, Tin dioxide thin film-based ethanol sensor prepared by spray pyrolysis, *Sens. Mater.* 21 (2009) 95–104.
- [14] Z. He, J. Zhou, Synthesis, characterization, and activity of tin oxide nanoparticles: influence of solvothermal time on photocatalytic degradation of rhodamine B, *Mod. Res. Catal.* 2 (2013) 13–18.
- [15] U.I. Gaya, A.H. Abdullah, Heterogeneous photocatalytic degradation of organic contaminants over titanium dioxide: a review of fundamentals, progress and problems, *J. Photochem. Photobiol. C* 9 (2008) 1–12.
- [16] H. Wang, F. Sun, Y. Zhang, L. Li, H. Chen, Q. Wu, J.C. Yu, Photochemical growth of nanoporous SnO₂ at the air–water interface and its high photocatalytic activity, *J. Mater. Chem.* 20 (2010) 5641–5645.
- [17] R. Ullah, J. Dutta, Photocatalytic degradation of organic dyes with manganese-doped ZnO nanoparticles, *J. Hazard. Mater.* 156 (2008) 194–200.
- [18] A.M. Al-Hamdi, M. Sillanpää, J. Dutta, Photocatalytic degradation of phenol in aqueous solution by rare earth-doped SnO₂ nanoparticles, *J. Mater. Sci.* 49 (2014) 5151–5159.
- [19] A.M. Al-Hamdi, M. Sillanpää, J. Dutta, Photocatalytic degradation of phenol by iodine doped tin oxide nanoparticles under UV and sunlight irradiation, *J. Alloys Compd.* 618 (2015) 366–371.
- [20] H. Wang, A.L. Rogach, Hierarchical SnO₂ nanostructures: recent advances in design, synthesis, and applications, *Chem. Mater.* 26 (2013) 123–133.
- [21] M. Batzill, U. Diebold, The surface and materials science of tin oxide, *Prog. Surf. Sci.* 79 (2005) 147–154.
- [22] G. Zhang, C. Xie, S. Zhang, S. Zhang, Y. Xiong, Defect chemistry of the metal cation defects in the p- and n-doped SnO₂ nanocrystalline films, *J. Phys. Chem. C* 118 (2014) 18097–18109.
- [23] S. Shanthi, C. Subramanian, P. Ramasamy, Growth and characterization of antimony doped tin oxide thin films, *J. Cryst. Growth* 197 (1999) 858–864.
- [24] M. Kojima, H. Kato, M. Gatto, Blackening of tin oxide thin films heavily doped with antimony, *Philos. Mag. B* 68 (1993) 215–222.
- [25] C.A. Vincent, The nature of semiconductivity in polycrystalline tin oxide, *J. Electrochem. Soc.* 119 (1972) 515–518.
- [26] K.H. Kim, S.W. Lee, D.W. Shin, C.G. Park, Effect of antimony addition on electrical and optical properties of tin oxide film, *J. Am. Ceram. Soc.* 77 (1994) 915–921.
- [27] Y. Nakanishi, Y. Suzuki, T. Nakamura, Y. Hatanaka, Y. Fukuda, A. Fujisawa, G. Shimaoka, Coloration of SnSbO thin films, *Appl. Surf. Sci.* 48 (1991) 55–58.
- [28] T.K. Tseng, Y.S. Lin, Y.J. Chen, H. Chu, A review of photocatalysts prepared by sol-gel method for VOCs removal, *Int. J. Mol. Sci.* 11 (2010) 2336–2361.
- [29] I.A. Rahman, V. Padavettan, Synthesis of silica nanoparticles by sol-gel: size-dependent properties surface modification, and applications in silica-polymer nanocomposites—a review, *J. Nanomater.* 2012 (2012) 15.
- [30] O. Sheikhejad-Bishe, F. Zhao, A. Rajabtabar-Darvishi, E. Khodadad, A. Mostofizadeh, Y. Huang, Influence of temperature and surfactant on the photocatalytic performance of TiO₂ nanoparticles, *Int. J. Electrochem. Sci.* 9 (2014) 4230–4240.
- [31] A. Das, V. Bonu, A.K. Prasad, D. Panda, S. Dhara, A.K. Tyagi, The role of SnO₂ quantum dots in improved CH₄ sensing at low temperature, *J. Mater. Chem. C* 2 (2014) 164–171.
- [32] K. Melghit, K. Bouziane, One step aqueous solution preparation of nanosize iron-doped tin oxide from SnO₂·xH₂O gel, *Mater. Sci. Eng. B* 128 (2006) 58–62.
- [33] K. Melghit, K. Bouziane, Low-temperature preparation and magnetic properties of V-doped SnO₂ nanoparticles, *J. Am. Ceram. Soc.* 90 (2007) 2420–2423.
- [34] R. Liu, Y. Huang, A. Xiao, H. Liu, Preparation and photocatalytic property of mesoporous ZnO/SnO₂ composite nanofibers, *J. Alloys Compd.* 503 (2010) 103–110.
- [35] H. Zou, C. Yi, L. Wang, H. Liu, W. Xu, Thermal degradation of poly(lactic acid) measured by thermogravimetry coupled to Fourier transform infrared spectroscopy, *J. Therm. Anal. Calorim.* 97 (2009) 929–935.
- [36] W. Xie, Z. Gao, K. Liu, W.-P. Pan, R. Vaia, D. Hunter, A. Singh, Thermal characterization of organically modified montmorillonite, *Thermochim. Acta* 367 (2001) 339–350.
- [37] Y. Feng, Y. Cui, B. Logan, Z. Liu, Performance of Gd-doped Ti-based Sb-SnO₂ anodes for electrochemical destruction of phenol, *Chemosphere* 70 (2008) 1629–1636.
- [38] E.E. Bamaiza-Pemu, E. Chirwa, Profile of aromatic intermediates of titanium dioxide mediated degradation of phenol, *Chem. Eng. Trans.* 35 (2013) 1333–1338.

Publication IV

A. A. M. Al-Hamdi, M. Sillanpää, J. Dutta
**Gadolinium doped tin dioxide nanoparticles:
an efficient visible light active photocatalyst.**

Reprinted with permission from
Journal of Rare Earths
Vol. 33, pp 1275–1283, 2015
© 2015, Elsevier



Available online at www.sciencedirect.com

ScienceDirect

JOURNAL OF RARE EARTHS, Vol. 33, No. 12, Dec. 2015, P. 1275



www.re-journal.com/en/

Gadolinium doped tin dioxide nanoparticles: an efficient visible light active photocatalyst

Abdullah M Al-Hamdi¹, Mika Sillanpää¹, Joydeep Dutta^{2,3,*}

(1. Laboratory of Green Chemistry, Lappeenranta University of Technology, Sammonkatu 12, 50130 Mikkeli, Finland; 2. Chair in Nanotechnology, Water Research Center, Sultan Qaboos University, P.O. Box 17, 123 Al-Khoudh, Sultanate of Oman; 3. Functional Materials Division, School of Information and Communication Technology, KTH Royal Institute of Technology, Isaffordsgatan 22, SE-16440 Kista, Stockholm, Sweden)

Received 31 March 2015; revised 20 July 2015

Abstract: Photocatalytic degradation of phenol with sol-gel prepared rare earth doped tin dioxide (SnO₂) nanoparticles was reported. Gadolinium doped tin dioxide (SnO₂:Gd) nanoparticles were found to absorb higher visible light compared to lanthanum, neodymium and cerium doped materials that were studied in detail. Photocatalytic degradation of phenol under artificial white light and sunlight in the presence of SnO₂:Gd nanoparticles was studied with high performance liquid chromatography (HPLC), capillary electrophoresis (CE), total organic carbon (TOC) measurements and the determination of chemical oxygen demand (COD). Clear correlations between the results obtained from these multiple measurements were found, and a kinetic pathway for the degradation process was proposed. Within 150 min of solar irradiation, the TOC of a 10 ppm phenol solution in water was reduced by 95%–99%, thus demonstrating that SnO₂:Gd nanoparticles are efficient visible light photocatalysts.

Keywords: rare earth dopants; solar irradiation; phenol photo-degradation; tin dioxide nanoparticles; organic by-products

Increased water pollution across the world, has drawn considerable attention for the need of environmentally friendly, clean chemical technologies to remove the contaminants. Natural water sources today are threatened by the high concentration of hazardous chemical substances, such as phenol, bisphenol A, phthalates, azo dyes, herbicides, pesticides among others, most being the contribution from oil refining and industrial discharges^[1,2]. Excess use of fertilizers and pesticides^[3], pharmaceutical residues^[4], land filling of domestic wastes^[5] from rotting of vegetation^[6] contribute to pollute water resources. Phenol is a hazardous and a recalcitrant water pollutant, difficult to be completely degraded through common waste water treatment methods, leading to toxicity towards microorganisms, causing serious environmental concerns. It is a necessity to remove these toxic compounds from natural water prior to its use.

Advanced oxidation processes (AOPs) are the best technologies for the treatment of persistent organic pollutants to harmless end products. These techniques are based on the generation of reactive species such as hydroxyl radicals. Semiconductor photocatalysts are increasingly applied technology for the reduction of organic and inorganic compounds in water. Many researchers have reported that titanium dioxide (TiO₂), zinc oxide (ZnO) and tin dioxide (SnO₂) are active catalysts capable of degrading dyes, phenols and pesticides^[7–10]. Furthermore, these semiconductors have been recognized

as preferable materials for photocatalytic processes because of their high photosensitivity, nontoxic nature, low cost of production^[11] and chemical stability^[10,12–15]. In the photocatalytic oxidation process, organic pollutants are decomposed in the presence of a wide-band gap semiconductor that promote reactions in the presence of UV light without being consumed in the overall reaction^[16]. Though the band gap of SnO₂ (3.6 eV), ZnO (3.3 eV) and TiO₂ (3.2 eV) are quite comparable^[17–19], SnO₂ is not used very frequently compared to the other two photocatalysts^[18]. Photocatalytic degradation of organic compounds is mainly achieved through irradiation with ultraviolet lamps, whose sources are mainly mercury vapor lamps that require relatively high energy to run, contain hazardous mercury, and needs cooling, leading to a short life time. An option to replace Hg lamps is the use of light emitting diodes (LED)^[20–22]. Another alternative is the utilization of solar light, which is abundant free source of energy for providing environmentally friendly, green chemical processes. Recent interest has developed in the synthesis of SnO₂ nanoparticles of different sizes^[23,24].

In order to render the large band gap metal oxide semiconductors photoactive in the visible region, several attempts have been reported like doping TiO₂ with nitrogen^[25], ZnO with transition metals^[15] or with rare earth metals among others^[24]. Incorporation of rare earth metal ions into the SnO₂ matrix introduces defects lowering the optical gap and hence leading to a better

* Corresponding author: Joydeep Dutta (E-mail: dutta@squ.edu.om, joydeep@kth.se; Tel.: +46737652186)
DOI: 10.1016/S1002-0721(14)60557-3

photoactivity in the visible region^[24,26,27]. Several studies of SnO₂ doping with different metals to produce nanocrystals have been reported in recent years^[28–30]. On SnO₂ stoichiometric surfaces, Sn⁴⁺ is easily reduced to Sn²⁺ changing the surface electronic structure of the material, leading to the formation of Sn₂S. Also, oxygen atoms residing on the nanoparticle surface lead to energetically favorable reconstructions of the SnO₂ (110) and (101) surfaces^[31]. The oxygen vacancies thus produced, easily bind with electrons to form an excitation energy level below the conduction band of SnO₂. It is well known that the influence of rare earth (RE) cations on the catalytic properties of SnO₂ is associated with acid/base characteristics of the oxides involved^[32–35]. SnO₂ is an oxide (isoelectronic point, $\text{iep} \sim 4-7$), whereby (RE) basic characters favor some catalytic aspects^[36]. Also (RE) metals incompletely occupy 4f and empty 5d orbitals, imbuing the formation of labile oxygen vacancies with relatively high mobility of bulk oxygen species^[25]. Doping with (RE) cations influences the material's electronic distribution, causing the absorption of oxygen species and producing high surface area and smaller sized particles^[37–39]. Rare earth metals co-doped TiO₂ have shown potential in red shifting absorption and thus improving the photocatalytic activity of TiO₂ more than undoped TiO₂ under visible light irradiation^[40].

The most widely used solution for the synthesis of SnO₂ nanoparticle is sol-gel processes, based on hydrolysis of a reaction of metal alkoxides in water:

$$\text{Sn}(\text{C}_2\text{H}_5\text{O})_4 + 4\text{H}_2\text{O} \xrightarrow{\text{Hydrolysis}} \text{Sn}(\text{OH})_4 + 4\text{C}_2\text{H}_5\text{OH} \quad (1)$$

The alkoxy groups are substituted by hydroxide groups with the evolution of an inorganic network (sol) that is followed by a second reaction (condensation) as follows:

$$2\text{Sn}(\text{OH})_4 \xrightarrow{\text{Con-dens-ation}} 2\text{SnO}_2 + 4\text{H}_2\text{O} \quad (2)$$

Two hydrolyzed molecules liberate water (gel), upon linking together that occurs through the destruction of the gel with the subsequent formation of nanoparticulate materials^[24,26,27]. Sol-gel method offers several advantages, such as high purity, better homogeneity, precise control over the stoichiometry, and capability in controlling the powder size and surface of metal oxide at lower temperatures. In this work, visible light active tin dioxide nanoparticles doped with rare earth metals were synthesized and detailed studies of photocatalytic activity studies under visible light irradiation were presented for gadolinium doped SnO₂ nanoparticles with phenol in water as a test contaminant.

1 Experimental

1.1 Materials

Analytical-grade tin (IV) chloride (SnCl₄, Sigma Aldrich,

purity: 99.99%), sodium tetraborate (Na₂B₄O₇, Merck, 99.99%), sodium dihydrogen phosphate (NaH₂PO₄, Merck, 99.99%), lanthanum nitrate hexahydrate (La(NO₃)₃·6H₂O, Fluka), cerium (III) chloride anhydrous (CeCl₃, Sigma Aldrich, 99%), (ammonium cerium (IV) nitrate (NH₄)₂Ce(NO₃)₆, Sigma Aldrich, 99%), (neo-dymium (III) nitrate hexahydrate (Nd(NO₃)₃·6H₂O, Sigma Aldrich, 99%), gadolinium (III) chloride (GdCl₃, Sigma Aldrich, 99.9%), ethanol, (C₂H₅OH, ETAX Aa Merck Absolute), phenol (C₆H₅OH Sigma Aldrich, purity: 99.99%), *p*-benzoquinone (O: C₆H₄:O, BDH, AnalaR 99.99%), resorcinol (C₆H₄(OH)₂, BDH, AnalaR 99%), acetic acid (C₂H₄O₂, Sigma Aldrich, purity: 99.99%), catechol (C₆H₆O₂, Sigma Aldrich, purity: 99.99%), hydroquinone (Sigma Aldrich, purity: 99.99%), (sulfuric acid (H₂SO₄, Sigma Aldrich, 99.99%), hydrochloric acid (HCl, Sigma Aldrich, 99%), sodium hydroxide pellets (NaOH, SigmaAldrich, 99%), and methanol (CH₃OH, Sigma Aldrich, 99% HPLC grade), sodium chloride (NaCl, BDH 99% AnalaR grade) were used in the experimental studies. Double deionized water with a high purity from Ultra Clear Water SG was used for the preparation of all solutions.

1.2 Photocatalyst preparation

1.2.1 Synthesis of pure and doped-SnO₂ nanoparticles SnO₂ nanoparticles containing different mass percentages of rare earth metal (gadolinium, lanthanum, cerium and neodymium) ions in the starting solution were synthesized by sol-gel process, according to the following procedure: 3.80825 mL of SnCl₄ mixed in 50 mL absolute alcohol (ethanol) and 50 mL ultra-pure water in a round bottom flask and used as precursor for synthesizing control (undoped SnO₂) nanoparticles. The mixture was subjected to vigorous stirring for 3 h at room temperature, until a colourless solution was obtained. For the synthesis of rare earth metals doped tin oxide nanoparticles, different concentrations of rare earth metals (0.2 wt.%, 0.4 wt.%, and 0.6 wt.%) were mixed and dissolved separately in ethanol and added to the precursor solution. A turbid colloidal solution of tin alkoxide started to appear after adding 25% aqueous ammonia drop by drop into the solution with continuous stirring until a pH value of 8 was reached. The sol was left for 48 h for aging in air until the gel was formed. Filtration and successive washing with ultra-pure water was repeated several times to remove both ammonia and chloride ions until all chloride ions had been removed (determined by examining the filtrate solution using aqueous silver nitrate solution). Later a series of samples were synthesized in the same way by changing the concentration of tin tetrachloride and the mass percentage amount of the required dopant. Each dopant was added carefully and under vigorous stirring to the total solution containing pure tin tetrachloride. They were then subjected to dissolution in ethanol

and synthesis was carried out by using the same process as explained for the undoped tin dioxide. The dopant concentration studied in this work was kept up to 0.6 wt.%, because as we reported in our earlier work^[24] higher dopant concentration did not further improve photocatalytic activity of the material.

1.2.2 Material characterization

Optical absorption spectra were recorded in colloidal suspension in a double beam spectrometer (Perkin Elmer, Lambda 45). To study the surface morphology of the prepared SnO₂ and SnO₂:Gd samples, transmission electron microscopy (TEM) were carried out with JEOL (Japan) (JEM 2100F) working at 200 kV. The crystalline phase of the synthesized SnO₂ and doped SnO₂ nanoparticles were analyzed by X-ray powder diffraction (XRD) using a MiniFlex 600 diffractometer (Rikagu, Japan) with Cu K α radiation (wavelength=0.154 nm). Diffraction patterns of powders were recorded in 2 θ scan configuration, in the 10°–80° 2 θ range, with the data collected at steps of 0.02°. 200–300 mg of sample was degassed at 300 °C for 3 h under nitrogen (N₂) flow followed by a six point N₂ adsorption carried out at p/p_0 of 1 to 5 in a Nova[®] 2200 analyzer. Surface area was determined by gas adsorption technique using Nova[®] 2200 (Brunauer-Emmett-Teller (B.E.T.) method).

1.3 Photocatalysis experiments

1.3.1 Visible light photocatalytic reactor

Pyrex-glass reactor was used with a cooling water jacket in 250 mL capacity, 100 mm internal diameter and 200 mm height. A 300 W xenon lamp simulated solar light source (PLS-SXE300C, Beijing Perfect light Co., Ltd., China), and was placed 71 mm above the surface of contaminant during the photocatalysis studies.

1.3.2 Solar light degradation

The second photoreactor was a borosilicate glass container with a 250 mL capacity, 100 mm internal diameter and 200 mm height. Sun-light was positioned axially at the center of the reactor for the photocatalysis studies and the degradation studies were carried out at similar periods of a day.

1.4 Experimental procedure

To investigate the effects of different dopants on the photocatalytic activity of SnO₂, oxidative photodegradation of phenol was chosen to evaluate the photocatalytic activity of synthesized nanoparticles. The study of degradation of phenol in water was carried out at 25 °C using the water-cooled cylindrical glass batch photoreactor of 250 mL volume. The experimental conditions were varied as follows: amount of catalyst powder (photocatalyst) was kept at 0.065 mg in 50.00 mL; initial concentration of the pollutant was varied from 5–100 ppm and the pH of the solution was adjusted by addition of 0.5 mmol/L NaOH to fix pH at 5.7. 10 mg/L phenol solution was

used to carry out photocatalysis experiments. Before each test, the mixture was kept in the dark for 30 min under constant magnetic stirring to ensure that the adsorption-desorption equilibrium was reached before illumination. The sample was then taken out at the end of the dark adsorption period, prior to turning the light on or before exposing to sunlight. When the lamp was turned on, the irradiation time varied from 2–3 h; aliquots of the suspensions were collected and removed from the reactor every 15 or 30 min. At the given time intervals, the photocatalyst particles were removed from the samples first by centrifugation (4000 r/min, 5 min) using Eppendorf Centrifuge (system model 5810R) and then filtered through a 0.2 μ m Millipore filters.

1.5 Analytical methods

The total organic carbon was determined by a Total Organic Carbon Analyzer (TOC-VCPH Shimadzu) equipped with an auto sampler (ASI-V Shimadzu). Prior to the TOC determination, the solution was filtered through a syringe filter of 0.2 μ m pore size to remove photocatalysts from the solution. To determine the COD in phenol and its byproducts, samples were treated as follows: 2 mL of supernatant in a screw cap tube was amended with 0.05 g of mercury sulfate, 0.5 mL of 1.0 N potassium dichromate and 2.5 mL of concentrated sulfuric acid (containing 5.5 mg silver sulfate per gram), and refluxed for 2 h at 150 °C in a heater model DRB 200. After cooling, COD was determined by absorbance using a Hach Lange model DR-2000 spectrophotometer (Hach Company, USA) according to manufacturer's instructions.

Phenol photodegradation byproducts were analyzed using high performance liquid chromatography (HPLC), containing a P580 high-precision pump from Dionex (Germering, Germany), and fulfilling the requirement for a measured delivery rate of the mobile phase. The injector was a Rheodyne (Cotati) 8125 valve fitted with a 20 μ L loop. The analysis was carried out using a C18 column (5 μ m silica) maintained at room temperature. After elution from the column, the eluent passed through a Dionex UVD 170S diode array detector set at 245 nm for phenol detection. The mobile phase for the HPLC separation was prepared by mixing methanol with water in the ratio 45:55 and then adjusting the pH at 3.0 by adding sulphuric acid (H₂SO₄). The mobile phase was degassed in an ultrasonic bath, and then passed through a Millipore filtration apparatus (0.2 μ m). Photodegraded phenol and control samples were then eluted at a flow rate of 1 mL/min.

Capillary electrophoresis was used for monitoring phenol and its byproducts with the P/Ace MDQ capillary electrophoresis system (Beckmann Coulter Inc., Fullerton, Ca, USA). The data were collected and processed with 32 Karat software (Beckmann Coulter Inc.). The

buffer was prepared with 10 mmol/L sodium tetraborate with 10 mmol/L sodium dihydrogen phosphate in milli-Q-purified water. The pH of the buffer was 8.0. Standards and samples were injected by using 20 psi pressure. Separation was carried out at 20 kV (reversed polarity), at a constant capillary temperature 25 °C. Fused silica capillary with a total length of 50 cm was used and direct UV detection at 254 nm was done.

2 Results and discussion

2.1 Crystallinity of SnO₂ nanoparticles doped with rare earth metals

The XRD pattern of undoped SnO₂ sample showed the presence of (110), (101), (200), (211), (002), (221) and 81 respectively, matching with the standard XRD file of SnO₂ (JCPDS-#41-1445) regarded as an attributive indication of rutile SnO₂ structure^[41–44]. The doped samples also show the SnO₂ phases and no substantial differences in XRD patterns could be observed as dopant concentration of Gd, La, Ce and Nd was less than 1% in the starting solution. Typical XRD patterns of Gd doped SnO₂ and undoped tin dioxide samples are shown in Fig. 1. No observable changes could be seen in the XRD patterns of the other doped samples. The SnO₂ crystallite sizes obtained from the Debye Scherrer equation considering the most intense peak (110) peak follows the well-known trend of crystallite size reduction upon doping, inducing the most significant crystallite size reduction, from 7.5 nm for undoped SnO₂ particles to 3.2 nm for the gadolinium doped tin dioxide (SnO₂:Gd) samples, as shown in Table 1.

The specific surface area of undoped SnO₂ particles from gas adsorption studies was found to be 28 m²/g, increasing up to 58 m²/g for the 0.6 wt.% Gd doped tin dioxide.

Table 2 shows the changes in the surface area of rare earths (RE) doped tin dioxide nanoparticles where gado-

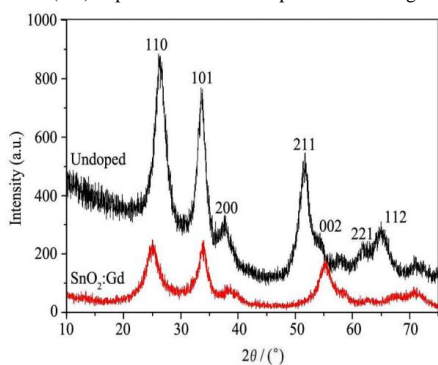


Fig. 1 XRD patterns of typical samples undoped, and SnO₂:Gd particles synthesized by sol-gel process

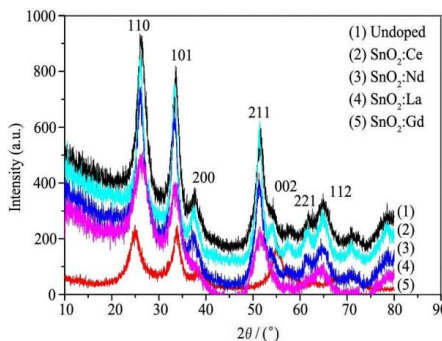


Fig. 2 XRD patterns of typical samples undoped tin dioxide particles, cerium doped tin dioxide particles, neodymium doped tin dioxide particles, lanthanum doped tin dioxide particles, and gadolinium doped tin dioxide particles synthesized by sol-gel process

Table 1 Estimated crystallite size of rare earth doped SnO₂ nanoparticles from (110) peak using the Scherrer equation

No.	Dopant	Size/nm
1	Undoped	7.5
2	SnO ₂ :Ce (0.6%)	5.5
3	SnO ₂ :Nd (0.6%)	4.1
4	SnO ₂ :La (0.6%)	3.4
5	SnO ₂ :Gd (0.6%)	3.2

Table 2 Comparison of different surface areas for rare earth doped SnO₂ nanoparticles

No.	Dopant	Surface area/(m ² /g)
1	Undoped	28
2	SnO ₂ :Ce (0.6%)	30
3	SnO ₂ :Nd (0.6%)	35
4	SnO ₂ :La (0.6%)	40
5	SnO ₂ :Gd (0.6%)	58

Gadolinium doped nanoparticles showed nearly double highest surface area compared to the undoped samples.

Gadolinium doping led to a prominent increase in the visible light absorption of SnO₂ nanoparticles compared to the nanoparticles doped with other rare earth cations as shown in Fig. 3. Thus, for all further studies, 0.6% Gd doped SnO₂ nanoparticles were chosen in this work.

2.2 Morphology of Gd-doped SnO₂ nanoparticles

Typical electron micrographs (TEM) are shown in Fig. 4. Upon doping with gadolinium, the average grain size of SnO₂ nanoparticles were found to decrease that is in agreement with the observations made from XRD and gas adsorption measurements. The crystallite sizes are comparable to what was estimated from XRD (Table 1). Similar observations were made for samples doped with other rare earths studied in this work (not shown).

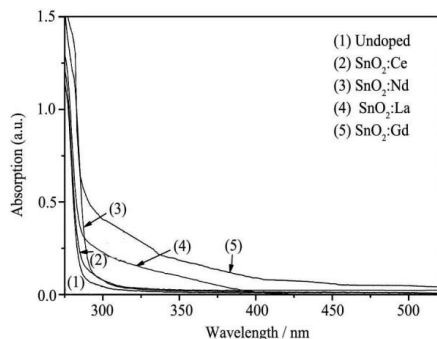


Fig. 3 Typical optical absorption of undoped SnO₂, Ce doped SnO₂, Nd doped SnO₂, La doped SnO₂ and Gd doped SnO₂ dried samples collected from a suspension in aqueous media

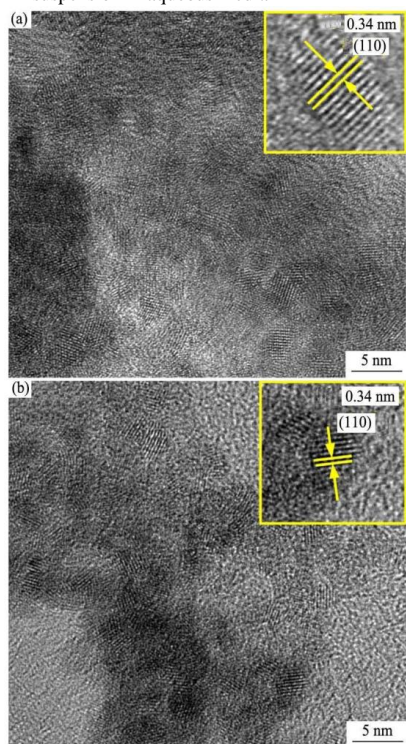
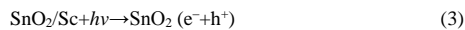


Fig. 4 Typical scanning electron micrograph of undoped (a) and gadolinium doped (b) tin dioxide nanoparticles synthesized by sol-gel process

2.3 Photocatalytic degradation of phenol

A red shift in the optical absorption could be attributed to defect states of the dopants SnO₂ in the lattice. The primary step in photodegradation begins with the photo-excitation of SnO₂ generating electron-hole pairs; photo-generated holes, h⁺ migrates to the catalyst surface and

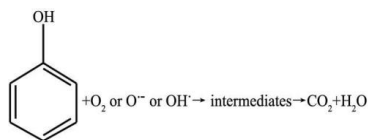
reacts with water molecules absorbed on the surface H₂O_{ab}. Photogenerated electrons, e⁻ migrate to the catalyst surface and molecular oxygen acts as acceptor species in the electron-transfer reaction as follows:



Superoxide anions formed during the process as given below, also leads to the mineralization of phenol.



Eventually all the parent compounds and intermediates will be oxidized into CO₂. High performance liquid chromatography (HPLC) was utilized to monitor the photocatalytic degradation behavior of phenol and to identify the byproducts occurring at different irradiation time. Six photoproducts were clearly identified in the analysis: hydroquinone, resorcinol, catechol, benzoquinone, 2-propanol and acetic acid. The qualitative and the quantitative analysis by (HPLC), as shown in Fig. 5



shows the trends of the amount of six intermediates produced during the photocatalytic degradation. According to the substitution rules, OH radicals attack the phenol molecules with higher probability in 1 and 4 positions versus OH group of the aromatic ring. Steady decline of phenol concentration upon photocatalytic degradation over an extended period of time could be observed. Appearance of hydroquinone followed by catechol, benzoquinone, resorcinol, propanol and acetic acid was recorded. The equilibrium between the degraded phenol and the phenol remaining in the solution determines the degradation phenomenon.

In order to further confirm the results obtained from Fig. 5, the photochemical oxidation process of phenol

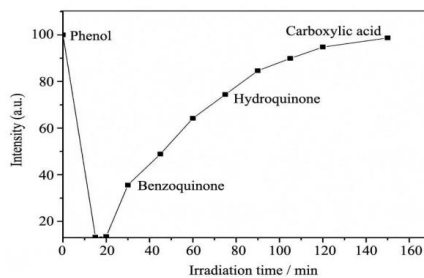


Fig. 5 Phenol photodegradation before and after 150 min by gadolinium doped tin dioxide nanoparticles under optimized HPLC conditions and appearance of its different byproducts

degradation was monitored by capillary electrophoresis (CE). Fig. 6 illustrates the trends of the amount of different intermediates produced during the photocatalytic degradation of phenol. In Fig. 6 from the six byproducts, hydroquinone was detected after 3 min retention time, but catechol was detected after 2.5 min running time. After 60 min of photocatalysis, the concentration of phenol and some of its byproducts were found to decrease slightly and they went on decreasing with extended irradiation time. The presence of the three byproducts acetic acid, propanol and benzoquinone were detected before 1 min, but resorcinol was observed at 2 min retention time. These results are in agreement with the observations made with the HPLC studies on the photodegradation process of phenol. Following the observations made from HPLC and CE studies, and reports in the literatures^[45,46]. The current experimental conditions are proposed in Fig. 7.

In Fig. 8 we observe that the COD concentration decreased with increasing irradiation time, showing that degradation of total phenol was possible in about less than 3 h using 0.6 wt.%Gd:SnO₂ and solar photocatalytic degradation. The degradation of COD matches reasonably well with the phenol reduction as observed during HPLC studies (Fig. 5).

With regard to TOC in Fig. 9, the process exhibiting the highest mineralization rate is also the combination of 0.6 wt.%Gd:SnO₂ with solar light irradiation, achieving a 95%–99% of TOC reduction after 150 min of treatment. In the case of lower gadolinium percentages of 0.2 wt.% Gd:SnO₂, the TOC diminution is slower in the initial stages, attaining a higher degree of mineralization during the second hour of treatment reached with TOC removal up to 75% after 150 min of irradiation time. Whereas with the 0.4 wt.%Gd:SnO₂ the degree of mineralization achieved after 150 min of photoirradiation is 89%.

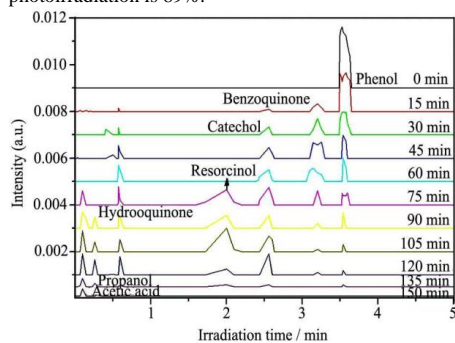


Fig. 6 Spectra of phenol photodegradation and reduction in the intensity of phenol peak observed by chemical electrophoresis upon solar light degradation of phenol in the presence of 0.6 wt.% gadolinium doped SnO₂ nanoparticles (Different phenol byproducts appeared in the figure)

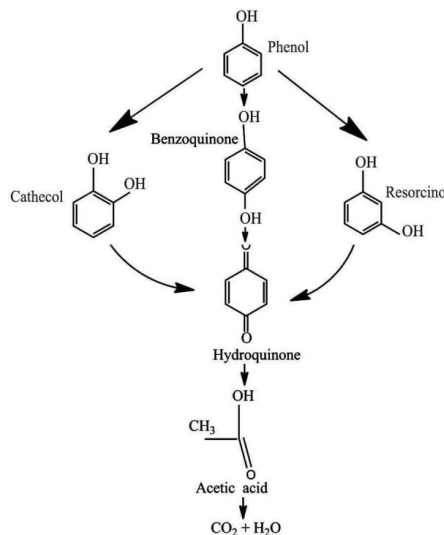


Fig. 7 Different chemical photoproducts produced from phenol photodegradation before its mineralization by CO₂ and water as it is analyzed by HPLC and CE

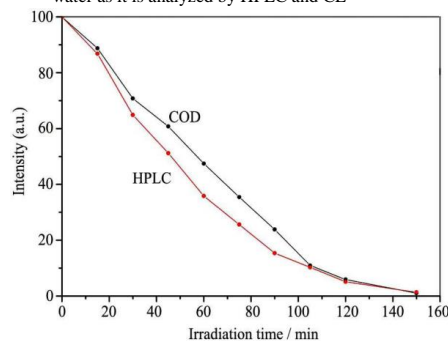


Fig. 8 High performance liquid chromatography (HPLC) and chemical oxygen demand (COD) removal from phenol solutions during 2 h of photocatalytic degradation by SnO₂:Gd under solar light irradiation

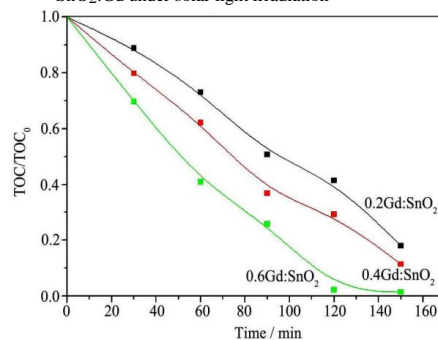


Fig. 9 Total organic carbon (TOC) removal from phenol solutions during 2 h of photocatalytic degradation by different Gd-doped-SnO₂ under solar light irradiation

With Ce³⁺ doped SnO₂ samples, after 150 min irradiation, 66% of phenol was found to be removed, while 71% of TOC mineralization was achieved in the presence of Nd doped SnO₂ within 150 min of irradiation time, while 87% of phenol mineralization was observed in the presence of La doped SnO₂ during the same period. It can also be seen from Fig. 10 that 99% of TOC re-moval was achieved in the presence of Gd³⁺ doped SnO₂. Recent literature reported that RE metal doped titania exhibited the highest photocatalytic activity because of its ability of higher adsorption sites, increase of BET surface area, decrease of the crystallite size and prevention of electron-hole recombination^[47,48]. Upon doping the catalyst with Gd the TOC mineralization was found to increase from 33% with undoped tin dioxidenanoparticles to 99% SnO₂:Gd. Thus a threefold improvement in phenol removal was observed when Gd doped nanoparticles were used upon 150 min irradiation as can be seen from Table 3.

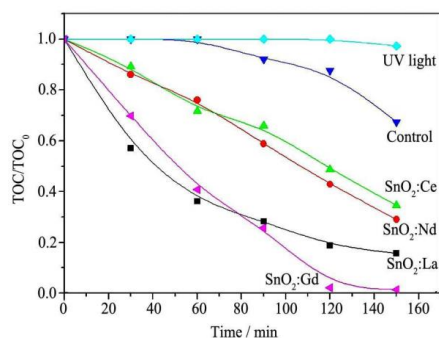


Fig. 10 Total organic carbon (TOC) removal from phenol solutions during 2 h of photocatalytic degradation by different Gd-doped SnO₂, La-doped SnO₂, Nd-doped SnO₂, Ce-doped-SnO₂, control and irradiation only

Table 3 Comparison of photocatalytic performance of different RE doped tin dioxide nanoparticles on phenol degradation

Catalyst	Phenol degradation by TOC after 150 min irradiation/wt. %	Phenol degradation by HPLC after 150 min irradiation/wt. %
Control	32.6	46
SnO ₂ :Ce	65.5	88.3
SnO ₂ :Nd	70.8	95
SnO ₂ :La	86.6	100
SnO ₂ :Gd	98.5	100

3 Conclusions

Sol-gel synthesized tin dioxide nanoparticles were shown to be visible light active for photocatalysis upon doping with rare earth metals. Gadolinium doped tin dioxide (SnO₂:Gd) nanoparticles were found to have the highest visible light absorption and was used to study the

mineralization process of phenol in water. Increase in dopant concentration in the photocatalyst improved the photodegradation. From the study of the byproducts obtained upon photocatalytic degradation of phenol a reaction pathway was proposed. It was observed that Gd doped SnO₂ nanoparticles are effective photocatalysts that can find applications in the real world.

Acknowledgements: Authors would like to thank partial financial support from the Chair in Nanotechnology Programme of the Research Council of Oman and the College of Science for giving this opportunity to carry out the research at Sultan Qaboos University.

References:

- [1] Phipps G L, Holcombe G W, Fiandt J T. Acute toxicity of phenol and substituted phenols to the fathead minnow. *Bull. Environ. Contam. Toxicol.*, 1981, **26**: 585.
- [2] Fakhru'l-Razi A, Pendashteh A, Abdullah L C, Biak D R A, Madaeni S S, Abidin Z Z. Review of technologies for oil and gas produced water treatment. *J. Hazard. Mater.*, 2009, **170**: 530.
- [3] Aktar W, Sengupta D, Chowdhury A. Impact of pesticides use in agriculture: their benefits and hazards. *Interdiscip. Toxicol.*, 2009, **2**: 1.
- [4] Fatta-Kassinos D, Meric S, Nikolaou A. Pharmaceutical residues in environmental waters and wastewater: current state of knowledge and future research. *Anal. Bioanal. Chem.*, 2011, **399**: 251.
- [5] Jiang J Q, Zhou Z, Sharma V. Occurrence, transportation, monitoring and treatment of emerging micro-pollutants in waste water-a review from global views. *Microchem. J.*, 2013, **110**: 292.
- [6] Valette C, Andary C, Geiger J, Sarah J, Nicole M. Histochemical and cytochemical investigations of phenols in roots of banana infected by the burrowing nematode *Radopholus similis*. *Phytopathology*, 1998, **88**: 1141.
- [7] Ahmed S, Rasul M, Martens W N, Brown R, Hashib M. Advances in heterogeneous photocatalytic degradation of phenols and dyes in wastewater: a review. *Water Air Soil Poll.*, 2011, **215**: 3.
- [8] Zhang L, Liu J, Tang C, Lü J, Zhong H, Zhao Y, Wang X. Palygorskite and SnO₂-TiO₂ for the photodegradation of phenol. *Appl. Clay Sci.*, 2011, **51**: 68.
- [9] Kruefu V, Ninsonti H, Wetchakun N, Inceesungvorn B, Pookmanee P, Phanichphant S. Photocatalytic degradation of phenol using Nb-loaded ZnO nanoparticles. *Eng. J.*, 2012, **16**: 91.
- [10] Neppolian B, Choi H C, Sakthivel S, Arabindoo B, Murugesan V. Solar/UV-induced photocatalytic degradation of three commercial textile dyes. *J. Hazard. Mater.*, 2002, **89**: 303.
- [11] Hu J, Men J, Ma J H, Huang H. Preparation of LaMnO₃/gra-phene thin films and their photocatalytic activity. *J. Rare Earths*, 2014, **32**: 1126.
- [12] Senthilkumaar S, Porkodi K, Vidyalakshmi R. Photodegradation of a textile dye catalyzed by sol-gel derived

- nanocrystalline TiO₂ via ultrasonic irradiation. *J. Photoch. Photobio. A*, 2005, **170**: 225.
- [13] Konstantinou I K, Albanis T A. Photocatalytic transformation of pesticides in aqueous titanium dioxide suspensions using artificial and solar light: intermediates and degradation pathways. *Appl. Catal. B-Environ.*, 2003, **42**: 319.
- [14] Lakshmi B B, Patrisi C J, Martin C R. Sol-gel template synthesis of semiconductor oxide micro- and nanostructures. *Chem. Mater.*, 1997, **9**: 2544.
- [15] Ullah R, Dutta J. Photocatalytic degradation of organic dyes with manganese-doped ZnO nanoparticles. *J. Hazard. Mater.*, 2008, **156**: 194.
- [16] Hara K, Horiguchi T, Kinoshita T, Sayama K, Sugihara H, Arakawa H. Highly efficient photon-to-electron conversion with mercurochrome-sensitized nanoporous oxide semiconductor solar cells. *Sol. Energy Mater. Sol. Cells*, 2000, **64**: 115.
- [17] Hagfeldt A, Graetzel M. Light-induced redox reactions in nanocrystalline systems. *Chem. Rev.*, 1995, **95**: 49.
- [18] Thompson T L, Yates J T. Surface science studies of the photoactivation of TiO₂: new photochemical processes. *Chem. Rev.*, 2006, **106**: 4428.
- [19] Coey J, Venkatesan M, Fitzgerald C. Donor impurity band exchange in dilute ferromagnetic oxides. *Nat. Mater.*, 2005, **4**: 173.
- [20] Vilhunen S H, Sillanpää M E. Ultraviolet light emitting diodes and hydrogen peroxide in the photodegradation of aqueous phenol. *J. Hazard. Mater.*, 2009, **161**: 1530.
- [21] Vilhunen S, Särkkä H, Sillanpää M. Ultraviolet light-emitting diodes in water disinfection. *Environ. Sci. Pollut. Res.*, 2009, **16**: 439.
- [22] Repo E, Rengaraj S, Pulkka S, Castangnoli E, Suihkonen S, Sopanen M, Sillanpää M. Photocatalytic degradation of dyes by CdS microspheres under near UV and blue LED radiation. *Sep. Purif. Technol.*, 2013, **120**: 206.
- [23] Al-Hamdi A M, Sillanpää M, Dutta J. Photocatalytic degradation of phenol by iodine doped tin oxide nanoparticles under UV and sunlight irradiation. *J. Alloys Compd.*, 2014, **618**: 366.
- [24] Al-Hamdi A, Sillanpää M, Dutta J. Photocatalytic degradation of phenol in aqueous solution by rare earth-doped SnO₂ nanoparticles. *J. Mater. Sci.*, 2014, **49**: 5151.
- [25] Liu C, Tang X H, Mo C H, Qiang Z M. Characterization and activity of visible-light-driven TiO₂ photocatalyst codoped with nitrogen and cerium. *J. Solid State Chem.*, 2008, **181**: 913.
- [26] Pawar B G, Pinjari D V, Kolekar S S, Pandit A B, Han S H. Effect of sintering temperatures on the synthesis of SnO₂ nanospheres. *Int. Sch. Res. Not.*, 2012, **2012**: 7.
- [27] Novinrooz A, Sarabadani P, Garousi J. Characterization of pure and antimony doped SnO₂ thin films prepared by the sol-gel technique. *Iran. J. Chem. Chem. Eng.*, 2006, **25**: 31.
- [28] Sadeh A, Sladkevich S, Gelman F, Prikhodchenko P, Baumberg I, Berezin O, Lev O. Sol-gel-derived composite antimony-doped, tin oxide-coated clay-silicate semitransparent and conductive electrodes. *Anal. Chem.*, 2007, **79**: 5188.
- [29] Wang Y, Ramos I, Santiago-Aviles J J. Optical bandgap and photoconductance of electrospun tin oxide nanofibers. *J. Appl. Phys.*, 2007, **102**: 093517-093517-5.
- [30] Chinnappa L, Ravichandran K, Periyambal T, Muruganatham G, Sriram S, Sakhivel B. Influence of solvent volume on solar cell related electrical and optical properties of antimony doped tin oxide films synthesized using a low-cost spray technique. *J. Appl. Sci.*, 2012, **12**: 5.
- [31] Bergermayer W, Tanaka I. Reduced SnO₂ surfaces by first-principles calculations. *Appl. Phys. Lett.*, 2004, **84**: 909.
- [32] Xu A W, Gao Y, Liu H Q. The preparation, characterization, and their photocatalytic activities of rare-earth-doped TiO₂ nanoparticles. *J. Catal.*, 2002, **207**: 151.
- [33] Jinkawa T, Sakai G, Tamaki J, Miura N, Yamazoe N. Relationship between ethanol gas sensitivity and surface catalytic property of tin oxide sensors modified with acidic or basic oxides. *J. Mol. Catal. A: Chem.*, 2000, **155**: 193.
- [34] Weber I T, Valentini A, Probst L, Longo E, Leite E R. Influence of noble metals on the structural and catalytic properties of Ce-doped SnO₂ systems. *Sensor. Actuat. B-Chem.*, 2004, **97**: 31.
- [35] Carreño N, Fajardo H V, Maciel A P, Valentini A, Pontes F M, Probst L F, Leite E R, Longo E. Selective synthesis of vinyl ketone over SnO₂ nanoparticle catalysts doped with rare earths. *J. Mol. Catal. A: Chem.*, 2004, **207**: 91.
- [36] Reed J S. Principles of Ceramics Processing, 2nd ed., Wiley, 1995.
- [37] Leite E R, Weber I T, Longo E, Varela J A. A new method to control particle size and particle size distribution of SnO₂ nanoparticles for gas sensor applications. *Adv. Mater.*, 2000, **12**: 965.
- [38] Weber I, Maciel A, Lisboa-Filho P, Longo E, Leite E, Paiva-Santos C, Maniette Y, Schreiner W H. Effects of synthesis and processing on supersaturated rare earth-doped nanometric SnO₂ powders. *Nano Lett.*, 2002, **2**: 969.
- [39] Leite E R, Maciel A P, Weber I T, Lisboa-Filho P N, Longo E, Paiva-Santos C, Andrade A, Pakoscimias C, Maniette Y, Schreiner W H. Development of metal oxide nanoparticles with high stability against particle growth using a metastable solid solution. *Adv. Mater.*, 2002, **14**: 905.
- [40] Reszeczyńska J, Grzyb T, Sobczak J W, Lisowski W, Gazda M, Ohtani B, Zaleska A. Lanthanide co-doped TiO₂: the effect of metal type and amount on surface properties and photocatalytic activity. *Appl. Surf. Sci.*, 2014, **307**: 333.
- [41] Das A, Bonu V, Prasad A K, Panda D, Dhara S, Tyagi A K. The role of SnO₂ quantum dots in improved CH₄ sensing at low temperature. *J. Mater. Chem. C*, 2014, **2**: 164.
- [42] Melghit K, Bouziane K. One step aqueous solution preparation of nanosize iron-doped tin oxide from SnO₂·xH₂O gel. *Mater. Sci. Eng., B*, 2006, **128**: 58.
- [43] Melghit K, Bouziane K. Low-temperature preparation and magnetic properties of V-doped SnO₂ nanoparticles. *J. Am. Ceram. Soc.*, 2007, **90**: 2420.
- [44] Liu R L, Huang Y X, Xiao A H, Liu H Q. Preparation and photocatalytic property of mesoporous ZnO/SnO₂ composite nanofibers. *J. Alloys Compd.*, 2010, **503**: 103.
- [45] He Z Q, Wang C, Wang H Y, Hong F Y, Xu X H, Chen J M, Song S. Increasing the catalytic activities of iodine

- doped titanium dioxide by modifying with tin dioxide for the photodegradation of 2-chlorophenol under visible light irradiation. *J. Hazard Mater.*, 2011, **189**: 595.
- [46] Gaya U I, Abdullah A H. Heterogeneous photocatalytic degradation of organic contaminants over titanium dioxide: a review of fundamentals, progress and problems. *J. Photochem. Photobiol. C: Photochem. Rev.*, 2008, **9**: 1.
- [47] Reszczyńska J, Grzyb T, Sobczak J W, Lisowski W, Gazda M, Ohtani B, Zaleska A. Visible light activity of rare earth metal doped (Er^{3+} , Yb^{3+} or $\text{Er}^{3+}/\text{Yb}^{3+}$) titania photocatalysts. *Appl. Catal. B-Environ.*, 2015, **163**: 40.
- [48] Du J, Wu Q, Zhong S, Gu X, Lin J, Guo H Z, Zhang W L, Peng H L, Zou J G. Effect of hydroxyl groups on hydrophilic and photocatalytic activities of rare earth doped titanium dioxide thin films. *J. Rare Earths*, 2015, **33**:148

Publication V

A. M. AHamdi, Mika Sillanpää, J. Dutta

**Intermediate formation during photodegradation of phenol using
lanthanum doped tin dioxide nanoparticles**

Reprinted with permission from
Journal of Research on Chemical Intermediates
Vol. 42, pp. 3055-205, 3069
© 2015, Springer

Intermediate formation during photodegradation of phenol using lanthanum doped tin dioxide nanoparticles

Abdullah M. Al-Hamdi¹ · Mika Sillanpää¹ ·
Joydeep Dutta^{2,3} 

Received: 5 May 2015 / Accepted: 24 July 2015 / Published online: 4 August 2015
Springer Science+Business Media Dordrecht 2015

Abstract Lanthanum (La)-doped tin dioxide (SnO₂) nanoparticles were synthesized by a modified sol–gel method at room temperature. The samples were characterized by X-ray diffraction, scanning electron microscopy, and transmission electron microscopy. The photocatalytic activity of La:SnO₂ samples was investigated by studying the degradation profile of phenol and its by-products in water. The treated samples were analyzed by HPLC–UV and a UV–Vis spectrophotometer. Benzoquinone, catechol, resorcinol, hydroquinone, acetic acid, and 2-propanol were identified as phenol degradation intermediates. Maximum concentration acquired was in the order of catechol, resorcinol, hydroquinone, and benzoquinone, which was observed in the beginning stages while iso-propanol and acetic acid were observed in the final stages of phenol degradation. We achieved a complete photodegradation of a 10 ppm aqueous phenol solution and intermediates with 0.6 % of SnO₂:La nanoparticles in 120 min under artificial solar irradiation. A maximum degradation rate constant of 0.02228 min⁻¹ of propanol and a minimum of acetic acid 0.013412 min⁻¹ were recorded at 37 °C.

✉ Joydeep Dutta
joydeep@kth.se; dutta@squ.edu.om

Abdullah M. Al-Hamdi
Abdullah.Al.hamdi@lut.fi

Mika Sillanpää
Mika.sillanpaa@lut.fi

- ¹ Laboratory of Green Chemistry, Lappeenranta University of Technology, Sammonkatu 12, 50130 Mikkeli, Finland
- ² Chair in Nanotechnology, Water Research Center, Sultan Qaboos University, PO Box 33, 123 Al-Khoudh, Muscat, Sultanate of Oman
- ³ Functional Materials Division, ICT, KTH Royal Institute of Technology, Isafjordsgatan 22, 164 40 Kista, Stockholm, Sweden

Keywords Photocatalysis SnO₂ Rare earth metal Lanthanum By-product Phenol

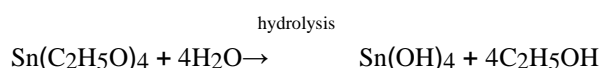
Introduction

The overuse of pesticides, pharmaceuticals, and personal care products in modern society leads to many kinds of organics polluting the environment. Phenols or derivatives of phenols are commonly encountered organic pollutants in toxic waste discharged in industrial effluents [1, 2]. The accumulation of these toxic pollutants can adversely affect human life and derail sustainable development [3, 4] because of their toxicity, endocrine disrupting abilities, and carcinogenic behavior [5]. Phenol and its by-products are released into the air and water as a result of industrial activities [6]. Sources of phenol and its derivatives in water has been found in waste water discharged from refining activities of oil and coal tar industries [7], distillation of wood or coal [6], phenolic chemicals used in livestock dips [8], and discharges of domestic sewage or rotting vegetation [9]. The European Union and other countries have included some phenols in their list of priority pollutants [10], thus; it is important to develop new and effective treatment processes for the removal of organic and inorganic pollutants from water.

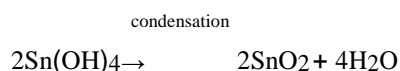
Advanced oxidation processes (AOP) are among the most effective technologies for the treatment of organic pollutants, because they can generate strong oxygen-based oxidizers (OH) [11], which can react non-selectively with different types of organics and can achieve complete oxidation [12]. AOP techniques can be built up using a combination of chemical and physical agents such as a catalyst and ultraviolet light [13].

Photocatalysis is a green technology for water treatment to remove recalcitrant organic compounds. Tin dioxide or stannic oxide (SnO₂) is one of the most promising metals oxide semiconductor photocatalysts, in which the inherent oxygen vacancies act as n-type dopants leading to effective charge separation in the presence of a pollutant [14]. SnO₂ has a rutile type tetragonal crystal structure, and its band gap is 3.6 eV at room temperature [15]. There are numerous applications of SnO₂, as gas sensors, pH sensors, and biosensors [16], in lithium ion batteries [17], transparent conductive electrodes, [18] etc. SnO₂ is, however, less studied compared to the other photocatalysts such as titanium oxide TiO₂ and ZnO [19]. Thus, it is of interest to investigate the influence of dopants on the enhancement of the photocatalytic activities of SnO₂ [20]. In addition, these semiconductors have been recognized as preferable materials for photocatalytic processes due to their high photosensitivity, nontoxic nature, low cost, and well-known chemical stability [21–25]. Apart from these properties, a good visible-light photocatalyst should have a high specific surface area and an adequate optical absorption band to be able to absorb sunlight. Incorporation of metal ions into the SnO₂ matrix could introduce defects lowering the effective optical gap and, hence, leading to a better photocatalytic activity [26, 27]. Renewed interest in the synthesis of SnO₂ nanoparticles of different sizes has probably arisen to address these problems [28–30].

Photocatalytic degradation of organic compounds is mainly achieved by ultraviolet light irradiation due to the wide metal oxide bandgap. A better alternative is to use visible light, or solar irradiation as it is an abundant free source of energy. Many ways have been developed for rendering the wide band gap metal oxide semiconductors photoactive in the visible region [31]. Of these, incorporation of defects in the metal oxides with transition metals is very popular [28]. For example, rare earth metal ions incorporated into the SnO₂ matrix introduces defects in the valence band tail states, effectively lowering the optical gap and, hence, leading to a better photoactivity in the visible region [32–34]. Several studies of SnO₂ doping with different metals to produce nanocrystals have been reported in recent years. [35–37] Sn⁴⁺ can be easily reduced to Sn²⁺ leading to a change in the surface electronic structure of SnO₂. Oxygen atoms on the surface of SnO₂ nanoparticles lead to energetically favorable reconstructions of the SnO₂ (110) and (101) surfaces [38]. These oxygen vacancies bind with electrons forming an excitation energy level below the conduction band of SnO₂. As rare earth metals incompletely occupy 4f and 5d orbital's, formation of labile oxygen vacancies with relatively high mobility of bulk oxygen species can occur very easily [39]. Sol–gel synthesis of SnO₂ nanoparticle is very popular as it is based on simple hydrolysis of metal alkoxides in aqueous media:



The alkoxy groups are replaced by hydroxide groups forming an inorganic network (sol) that is followed by a second reaction (condensation) as follows:



The sol–gel method offers several advantages, including the formation of homogeneous nanoparticles, precise control over the stoichiometry, and purity while the reaction takes place at lower temperatures.

In this work we describe the preparation of La doped tin dioxide nanoparticles at room temperature, using the sol–gel synthesis method. The photocatalytic properties SnO₂:La nanoparticles were evaluated by studying the degradation profile of phenol and its intermediates that will contribute to a better understanding of the phenol degradation processes. This work provides a framework for studying degradation pathways in similar and for complex organic toxins.

Experimental

Materials

Analytical-grade tin (IV) chloride (SnCl₄·, Sigma Aldrich, Purity: 99 %), lanthanum nitrate hexahydrate (La (NO₃)₃ 6H₂O, Fluka), ethanol (C₂H₅OH, ETAX Aa Merck Absolute), phenol (C₆H₅OH, Sigma. Aldrich, 99 %), catechol (C₆H₆O₂, Sigma Aldrich, Purity: 99.99 %), hydroquinone (Sigma Aldrich, Purity: 99.99 %),

p-benzoquinone (O: C₆H₄:O, BDH, AnalaR 99.99 %), resorcinol (C₆H₄(OH)₂, BDH, AnalaR 99. %), acetic acid (C₂H₄O₂, Sigma Aldrich, Purity: 99.99 %), propan-2-ol ((CH₃)₂CHOH, Sigma Aldrich, Purity: 99.99 %), sulfuric acid (H₂SO₄, Sigma Aldrich, Purity: 99 %), hydrochloric acid (HCl, Sigma. Aldrich, 99 %), sodium hydroxide pellets (NaOH, Sigma. Aldrich, 99 %) and methanol (CH₄O, Sigma. Aldrich, 99 % HPLC grade) were used in the experimental studies. Double deionized water with a high purity from Ultra Clear Water SG was used for the preparation of all solutions.

Photocatalyst preparation

Synthesis of pure and doped-SnO₂ nanoparticles

Nanoparticles containing various molar compositions of SnO₂ were chemically synthesized by the sol–gel method, following the procedure described below: 3.80825 ml of SnCl₄ mixed in 50 ml absolute alcohol (ethanol) and 50 ml ultra-pure water in a round bottom flask and used as a precursor for synthesizing undoped SnO₂ nanoparticles. The mixture was subjected to vigorous stirring for 3 h at room temperature, until a colourless solution was obtained. For the synthesis of lanthanum metal doped tin oxide nanoparticles, a certain concentration of this metal was mixed and dissolved separately in ethanol and added to the precursor solution. A turbid colloidal solution of tin alkoxide started to appear after adding (25 %) of aqueous ammonia drop by drop into the solution upon continuous stirring until a pH value of 8 was reached. The sol was aged for 48 h in air until a gel was formed. Filtration and successive washing with ultra-pure water was repeated several times to remove both ammonia and chloride ions until all chloride ions had been removed (determined by examining the filtrate solution using aqueous silver nitrate solution). The dopant concentration studied in this work was kept up to 0.6 %, following our previously reported work [32].

Material characterization

Optical absorption spectra of colloidal suspension were recorded in a double beam spectrometer (Perkin Elmer, Lambda 45). To study the surface morphology of the SnO₂:La samples, scanning electron microscopy (SEM) was carried out with JEOL (JSM-5600LY) (Japan) working at 30 kV. High resolution transmission electron microscopy (HRTEM) was carried out with JEOL (JEM 2100F) (Japan) working at 200 kV. The crystalline phase of the synthesized SnO₂ nanoparticles were analyzed by X-ray powder diffraction (XRD) using a MiniFlex 600 diffractometer (Rikagu,

Japan) with Cu K_α radiation (wavelength = 1.54 Å). Diffractograms of powder was recorded in a 2θ scan configuration, in the 10°–80° 2θ range, with the data collected at steps of 0.02°. Then, 200–300 mg of sample was degassed at 300 °C for 3 h under nitrogen (N₂) flow, followed by a six point N₂ adsorption carried out at p/p₀ of 1–5 in a Nova 2200 analyzer. The surface area was determined by a gas adsorption technique using the Nova 2200 (Brunauer–Emmett–Teller (BET) method).

Photocatalytic experiments

UV photocatalytic reactor

The photoreactor was a cylindrical Pyrex-glass container of 50 mm internal diameter and 300 mm in height with 250 mL capacity. An 8 W medium pressure mercury lamp (Osaka, Japan) was used with an intensity of about 80 W/m^2 and the reaction temperature was kept at 25 LC by cooling with water.

Visible light photocatalytic reactor

The Pyrex-glass reactor was used with a cooling water jacket with a 250 ml capacity, 100 mm internal diameter, and 200 mm height. A 300 W xenon lamp simulating a solar light source (PLS-SXE300C, Beijing Perfect light Co. Ltd., China) was placed 71 mm above the surface of contaminant during the photocatalysis studies.

Experimental procedure

To investigate the effects of $\text{SnO}_2\text{:La}$, oxidative photodegradation of phenol and its intermediates were chosen to evaluate the photocatalytic activity of synthesized nanoparticles. The study of degradation of phenol and its by-products in water was carried out at 25 LC using the water-cooled cylindrical glass batch photoreactor of 250 mL volume. The experimental conditions were varied as follows: The amount of catalyst powder (photocatalyst) was kept at 0.065 g in 50.00 mL; the initial concentration of the pollutant was varied from 5–100 ppm and the pH of the solution was adjusted by the addition of 0.5 N NaOH to fix pH at 5.7. Then, 10 mg/L phenol solution was used to carry out photocatalysis experiments. Before each test, the mixture was kept in the dark for 30 min under constant magnetic stirring to ensure that the adsorption–desorption equilibrium was reached before illumination. The sample was then taken out at the end of the dark adsorption period, prior to turning the light on or before exposure to sunlight. When the lamp was turned on, the irradiation time varied from 2 to 3 h; aliquots of the suspensions were collected and removed from the reactor every 15 or 30 min. At the given time intervals, the photocatalyst particles were removed from the samples first by centrifugation (4000 rpm, 5 min) using an Eppendorf Centrifuge (system model 5810R) and then filtered through 0.2 μm Millipore filters.

Analytical methods

Phenol photodegradation by-products were analyzed using high performance liquid chromatography (UHPLC focused), containing a P580 high-precision pump from Thermo Scientific (Germering, Germany), and fulfilling the requirement for a measured delivery rate of the mobile phase. The injector was a Rheodyne (Cotati) 8125 valve fitted with a 20 μL loop. The analysis was carried out using a C18 column (5 μm silica) maintained at room temperature. After elution from the

column, the eluent passed through a Variable Wavelength Detectors (VWD-3400RS) set at 245 nm for phenol and its intermediates detection. The mobile phase for the HPLC separation was prepared by mixing methanol with water in the ratio 45:55 and then adjusting the pH at 3.0 by adding sulfuric acid (H_2SO_4). The mobile phase was degassed in an ultrasonic bath, and then passed through a Millipore filtration apparatus (0.2 μm). Photodegraded phenol and control samples were then eluted at a flow rate of 1 mL/min.

The change in phenol concentration in each photodegraded solution was also monitored by an ultraviolet–visible (UV–Vis) spectrometer (Perkin Elmer Lambda 45), and the maximum absorbance of phenol was measured at $k_{\text{max}} = 269 \text{ nm}$.

Results and discussion

Crystallinity of SnO_2 nanoparticles doped with lanthanum

The XRD pattern (Fig. 1) showed that the diffraction angles at $2\theta = 26.3^\circ$, 33.6° , 51.5° , and 65° that can be assigned to (110), (101), (211), and (112) planes of the SnO_2 , respectively, matching with the standard XRD file of the rutile phase of SnO_2 (JCPDS-#41-1445) [40–43]. SnO_2 crystallite sizes obtained from the Debye Scherrer equation considering the most intense peak (110) follows the well-known trend of crystallite size reduction upon doping. An increase in surface area was also observed, which was attributed to the decrease in grain size as it can be seen from Table 1.

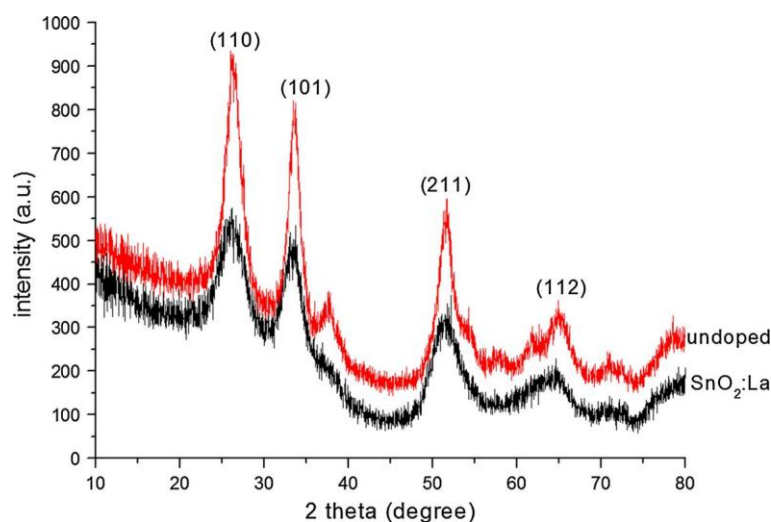


Fig. 1 X-ray diffraction (XRD) patterns of $\text{SnO}_2\text{:La}$ and pure undoped particles synthesized by the sol–gel process

Table 1 Comparison of surface areas and estimated crystallite sizes for undoped and lanthanum doped SnO₂ nanoparticles

Dopant	Size nm	Surface area
Undoped	7.5	28
SnO ₂ :La	3.4	40

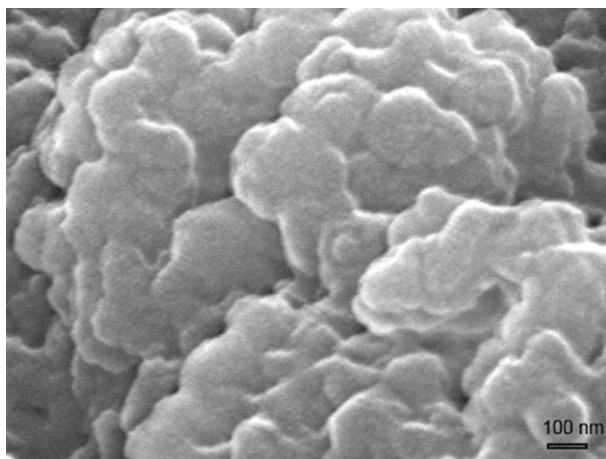


Fig. 2 Typical scanning Electron Micrograph of SnO₂:La nanoparticles synthesized by the sol-gel process

The 3.4 nm crystallites agglomerate to form 50 nm particles as observed by SEM (Fig. 2). In order to get a better insight into the morphology, we carried out high resolution HRTEM as shown in Fig. 3. The crystallite sizes are comparable to what was estimated from the XRD. The surface area of the synthesized nanoparticles was found to be between around 28–40 m²/g.

Photocatalytic degradation

Photodegradation occurs due to the formation of active radicals during redox reaction. When a photocatalyst absorbs a photon of light ($h\nu$), it is enough to excite the electrons to the higher states creating an electron (e^-) and a positive-hole (h^+) pair



The holes (h^+) dissociates water molecules to generate hydroxyl radicals and hydrogen gas

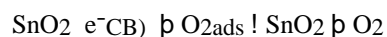


The holes (h^+) mostly react with water (i.e., hydroxide ions, OH^-) to produce OH^\bullet , which is very a powerful oxidant.

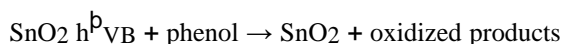
Fig. 3 Typical high resolution transmission Electron micrograph of SnO₂:La nanoparticles synthesized by the sol-gel process



The electron reacts with an oxygen molecule to form superoxide radicals (O_2^-). The hydroxyl radical is an extremely powerful oxidation agent, and the cycle continues until light is available.



The hydroxyl radical will oxidize the pollutant and any intermediates, and the final product is carbon dioxide and water.



UV-Vis spectroscopy

UV scans (200–400) were used to investigate possible intermediates formed in solution during photodegradation of phenol by using SnO₂:La. Previous research on phenol degradation has shown that phenol first degrades to benzoquinone and then the ring is opened to form other smaller byproducts like the carboxylic acids [44, 45]. The adsorption ability of the samples were tested, and it was found that after 30 min in dark conditions, very minimal changes of phenol adsorption were observed on the SnO₂:La nanoparticles. The UV-Vis spectra at different time intervals during phenol photodegradation with SnO₂:La are shown in Fig. 4. At the outset only one broad peak was present at 269 nm that was observed due to

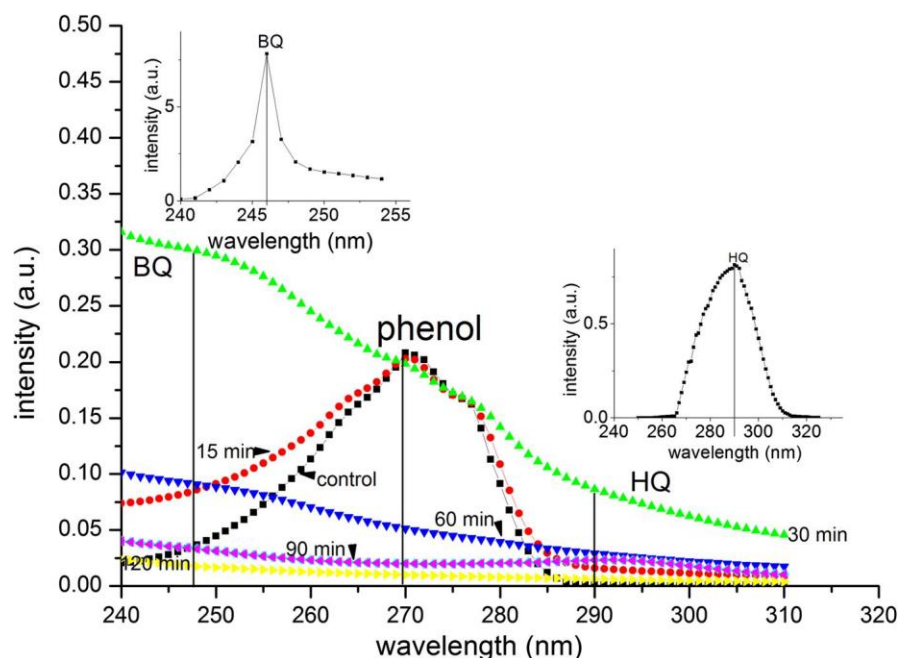


Fig. 4 Spectra of phenol photodegradation and reduction in the intensity of phenol peak observed by UV–Vis spectrophotometry in the presence of 0.6 wt% lanthanum doped SnO₂ nanoparticles. The appearance of different phenol byproducts appear in the Figure

absorption in the aromatic ring. This absorption band was used as a reference for the photodegradation analysis. A clear decrease of the 269 nm absorbance band intensity was observed with increasing photo irradiation time (Fig. 4). A slight decrease of the 269 nm absorbance band, but a simultaneous increase at the 290 nm band and a higher increase of the 246 nm absorbance band can be associated with the formation of phenol, hydroquinone (HQ), and benzoquinone (BQ), respectively, within 15 min of photo irradiation. After 30 min of light irradiation, the phenol absorbance band was reduced, but a concurrent increase and broadening of the 290 nm band and a rising increment with broadening of a 246 nm band was observed. After 60 min of irradiation, the characteristic peak at 290 nm reduces, and the 246 nm peak intensity decreases with the disappearance of the phenol peak. After 90 min of irradiation, it is clear that all phenol was degraded and also the formed intermediates are being further degraded.

Intermediates of phenol degradation

HPLC separation technique

In order to conclusively characterize the byproducts formed during the photocatalytic reaction, chromatographic techniques were used to study the degraded phenol

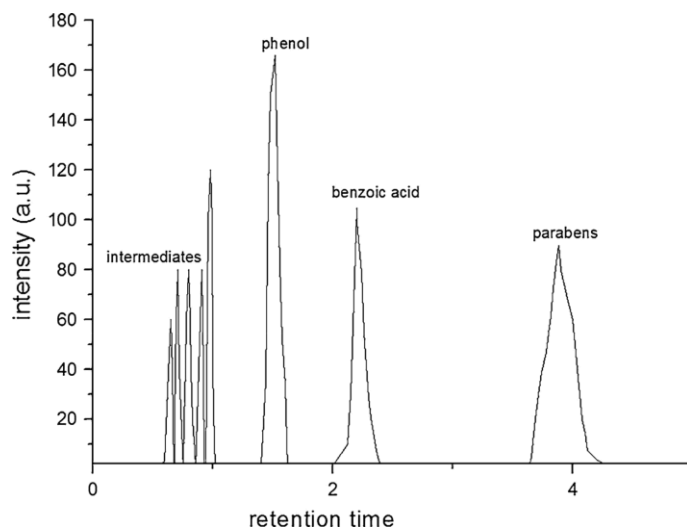


Fig. 5 Separation of phenol and its by-products from benzoic acid and paraben mixture observed by (HPLC)

mixture. Degradation of phenol in water, followed by the formation of many intermediates, some of which could be more toxic than phenol itself, which causes symptoms such as muscle weakness, convulsions, and coma upon contact to human skin. Phenol, upon oxidation, produces several aromatic intermediates, such as benzoquinone, catechol, resorcinol, and some acyclic compounds, including oxalic acid, formic acid maleic acid, and fumaric acid. We have been able to separate phenol by-products in solutions during photocatalysis, by different techniques such as GC/MS and also using techniques to quantify these intermediates by HPLC and CE. Here, we used a simple reverse phase HPLC technique to separate the parabens, benzoic acid, phenol, benzoquinone, catechol, resorcinol, hydroquinone, acetic acid, and isopropanol in less than 5 min as shown in Fig. 5. Maximum concentration of intermediates obtained is in the order catechol [resorcinol [hydroquinone [benzoquinone as shown in Fig. 6.

In fact OH generated from photocatalytic degradation of phenol reacts with OH^- , either to produce catechol or hydroquinone. Catechol or hydroquinone reacts with OH^- to form benzoquinone. Upon continuous oxidation, the benzene ring will be opened leading to the formation of aliphatic compounds, which would finally mineralize to CO_2 and water. The degradation as observed by optical spectroscopy is different from what was registered using chromatography as the extinction coefficients play a part in the final optical absorption of the by-products. For example, benzoquinone absorbs nearly ten times more than phenol around 269 nm, which is the peak absorption of phenol. Thus, the formation of the by-products would mask the degradation level of phenol if only optical spectroscopy is used. In effect UV-Vis spectroscopy would not render a correct picture of the phenol degradation process, thus all subsequent discussion are based on chromatographic studies (Fig. 7).

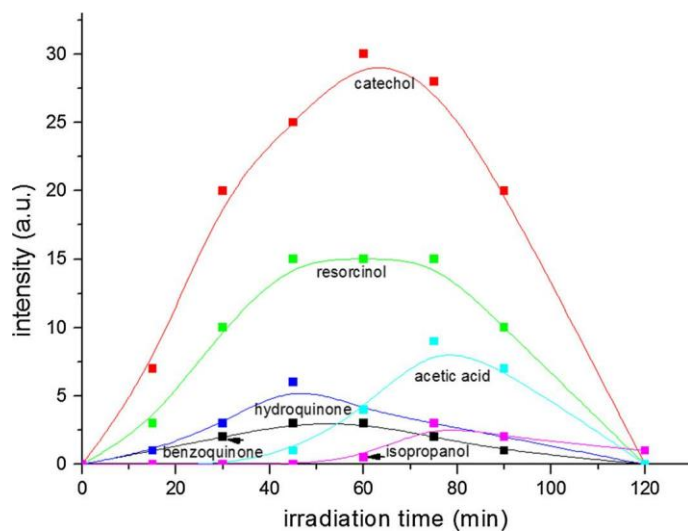


Fig. 6 Evolution of phenol by-products during phenol photodegradation in the presence of SnO₂:La nanoparticles in a 10 ppm aqueous phenol solution

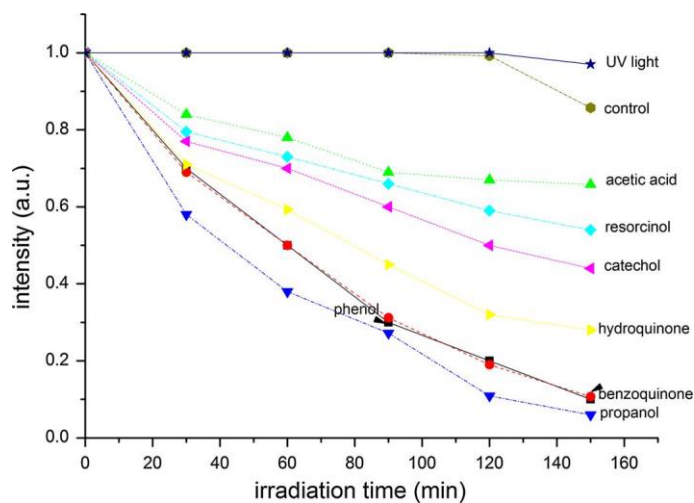


Fig. 7 Degradation of phenol and its by-products after 2 h treatment with SnO₂:La

Degradation mechanism of phenol involving the O–H bond

Formation mechanism In order to better understand the degradation mechanism, the major degradation by-products were studied independently upon photo irradiation.

The reaction of phenol starts by breaking the O–H bonds resulting in giving up a proton thus forming an anion stabilized by the aromatic ring as shown in Fig. 8.

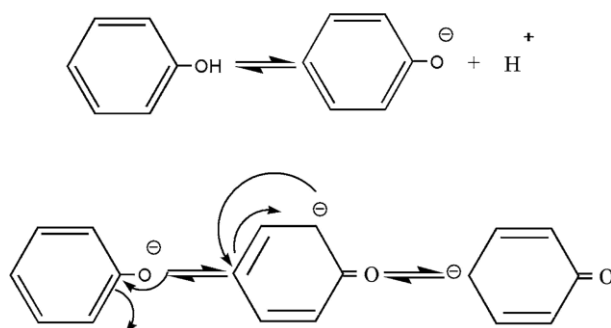


Fig. 8 Possible degradation mechanism of phenol and resonance stability of phenoxide, and the formation of the benzoquinone intermediate

Activation of the phenol by hydroxyl radicals will produce phenoxy radicals, which are in resonance with radical structures in ortho and para positions [46]. The three mesomeric forms of the radical are the initial formation of the different intermediates. These radicals can react with the hydroxyl radicals to form compounds such as hydroquinone, benzoquinone, and catechol as explained above.

Benzoquinone

Benzoquinone was traced in the degradation process for the first 30 min of photodegradation. The formation rate of benzoquinone was found to be 0.0107 ppm/min, and the degradation rates were calculated from the reduction of benzoquinone peak to be 0.00357 ppm/min.

Catechol

Degradation of phenol produces higher concentrations of catechol compared to any other by-products, which might be related to the ortho directed properties group of phenol. Catechol was formed within 15 min of phenol degradation and its concentration increased to a maximum of 0.7 ppm, and kept increasing until it reached 3 ppm after 45 min increasing at a rate of 0.1249 ppm/min. After 75 min, concentration of catechol decreased at a rate of 0.0292 ppm/min. We can observe from the graph that catechol keeps being produced until all the phenol is degraded.

Resorcinol

Resorcinol appeared from the beginning, and its concentration increased from 0.3 ppm until it reached to 1.5 ppm and became stable at that point after 75 min of photocatalytic degradation at a rate of 0.0075 ppm/min. The almost stable concentration of resorcinol production in our mixture means that it will be produced by the same rate until all phenol can be removed from the solution. We also noticed that resorcinol concentrations were higher than hydroquinone. In this

case it seems that the substitution rules of OH radicals attacking the phenol molecule with higher probability in 1 and 4 positions (ortho and para directing effect) are weaker than the nonselective nature of attack of the OH group of the aromatic ring.

Hydroquinone

During phenol degradation, hydroquinone appeared after 30 min, and it was at a maximum after 45 min of photo-irradiation at a rate of 0.0025 ppm/min. After 60 min of phenol photodegradation, benzoquinone concentrations decrease sharply and further slow reduction was observed until all phenol was removed from the solution.

Acetic acid

Ring opening of the by-products lead to the formation of acetic acid; pH also increases (results not shown) [47]. Acetic acid appeared in the reaction medium after 45 min at a rate of 0.0015 ppm/min.

Iso-propanol

The 2-Propanol is also known as isopropanol, and has a neutral pH level of approximately 7 (as we obtained from our previous analysis, result not shown) [47], almost similar to pure water. It seems that propionic acid competes with acetic acid, a reason why we are getting traces of this compound sometimes before acetic acid, and at other occasions, after acetic acid. Iso-propanol appeared in the solution after 75 min of photocatalytic degradation at a rate of 0.0813 ppm/min.

Photocatalytic degradation of different aromatic compounds

To compare the photocatalytic activity of phenol and its intermediates, the photocatalytic activity of phenol and its by-products in lanthanum doped tin dioxide was investigated in a series of experiments with a control and 0.6 wt% La^{3+} - SnO_2 . The influence of lanthanum doped tin dioxide nanoparticles on the degradation of phenol and removal of its by-products in aqueous solution is presented in Fig. 7. The overall degradation rate of phenol and its by-products was higher upon using $\text{SnO}_2:\text{La}$ than those with pure (control) tin dioxide nanoparticles (Fig. 9).

A maximum rate of removal of the by-products, such as phenol was achieved using $\text{La}:\text{SnO}_2$ (Fig. 9). An observed rate of phenol degradation was fitted with first-order rate constants (Table 2). The rate of degradation of propanol was quite similar to phenol. The rate of degradation of phenol was slightly higher than that of acetic acid. Slower degradation rates were also observed with catechol and resorcinol.

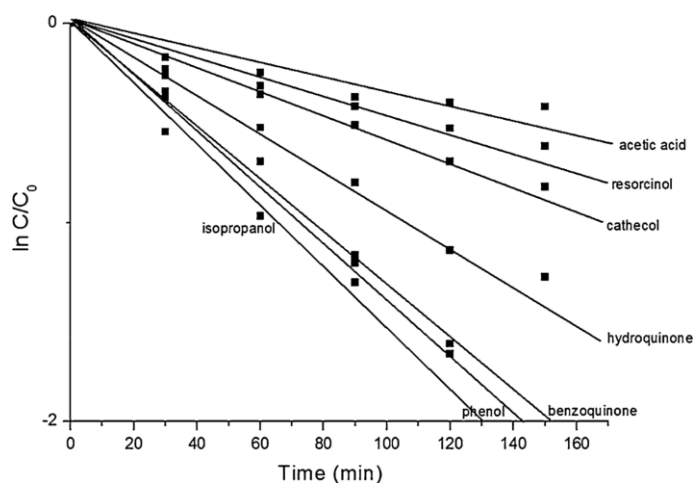


Fig. 9 Kinetic study of photodegradation of phenol and its intermediates in the presence of 0.6 wt% lanthanum doped SnO₂ nanoparticles

Table 2 Kinetic parameters of phenol and its byproducts degradation in a photocatalysis process by La:SnO₂ nanoparticles

Organic molecule	Rate constant K (min ⁻¹)	R ²
Phenol	0.02228	0.9977
Propanol	0.02228	0.9961
Benzoquinone	0.0209	0.9952
Hydroquinone	0.017066	0.9834
Catechol	0.013839	0.9544
Resorcinol	0.013753	0.9158
Acetic acid	0.013412	0.9135

Conclusions

In summary, undoped and La doped SnO₂ nanoparticles were successfully synthesized by the sol-gel method, and the phenol intermediates formed during photodegradation were studied. Photocatalytic experiments showed that La doped SnO₂ degraded all the by-products albeit with different rate constants. La doped SnO₂ nanoparticles are expected to be a promising candidate for effective photocatalysis processes using sunlight irradiation that can find applications in the real world.

Acknowledgments The authors would like to thank partial financial support from the Chair in the Nanotechnology programme of the Research Council of Oman and the college of science (Chemistry Department) for giving us this opportunity to carry out the research at Sultan Qaboos University.

References

1. S. Vilhunen, H. Sa'rkka', M. Sillanpa'a', Environ. Sci. Pollut. Res. 16, 439–442 (2009)
2. D.T. Sponza, Ecotoxicol. Environ. Saf. 54, 74–86 (2003)
3. R.A. Rudel, J.M. Gray, C.L. Engel, T.W. Rawsthorne, R.E. Dodson, J.M. Ackerman, J. Rizzo, J.L. Nudelman, J.G. Brody, Environ. Health Perspect. 119, 914–920 (2011)
4. N. Abdelouahab, Y. Ainmelk, L. Takser, Reprod. Toxicol. 31, 546–550 (2011)
5. WH Organization. WHO, Geneva (1994)
6. J. Michalowicz, W. Duda, Pol. J. Environ. Stud. 16, 347–362 (2007)
7. G.L. Phipps, G.W. Holcombe, J.T. Fiandt, Bull. Environ. Contam. Toxicol. 26, 585–593 (1981)
8. P.S. Hooda, A.C. Edwards, H.A. Anderson, A. Miller, Sci. Total Environ. 250, 143–167 (2000)
9. X. Peng, Y. Yu, C. Tang, J. Tan, Q. Huang, Z. Wang, Sci. Total Environ. 397, 158–166 (2008)
10. U. European, Off. J. Eur. Communities L331(20), 1–5 (2001)
11. W.H. Glaze, J.-W. Kang, D.H. Chapin, Ozone-Sci. Eng. 9, 335–352 (1987)
12. P.R. Gogate, A.B. Pandit, Adv. Environ. Res. 8, 501–551 (2004)
13. A. Matilainen, M. Sillanpa'a', Chemosphere 80, 351–365 (2010)
14. S. Tojo, T. Tachikawa, M. Fujitsuka, T. Majima, J. Phys. Chem. C 112, 14948–14954 (2008)
15. S. Chacko, N. Sajeeth Philip, V. Vaidyan, Phys. Status Solidi (a) 204, 3305–3315 (2007)
16. F. Gyger, M. Hubner, C. Feldmann, N. Barsan, U. Weimar, Chem. Mater. 22, 4821–4827 (2010)
17. S. Ding, J.S. Chen, G. Qi, X. Duan, Z. Wang, E.P. Giannelis, L.A. Archer, X.W. Lou, J. Am. Chem. Soc. 133, 21–23 (2011)
18. J.F. Wager, Science 300, 1245–1246 (2003)
19. J.-M. Herrmann, Environ. Sci. Pollut. Res. 19, 3655–3665 (2012)
20. R. Abe, M. Higashi, K. Sayama, Y. Abe, A.H. Sugihara, J. Phys. Chem. B 110, 2219–2226 (2006)
21. K. Hara, T. Horiguchi, T. Kinoshita, K. Sayama, H. Sugihara, H. Arakawa, Sol. Energy Mater. Sol. Cells 64, 115–134 (2000)
22. I.K. Konstantinou, T.A. Albanis, Appl. Catal. B Environ. 42, 319–335 (2003)
23. B.B. Lakshmi, C.J. Patrissi, C.R. Martin, Chem. Mater. 9, 2544–2550 (1997)
24. B. Neppolian, H.C. Choi, S. Sakthivel, B. Arabindoo, V. Murugesan, J. Hazard. Mater. 89, 303–317 (2002)
25. S. Senthilkumar, K. Porkodi, R. Vidyalakshmi, J. Photochem. Photobiol. A 170, 225–232 (2005)
26. V. Stengl, S. Bakardjieva, N. Murafa, Mater. Chem. Phys. 114, 217–226 (2009)
27. J. Hays, A. Punnoose, R. Baldner, M.H. Engelhard, J. Peloquin, K. Reddy, Phys. Rev. B 72, 075203 (2005)
28. R. Ullah, J. Dutta, J. Hazard. Mater. 156, 194–200 (2008)
29. Z.M. El-Bahy, A.A. Ismail, R.M. Mohamed, J. Hazard. Mater. 166, 138–143 (2009)
30. C.M. Teh, A.R. Mohamed, J. Alloys Compd. 509, 1648–1660 (2011)
31. S.J. Moniz, S.A. Shevlin, D.J. Martin, Z.-X. Guo, J. Tang, Energy Environ. Sci. 8, 731–759 (2015)
32. A.M. Al-Hamdi, M. Sillanpa'a', J. Dutta, J. Mater. Sci. 49, 5151–5159 (2014)
33. B.G. Pawar, D.V. Pinjari, S.S. Kolekar, A.B. Pandit and S.H. Han, ISRN Chem. Eng. 2012 (2012). doi:10.5402/2012/954869
34. A. Novinrooz, P. Sarabadani, J. Garousi, Iran. J. Chem. Chem. Eng. 25, 31–38 (2006)
35. A. Sadeh, S. Sladkevich, F. Gelman, P. Prihodchenko, I. Baumberg, O. Berezin, O. Lev, Anal. Chem. 79, 5188–5195 (2007)
36. Y. Wang, I. Ramos, J.J. Santiago-Aviles, Departmental Papers (ESE), 315 (2007)
37. L. Chinnappa, K. Ravichandran, T. Periatthambi, G. Muruganatham, S. Sriram, B. Sakthivel, J. Appl. Sci. 12, 1651 (2012)
38. W. Bergermayer, I. Tanaka, Appl. Phys. Lett. 84, 909–911 (2004)
39. C. Liu, X. Tang, C. Mo, Z. Qiang, J. Solid State Chem. 181, 913–919 (2008)
40. A. Das, V. Bonu, A.K. Prasad, D. Panda, S. Dhara, A.K. Tyagi, J. Mater. Chem. C 2, 164–171 (2014)
41. K. Melghit, K. Bouziane, Mater. Sci. Eng. B 128, 58–62 (2006)
42. K. Melghit, K. Bouziane, J. Am. Ceram. Soc. 90, 2420–2423 (2007)
43. R. Liu, Y. Huang, A. Xiao, H. Liu, J. Alloys Compd. 503, 103–110 (2010)
44. Y.-H. Cui, Y.-J. Feng, J. Liu, N. Ren, J. Hazard. Mater. 239–240, 225–232 (2012)
45. E.E. Bamuza-Pemu, E. Chirwa, Chem. Eng. Trans. 35, 1333 (2013)
46. A.M. Peiro', J.A. Aylo'n, J. Peral, X. Dome'nech, Appl. Catal. B 30, 359–373 (2001)
47. A.M. Al-Hamdi, M. Sillanpa'a', J. Dutta, J. Alloys Compd. 618, 366–371 (2015)

Publication VI

A. M. AHamdi, Uwe Rinner, Mika Sillanpää

Tin dioxide as a photocatalyst for water treatment: A review

Reprinted with permission from
Process Safety and Environmental Protection
Vol. 107, pp. 190-205, 2017
© 2017, Elsevier



Contents lists available at [ScienceDirect](http://www.sciencedirect.com)

Process Safety and Environmental Protection

journal homepage: www.elsevier.com/locate/psep

IChemE ADVANCING CHEMICAL ENGINEERING WORLDWIDE

Tin dioxide as a photocatalyst for water treatment: A review



Abdullah M. Al-Hamdi^{a,b,*}, Uwe Rinner^b, Mika Sillanpää^a

²⁶ ^a Laboratory of Green Chemistry, Lappeenranta University of Technology, Sammonkatu 12, 50130 Mikkeli, Finland

^b Department of Chemistry, Sultan Qaboos University, P.O. Box 17, 123 Al-Khouldh, Oman

ARTICLE INFO

Article history:

Received 16 October 2016

Received in revised form 19 January 2017

Accepted 24 January 2017 Available online 3 February 2017

Keywords:

Tin(IV) oxide
Photodegradation
Photocatalysis
SnO₂ doping

ABSTRACT

Many phenols, phthalates and other toxins are released into the environment from industrial or agricultural processes, or household waste. These compounds are often stable and difficult to degrade in wastewater facilities, thus posing a serious long-time risk. The development of novel and efficient technologies for the environmentally sustainable removal of these dangerous compounds from different sources is of crucial importance. The photocatalytic oxidation of organic pollutants in the presence of semiconductors such as tin(IV) oxide (SnO₂) is a green technology and seems to be a highly promising technique for water treatment and for the removal of recalcitrant compounds. The photocatalytic efficiency of SnO₂ can be enhanced via modifications in the design of the metal oxide, resulting in a lower recombination rate of electron–hole pairs and an increase in the efficiency of the semiconductor during the excitation state, which allows the degradation process of toxins to proceed under UV or visible light irradiation. This review article summarizes some of the most relevant investigations and fundamental aspects related to SnO₂ and its activity and discusses recent achievements in the modification of SnO₂ as a photocatalyst for phenol degradation.

© 2017 Institution of Chemical Engineers. Published by Elsevier B.V. All rights reserved.

Contents

1. Introduction	191
2. Structure and properties of SnO ₂	191
3. Photocatalytic activity of SnO ₂ in water—mechanistic aspects	193
4. Application of undoped SnO ₂ in the photocatalytic degradation of organic pollutants	193
5. Improving SnO ₂ photodegradation efficiency	193
5.1. Improving photodegradation efficiency by selective doping of SnO ₂	194
5.1.1. SnO ₂ coupled with other semiconductors	194
5.1.2. SnO ₂ doped with metals and metalloids	195
5.1.3. SnO ₂ doped with non-metals	198
6. Parameters affecting the photodegradation of organic pollutants in aqueous dispersion of SnO ₂	198
6.1. Catalyst loading	198
6.2. Contaminant concentration	199
6.3. Effect of the pH of the solution	199

* Corresponding author at: Laboratory of Green Chemistry, Lappeenranta University of Technology, Sammonkatu 12, 50130 Mikkeli, Finland.

E-mail addresses: Abdullah.Al.Hamdi@lut.fi, alhamdi@sq.edu.om (A.M. Al-Hamdi).
<http://dx.doi.org/10.1016/j.psep.2017.01.022>

0957-5820/© 2017 Institution of Chemical Engineers. Published by Elsevier B.V. All rights reserved.

6.4. Temperature	200
6.5. Light intensity and wavelength	200
6.6. Crystallinity and surface area	200
7. Conclusion	200
Acknowledgement	201
References	201

1. Introduction

Organic toxins are produced in numerous processes and released in often substantial quantities from industrial and agricultural plants or household waste (Michalowicz and Duda, 2007; Peng et al., 2008; Phipps et al., 1981). Many of these compounds have carcinogenic properties and pose an immediate and also long-term threat to our society and the environment in general (Ritter et al., 2002; Sponza, 2003).

Over the last few years, protocols have been developed and applied to remove such toxins from various sources. Most procedures are designed to purify wastewater via coagulation, flocculation, precipitation, adsorption, ion exchange and membrane processing (Sun et al., 2015a). Although great progress has been achieved in this field, many of these techniques are often unfeasible for large-scale applications and many protocols are costly or have other limitations (Zhou and Smith, 2002). Advanced oxidation processes (AOPs) are among the most promising methods for removing organic toxins from water or other sources, even on a large scale (Stasinakis, 2008; Wang and Xu, 2012). The mechanistic rationale behind the application of AOPs is to create reactive hydroxyl radicals (OH^\cdot) on the catalyst surface, which then oxidatively degrade the toxins present in the sample. In most cases, the catalysts have well characterized properties and display diverse oxidative behavior when exposed to light (Maciel et al., 2004). Such photocatalytic protocols are extremely effective as the intermediary formed hydroxyl radical has an oxidation potential of 2.8 V, which is even higher than the oxidation potential of hydrogen peroxide (H_2O_2) and only slightly smaller than the potential of fluorine (F_2) as outlined in Table 1 (Bamuza-Pemu, 2014).

Many scientists have used photocatalysis to tackle environmental problems and to remove hazardous chemicals from various sources. This innovative field of research was pioneered by Fujishima, who reported the photo-electrochemical degradation of water on a TiO_2 electrode upon exposure to UV irradiation as early as 1972 (Fujishima, 1972). Since then, many groups have been active in this field of research and many protocols and processes have been developed.

A variety of (different) light sources has been employed in photo-degradation studies. Many studies focus on the utilization of UV light as it possesses sufficient energy to generate electron hole pairs ($e^- - h^+$) within the catalyst, which trigger the formation of radicals and the oxidative degradation of the pollutants. Most research groups have used mercury vapor lamps, which mainly emit UV radiation at $\lambda = 253.7$ nm (UV-C) (Brickner et al., 2003). However, mercury vapor lamps have a short life span and are quite expensive during operation and their environmentally benign disposal is costly. Xenon lamps, which show emission at 240 nm are more practical although accumulation of ozone has been reported when these lamps are operated for prolonged periods (Miller et al., 2013). The least expensive source of UV radiation is sunlight, which accounts for about 4–5% of radiation in the UV-region of the electromagnetic spectrum with sufficient energy

Table 1-Oxidation potential

Oxidant	Oxidation potential (V)
Fluorine (F_2)	3.03
Hydroxyl radical (OH^\cdot)	2.80
Ozone (O_3)	2.07
Hydrogen peroxide (H_2O_2)	1.78
Potassium permanganate (KMnO_4)	1.68
Chlorine (Cl_2)	1.36

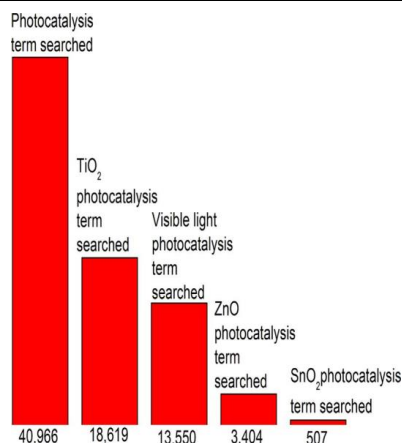


Fig. 1 – Representative search terms for the application of photocatalysis.

(source: Scopus, January 2017) to produce reactive radicals (Thompson and Yates, 2006). Additionally, this source seems unlimited as in only 60 min the solar energy impact on our planet equals the total energy consumption of humankind in one year (Lewis, 2007). Applications of photocatalytic processes with sunlight have attracted considerable attention and have been reviewed elsewhere (Kudo and Miseki, 2009).

Various metal oxides have been investigated and evaluated as potential photocatalysts. The most prominent examples are titanium dioxide (TiO_2), zinc oxide (ZnO), and tin(IV) oxide (SnO_2). The great interest in the development of active photocatalysts is evidenced by the vast number of research publications presented over the last few years. The result of a literature search with relevant keywords is summarized in Fig. 1 (source: Scopus, January 2017). According to this survey; approximately 40,966 papers on the application of TiO_2 and ZnO as photocatalyst have been reported with the majority dealing with TiO_2 . SnO_2 has received less attention (approximately 500 research papers) despite the great advantages of this material and the complete absence of secondary pollution due to photoerosion.

The purpose of this review article is to summarize significant developments in the field of SnO_2 -mediated photooxidation of pollutants and to draw attention to this environmentally friendly and sustainable method. Following a brief outline of the structural properties of SnO_2 , a section is devoted to the discussion of possible modifications to improve the efficiency of the photocatalyst, followed by a summary of parameters responsible for the degradation of phenol in aqueous solution. Because of the limitations of this review, results obtained with other photocatalysts are omitted and the reader is referred to recent review articles (Lazar et al., 2012; Lee et al., 2016; Teh and Mohamed, 2011).

2. Structure and properties of SnO_2

Tin(VI) oxide or stannic oxide (not to be confused with stannous oxide with tin in the oxidation state of 2+ (Batzill and Diebold, 2005)), also known as cassiterite (He and Zhou, 2013),

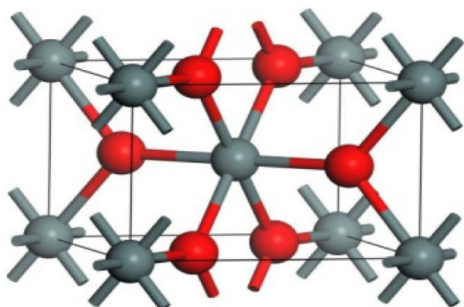


Fig. 2 – SnO₂ unit cell structure (Ben Mills (Public Domain) Rutile structure, 07.01.2016. <https://en.wikipedia.org/wiki/Rutile#/media/File:Rutile-unit-cell-3D-balls.png>).

Table 2 – Properties of SnO₂ (Chaisitsak, 2011; Du et al., 2010).

Crystal structure	Rutile structure
Lattice constant	a = 0.47374 nm and c = 0.31864 nm
Molecular weight	150.69 g/mol
Density	6.90 g/mol
Melting point	1500–1630 °C
Boiling point	1800–1900 °C

is an amphoteric colorless solid. This inorganic compound shows high optical transparency and high reflectivity in the infrared region and the material is characterized by its good chemical and thermal stability (Bouras et al., 2014; Yadav et al., 2014). Because of these properties, SnO₂ has been considered for many applications. Among others, the material was evaluated as a catalyst, as a sensor, and as a raw material for transparent films, infra-red mirrors or optoelectronic devices (Anandan and Rajendran, 2015b). Also, the strongly oxidizing properties make the oxide an ideal tool for the elimination of pollutants from water and many other sources.

The crystal structure type of SnO₂ is similar to the rutile phase structure of TiO₂ (Dou and Persson, 2013) (dimensions of the unit cell: a = b = 0.47374 nm and c = 0.31864 nm, polar crystal with octahedral and space group no. 136 P4₂/mmm (Yu et al., 2015)). In one unit cell, the tin(IV) ion is surrounded by 6 oxygen ions and every oxygen is bordered by 3 tin(IV) ions, resulting in a (6, 3) coordination structure (Entradas et al., 2014) as shown in Fig. 2.

The discovery of the photocatalytic properties of TiO₂ also led to a range of proposals for photocatalytic applications of related oxides. The high photosensitivity and thermostability, as well as their low cost and toxicity made ZnO and SnO₂ valuable alternatives as photocatalysts (Chaisitsak, 2011; Morimitsu et al., 2000; Rakibuddin and Ananthakrishnan, 2016). The octahedral network is considered a prerequisite for high photocatalytic activity because it increases the mobility of e⁻–h⁺ pairs and consequently affects the probability of their reaching the reaction sites on the surface of the photocatalyst (Abe et al., 2006; Madelung et al., 1998).

Some of the physicochemical characteristics of SnO₂ are summarized in Table 2.

Generally in semiconductors the lower energy band (conduction band, CB) is packed with electrons while the upper band (valence band, VB) is free of electrons. The energy dif-

Table 3 – Band gap of selected photocatalysts (Bamuza-Pemu, 2014; Kruefu et al., 2012; Low et al., 2008; Yu et al., 2010; Zhang et al., 2005).

Photo-catalyst	Band-gap energy (eV)
Si	1.1
TiO ₂ (rutile)	3.0
SnO ₂	3.6
WO ₃	2.7
ZnS	3.7
ZnO	3.3
TiO ₂ (anatase)	3.2
SnO	~2.5–3.0
CdS	2.4
ZnO	3.2

ference between these bands, also called the energy band gap (E_{bg}), is responsible for the electronic properties of the material (Linsebigler et al., 1995). Together with the Fermi level (hypo-theoretical energy level of electrons), the band gap is an important parameter for describing the potential of a material to act as semiconductor (Van Eldik and Hubbard, 2009). Generally less energy is required to excite electrons if the energy band gap between CB and VB decreases.

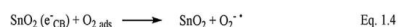
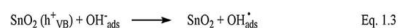
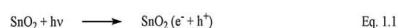
The electronic properties of semiconductors are also, and to a much greater extent, determined by the presence of small amounts of impurities in the lattice structure of the metal oxide. These impurities either create an excess of free holes (p-type semiconductor) or free electrons (n-type semiconductor) (Kim et al., 2012). The doping process changes the Fermi level by shifting the CB in the n-type or the VB in the p-type semiconductor, and thus narrows the E_{bg} . As a consequence, less energy is required to generate excited electrons and photocatalytic activity can be observed upon irradiation of the catalyst with electromagnetic radiation in the visible range (Mete et al., 2009; Sun et al., 2016).

The electrical conductivity of SnO₂ can moreover be attributed to the presence of the inherent defects in the metal oxide (Zhang et al., 2014). Such defects contribute to a significant narrowing of the E_{bg} band, thus improving the properties of the material as a semiconductor. In this respect, additional oxygen anions trigger the oxidation of Sn²⁺ to Sn⁴⁺ in order to maintain the overall electrical neutrality (Sanal and Jayaraj, 2013; Zulfiqar et al., 2016).

The large band gap energy of SnO₂ of 3.6 eV, which corresponds to photoactivation in the UV range of the electromagnetic spectrum, makes this material, as well as ZnO and SiO₂, ideal photocatalysts for the degradation of a variety of organic pollutants (Ahmed et al., 2011). Modification of the metal oxides reduces the band gap energy and electromagnetic radiation with lower energy can be utilized for the activation of the catalyst. The band gaps of silicon and a variety of metal oxides are shown in Table 3 (Kruefu et al., 2012; Low et al., 2008).

In summary, SnO₂ combines many positive properties, such as low electrical resistance, high electrical conductivity and high optical transparency in the visible region of the electromagnetic range and the material has found many useful applications (Mistry et al., 2016). In addition to the application as a catalyst for the degradation of organic toxins, the high affinity of the metal oxide towards CO and H₂ promotes its use as a sensing material (Yamazoe and Miura, 1992).

Also, in comparison to other semiconductors, SnO₂ photo-anodes have many advantages in materials like dye synthesized solar cells, which are characterized by high



Scheme 1 – Formation of reactive radical intermediates during the photoactivation of SnO₂.

recombination resistances, faster charge transport, and more efficient charge separation size distributions, all of which make important contributions to the physical properties of the oxide (Azam et al., 2010; Xi and Ye, 2010).

3. Photocatalytic activity of SnO₂ in water—mechanistic aspects

As noted above, SnO₂ is often characterized by oxygen vacancies which enhance its properties as an n-type semiconductor. Because of the band gap of 3.6 eV, corresponding to activation with photons of a wavelength of 350 nm (UV-A range), the material is perfectly suited as a photocatalyst (Bhattacharjee and Ahmaruzzaman, 2015).

When exposed to light of sufficient energy, $e^- - h^+$ pairs are generated which trigger the oxidative degradation of organic molecules. Because of the high stability and low toxicity of insoluble SnO₂, the metal oxide can be utilized in the decomposition of environmentally harmful compounds and toxins in waste water (Al-Hamdi et al., 2016b). Over the last few years, many researchers have explored the application of photocatalysts for the purification of water and developed sustainable protocols for the photodegradation of phenols and other pollutants (Bhatkhande et al., 2002; Yawalkar et al., 2001).

The overall process is illustrated in Scheme 1 in abbreviated and simplified form (Al-Hamdi et al., 2015a). The route commences with the activation of the photocatalyst and the formation of $e^- - h^+$ pairs (Eq. 1.1). These $e^- - h^+$ pairs migrate to the surface of the metal oxide and generate highly reactive radicals. While h^+ is capable of generating hydroxyl radicals, either via the reaction of adsorbed water (Eq. 1.2) or hydroxyl anions (Eq. 1.3), e^- triggers the formation of peroxy radical anions (and hydroperoxyl radicals, Eq. 1.4) upon reaction with dissolved oxygen (Bielski et al., 1985). These radical anions are then protonated and form highly reactive hydroperoxyl radicals in the presence of H^+ (Eq. 1.5) or H_2O (Eq. 1.6) (Gaya and Abdullah, 2008).

Ultimately, organic toxins are converted into CO₂ and H₂O upon reaction with the abovementioned reactive species via a cascade of reactions. The process is shown in Eq. 1.7 in highly abbreviated form. The overall process is schematically outlined in Fig. 3.

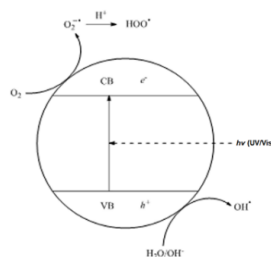


Fig. 3 – Schematic representation of the oxidation process taking place on the crystal surface (Herrmann, 1999; Yang et al., 2010).

4. Application of undoped SnO₂ in the photocatalytic degradation of organic pollutants

Although most applications take advantage of doped SnO₂ in the photodegradation of organic pollutants, some examples have been reported that demonstrate the ability of the pure, undoped material in the photocatalytic process. Although the process is highly efficient, UV light must be used to activate the metal oxide as visible light does not have sufficient energy to trigger the formation of $e^- - h^+$ pairs because of the large band gap energy of pure SnO₂. Recent examples are summarized below.

SnO₂ nanocrystals, synthesized from amino-acid chelated tin salts were employed in degradation studies of rhodamine B. This combination resulted in a close to 100% decrease of the rhodamine B concentration after irradiation of the sample for 150 min (Tammina and Mandal, 2016; Wu et al., 2009). Similar results were also obtained when nanocrystalline SnO₂ particles prepared from tin oxalate using an eggshell membrane were used for the rhodamine B degradation. The authors reported an excellent 95% decrease in the concentration of the dye after exposure of the solution to UV light for 1 h (Sangami and Dharmaraj, 2012). Undoped SnO₂ nanoparticles were also successfully employed in the oxidative degradation of methylene blue, eosin Y (Diallo et al., 2016), congo red (Haritha et al., 2016) and violet 4 dye (Tammina and Mandal, 2016).

The applications of undoped SnO₂ are summarized in Table 4.

5. Improving SnO₂ photodegradation efficiency

Despite the great potential of SnO₂ semiconductors for photocatalytic applications, the practical applicability of the pure material is limited due to the high activation energy of the compound (equivalent to irradiation with UV light) and the swift recombination rate of the photogenerated electrons (e^-_{CB}) and electron holes (h^+_{VB}) (Yang et al., 2010). In order to facilitate industrial applications, and to enhance the photocatalytic activity, the recombination of the $e^- - h^+$ pairs needs

to be inhibited (Stengl et al., 2009). One possibility is to add

Table 4 – Some selected photocatalytic activities of SnO₂.

Pollutant	Light source	Experimental conditions	Results	Ref.
RhB	250 W Hg lamp, > 365 nm	C: 50 mg/50 mL; P: 1.0×10^{-5} M	Excellent photocatalytic activity; small particle size of SnO ₂	Wu et al. (2009)
RhB	UV	Different conc. of SnO ₂ ; P: 1.0×10^{-6} M	94% degradation after 60 min	Sangami and Dharmaraj (2012)
MB; Eosin Y; Congo red	UV	C: 2.5×10^{-6} M SnO ₂ ; P: 2.7×10^{-6} M	50% degradation after 20–30 min	Diallo et al. (2016)
Congo red	> 365 nm	C: 0.25 g SnO ₂ ; P: 1.0×10^{-6} M	Pseudo 1st order; rate k = 0.9212	Haritha et al. (2016)
Violet 4 BSN dye	125 W UV lamp, 254 nm	C: 10 mg SnO ₂ ; P: 25 mg/L	100% degradation of the dye in 40 min	Tammina and Mandal (2016)

Abbreviations: rhodamine B: RhB; methylene blue: MB; concentration of catalyst: C; concentration of pollutant: P.

other semiconductors to the metal oxide with different elec-tron gap energies. Ideally, the doped material then shows an enhanced photocatalytic activity due to the decreased recom-bination rate of $e^- - h^+$ pairs and the lower activation energy (Tojo et al., 2008; Kovács et al., 2015).

The method used to prepare the doped material has a significant influence on the photocatalytic properties of the material (Cristante et al., 2007). However, external parameters also significantly alter the overall efficiency of the photocat-alytic process. In this respect, the temperature of the reaction mixture (Chong et al., 2010), the pH of the aqueous solution (Anju et al., 2012), and the light intensity or the wavelength of the photon source are important factors which need to be carefully optimized (Cassano and Alfano, 2000).

The following section is devoted to a discussion of possi-ble strategies to improve the properties of the metal oxide to guarantee enhanced catalytic activity.

5.1. Improving photodegradation efficiency by selective doping of SnO₂

5.1.1. SnO₂ coupled with other semiconductors

The photocatalytic activity of SnO₂ is significantly improved when the metal oxide is doped with either short or wide band gap semiconductors (Srinivasan and Bandyopadhyaya, 2016). SnO₂ has frequently been used in combination with TiO₂ semi-conductors (Xiong and Balkus, 2007). Vinodgopal and Kamat (1995) reported the successful photodegradation of an azo dye (acid orange 7) in the presence of doped SnO₂. The group found a ratio of SnO₂ to TiO₂ of 2:1 to be most effective for the degradation process (Vinodgopal and Kamat, 1995). Peng et al. (2008) synthesized SnO₂/TiO₂ nanotubes with different SnO₂ concentrations and were able to show that the composite material allowed an increased absorption of methylene blue on the catalyst surface, resulting in enhanced catalytic activity of the metal oxide (Hou et al., 2007). The best photocatalytic activity was achieved when a 5 wt.% of SnO₂ suspension of nanotubes was used. Similar results with methylene blue as pollutant were also reported by Sang and co-workers (Tu et al., 2009). Additionally, comparable SnO₂/TiO₂ composite material also showed good results for the degradation of rhodamine B (Abdel-Messih et al., 2013).

The increased activity of the composite material could be explained by directing electrons from TiO₂ into the CB of SnO₂ and the simultaneous migration of the photogenerated elec-tron holes (h^+) into the VB of TiO₂. This enhanced charge separation then results in an increased oxidizing power of TiO₂ and the composite material (Tu et al., 2009).

ZnO doped SnO₂ nanocomposite material was investigated for its photocatalytic activity in the degradation of methyl orange under UV light irradiation. The authors reported that the calcination temperature strongly affected the particle size and further that the composite material showed better pho-tocatalytic activity for the degradation of methyl orange than either semiconductor alone (Zhang et al., 2005).

Mesoporous SnO₂ doped with ZnO (m-SnO₂/ZnO) was investigated for its activity in the photocatalytic oxidation of rhodamine B under UV-irradiation. Again, the results showed that the photocatalytic activity of m-SnO₂/ZnO was higher than that of m-ZnO (Wen et al., 2007). Even a low concentration of ZnO produced a significantly positive effect on the photocat-alytic properties of SnO₂. The improved photocatalytic activity in the degradation of the dye under UV light irradiation could be explained by the formation of a ZnO/SnO₂ hetero-junction which triggered the separation of $e^- - h^+$ pairs (Zhang et al., 2010).

Wang, Xu, and co-workers prepared a ternary mixture of ZnO, TiO₂, and SnO₂ and tested the material for its pho-tocatalytic properties in the degradation of methyl orange. The mixture showed enhanced activity compared to that of pure metal oxides. The photocatalytic activity of the mix-ture decreased when the calcination temperature exceeded 700 °C due to the formation of photoinactive ZnTiO₄, Zn₂SnO₄, and Zn₂Ti_{0.5}Sn_{0.5}O₄. When heated to 1300 °C for a prolonged time, the mixture completely lost its photocatalytic properties (Wang et al., 2005).

All results discussed above are summarized in Table 5.

In 2013, Gambhire reported the preparation of Cr₂O₃/SnO₂ nanocomposite (Bhosale et al., 2013). The material was suc-cessfully employed in the photocatalytic decomposition of rhodamine B. Zhuang and co-workers explored the photocat-alytic activity of Fe₂O₃/SnO₂ nanocomposite material. During this investigation, a sample of acid blue 62 was irradiated with visible light (> 400 nm) for 3 h. The researchers found that samples with a molar ratio of iron to tin of 2:1 showed the highest photocatalytic activity. Also, the photocatalytic activ-ity increased markedly as particle size decreased and was highest for particles with a diameter of 15 nm (Xia et al., 2008). SnO₂/a Fe₂O₃ showed enhanced photocatalytic ability under visible or UV irradiation when compared to pure a Fe₂O₃ (Niu et al., 2010). The same effect was observed for SnO₂/V₂O₅ nanowires, which showed higher photocatalytic activity for the degradation of the dye under UV light than pure V₂O₅ (Shahid et al., 2010). Again, this improved photocatalytic per-formance was attributed to the increase in the surface area of the couple structure and the effective charge separation of

Table 5 – Improved SnO₂ photocatalytic efficiency by TiO₂ and ZnO semiconductors.

Catalyst	Light source/pollutant	Experimental conditions	Photodegradation efficiency	Ref.
SnO ₂ /TiO ₂	250 W Xe lamp; P: acid orange 7	C: 0.54 mg/cm ² ; P: 1.2 × 10 ⁻⁴ mol/L	The coupled oxide enhanced the rate of photocatalytic degradation of the dye more than pure oxide	Vinodgopal and Kamat (1995)
SnO ₂ /TiO ₂	2 × 30 W UV lamps; P: MB	C: 0.05 g/100 mL; P: 5 × 10 ⁻⁵ mol/L	TiO ₂ doped with 5 wt.% SnO ₂ showed best photocatalytic activity	Hou et al. (2007)
TiO ₂ /SnO ₂	300 W Hg lamp; P: MB	C: 0.05 g/100 mL; P: 2 × 10 ⁻⁵ mol/L	TiO ₂ doped with 5.6% Sn showed best photocatalytic activity	Tu et al. (2009)
SnO ₂ /TiO ₂	UV lamp; P: RhB	C: 0.1 g/100; P: 1 × 10 ⁻⁵ mol/L	70% more degradation than with pure oxide; about 92% more decolorization for RhB	Abdel-Messih et al. (2013)
ZnO/SnO ₂	UV Hg lamp; P: MO	C: 0.25 g/100 mL; P: 20 mg/L	The calcination temperature affected the particle sizes.	Zhang et al. (2005)
ZnO/SnO ₂	500 W Xe lamp; P: RhB	C: 0.01 g/10 mL; P: 1 × 10 ⁻⁵ mol/L	The coupled semiconductor exhibited higher photocatalytic activity than pure ZnO or SnO ₂	Wen et al. (2007)
ZnO/SnO ₂	50 W Hg lamp; P: RhB	P: 100 mL/10.0 ppm	Increased photocatalytic activity of ZnO/SnO ₂ nanofibers	Zhang et al. (2010)
ZnO/TiO ₂ /SnO ₂	500 W Hg lamp; P: MO	not available	Greatly increased photocatalytic activity	Wang et al. (2005)

Abbreviations: rhodamine B: RhB; methyl orange: MO; methylene blue: MB; concentration of catalyst: C; concentration of pollutant: P.

SnO₂/V₂O₅. SnO₂ was also shown to have a positive effect on the photocatalytic activity of Cu₂O for wastewater treatment (Du et al., 2010). Moreover, a comparative study suggested that CuO/TiO₂/SnO₂ catalysts exhibited much higher catalytic activity than CuO/TiO₂ and CuO/SnO₂ catalysts (Li et al., 2009).

Zhuang and co-workers also prepared a CuO/SnO₂ nanocomposite for the photodegradation of acid blue 42 under xenon light irradiation. The highest photocatalytic activity was achieved when a mixture of CuO and SnO₂ in a molar ratio of 1:1 was calcined at 500 °C for 1 h as the material obtained from this process was characterized by a high surface area (Xia et al., 2007).

Zhang and co-workers developed a visible-light driven SnS₂/SnO₂ nanocomposite photocatalyst. The material showed highly promising photocatalytic properties when tested for the degradation of methyl orange and was superior to SnS₂ or SnO₂ nanoparticles or physically mixed SnS₂/SnO₂ particles. The significant catalytic activity was explained by the matched band potentials of both semiconductors but slightly narrower band gap of SnS₂, which triggers the transfer of electrons from the CB of SnS₂ to SnO₂ after photoactivation (Zhang et al., 2011).

Foletto prepared CeO₂/SnO₂ nanocomposites and investigated the catalytic potential of the material in the degradation of an azo dye under irradiation with sunlight in an aqueous solution (Foletto et al., 2012). A combination of Cr₂O₃/SnO₂ was also confirmed to be a highly effective photocatalyst as the concentration of rhodamine B decreased by 98% when an aqueous solution was exposed to sunlight for 60 min. The activity of this nanocomposite was shown to be significantly higher (approximately 3.5 fold) than the activity achieved with the standard P25 photocatalyst (Bhosale et al., 2013).

A novel visible-light-driven SnS₂/SnO₂ nanocomposite catalyst was described by Zhang and co-workers. The group employed this material in the oxidative degradation of methyl

orange. Combining CdS with a small band gap of 2.4 eV with SnO₂ with a band gap of 3.6 eV was also found to be beneficial. The photocatalytic activity for the oxidation of benzyl alcohol to benzaldehyde under visible light irradiation was higher than for the pure semiconductors because of the improved e⁻-h⁺ pairs separation and the extended lifetime of electrons and electron holes (Liu et al., 2015). Coupling BiOCl with SnO₂ nanoparticles, prepared via a two-step route, also showed enhanced photocatalytic activity for the degradation of rhodamine B under visible light irradiation (Sun et al., 2015b).

Some of the most promising results discussed above are summarized in Table 6.

Finally, as a last example in this section, an application of SnO₂-based nanocomposites in biological studies is highlighted. Karakas and co-workers investigated the photocatalytic antimicrobial activity of Pd on both SnO₂ and TiO₂ thin film samples against *Escherichia coli* (*E. coli*), *Staphylococcus aureus* (*S. aureus*), *Saccharomyces cerevisiae* (*S. cerevisiae*) and *Aspergillus niger* (*A. niger*) spores. The results indicated higher antimicrobial activity of TiO₂ than of SnO₂. However, the addition of Pd enhanced the activity of both metal oxides. The photocatalytic antimicrobial efficiency for different microorganisms and spores decreased in the order *E. coli* > *S. aureus* > *S. cerevisiae* > *A. niger* (Erkan et al., 2006).

5.1.2. SnO₂ doped with metals and metalloids

In recent years numerous applications of SnO₂ doped with metal ions have been reported. The following section provides an overview of these efforts. For ease of reading, this section is divided into applications of SnO₂ doped with metalloids, transition metals, and rare earth elements.

5.1.2.1 SnO₂ doped with metalloids. Antimony is one of the most commonly used n-type dopants for SnO₂, especially for the preparation of n-type SnO₂ thin film and the

Table 6 – Improved SnO₂ photocatalytic efficiency by coupled semiconductors.

Catalyst	Light source/pollutant	Experimental conditions	Photodegradation efficiency	Ref.
Cr ₂ O ₃ /SnO ₂	Sunlight; P: RhB	C: 0.5 g/L; P: 0.5 g/L	98.0% degradation under visible light irradiation	Bhosale et al. (2013)
SnO ₂ /Fe ₂ O ₃	1000 W Xe lamp; P: acid blue 62	P: 50 mg/L;	98.0% of Acid blue 62 in 60 min under visible light at > 400 nm.	Xia et al. (2008)
SnO ₂ /aFe ₂ O ₃	4 W UV lamps; P: MB	C: 50 mg/150 mL; P: 1 x 10 ⁻⁵ mol/L	High activity of catalyst under visible or UV irradiation	Niu et al. (2010)
SnO ₂ /V ₂ O ₅	SnO ₂ /V ₂ O ₅ . P: toluidine blue "O"	C: 15 mg/50 mL; P: 0.5 mmol	High activity of nanowires	Shahid et al. (2010)
SnO ₂ /Cu ₂ O	400 W Hg lamp; P: trifluralin	C: 50 mg/80 mL; P: 50 mg/L	High activity of nanocrystals	Du et al. (2010)
SnS ₂ /SnO ₂	1000 W Xe lamp; P: acid blue 62	C: 300 mg/L; P: 40 mg/L	High activity of nanocrystals	Zhang et al. (2011)
CdS/SnO ₂	300 W Xe lamp; P: benzyl alcohol	C: 50 mg/20 mL CH ₃ CN	Oxidation of benzyl alcohol to benzaldehyde	Liu et al. (2015)
BiOCl/SnO ₂	500 W Xe lamp; P: RhB; MO; MB	C: 25 mg/L; P: 0.01 mol/L	high photocatalytic activity for RhB degradation under visible light irradiation	Sun et al. (2015b)

Abbreviations: rhodamine B: RhB; methyl orange: MO; methylene blue: MB concentration of catalyst: C; concentration of pollutant: P.

properties of these mixtures have been thoroughly studied (Fadavieslam, 2016). Because of their comparable ionic radii (Sn⁴⁺ ~ 0.071 nm and Sb⁵⁺ ~ 0.065 nm), pentavalent Sb⁵⁺ ions can replace tetravalent Sn⁴⁺ ions, especially at low concentrations of antimony (Al-Hamdi et al., 2016a). The addition of Sb results in an excess of electrons and improved electrical conductivity (Li et al., 2015; Shanthi et al., 1999) and significantly modifies the band structure of SnO₂ (Mishra et al., 1995). Sb doped SnO₂ showed typical n-type conductivity with a wide optical gap and a high charge carrier density. Doping SnO₂ with antimony can also enhance the photocatalytic activity by slowing down the recombination rate of e⁻-h⁺ pairs. Antimony acts as an e⁻-h⁺ pair trap, leading to an increased charge separation in the photocatalyst. The Sb/SnO₂ nanocomposite displayed lower resistance, and remained transparent at a wavelength that included the visible and the UV regions (Assia and Ratiba, 1999). Borrás et al. (2006) described the oxidation of *p*-methoxy-phenol (PMP) in aqueous solution in the presence of antimony doped SnO₂ and observed the formation of CO₂ (Borrás et al., 2006). In another study, the photocatalytic activity of 0.6 wt% Sb doped SnO₂ was investigated in the degradation of phenol under irradiation with sunlight (Al-Hamdi et al., 2016a).

Other scholars used nickel for doping on the doped Sb/SnO₂ electrodes, and the products were investigated for the electrochemical degradation of toxic organic compounds. Enhancement of the electrodes was attributed to the production of highly reactive hydroxyl radicals (Wang et al., 2006).

Results discussed above are summarized in Table 7.

5.1.2.2. SnO₂ doped with transition metals. Doping semiconductors with metal ions is one of the best ways of improving visible light photocatalytic activity for the oxidative degradation of organic compounds (Kim et al., 2005). Many transition metals have been used to modify the electronic properties of SnO₂. The most frequently tested transition metals for this purpose include gold, manganese, silver, cobalt, and iron. A representative overview of results obtained with these elements is provided below.

Sn²⁺ doped SnO_{2-x} nanocrystals are tremendously active photocatalysts for the photodegradation of organic pollutants.

Xu and co-workers used this self-doped material for the degradation of methyl orange under visible light irradiation. As Sn²⁺ replaces Sn⁴⁺ ions in the rutile structure, oxygen vacancies are generated to maintain the overall neutral charge of the metal oxide, thereby reducing the band gap energies and facilitating activation of the photocatalyst with visible light (Fan et al., 2013).

A recent study by Guang and co-workers confirmed that the temperature during the calcination process has a major effect on the photocatalytic properties of doped SnO₂ nanocrystals. As the calcination temperature increased, the photocatalytic properties of the nanomaterial were observed to decrease.

Small amounts of transition metal ions (and also rare earth elements) such as manganese, Mn²⁺ (or cerium, Ce³⁺) helped to increase the oxygen vacancies (Anandan and Rajendran, 2015a), resulting in enhanced electronic properties and the luminescence activity of the semiconductor (Gu et al., 2004). Such modifications with inexpensive additives will help eventually to develop cost-efficient photocatalysts for industrial applications characterized by the required narrow energy band gaps, good optical absorption quality, high chemical stability, and high surface area.

Another additive proven to significantly enhance the photocatalytic activity of SnO₂ is gold. Mulvaney and co-workers confirmed that gold-coated SnO₂ particles were suitable catalysts as the dopant attracts electrons, resulting in a more efficient charge distribution in the material (Oldfield et al., 2000). Wu and his group applied gold doped SnO₂ hybrid nanostructures and confirmed the increased photocatalytic activity of the doped catalyst for the degradation of the organic dye rhodamine B. Importantly, the photocatalyst was characterized by an increased surface area and showed enhanced absorption of visible light (Wu et al., 2013). Yang, Wang, and co-workers prepared gold doped SnO₂ nanoparticles and used the material for the photocatalytic degradation of rhodamine 6G (R6G). Again, the authors could demonstrate the superior properties of the nanocomposite due to the e⁻-h⁺ separation at the SnO₂/Au interface and the high specific surface area (You et al., 2013).

Cho and co-workers used silver in the preparation of photocatalytically enhanced SnO₂ nanocomposites using an

Table 7 – Improved SnO₂ photocatalytic efficiency by Sb doped SnO₂ semiconductors.

Catalyst	Light source/pollutant	Experimental conditions	Photodegradation efficiency	Ref.
Sb/SnO ₂	Electrode potential; P: PMP	P: 0.1 M	Decreased degradation rate with increasing pollutant concentration	Borras et al. (2006)
Sb/SnO ₂	UV light solar light phenol	C: 65 mg/50 mL; P: 10 ppm	Highly photocatalytic degradation and indication of mineralization process	Al-Hamdi et al. (2016a)
Ni/Sb/SnO ₂	Potentiostat P: 4-CP	P: 8 mM (1028 mg/L)	High activity of doped material because of increased OH [•] formation	Wang et al. (2006)

Abbreviations: 4-chlorophenol: 4-CP; *p*-methoxy phenol: PMP; concentration catalyst: C; concentration of pollutant: P.

electrochemically active biofilm. The material was evaluated in degradation studies of a variety of organic dyes and toxins, such as methyl orange, methylene blue, 4-nitrophenol, and 2-chlorophenol, and showed enhanced activity compared to pure SnO₂ nanostructures upon irradiation with light in the visible region (Ansari et al., 2014).

In addition to narrowing the band gap energies, doping of SnO₂ with transition metals or metalloids also has a major influence on the particle size of the nanocomposites and the surface area. For example, cobalt doped SnO₂ nanoparticles show significantly reduced grain size, concomitantly resulting in an increased photocatalytic activity. Entradas et al. (2014) demonstrated the photocatalytic activity of cobalt doped SnO₂ nanocomposites in the degradation of 4-hydroxybenzoic acid (4-HBA). After irradiation of the sample with UV light for one hour, no perceptible amount of the aromatic compound was found (Entradas et al., 2014).

Zn-doped SnO₂ nanorods used to decompose acid fuchsin showed a much higher degradation rate than the pure nanoparticles (Huang et al., 2012).

Iron doped SnO₂ nanoparticles showed superior behavior when prepared via a sol-gel hydrothermal route, instead of the common sol-gel calcination process. The nanoparticles were characterized by a narrow size distribution and a large specific surface area. The nanoparticles also showed improved thermal stability. With increasing amounts of Fe³⁺, a significant red shift in the UV absorption was observed (Fang et al., 2008), equivalent to the intended decrease of activation energy. When used in degradation studies of organic dyes, nanoparticles containing 5% Fe³⁺ helped to decrease the concentration of the pollutant by 50% after an irradiation time of 2 h (Davis et al., 2013).

Quenching in green luminescence intensity was observed in V doped SnO₂ compared to the undoped control substance. In addition, the sample demonstrated superior photocatalytic activity for degrading methylene blue and rhodamine B (Mazloom et al., 2015). The addition of selenium to SnO₂ resulted in an improved electronic character of the nanomaterial with an decreased energy band gap (Kumar et al., 2016).

All results discussed above are summarized in Table 8.

5.1.2.3. SnO₂ doped with rare earth metals. The addition of rare earth elements to TiO₂ or SnO₂ significantly enhances the photocatalytic properties of the semiconductors. Moreover, the doped metal oxide shows satisfactory catalytic activity even in the visible range of the electromagnetic spectrum (Reszczyńska et al., 2014). One reason for the enhanced catalytic properties is the smaller particle size of doped SnO₂ and the increased surface area as determined by the Brunauer Emmet Teller (BET) method. Additionally, the e⁻-h⁺ pair

recombination is inhibited, resulting in better charge separation and increased formation of reactive species on the surface of the photocatalyst (Reszczyńska et al., 2015). The effects mentioned above are further enhanced as doping results in the formation of defects in the matrix which lower the effective optical band gap energies and increase photocatalytic properties of the semiconductor (Hays et al., 2005).

Besides their application as photocatalysts for the degradation of organic pollutants, rare earth doped semiconductors have also found other useful applications: Some rare earth metals have been used in the production of lasers because of their intense luminescent properties and these compounds serve as fluorescent displays and lamps (Piguet et al., 1993).

The catalytic properties of semiconductors are also closely related to their acid/base characteristics (Carreno et al., 2004). SnO₂ is an acidic oxide, which has an isoelectronic point (iep) between 4 and 7. Rare earth oxides are mostly basic. For example, the iep for La₂O₃ is in the range 10–12 and the iep for Y₂O₃ is approximately 11. The importance of the acid/base properties of the dopant became obvious when La₂O₃ doped SnO₂ was employed as sensor for ethanol gas. The semiconductor became very sensitive to slight changes in the pH and thus to the concentration of ethanol (Harrison and Maunders, 1984; Matsushima et al., 1989). A similar result was also obtained in the oxidation of methanol (Carreno et al., 2002).

Cerium doping has received much attention because the redox couple (Ce³⁺/Ce⁴⁺) enables a shift from RO_x to R₂O_{x+1} (such as CeO₂ to Ce₂O₃) under oxidizing and reducing conditions. Also, the facile formation of oxygen vacancies with their high mobility increases the photocatalytic properties (Li et al., 2005). Furthermore, the combination of incompletely occupied 4f and empty 5d orbitals helps in the formation of e⁻-h⁺ pairs (Liu et al., 2008).

Samarium doped SnO₂ was characterized by an enlarged surface area of the nanoparticles and a decreased band gap, which resulted in the enhanced photocatalytic degradation of different dyes (Singh et al., 2014). Ti/Sb/SnO₂ electrodes were doped with various rare earth metals and applied in degradation studies on organic pollutants. Also, gadolinium and europium were used as dopants for SnO₂ and an increased activity of the photocatalyst was observed. Interestingly, in this study, cerium increased the activity of the catalyst only marginally (Cui et al., 2012).

Al-Hamdi et al. (2014) showed that lanthanum doped SnO₂ was extremely efficient for the light-induced degradation of phenol. After an irradiation time of 2 h with UV-light, more than 95% of the phenol was oxidatively removed from the water sample. The doped material was much more efficient than a pure sample of SnO₂ (Al-Hamdi et al., 2014). Gadolin-

Table 8 – Enhanced photocatalytic activity of SnO₂ by metal doping.

Catalyst	Light source; pollutant	Experimental conditions	Photodegradation efficiency	Ref.
Sn/SnO ₂	300 W Xe lamp; P: MO	C: 50 mg/50 mL; P: 10 mg/L	High activity in visible light	Fan et al. (2013)
Au/SnO ₂	Hg-W lamp; P: RhB	C: 100 mg/40 mL; P: 10 ppm/500 mL	High activity of nanocrystals	Wu et al. (2013)
Au/SnO ₂	300 W Hg; = 365 nm; P: R6G	C: .015 g/50 mL; P: 1 mmol/L	High activity of nanocrystals	You et al. (2013)
Ag/SnO ₂	Visible light irradiation; MO MB 4-NP 2-CP	C: 2 mg/20 mL; P: MO 10 mg/L; MB 10 mL/L; 4-NP: 5 mg/L; 2-Cp: 50 mg/L	High activity of nanocrystals under visible light irradiation	Ansari et al. (2014)
Co/SnO ₂	450 W Hg lamp; P: 4-HBA	C: 3 g/L; P: 10 mg/L	Complete photodegradation of 4-HBA after 60 minutes	Entradas et al. (2014)
Zn/SnO ₂	500 W Hg lamp; P: acid fuchsin	C: 100 mg/L; P: 4 mg/L	Degradation increased 8-fold compared to undoped material; 60 min irradiation	Huang et al. (2012)
Fe/SnO ₂	250 W UV lamp; RhB	C: 25 mg/50 mL; P: 25 mg/L	55% of RhB degraded after 2 hours	Davis et al. (2013)
V/SnO ₂	400 W UV lamp; MB RhB	C: 50 mg/50 mL; P: 30 ppm for both dyes	High activity of nanocrystals	Mazloom et al. (2015)

Abbreviations: 4-hydroxy benzoic acid: 4-HBA; rhodamine B; rhodamine 6G: R6G; methyl orange: MO; methylene blue: MB; 4-nitrophenol: 4-NP; 2-chlorophenol: 2-CP; concentration catalyst: C; concentration of pollutant: P.

ium doped SnO₂ yielded comparable results (Al-Hamdi et al., 2015a).

Lanthanum doped SnO₂ also revealed higher photo-catalytic phenol degradation. Irradiation of the sample with sunlight resulted in a nearly quantitative removal of the pollutant in less than 2.5 h (Al-Hamdi et al., 2016b).

Some of the most promising results discussed above are summarized in Table 9.

5.1.3. SnO₂ doped with non-metals

Many researchers have used TiO₂ nanoparticles co-doped with iodine and fluorine to improve the degradation of organic compounds under visible light irradiation (Wen et al., 2009). Iodine doped TiO₂ was found to exhibit enhanced photocatalytic properties for the oxidative degradation of phenol under UV and visible light irradiation. The nanoparticles exhibited stronger absorption in the 400–550 nm range and were therefore able to efficiently oxidize pollutants at longer wavelengths (Hong et al., 2005). The catalytic efficiency of the doped material was also increased when SnO₂ was added to the composite material (He et al., 2011).

While Sb doped SnO₂ shows typical n-type conductivity with a wide optical gap of >4 eV (larger than undoped SnO₂) and a high charge carrier density, iodine doped SnO₂ has isolated gap states below the Fermi energy consisting of the oxygen 2p and the tin 5s orbitals, which narrowed the optical band gap to 3.5 eV (Behtash et al., 2015).

Fluorine doped SnO₂ exhibited not only high chemical and structural stability but also good electronic conductivity (Banyamin et al., 2014). With increasing fluorine concentration, the energy of the CB increased (Velikokhatnyi and Kumta, 2011). Also, fluorine-doped SnO₂ is characterized by oxygen vacancies which further improve the photocatalytic properties of the material. As a consequence, fluorine-doped SnO₂ demonstrated a very high photocatalytic efficiency for the degradation of rhodamine B (Kumar et al., 2011).

The charge separation in iodine-doped SnO₂ is further improved by the concentration gradient of the dopant in the semiconductor. The concentration of the halide is at maximum close to the surface of the catalyst, and it rapidly decreases within the crystal structure because of unfavorable iodine-oxygen interactions (Liu et al., 2009a). Thus the

recombination of the e⁻-h⁺ pairs is inhibited and electrons released during the irradiation of the photocatalyst are directed towards the surface of the material (Tojo et al., 2008). Additionally, the photocatalytic properties are further enhanced by oxygen deficiencies which are stabilized, as pointed out in a previous section, by the multi-valence of tin (Kilic and Zunger, 2002).

Seema et al. (2012) prepared a graphene/SnO₂ composite. This material displayed not only excellent electrical conductivity but also a dramatically improved potential for the photocatalytic degradation of pollutants. When irradiated with sunlight, the organic dye methylene blue was rapidly and completely degraded.

The results discussed above are summarized in Table 10.

6. Parameters affecting the photodegradation of organic pollutants in aqueous dispersion of SnO₂

While the previous section provides an overview of the effect of different dopants on photocatalytic activity, the following section briefly discusses external parameters, such as catalyst loading, temperature, pH, and contaminant concentration.

6.1. Catalyst loading

The amount of catalyst required for any large-scale application is of fundamental importance to evaluate the overall efficiency of the process. Thus many groups have commented on the optimum concentration of SnO₂-based photocatalysts in the degradation of organic pollutants.

Among others, Ismat-Shah and co-workers have stated that the photocatalytic degradation rate initially increases with an increased concentration of the catalyst, followed by a steady decrease once the optimum catalyst loading is exceeded (Barakat et al., 2005; Ibhaddon and Fitzpatrick, 2013). The initial increase in photocatalytic activity is easily explained by the net increase in the active surface area of the catalyst in the suspension. However, as the concentration of the catalyst increases, turbidity also increases and the light transmission in the suspension is reduced (Wei et al.,

Table 9 – Improved photocatalytic efficiency by rare earth metals.

Catalyst	Light source/pollutant	Experimental conditions	Photodegradation efficiency	Ref.
Sm/SnO ₂	260 nm; UV light; P: EV, BG	C: 0.233 gm/10 mL EV; 2.5 × 10 ⁻⁴ M; BG 2.5 × 10 ⁻⁴ M	The photocatalytic degradation was enhanced in the presence of Sm ³⁺ ions	Singh et al. (2014)
Ti/Sb/SnO ₂ Ti/Ce/Sb/SnO ₂ Ti/Gd/Sb-SnO ₂ Ti/Eu/Sb-SnO ₂	Potentiostat for organic degradation studies; P: BQ HQ, catechol	P: 200 mg/L C: 100 mg/L	Faster degradation of BQ because of electrophilic attack of OH [•]	Cui et al. (2012)
La/SnO ₂	8 W Hg lamp phenol	C: 65 mg/50 mL P: 10 ppm	Complete photodegradation in less than 2.5 h	Al-Hamdi et al. (2014)
La/SnO ₂	8 W Hg lamp, Solar light; phenol	C: 65 mg/50 mL P: 10 ppm	95–99% decrease of pollutant concentration after 2 h under irradiation with solar light	Al-Hamdi et al. (2016b)
Gd/SnO ₂	Visible light; phenol	C: 65 mg/50 mL P: 10 ppm	95–99% decrease in pollutant concentration after 2 h under irradiation with solar light	Al-Hamdi et al. (2015a)

Abbreviations: Ethyl violet: (EV); Brilliant green: (BG); benzoquinone: BQ; hydroquinone: HQ; concentration catalyst: C; concentration of pollutant: P.

Table 10 – Enhanced photocatalytic activity of SnO₂ by non-metal doping.

Catalyst	Light source; pollutant	Experimental conditions	Photodegradation efficiency	Ref.
F-doped SnO ₂	125 W Hg lamp; P: RhB	C: 0.1 g/100 mL P: 5 × 10 ⁻⁶ M,	High photocatalytic activity	Kumar et al. (2011)
I-doped SnO ₂	8 W UV solar light; phenol	C: 65 mg/50 mL P: 10 mg/L	High activity in UV and visible light	Al-Hamdi et al. (2015b)
Graphene/SnO ₂	350 W Xe lamp, sunlight; MB	C: 10 mg/50 mL P: 2.7 × 10 ⁻⁵ M	Complete degradation of MB after 6 h	Seema et al. (2012)

Abbreviations: rhodamine B: RhB; methylene blue: MB; concentration catalyst: C; concentration of pollutant: P.

2009). Thus, further increase in the catalyst loading will pre-vent light from passing through the solution and only catalyst particles close to the surface remain photocatalytically active (Pardeshi and Patil, 2008). We could confirm this general trend in the photocatalytic degradation of phenol as the process yields the best results when only 65 mg of the doped SnO₂ catalyst were suspended in 50 mL of the solution. Further increase in the catalyst loading resulted in a decrease of the activity of the catalytic oxidation as discussed above. The same correlation has also been observed for other photocatalytically active nanoparticles. TiO₂ shows optimum activity which decreases with increasing catalyst loading as the light penetration becomes significantly lower (Maddila et al., 2016; Sobczynski et al., 2004). Thus the degradation rate of phenol steadily decreased above a certain concentration of the catalyst (Kashif and Ouyang, 2009).

6.2. Contaminant concentration

The efficiency of the photodegradation generally decreases with increasing contaminant concentration (Khataee and Zarei, 2011). One of the reasons is the light absorption of organic dyes and the resulting decrease in the radiation available to activate the catalyst nanoparticles. Additionally, if all active sites on the surface of the catalyst are occupied, the rate of the reaction decreases and additional pollutant molecules are only degraded after the active sites once again become available (Davis et al., 1994; Konstantinou and Albanis, 2004). In our work the photocatalytic degradation of phenol was carried out at different initial concentrations from 5 ppm to 50 ppm. The results indicated fast degradation of phenol at a concentration of 10 ppm, which decreased slightly once the initial concentration exceeded 15 ppm (Al-Hamdi et al., 2016a)

6.3. Effect of the pH of the solution

The pH of the polluted solution is of great importance for the overall efficiency of the photocatalytic degradation of aromatic dyes. The pH does not only have a significant influence on the oxidation potential, but also determines the charge of the pollutant (many organic pollutants have acidic functional groups) and/or the surface of the photocatalyst. It is essential that the reaction is carried out within the range of acceptable stability of the photocatalyst.

In many cases lower pH ranges were found to be beneficial for the degradation rate of organic pollutants (Wu et al., 2001). Enhanced degradation of phenol under slightly acidic conditions has been repeatedly mentioned by researchers active in this area (Anju et al., 2012). A slightly acidic pH range increases the attraction of the pollutant to the surface of the photocatalyst and guarantees enhanced degradation rates (Ahmed et al., 2011). However, if the pH of the reaction mixture drops below a certain threshold, the rate of the reaction decreases significantly.

Abdullah et al. (2013) reported that the photodegradation of chlorophenoxyacetic acid is enhanced when the pH of the reaction mixture is kept slightly above the pK_a value of the organic acid, but below the pH of the point of zero charge (pH_{ZPC}) of the nanocomposite. This ensures optimal electro-static interaction of the deprotonated acid with the positively charged surface of the photocatalyst with enhanced reaction rates (Abdullah et al., 2013).

As the pH is of crucial importance, careful control of the reaction is required and the settings must be optimized if different pollutants or catalysts are used as the pK_a value is different for every organic dye and the point of zero charge varies for different photocatalysts (Trellu et al., 2016).

6.4. Temperature

Although the activation of the catalyst is dependent on light, the overall rate of the photodegradation also depends slightly on the temperature of the system (Horovitz et al., 2016). When the reaction is carried out at elevated temperature, absorption, degradation, and desorption proceed at higher rates (Chong et al., 2010). Additionally, the mobility of charge carriers is enhanced at higher temperatures, which also results in faster reaction rates. However, the temperature should not exceed a certain range. Groups active in this area have reported that best results are obtained when the temperature is kept between 20 °C and 80 °C (Malato et al., 2003).

6.5. Light intensity and wavelength

Since the activation of the catalyst depends on irradiation with light of a certain wavelength, the light intensity is of crucial importance (Hansen et al., 2015). Naturally, the efficiency of the photocatalytic system increases with increasing light intensity with energies greater than the activation threshold (Cassano and Alfano, 2000; Ollis, 1991; Bahnemann, 2004; Sumita et al., 2001).

Light of high intensity and energy is moreover capable of producing radicals such as OH^* , even in the absence of suitable photocatalysts. This additional mechanism for the generation of reactive radicals is responsible for further rate increase when light of high intensity and wavelength is applied to the sample (Faramarzpour et al., 2009; Liu et al., 2009b; Mahalakshmi et al., 2007; Pourata et al., 2009).

Besides the intensity of the light source, the energy of the photons is of great importance. Because of energy quantization, excitation can only take place when photons of sufficient energy hit the surface of the photocatalyst. Depending on the band gap of the photocatalyst, different light sources need to be used. While a band gap of 3.1–3.9 eV requires an excitation wavelength of 315–400 nm (UV-A), band gaps of 3.9–4.4 eV need light with wavelengths of 280–315 nm (UV-B). Should the band gap exceed the values given above, light with even higher energy is required (3.1–3.94 eV) and the process becomes impractical (Cutler and Zimmerman, 2011; Rincón and Pulgarin, 2005). Typically, the band gap in SnO_2 with suitable dopants is smaller than 3.1 eV, which renders possible the excitation of the photocatalyst with visible light and guarantees broad application of the semiconductor.

Ideally, light sources which emit light with different wavelengths are used for the excitation of catalysts with broad energy bands to increase the overall efficiency (Legrini et al., 1993).

6.6. Crystallinity and surface area

The crystallinity of the catalyst plays an important role for the overall efficiency (Sarkar et al., 2016). Heterogeneous catalysts with large surface areas are generally better suited as they allow increased absorption of the reactants. As doping of SnO_2 modifies and disturbs the crystal structure of the metal oxide, the process also causes a decrease of crystal size and an increase of active surface area. Thus doping of SnO_2 fulfills a dual purpose as it alters the electronic properties of the semiconductor by lowering the band gap and simultaneously enlarges the contact area of catalyst and pollutant (Alanko et al., 2012; Jiang et al., 2016; Terrier et al., 1995). We could observe this effect in our group's work when a sample of SnO_2

Table 11 – Calculated crystallite of different 0.6% doped and undoped SnO_2 nanoparticles from (110) peak using the Debye–Scherrer analysis.

Dopant	Size (nm)	Surface area (m^2/g)
Undoped	8.4	28
SnO_2/Ce (0.6 wt%)	5.5	30
SnO_2/Nd (0.6 wt%)	4.1	35
SnO_2/La (0.6 wt%)	3.4	40
SnO_2/Gd (0.6 wt%)	3.2	58
SnO_2/Sb (0.6 wt%)	1.8	54
SnO_2/I (1.0 wt%)	2.5	50

Table 12 – Calculated crystallite size of different SnO_2/Sb nanoparticles from (110) peak using the Debye–Scherrer analysis.

Dopant	Size (nm)
Undoped	8.4
SnO_2/Sb (0.2 wt%)	3.5
SnO_2/Sb (0.4 wt%)	2.5
SnO_2/Sb (0.6 wt%)	1.8
SnO_2/Sb (0.8 wt%)	2.1

was doped with different metals of varying concentrations. In all cases the surface area of the photocatalyst increased, resulting in higher catalytic activity. This steady increase was observed up to a certain threshold, which varied for each contaminant (depending on the charge, the size of the ion, and other factors). A summary of this study is provided in Tables 11 and 12.

7. Conclusion

Our understanding of Nature and the sensitivity and vulnerability of environmental processes has advanced significantly in recent years. With this information, we begin to see the interconnections of biological systems which have long been considered independent entities. With this advanced improved understanding of natural processes—and their impact on humans, we must take precautions to use the resources available to us wisely, and we must put emphasis on sustainable methods and waste removal.

Much effort has been put into the development of novel methods for the environmentally sustainable disposal of chemical waste and the purification of polluted areas. Several of these methods appear promising and will be further developed over the next few years. One approach to degrading toxins in wastewater and other sources is the application of advanced oxidation processes. This strategy has received considerable attention from the scientific community and the basic idea behind this concept is quite simple: Pollutants should be oxidatively degraded and thus removed from our environment. Many protocols have been developed and the purpose of this article is to review recent progress in the utilization of SnO_2 as inexpensive and readily available photocatalyst for the oxidative degradation of organic pollutants.

As evidenced by the numerous impressive examples, semi-conductors, such as SnO_2 , are well suited to degrading organic pollutants in wastewater and other sources. Upon irradiation with light of suitable energy, reactive radicals are generated at the surface of the photocatalyst, which oxidatively destroy many pollutants known to cause problems to our environment and health. The addition of dopants to SnO_2 further improves the photocatalytic properties, reduces the band gap, and thus

decreases the energy required for the activation of the catalyst. While undoped SnO₂ requires irradiation with UV light, visible light is suitable for the application of doped material.

The application of semiconductors as photocatalysts for the oxidative degradation of organic pollutants is a relatively new area of research. Although impressive results have been obtained in the last few years, it is also necessary to mention aspects and problems which have not yet been solved: Only pollutants with conjugated double bonds can so far be easily oxidatively attacked. However, most pollutants do not contain such delocalized p-systems. A representative list of such pollutants should be included in future studies. Also, although the catalysts are well suited for the degradation of organic pollutants, an efficient way to regenerate these nanocomposites must be developed to prevent these highly active materials from escaping into the environment on a large scale. This is of even greater importance as these metal oxides, if released as dust, may have negative effects on human health. Additionally, studies should include different catalysts in order to assess which nanomaterial is best suited for the degradation of specific pollutants.

It is important to address these issues in future work to fully demonstrate the scope of the method and prepare the ground for possible industrial applications. With this review article, we seek not only to provide an overview of recent developments in the SnO₂-mediated oxidative degradation of pollutants from environmental sources, but also to encourage further research in this area and attract researchers to join this field. With the impressive progress over the last few years and clear goals for future work, we look forward to seeing many fascinating research articles in the near future.

Acknowledgement

The authors thank Virginia Mattila for careful proofreading of the manuscript

References

- Abdel-Messih, M.F., Ahmed, M.A., El-Sayed, A.S., 2013. Photocatalytic decolorization of rhodamine B dye using novel mesoporous SnO₂-TiO₂ nano mixed oxides prepared by sol-gel method. *J. Photochem. Photobiol. A: Chem.* 260, 1–8.
- Abdullah, A.H., Mun, L.K., Zainal, Z., Hussein, M.Z., 2013. Photodegradation of chlorophenoxyacetic acids by ZnO/[gamma]-Fe₂O₃ nanocatalysts: a comparative study. *Int. J. Chem.* 5, 56.
- Abe, R., Higashi, M., Sayama, K., Abe, Y., Sugihara, H., 2006. Photocatalytic activity of R₃MO₇ and R₂Ti₂O₇ (R = Y, Gd, La; M = Nb, Ta) for water splitting into H₂ and O₂. *J. Phys. Chem. B* 110, 2219–2226.
- Ahmed, S., Rasul, M., Martens, W.N., Brown, R., Hashib, M., 2011. Advances in heterogeneous photocatalytic degradation of phenols and dyes in wastewater: a review. *Water Air Soil Pollut.* 215, 3–29.
- Al-Hamdi, A.M., Sillanpää, M., Dutta, J., 2014. Photocatalytic degradation of phenol in aqueous solution by rare earth-doped SnO₂ nanoparticles. *J. Mater. Sci.* 49, 5151–5159.
- Al-Hamdi, A.M., Sillanpää, M., Dutta, J., 2015a. Gadolinium doped tin dioxide nanoparticles: an efficient visible light active photocatalyst. *J. Rare Earths* 33, 1275–1283.
- Al-Hamdi, A.M., Sillanpää, M., Dutta, J., 2015b. Photocatalytic degradation of phenol by iodine doped tin oxide nanoparticles under UV and sunlight irradiation. *J. Alloys Compd.* 618, 366–371.
- Al-Hamdi, A.M., Sillanpää, M., Bora, T., Dutta, J., 2016a. Efficient photocatalytic degradation of phenol in aqueous solution by SnO₂:Sb nanoparticles. *Appl. Surf. Sci.* 370, 229–236.
- Al-Hamdi, A.M., Sillanpää, M., Dutta, J., 2016b. Intermediate formation during photodegradation of phenol using lanthanum doped tin dioxide nanoparticles. *Res. Chem. Intermed.* 42, 3055–3069.
- Alanko, G.A., Thurber, A., Hanna, C.B., Punnoose, A., 2012. Size, surface structure, and doping effects on ferromagnetism in SnO₂. *J. Appl. Phys.* 111, 07C321.
- Anandan, K., Rajendran, V., 2015a. Influence of dopant concentrations (Mn = 1, 2 and 3 mol%) on the structural, magnetic and optical properties and photocatalytic activities of SnO₂ nanoparticles synthesized via the simple precipitation process. *Superlattices Microstruct.* 85, 185–197.
- Anandan, K., Rajendran, V., 2015b. Influence of dopant concentrations (Mn = 1, 2 and 3 mol%) on the structural, magnetic and optical properties and photocatalytic activities of SnO₂ nanoparticles synthesized via the simple precipitation process. *Superlattice Microstruct.* 85, 185–197.
- Anju, S., Yesodharan, S., Yesodharan, E., 2012. Zinc oxide mediated sonophotocatalytic degradation of phenol in water. *Chem. Eng. J.* 189, 84–93.
- Ansari, S.A., Khan, M.M., Ansari, M.O., Lee, J., Cho, M.H., 2014. Visible light-driven photocatalytic and photoelectrochemical studies of Ag-SnO₂ nanocomposites synthesized using an electrochemically active biofilm. *RSC Adv.* 4, 26013–26021.
- Assia, S., Ratiba, O., 1999. Optical reflectance of pure and doped tin oxide: from thin films to poly-crystalline silicon/thin film device. *Int. J. Biol. Chem. Eng.* 2, 48–50.
- Azam, A., Ahmed, A.S., Ansari, M.S., Shafeeq, M.M., Naqvi, A.H., 2010. Study of electrical properties of nickel doped SnO₂ ceramic nanoparticles. *J. Alloy Compd.* 506, 237–242.
- Bahnemann, D., 2004. Photocatalytic water treatment: solar energy applications. *Sol. Energy* 77, 445–459.
- Bamuza-Pemu, B.E., 2014. Photocatalytic degradation of phenolic compounds and algal metabolites in water. Ph.D. Thesis. University of Pretoria, South Africa.
- Banyamin, Z.Y., Kelly, P.J., West, G., Boardman, J., 2014. Electrical and optical properties of fluorine doped tin oxide thin films prepared by magnetron sputtering. *Coatings* 4, 732–746.
- Barakat, M., Schaeffer, H., Hayes, G., Ismat-Shah, S., 2005. Photocatalytic degradation of 2-chlorophenol by Co-doped TiO₂ nanoparticles. *Appl. Catal. B Environ.* 57, 23–30.
- Batzill, M., Diebold, U., 2005. The surface and materials science of tin oxide. *Prog. Surf. Sci.* 79, 47–154.
- Behtash, M., Joo, P.H., Nazir, S., Yang, K., 2015. Electronic structures and formation energies of pentavalent-ion-doped SnO₂: first-principles hybrid functional calculations. *J. Appl. Phys.* 117, 175101.
- Bhatkhande, D.S., Pangarkar, V.G., Beenackers, A.A.C.M., 2002. Photocatalytic degradation for environmental applications—a review. *J. Chem. Technol. Biotechnol.* 77, 102–116.
- Bhattacharjee, A., Ahmaruzzaman, M., 2015. Photocatalytic-degradation and reduction of organic compounds using SnO₂ quantum dots (via a green route) under direct sunlight. *RSC Adv.* 5, 66122–66133.
- Bhosale, R., Pujari, S., Muley, G., Pagare, B., Gambhire, A., 2013. Visible-light-activated nanocomposite photocatalyst of Cr₂O₃/SnO₂. *J. Nano Chem.* 3, 1–7.
- Bielski, B.H.J., Cabelli, D.E., Arudi, R.L., Ross, A.B., 1985. Reactivity of HO₂/O₂-2 radicals in aqueous solution. *J. Phys. Chem. Ref. Data* 14, 1041–1100.
- Borras, C., Berzoy, C., Mostany, J., Scharifker, B., 2006. Oxidation of p-methoxyphenol on SnO₂-Sb₂O₅ electrodes: effects of electrode potential and concentration on the mineralization efficiency. *J. Appl. Electrochem.* 36, 433–439.
- Bouras, K., Rehspringer, J.-L., Schmerber, G., Rinnert, H., Colis, S., Ferblantier, G., Balestrieri, M., Iliawakrim, D., Dinia, A., Slaoui, A., 2014. Optical and structural properties of Nd doped SnO₂ powder fabricated by the sol-gel method. *J. Mater. Chem. C* 2, 8235–8243.

- Brickner, P.W., Vincent, R.L., First, M., Nardell, E., Murray, M., Kaufman, W., 2003. The application of ultraviolet germicidal irradiation to control transmission of airborne disease: bioterrorism countermeasure. *Public Health Rep.* 118, 99.
- Carreno, L., Fajardo, H.V., Maciel, A.P., Valentini, A., Pontes, F.M., Probst, L.F., Leite, E.R., Longo, E., 2004. Selective synthesis of vinyl ketone over SnO₂ nanoparticle catalysts doped with rare earths. *J. Mol. Catal. A: Chem.* 207, 91–96.
- Carreno, N., Maciel, A., Leite, E., Lisboa-Filho, P.N., Longo, E., Valentini, A., Probst, L., Paiva-Santos, C., Schreiner, W., 2002. The influence of cation segregation on the methanol decomposition on nanostructured SnO₂. *Sens. Actuators B Chem.* 86, 185–192.
- Cassano, A.E., Alfano, O.M., 2000. Reaction engineering of suspended solid heterogeneous photocatalytic reactors. *Catal. Today* 58, 167–197.
- Chaisitsak, S., 2011. Nanocrystalline SnO₂:F thin films for liquid petroleum gas sensors. *Sensors* 11, 7127–7140.
- Chong, M.N., Jin, B., Chow, C.W., Saint, C., 2010. Recent developments in photocatalytic water treatment technology: a review. *Water Res.* 44, 2997–3027.
- Cristante, V.M., Jorge, S.M., Valente, J.P., Saeki, M.J., Florentino, A.O., Padilha, P.M., 2007. TiO₂ films organofunctionalized with 2-aminothiazole ligand and adsorbed Pd(II) ions applied in the photocatalytic degradation of phenol in an aqueous medium. *Thin Solid Films* 515, 5334–5340.
- Cui, Y.-H., Feng, Y.-J., Liu, J., Ren, N., 2012. Comparison of various organic compounds destruction on rare earths doped Ti/Sb-SnO₂ electrodes. *J. Hazard. Mater.* 239, 225–232.
- Cutler, T.D., Zimmerman, J.J., 2011. Ultraviolet irradiation and the mechanisms underlying its inactivation of infectious agents. *Anim. Health Res. Rev.* 12, 15–23.
- Davis, M., Hung-Low, F., Hikal, W.M., Hope-Weeks, L.J., 2013. Enhanced photocatalytic performance of Fe-doped SnO₂ nanoarchitectures under UV irradiation: synthesis and activity. *J. Mater. Sci.* 48, 6404–6409.
- Davis, R.J., Gainer, J.L., O'Neal, G., Wu, I.-W., 1994. Photocatalytic decolorization of wastewater dyes. *Water Environ. Res.* 66, 50–53.
- Diallo, A., Manikandan, E., Rajendran, V., Maaza, M., 2016. Physical & enhanced photocatalytic properties of green synthesized SnO₂ nanoparticles via *Aspalathus linearis*. *J. Alloy Compd.* 681, 561–570.
- Dou, M., Persson, C., 2013. Comparative study of rutile and anatase SnO₂ and TiO₂: band-edge structures, dielectric functions, and polaron effects. *J. Appl. Phys.* 113, 083703.
- Du, Y., Zhang, N., Wang, C., 2010. Photo-catalytic degradation of trifluralin by SnO₂-doped Cu₂O crystals. *Catal. Commun.* 11, 670–674.
- Entradas, T., Cabrita, J., Dalui, S., Nunes, M., Monteiro, O., Silvestre, A., 2014. Synthesis of sub-5 nm Co-doped SnO₂ nanoparticles and their structural, microstructural, optical and photocatalytic properties. *Mater. Chem. Phys.* 147, 563–571.
- Erkan, A., Bakir, U., Karakas, G., 2006. Photocatalytic microbial inactivation over Pd doped SnO₂ and TiO₂ thin films. *J. Photochem. Photobiol. A* 184, 313–321.
- Fadavieslam, M.R., 2016. Effect of Sb doping on the structural, electrical, and optical properties of SnO₂ thin films prepared through spray pyrolysis. *J. Mater. Sci.: Mater. Electron.* 27, 4943–4950.
- Fan, C.-M., Peng, Y., Zhu, Q., Lin, L., Wang, R.-X., Xu, A.-W., 2013. Synproportionation reaction for the fabrication of Sn²⁺ self-doped SnO_{2-x} nanocrystals with tunable band structure and highly efficient visible light photocatalytic activity. *J. Phys. Chem. C* 117, 24157–24166.
- Fang, L., Zu, X., Li, Z., Zhu, S., Liu, C., Zhou, W., Wang, L., 2008. Synthesis and characteristics of Fe³⁺-doped SnO₂ nanoparticles via sol-gel-calcination or sol-gel-hydrothermal route. *J. Alloy Compd.* 454, 261–267.
- Faramarzpour, M., Vossoughi, M., Borghai, M., 2009. Photocatalytic degradation of furfural by titania nanoparticles in a floating-bed photoreactor. *Chem. Eng. J.* 146, 79–85.
- Foletto, E.L., Battiston, S., Collazzo, G.C., Bassaco, M.M., Mazutti, M.A., 2012. Degradation of leather dye using CeO₂-SnO₂ nanocomposite as photocatalyst under sunlight. *Water Air Soil Pollut.* 223, 5773–5779.
- Fujishima, A., 1972. Electrochemical photolysis of water at a semiconductor electrode. *Nature* 238, 37–38.
- Gaya, U.I., Abdullah, A.H., 2008. Heterogeneous photocatalytic degradation of organic contaminants over titanium dioxide: a review of fundamentals, progress and problems. *J. Photochem. Photobiol. C: Photochem. Rev.* 9, 1–12.
- Gu, F., Wang, S.F., Lü, M.K., Zhou, G.J., Xu, D., Yuan, D.R., 2004. Photoluminescence properties of SnO₂ nanoparticles synthesized by sol-gel method. *J. Phys. Chem. B* 108, 8119–8123.
- Hansen, M.J., Velema, W.A., Lerch, M.M., Szymanski, W., Feringa, B.L., 2015. Wavelength-selective cleavage of photoprotecting groups: strategies and applications in dynamic systems. *Chem. Soc. Rev.* 44, 3358–3377.
- Haritha, E., Roopan, S.M., Madhavi, G., Elango, G., Al-Dhabi, N.A., Arasu, M.V., 2016. Green chemical approach towards the synthesis of SnO₂ NPs in argument with photocatalytic degradation of diazo dye and its kinetic studies. *J. Photochem. Photobiol. B* 162, 441–447.
- Harrison, P.G., Maunders, B.M., 1984. Tin oxide surfaces. Part 12.—a comparison of the nature of tin(IV) oxide, tin(IV) oxide-silica and tin(IV) oxide-palladium oxide: surface hydroxyl groups and ammonia adsorption. *J. Chem. Soc.* 80, 1341–1356.
- Hays, J., Punnoose, A., Baldner, R., Engelhard, M.H., Peloquin, J., Reddy, K., 2005. Relationship between the structural and magnetic properties of Co-doped SnO₂ nanoparticles. *Phys. Rev. B* 72, 075203.
- He, Z., Wang, C., Wang, H., Hong, F., Xu, X., Chen, J., Song, S., 2011. Increasing the catalytic activities of iodine doped titanium dioxide by modifying with tin dioxide for the photodegradation of 2-chlorophenol under visible light irradiation. *J. Hazard. Mater.* 189, 595–602.
- He, Z., Zhou, J., 2013. Synthesis, characterization, and activity of tin oxide nanoparticles: influence of solvothermal time on photocatalytic degradation of rhodamine B. *Mod. Res. Catal.* 2, 13.
- Herrmann, J.-M., 1999. Heterogeneous photocatalysis: fundamentals and applications to the removal of various types of aqueous pollutants. *Catal. Today* 53, 115–129.
- Hong, X., Wang, Z., Cai, W., Lu, F., Zhang, J., Yang, Y., Ma, N., Liu, Y., 2005. Visible-light-activated nanoparticle photocatalyst of iodine-doped titanium dioxide. *Chem. Mater.* 17, 1548–1552.
- Horovitz, I., Avisar, D., Baker, M.A., Grilli, R., Lozzi, L., Di Camillo, D., Mamane, H., 2016. Carbamazepine degradation using a N-doped TiO₂ coated photocatalytic membrane reactor: influence of physical parameters. *J. Hazard. Mater.* 310, 98–107.
- Hou, L.-R., Yuan, C.-Z., Peng, Y., 2007. Synthesis and photocatalytic property of SnO₂/TiO₂ nanotubes composites. *J. Hazard. Mater.* 139, 310–315.
- Huang, H., Tian, S., Xu, J., Xie, Z., Zeng, D., Chen, D., Shen, G., 2012. Needle-like Zn-doped SnO₂ nanorods with enhanced photocatalytic and gas sensing properties. *Nanotechnology* 23, 105502.
- Ibhadon, A., Fitzpatrick, P., 2013. Heterogeneous photocatalysis: recent advances and applications. *Catalysts* 3, 189.
- Jiang, J., Lu, Y., Kramm, B., Michel, F., Reindl, C.T., Kracht, M.E., Klar, P.J., Meyer, B.K., Eickhoff, M., 2016. Nitrogen incorporation in SnO₂ thin films grown by chemical vapor deposition. *Phys. Status Solidi B* 253, 1087–1092.
- Kashif, N., Ouyang, F., 2009. Parameters effect on heterogeneous photocatalysed degradation of phenol in aqueous dispersion of TiO₂. *J. Environ. Sci.* 21, 527–533.
- Khataee, A., Zarei, M., 2011. Photocatalysis of a dye solution using immobilized ZnO nanoparticles combined with photoelectrochemical process. *Desalination* 273, 453–460.
- Kilic, C., Zunger, A., 2002. Origins of coexistence of conductivity and transparency in SnO₂. *Phys. Rev. Lett.* 88, 095501.

- Kim, D.-H., Lee, G.-W., Kim, Y.-C., 2012. Interaction of zinc interstitial with oxygen vacancy in zinc oxide: an origin of n-type doping. *Solid State Commun.* 152, 1711–1714.
- Kim, S., Hwang, S.-J., Choi, W., 2005. Visible light active platinum-ion-doped TiO₂ photocatalyst. *J. Phys. Chem. B* 109, 24260–24267.
- Konstantinou, I.K., Albanis, T.A., 2004. TiO₂-assisted photocatalytic degradation of azo dyes in aqueous solution: kinetic and mechanistic investigations: a review. *Appl. Catal. B Environ.* 49, 1–14.
- Kovács, K., He, S., Mile, V., Csay, T., Takács, E., Wojnárovits, L., 2015. Ionizing radiation induced degradation of diuron in dilute aqueous solution. *Chem. Cent. J.* 9, 1.
- Kruefu, V., Ninsonti, H., Wetchakun, N., Inceesungvorn, B., Pookmanee, P., Phanichphant, S., 2012. Photocatalytic degradation of phenol using Nb-loaded ZnO nanoparticles. *Eng. J.* 16, 91–100.
- Kudo, A., Miseki, Y., 2009. Heterogeneous photocatalyst materials for water splitting. *Chem. Soc. Rev.* 38, 253–278.
- Kumar, S., Chauhan, P., Kundu, V., 2016. Sol–gel synthesis, structural, morphological and optical properties of Se-doped SnO₂ nanoparticles. *J. Mater. Sci. Mater. Electron.* 27, 3103–3108.
- Kumar, V., Govind, A., Nagarajan, R., 2011. Optical and photocatalytic properties of heavily F-doped SnO₂ nanocrystals by a novel single-source precursor approach. *Inorg. Chem.* 50, 5637–5645.
- Lazar, M., Varghese, S., Nair, S., 2012. Photocatalytic water treatment by titanium dioxide: recent updates. *Catalysts* 2, 572.
- Lee, K.M., Lai, C.W., Ngai, K.S., Juan, J.C., 2016. Recent developments of zinc oxide based photocatalyst in water treatment technology: a review. *Water Res.* 88, 428–448.
- Legrini, O., Oliveros, E., Braun, A., 1993. Photochemical processes for water treatment. *Chem. Rev.* 93, 671–698.
- Lewis, N.S., 2007. Toward cost-effective solar energy use. *Science* 315, 798–801.
- Li, F., Li, X., Hou, M., Cheah, K., Choy, W., 2005. Enhanced photocatalytic activity of Ce³⁺-TiO₂ for 2-mercaptobenzothiazole degradation in aqueous suspension for odour control. *Appl. Catal. A Gen.* 285, 181–189.
- Li, K., Wang, Y., Wang, S., Zhu, B., Zhang, S., Huang, W., Wu, S., 2009. A comparative study of CuO/TiO₂-SnO₂, CuO/TiO₂ and CuO/SnO₂ catalysts for low-temperature CO oxidation. *J. Nat. Gas Chem.* 18, 449–452.
- Li, Y., Liu, J., Liang, J., Yu, X., Li, D., 2015. Tunable solar-heat shielding property of transparent films based on mesoporous Sb-doped SnO₂ microspheres. *ACS Appl. Mater. Interfaces* 7, 6574–6583.
- Linsebigler, A.L., Lu, G., Yates Jr., J.T., 1995. Photocatalysis on TiO₂ surfaces: principles, mechanisms, and selected results. *Chem. Rev.* 95, 735–758.
- Liu, C., Tang, X., Mo, C., Qiang, Z., 2008. Characterization and activity of visible-light-driven TiO₂ photocatalyst codoped with nitrogen and cerium. *J. Solid State Chem.* 181, 913–919.
- Liu, G., Sun, C., Yan, X., Cheng, L., Chen, Z., Wang, X., Wang, L., Smith, S.C., Lu, G.Q.M., Cheng, H.-M., 2009a. Iodine doped anatase TiO₂ photocatalyst with ultra-long visible light response: correlation between geometric/electronic structures and mechanisms. *J. Mater. Chem. A* 19, 2822–2829.
- Liu, W., Chen, S., Zhao, W., Zhang, S., 2009b. Study on the photocatalytic degradation of trichlorfon in suspension of titanium dioxide. *Desalination* 249, 1288–1293.
- Liu, Y., Zhang, P., Tian, B., Zhang, J., 2015. Core–shell structural CdS@SnO₂ nanorods with excellent visible-light photocatalytic activity for the selective oxidation of benzyl alcohol to benzaldehyde. *ACS Appl. Mater. Int.* 7, 13849–13858.
- Low, J.J., Kreider, M.L., Pulsifer, D.P., Jones, A.S., Gilani, T.H., 2008. Band gap energy in silicon. *Am. J. Undergrad. Res.* 7, 27–32.
- Maciel, R., Sant'Anna, G., Dezotti, M., 2004. Phenol removal from high salinity effluents using Fenton's reagent and photo-Fenton reactions. *Chemosphere* 57, 711–719.
- Madelung, O., Rössler, U., Schulz, M., 1998. Tin dioxide (SnO₂) crystal structure, lattice parameters, thermal expansion. In: *Non-Tetrahedrally Bonded Elements and Binary Compounds I*. Springer Berlin Heidelberg, Berlin, Heidelberg, pp. 1–2.
- Maddila, S., Ndabankulu, V.O., Jonnalagadda, S.B., 2016. Photocatalytic ozonation for the degradation of tetradifon pesticide on Mn/TiO₂ under visible light. *Global NEST J.* 18 (2), 269–278.
- Mahalakshmi, M., Arabindoo, B., Palanichamy, M., Murugesan, V., 2007. Photocatalytic degradation of carbofuran using semiconductor oxides. *J. Hazard. Mater.* 143, 240–245.
- Malato, S., Blanco, J., Campos, A., Cáceres, J., Guillard, C., Herrmann, J., Fernández-Alba, A., 2003. Effect of operating parameters on the testing of new industrial titania catalysts at solar pilot plant scale. *Appl. Catal. B Environ.* 42, 349–357.
- Matsushima, S., Maekawa, T., Tamaki, J., Miura, N., Yamazoe, N., 1989. Role of additives on alcohol sensing by semiconductor gas sensor. *Chem. Lett.* 845–848.
- Mazloom, J., Ghodsi, F., Golmohjedeh, H., 2015. Synthesis and characterization of vanadium doped SnO₂ diluted magnetic semiconductor nanoparticles with enhanced photocatalytic activities. *J. Alloys Compd.* 639, 393–399.
- Mete, E., Uner, D., Gülseren, O., Ellialtıoğlu, S., 2009. Pt-incorporated anatase TiO₂ (001) surface for solar cell applications: first-principles density functional theory calculations. *Phys. Rev. B* 79, 125418.
- Michalowicz, J., Duda, W., 2007. Phenols—sources and toxicity. *Pol. J. Environ. Stud.* 16, 347–362.
- Miller, S.L., Linnes, J., Luongo, J., 2013. Ultraviolet germicidal irradiation: future directions for air disinfection and building applications. *Photochem. Photobiol.* 89, 777–781.
- Mishra, K., Johnson, K., Schmidt, P., 1995. Electronic structure of antimony-doped tin oxide. *Phys. Rev. B* 51, 13972.
- Mistry, B.V., Avasthi, D.K., Joshi, U.S., 2016. Tuning of optical and electrical properties of wide band gap Fe:SnO₂/Li:NiO p–n junctions using 80 MeV oxygen ion beam. *Appl. Phys. A* 122, 1024.
- Morimitsu, M., Ozaki, Y., Suzuki, S., Matsunaga, M., 2000. Effects of surface modification with platinum and ruthenium on temperature and humidity dependence of SnO₂-based CO gas sensors. *Sens. Actuators B Chem.* 67, 184–188.
- Niu, M., Huang, F., Cui, L., Huang, P., Yu, Y., Wang, Y., 2010. Hydrothermal synthesis, structural characteristics, and enhanced photocatalysis of SnO₂/a-Fe₂O₃ semiconductor nanoheterostructures. *ACS Nano* 4, 681–688.
- Oldfield, G., Ung, T., Mulvaney, P., 2000. Au@SnO₂ core-shell nanocapacitors. *Adv. Mater.* 12, 1519–1522.
- Ollis, D.F., 1991. Solar-assisted photocatalysis for water purification: issues, data, questions. In: *Photochemical Conversion and Storage of Solar Energy*. Springer, pp. 593–622.
- Pardeshi, S., Patil, A., 2008. A simple route for photocatalytic degradation of phenol in aqueous zinc oxide suspension using solar energy. *Solar Energy* 82, 700–705.
- Peng, X., Yu, Y., Tang, C., Tan, J., Huang, Q., Wang, Z., 2008. Occurrence of steroid estrogens, endocrine-disrupting phenols, and acid pharmaceutical residues in urban riverine water of the Pearl River Delta, South China. *Sci. Total Environ.* 397, 158–166.
- Phipps, G.L., Holcombe, G.W., Fiandt, J.T., 1981. Acute toxicity of phenol and substituted phenols to the fathead minnow. *Bull. Environ. Contam. Toxicol.* 26, 585–593.
- Piguet, C., Buenzli, J.C.G., Bernardinelli, G., Hopfgartner, G., Williams, A.F., 1993. Self-assembly and photophysical properties of lanthanide dinuclear triple-helical complexes. *J. Am. Chem. Soc.* 115, 8197–8206.
- Pourata, R., Khataee, A., Aber, S., Daneshvar, N., 2009. Removal of the herbicide bentazon from contaminated water in the presence of synthesized nanocrystalline TiO₂ powders under irradiation of UV-C light. *Desalination* 249, 301–307.
- Rakibuddin, M., Ananthakrishnan, R., 2016. A novel Ag deposited nanocoordination polymer derived porous SnO₂/NiO heteronanostructure for the enhanced photocatalytic

- reduction of Cr(vi) under visible light. *New J. Chem.* 40, 3385–3394.
- Reszczynska, J., Grzyb, T., Sobczak, J.W., Lisowski, W., Gazda, M., Ohtani, B., Zaleska, A., 2014. Lanthanide co-doped TiO₂: the effect of metal type and amount on surface properties and photocatalytic activity. *Appl. Surf. Sci.* 307, 333–345.
- Reszczynska, J., Grzyb, T., Sobczak, J.W., Lisowski, W., Gazda, M., Ohtani, B., Zaleska, A., 2015. Visible light activity of rare earth metal doped (Er 3+, Yb 3+ or Er 3+/Yb 3+) titania photocatalysts. *Appl. Catal. B Environ.* 163, 40–49.
- Rincón, A.-G., Pulgarin, C., 2005. Use of coaxial photocatalytic reactor (CAPHORE) in the TiO₂ photo-assisted treatment of mixed *E. coli* and *Bacillus* sp. and bacterial community present in wastewater. *Catal. Today* 101, 331–344.
- Ritter, L., Solomon, K., Sibley, P., Hall, K., Keen, P., Mattu, G., Linton, B., 2002. Sources, pathways, and relative risks of contaminants in surface water and groundwater: a perspective prepared for the Walkerton inquiry. *J. Toxicol. Environ. Health* 65, 1–142.
- Sanal, K.C., Jayaraj, M.K., 2013. Growth and characterization of tin oxide thin films and fabrication of transparent p-SnO/n-ZnO p–n hetero junction. *Mater. Sci. Eng. B* 178, 816–821.
- Sangami, G., Dharmaraj, N., 2012. UV–visible spectroscopic estimation of photodegradation of rhodamine-B dye using tin(IV) oxide nanoparticles. *Spectrochim. Acta A* 97, 847–852.
- Sarkar, A., Ghosh, A.B., Saha, N., Srivastava, D.N., Paul, P., Adhikary, B., 2016. Enhanced photocatalytic performance of morphologically tuned Bi₂S₃ NPs in the degradation of organic pollutants under visible light irradiation. *J. Colloid Interface Sci.* 483, 49–59.
- Seema, H., Kemp, K.C., Chandra, V., Kim, K.S., 2012. Graphene–SnO₂ composites for highly efficient photocatalytic degradation of methylene blue under sunlight. *Nanotechnology* 23, 355705.
- Shahid, M., Shakir, I., Yang, S.-J., Kang, D.J., 2010. Facile synthesis of core–shell SnO₂/V₂O₅ nanowires and their efficient photocatalytic property. *Mater. Chem. Phys.* 124, 619–622.
- Shanthi, S., Subramanian, C., Ramasamy, P., 1999. Growth and characterization of antimony doped tin oxide thin films. *J. Cryst. Growth* 197, 858–864.
- Singh, L., Luwang, M.N., Srivastava, S., 2014. Luminescence and photocatalytic studies of Sm³⁺ ion doped SnO₂ nanoparticles. *New J. Chem.* 38, 115–121.
- Sobczynski, A., Duczmal, L., Zmudzinski, W., 2004. Phenol destruction by photocatalysis on TiO₂: an attempt to solve the reaction mechanism. *J. Mol. Catal. A Chem.* 213, 225–230.
- Sponza, D.T., 2003. Application of toxicity tests into discharges of the pulp-paper industry in Turkey. *Ecotoxicol. Environ. Saf.* 54, 74–86.
- Srinivasan, N., Bandyopadhyaya, R., 2016. Sn_xTi_{1-x}O₂ solid-solution-nanoparticle embedded mesoporous silica (SBA-15) hybrid as an engineered photocatalyst with enhanced activity. *Faraday Discuss.* 186, 353–370.
- Stasinakis, A., 2008. Use of selected advanced oxidation processes (AOPs) for wastewater treatment—a mini review. *Global NEST J.* 10, 376–385.
- Stengl, V., Bakardjieva, S., Murafa, N., 2009. Preparation and photocatalytic activity of rare earth doped TiO₂ nanoparticles. *Mater. Chem. Phys.* 114, 217–226.
- Sumita, T., Yamaki, T., Yamamoto, S., Miyashita, A., 2001. A new characterization method of photocatalytic activity in semiconductor photocatalysts. *Jpn. J. Appl. Phys.* 40, 4007.
- Sun, G., Yan, J., Niu, P., Meng, D., 2016. Electronic structure and optical property of p-type Zn-doped SnO₂ with Sn vacancy. *J. Semicond.* 37, 023005.
- Sun, J., Li, X., Quan, Y., Yin, Y., Zheng, S., 2015a. Effect of long-term organic removal on ion exchange properties and performance during sewage tertiary treatment by conventional anion exchange resins. *Chemosphere* 136, 181–189.
- Sun, M., Zhao, Q., Du, C., Liu, Z., 2015b. Enhanced visible light photocatalytic activity in BiOCl/SnO₂: heterojunction of two wide band-gap semiconductors. *RSC Adv.* 5, 22740–22752.
- Tammina, S.K., Mandal, B.K., 2016. Tyrosine mediated synthesis of SnO₂ nanoparticles and their photocatalytic activity towards Violet 4 BSN dye. *J. Mol. Liq.* 221, 415–421.
- Teh, C.M., Mohamed, A.R., 2011. Roles of titanium dioxide and ion-doped titanium dioxide on photocatalytic degradation of organic pollutants (phenolic compounds and dyes) in aqueous solutions: a review. *J. Alloys Compd.* 509, 1648–1660.
- Terrier, C., Chatelon, J.P., Berjoan, R., Roger, J.A., 1995. Sb-doped SnO₂ transparent conducting oxide from the sol–gel dip-coating technique. *Thin Solid Films* 263, 37–41.
- Thompson, T.L., Yates, J.T., 2006. Surface science studies of the photoactivation of TiO₂ new photochemical processes. *Chem. Rev.* 106, 4428–4453.
- Tojo, S., Tachikawa, T., Fujitsuka, M., Majima, T., 2008. Iodine-doped TiO₂ photocatalysts: correlation between band structure and mechanism. *J. Phys. Chem. C* 112, 14948–14954.
- Trellu, C., Mousset, E., Pechaud, Y., Huguenot, D., van Hullebusch, E.D., Esposito, G., Oturan, M.A., 2016. Removal of hydrophobic organic pollutants from soil washing/flushing solutions: a critical review. *J. Hazard. Mater.* 306, 149–174.
- Tu, Y.-F., Huang, S.-Y., Sang, J.-P., Zou, X.-W., 2009. Synthesis and photocatalytic properties of Sn-doped TiO₂ nanotube arrays. *J. Alloy Compd.* 482, 382–387.
- Van Eldik, R., Hubbard, C.D., 2009. *Advances in Inorganic Chemistry*. Academic Press.
- Velikokhatnyi, O.I., Kumta, P.N., 2011. Ab-initio study of fluorine-doped tin dioxide: a prospective catalyst support for water electrolysis. *Physica B* 406, 471–477.
- Vinodgopal, K., Kamat, P.V., 1995. Enhanced rates of photocatalytic degradation of an azo dye using SnO₂/TiO₂ coupled semiconductor thin films. *Environ. Sci. Technol.* 29, 841–845.
- Wang, C., Xu, B.-Q., Wang, X., Zhao, J., 2005. Preparation and photocatalytic activity of ZnO/TiO₂/SnO₂ mixture. *J. Solid State Chem.* 178, 3500–3506.
- Wang, J.L., Xu, L.J., 2012. Advanced oxidation processes for wastewater treatment: formation of hydroxyl radical and application. *Crit. Rev. Environ. Sci. Technol.* 42, 251–325.
- Wang, Y., Chan, K., Li, X., So, S., 2006. Electrochemical degradation of 4-chlorophenol at nickel–antimony doped tin oxide electrode. *Chemosphere* 65, 1087–1093.
- Wei, L., Shifu, C., Wei, Z., Sujuan, Z., 2009. Titanium dioxide mediated photocatalytic degradation of methamidophos in aqueous phase. *J. Hazard. Mater.* 164, 154–160.
- Wen, C., Zhu, Y.-J., Kanbara, T., Zhu, H.-Z., Xiao, C.-F., 2009. Effects of I and F codoped TiO₂ on the photocatalytic degradation of methylene blue. *Desalination* 249, 621–625.
- Wen, Z., Wang, G., Lu, W., Wang, Q., Zhang, Q., Li, J., 2007. Enhanced photocatalytic properties of mesoporous SnO₂ induced by low concentration ZnO doping. *Cryst. Growth Des.* 7, 1722–1725.
- Wu, C., Liu, X., Wei, D., Fan, J., Wang, L., 2001. Photosonochemical degradation of phenol in water. *Water Res.* 35, 3927–3933.
- Wu, S., Cao, H., Yin, S., Liu, X., Zhang, X., 2009. Amino acid-assisted hydrothermal synthesis and photocatalysis of SnO₂ nanocrystals. *J. Phys. Chem. C* 113, 17893–17898.
- Wu, W., Liao, L., Zhang, S., Zhou, J., Xiao, X., Ren, F., Sun, L., Dai, Z., Jiang, C., 2013. Non-centrosymmetric Au–SnO₂ hybrid nanostructures with strong localization of plasmonic for enhanced photocatalysis application. *Nanoscale* 5, 5628–5636.
- Xi, G., Ye, J., 2010. Ultrathin SnO₂ nanorods: template- and surfactant-free solution phase synthesis, growth mechanism, optical, gas-sensing, and surface adsorption properties. *Inorg. Chem.* 49, 2302–2309.
- Xia, H.-l., Zhuang, H.-s., Zhang, T., Xiao, D.-c., 2007. Photocatalytic degradation of Acid Blue 62 over CuO–SnO₂ nanocomposite photocatalyst under simulated sunlight. *J. Environ. Sci.* 19, 1141–1145.
- Xia, H., Zhuang, H., Zhang, T., Xiao, D., 2008. Visible-light-activated nanocomposite photocatalyst of Fe₂O₃/SnO₂. *Mater. Lett.* 62, 1126–1128.

- Xiong, C., Balkus, K.J., 2007. Mesoporous molecular sieve derived TiO₂ nanofibers doped with SnO₂. *J. Phys. Chem. C* 111, 10359–10367.
- Yadav, B., Dixit, R., Singh, S., 2014. A review on synthesis, fabrication and properties of nanostructured pure and doped tin oxide films. *Int. J. Sci. Res.* 2, 41–57.
- Yamazoe, N., Miura, N., 1992. Some basic aspects of semiconductor gas sensors. *Chem. Sens. Technol.* 4, 19–42.
- Yang, Z., Lv, L., Dai, Y., Xu, Z., Qian, D., 2010. Synthesis of ZnO–SnO₂ composite oxides by CTAB-assisted co-precipitation and photocatalytic properties. *Appl. Surf. Sci.* 256, 2898–2902.
- Yawalkar, A.A., Bhatkhande, D.S., Pangarkar, V.G., Beenackers, A.A., 2001. Solar-assisted photochemical and photocatalytic degradation of phenol. *J. Chem. Technol. Biotechnol.* 76, 363–370.
- You, H., Liu, R., Liang, C., Yang, S., Wang, F., Lu, X., Ding, B., 2013. Gold nanoparticle doped hollow SnO₂ supersymmetric nanostructures for improved photocatalysis. *J. Mater. Chem. A* 1, 4097–4104.
- Yu, H., Wang, S., Xiao, C., Xiao, B., Wang, P., Li, Z., Zhang, M., 2015. Enhanced acetone gas sensing properties by aurelia-like SnO₂ micro-nanostructures. *Cryst. Eng. Commun.* 17, 4316–4324.
- Yu, J., Qi, L., Jaroniec, M., 2010. Hydrogen production by photocatalytic water splitting over Pt/TiO₂ nanosheets with exposed (001) facets. *J. Phys. Chem. C* 114, 13118–13125.
- Zhang, G., Xie, C., Zhang, S., Zhang, S., Xiong, Y., 2014. Defect chemistry of the metal cation defects in the p- and n-doped SnO₂ nanocrystalline films. *J. Phys. Chem. C* 118, 18097–18109.
- Zhang, M., Sheng, G., Fu, J., An, T., Wang, X., Hu, X., 2005. Novel preparation of nanosized ZnO–SnO₂ with high photocatalytic activity by homogeneous co-precipitation method. *Mater. Lett.* 59, 3641–3644.
- Zhang, Y.C., Du, Z.N., Li, K.W., Zhang, M., Dionysiou, D.D., 2011. High-performance visible-light-driven SnS₂/SnO₂ nanocomposite photocatalyst prepared via in situ hydrothermal oxidation of SnS₂ nanoparticles. *ACS Appl. Mater. Interfaces* 3, 1528–1537.
- Zhang, Z., Shao, C., Li, X., Zhang, L., Xue, H., Wang, C., Liu, Y., 2010. Electrospun nanofibers of ZnO–SnO₂ heterojunction with high photocatalytic activity. *J. Phys. Chem. C* 114, 7920–7925.
- Zhou, H., Smith, D.W., 2002. Advanced technologies in water and wastewater treatment. *J. Environ. Eng. Sci.* 1, 247–264.
- Zulfiqar, Yang, Y., Wang, J., Ye, W., Ye, Z., Lu, J., 2016. Structural and optical properties of (Zn, Co) co-doped SnO₂ nano particles. *J. Mater. Sci. Mater. Electron.* 27, 12119–12127.

ACTA UNIVERSITATIS LAPPEENRANTAENSIS

722. KOTISALO, KAISA. Assessment of process safety performance in Seveso establishments. 2016. Diss.
723. LAINE, IGOR. Institution-based view of entrepreneurial internationalization. 2016. Diss.
724. MONTECINOS, WERNER EDUARDO JARA. Axial flux permanent magnet machines – development of optimal design strategies. 2016. Diss.
725. MULTAHARJU, SIRPA. Managing sustainability-related risks in supply chains. 2016. Diss.
726. HANNONEN, JANNE. Application of an embedded control system for aging detection of power converter components. 2016. Diss.
727. PARKKILA, JANNE. Connecting video games as a solution for the growing video game markets. 2016. Diss.
728. RINKINEN, SATU. Clusters, innovation systems and ecosystems: Studies on innovation policy's concept evolution and approaches for regional renewal. 2016. Diss.
729. VANADZINA, EVGENIA. Capacity market in Russia: addressing the energy trilemma. 2016. Diss.
730. KUOKKANEN, ANNA. Understanding complex system change for a sustainable food system. 2016. Diss.
731. SAVOLAINEN, JYRKI. Analyzing the profitability of metal mining investments with system dynamic modeling and real option analysis. 2016. Diss.
732. LAMPINEN, MATTI. Development of hydrometallurgical reactor leaching for recovery of zinc and gold. 2016. Diss.
733. SUHOLA, TIMO. Asiakaslähtöisyys ja monialainen yhteistyö oppilashuollossa: oppilashuolto prosessi systemisenä palvelukokonaisuutena. 2017. Diss.
734. SPODNIAK, PETR. Long-term transmission rights in the Nordic electricity markets: An empirical appraisal of transmission risk management and hedging. 2017. Diss.
735. MONTONEN, JUHO. Integrated hub gear motor for heavy-duty off-road working machines – Interdisciplinary design. 2017. Diss.
736. ALMANASRAH, MOHAMMAD. Hot water extraction and membrane filtration processes in fractionation and recovery of value-added compounds from wood and plant residues. 2017. Diss.
737. TOIVANEN, JENNI. Systematic complaint data analysis in a supply chain network context to recognise the quality targets of welding production. 2017. Diss.
738. PATEL, GITESHKUMAR. Computational fluid dynamics analysis of steam condensation in nuclear power plant applications. 2017. Diss.
739. MATTHEWS, SAMI. Novel process development in post-forming of an extruded wood plastic composite sheet. 2017. Diss.
740. KÄHKÖNEN, TOMMI. Understanding and managing enterprise systems integration. 2017. Diss.

741. YLI-HUUMO, JESSE. The role of technical dept in software development. 2017. Diss.
742. LAYUS, PAVEL. Usability of the submerged arc welding (SAW) process for thick high strength steel plates for Arctic shipbuilding applications. 2017. Diss.
743. KHAN, RAKHSHANDA. The contribution of socially driven businesses and innovations to social sustainability. 2017. Diss.
744. BIBOV, ALEKSANDER. Low-memory filtering for large-scale data assimilation. 2017. Diss.
745. ROTICH, NICOLUS KIBET. Development and application of coupled discrete and continuum models in solid particles classification. 2017. Diss.
746. GAST, JOHANNA. The coopetition-innovation nexus: Investigating the role of coopetition for innovation in SMEs. 2017. Diss.
747. KAPOOR, RAHUL. Competition and disputes in the patent life cycle. 2017. Diss.
748. ALI-MARTTILA, MAAREN. Towards successful maintenance service networks – capturing different value creation strategies. 2017. Diss.
749. KASHANI, HAMED TASALLOTI. On dissimilar welding: a new approach for enhanced decision-making. 2017. Diss.
750. MVOLA BELINGA, ERIC MARTIAL. Effects of adaptive GMAW processes: performance and dissimilar weld quality. 2017. Diss.
751. KARTTUNEN, JUSSI. Current harmonic compensation in dual three-phase permanent magnet synchronous machines. 2017. Diss.
752. SHI, SHANSHUANG. Development of the EAST articulated maintenance arm and an algorithm study of deflection prediction and error compensation. 2017. Diss.
753. CHEN, JIE. Institutions, social entrepreneurship, and internationalization. 2017. Diss.
754. HUOTARI, PONTUS. Strategic interaction in platform-based markets: An agent-based simulation approach. 2017. Diss.
755. QU, BIN. Water chemistry and greenhouse gases emissions in the rivers of the "Third Pole" / Water Tower of Asia". 2017. Diss.
756. KARHU, PÄIVI. Cognitive ambidexterity: Examination of the cognitive dimension in decision-making dualities. 2017. Diss.
757. AGAFONOVA, OXANA. A numerical study of forest influences on the atmospheric boundary layer and wind turbines. 2017. Diss.
758. AZAM, RAHAMATHUNNISA MUHAMMAD. The study of chromium nitride coating by asymmetric bipolar pulsed DC reactive magnetron sputtering. 2017. Diss.
759. AHI, MOHAMADALI. Foreign market entry mode decision-making: Insights from real options reasoning. 2017. Diss.

